



## BUDAPEST UNIVERSITY OF TECHNOLOGY AND ECONOMICS

DOCTORAL THESIS

---

# Modelling of maize plant by the discrete element method

---

*Author:*  
Ádám KOVÁCS

*Supervisor:*  
Dr. György KERÉNYI

Department of Machine and Product Design  
1 Bertalan Lajos str., Budapest, H-1111



A dissertation submitted in fulfilment for the degree of

*Doctor of Philosophy*

*in the*

Géza Pattantyús-Ábrahám Doctoral School of Mechanical Engineering  
Faculty of Mechanical Engineering

September 13, 2019



# Declaration of Authorship

I, Ádám KOVÁCS, declare that this thesis titled, "Modelling of maize plant by the discrete element method" and the work presented in it are my own. I confirm that:

- this work was done entirely or mainly while in candidature for a PhD degree at this University;
- where any part of this thesis has previously been submitted for a degree or any other qualification at this University or any other institution, this has been clearly stated;
- where I have consulted the published work of others, this is always clearly attributed;
- where I have quoted from the work of others, the source is always given. With the exception of such quotations, this thesis is entirely my own work;
- I have acknowledged all main sources of help;
- where the thesis is based on work done by myself jointly with others, I have made clear exactly what was done by others and what I have contributed myself.

## In Hungarian:

Alulírott Kovács Ádám kijelentem, hogy ezt a doktori értekezést, "Kukorica növény feldolgozásának modellezése diszkrét elem módszerrel", magam készítettem és abban csak a megadott forrásokat használtam fel. minden olyan részt, amelyet szó szerint, vagy azonos tartalomban, de átfogalmazva más forrásból átvettettem, egyértelműen, a forrás megadásával megjelöltem.

## Publications based on this thesis:

- [1] **Ádám Kovács**, György Kerényi. Physical properties and mechanical behaviour of maize stalk for machine development. International Agrophysics. *Accepted, April 2019*.
- [2] **Ádám Kovács**, György Kerényi (2016). Stochastic variation in discrete element method (DEM) for agricultural simulations. Hungarian Agricultural Engineering, 30, 31-38.
- [3] **Ádám Kovács**, István J. Jóri, Katalin Gaál, Attila Piros, György Kerényi (2015). Development of measurement methods for a numerical simulation of corn plants. Mechanical Engineering Letters, Szent István University, 13, 88-96.
- [4] **Ádám Kovács**, Krisztián Kotrocz, György Kerényi (2015). The adaptability of discrete element method (DEM) in agricultural machine design. Hungarian Agricultural Engineering, 27, 14-19.
- [5] **Ádám Kovács**, György Kerényi (2018). A new method to calibrate discrete element models of fibrous agricultural materials. European Agricultural Engineering Conference 2018 (EurA-Eng 2018), Wageningen, the Netherlands, July 8-12, 2018.
- [6] **Ádám Kovács**, Péter Tamás Zwierczyk (2018). Coupled DEM-FEM simulation on maize harvesting. 32nd European Conference on Modelling and Simulation (ECMS 2018), Wilhelmshaven, Germany, May 22-25, 2018.

- [7] **Ádám Kovács**, István J. Jóri, György Kerényi (2017). A new discrete element model (DEM) for maize. 75th International Conference on Agricultural Engineering (Land.Technik AgEng 2017), Hannover, Germany, November 10-11, 2017.
- [8] **Ádám Kovács**, György Kerényi (2017). Modelling of corn ears by discrete element method (DEM). 31st European Conference on Modelling and Simulation (ECMS 2017), Budapest, Hungary, May 23-26, 2017.
- [9] **Ádám Kovács**, Péter János Rádics, György Kerényi (2017). A discrete element model for agricultural decision support. 31st European Conference on Modelling and Simulation (ECMS 2017), Budapest, Hungary, May 23-26, 2017.
- [10] **Ádám Kovács**, György Kerényi (2016). Comparative analysis of different geometrical structures of discrete element method (DEM) for fibrous agricultural materials. 4th CIGR International Conference of Agricultural Engineering (CIGR-AgEng 2016), Aarhus, Denmark, June 26-29, 2016.
- [11] **Ádám Kovács**, István J. Jóri, Katalin Gaál, Attila Piros, György Kerényi (2015). Development of measurement methods for a numerical simulation of corn plants. IV. Synergy International Conference - Engineering, Agricultural and Green Industry Innovation: Book of Papers, Paper P5-9-095, 1-6.
- [12] **Ádám Kovács**, György Kerényi (2018). Új kalibrálási módszer szálas mezőgazdasági anyagok diszkrét elemes modelljeihez. Mezőgazdasági Technika, 59(8), 2-5.
- [13] **Ádám Kovács**, Péter Tamás Zwierczyk, György Kerényi (2017). Kapcsolt véges és diszkrét elemes szimulációk (FEA-DEM) alkalmazása a mezőgazdasági géptervezésben. XXV. Nemzetközi Gépészeti Találkozó, Kolozsvár, Romania, April 27-30, 2017.
- [14] **Ádám Kovács**, György Kerényi (2016). Mezőgazdasági szálas anyagok modellezése diszkrét elemes módszerrel (DEM). Mezőgazdasági Technika, 57(10), 2-5.
- [15] **Ádám Kovács**, György Kerényi (2016). Diszkrét elemes módszer (DEM) alkalmazásának lehetősége a mezőgazdasági géptervezésben. XXIV. Nemzetközi Gépészeti Találkozó, Déva, Romania, April 21-24, 2016.
- [16] **Ádám Kovács**, István J. Jóri, György Kerényi, Katalin Gaál (2015). Mérési módszerek kifejlesztése kukorica növény numerikus szimulációjához. Mezőgazdasági Technika, 56(12), 2-5.

Signed:

---

Date:

---

*"Agriculture is not crop production as popular belief holds - it's the production of food and fiber from the world's land and waters. Without agriculture it is not possible to have a city, stock market, banks, university, church or army. Agriculture is the foundation of civilization and any stable economy."*

Allan Savory



BUDAPEST UNIVERSITY OF TECHNOLOGY AND ECONOMICS

## *Abstract*

Faculty of Mechanical Engineering  
Department of Machine and Product Design

Doctor of Philosophy

**Modelling of maize plant by the discrete element method**

by Ádám KOVÁCS

Numerical modelling is a powerful engineering tool that has been successfully applied across many fields, however, despite its ubiquity, the simulation of interactions among fibrous agricultural materials and machine parts during agricultural processes remain a challenge to simulate due to the complex structures of plants and the complex machine dynamics and scale. This study presents and validates a Discrete Element Method (DEM) simulation methodology for maize harvesting.

To explore the physical characteristic, mechanical behaviour and breakage of the plant, a measurement method was established that consists of in-situ and laboratory experiments. The method was successfully conducted through the days of harvesting. As related to the physical properties of the stalk, the distribution of the internodal diameter, length, mass and moisture content on the stalk were determined. The position, shape, diameter, length and mass of maize ears, as well as the diameter and length of the shank were also analysed regarding the physical properties. The mechanical behaviour of the stalk was analysed through sectional and local transversal compression, three-point bending, cantilever bending and dynamic cutting experiments, while, the mechanical behaviour of the shank and the ear was analysed by ear-detachment and drop tests. The results clearly demonstrate that the physical properties and mechanical behaviour of different parts of maize vary significantly. Therefore, different parts of maize require different considerations during model development.

A DEM model of the stalk, shank and maize ear was constructed. For the stalk a complex shell and core system, similar to the real stalk's structure, was created. A simplified geometrical structure (chain of spheres) was applied for the shank and the maize ear was created as one particle with multiple spherical surfaces. Particles were bonded together using a rigorous Timoshenko Beam Bond Model to form the plant. The influence of the bonded, non-bonded, bond-fabric and numerical model parameters on the mechanical behaviour and breakage of the virtual plant parts was analysed through the virtual representation of each laboratory experiment. Through an optimization process the optimal set of parameters was determined to simulate the mechanical behaviour and breakage of the plant in each loading case with the highest precision. The DEM simulated results of the virtual sample were compared with the outcomes of the real experiments. Finally, a technological simulation based on the process of maize harvesting was carried out by using the calibrated plant model and a virtual maize header unit. The conclusions clearly show that the accuracy of the presented DEM model with the determined parameter set is suitable for the analysis of the interactions between the maize stalk and the maize header during harvesting.



## *Acknowledgements*

The writing and completion of this Dissertation would not have been possible without the excellent assistance, support and guidance of my Supervisor, Dr György Kerényi, and the Head of the Department of Machine and Product Design at BUTE, Dr Péter Horák. I would also like to thank my friends and colleagues within the Agricultural Engineering Research Group: Prof István J. Jóri for his encouragement and guidance through my BSc, MSc and PhD studies; Dr János Péter Rádics for his suggestions regarding the project management and Dr Péter Tamás Zwierczyk (honorary agricultural machine designer ☺) for his advices regarding how to survive the PhD studies. Special thanks to Dr Gábor Székely from the Department of Polymer Engineering, Dr Imre Orbúló from the Department of Material Science and Engineering and Dr Tibor Poós from the Department of Building Services and Process Engineering at BUTE for the help they provided in the laboratory experiments. I also appreciate the provided meteorological data regarding the experimental plot by the Hungarian Meteorological Service (OMSZ).

I also would like to express my special thanks of gratitude to Prof Jin Y. Ooi and Dr John Paul Morrissey from the Institute for Infrastructure and Environment, School of Engineering, The University of Edinburgh for their endless help during the model formation. Without their assistance I would take the wrong approach. I appreciate the assistance and support of EDEM Team (DEM Solutions Ltd, Edinburgh, Scotland) as well, especially through discussions with Carles Bosch Padros and Stephen Cole; and permission for extra licenses by Julia Kokocinska and Jennifer Currie.

I really appreciate the advices of Prof Dr László Fenyvesi (Faculty of Mechanical Engineering, Szent István University, Gödöllő) and Dr Ferenc Safranyik (Savaria Institute of Technology, Faculty of Informatics, Eötvös Loránd University, Szombathely) to finalize my Dissertation.

At this point, I would like to thank my friend, László Soós for his assistance and cheerfulness during the experiments... ☺ I also appreciate the help of my friends: Dr Róbert Imre Csehi, Domonkos Ferenc Nagy, György Szakál, Szilárd Kardos and Tamás Bokor for proofreading my Dissertation and listening to my complaints all the time.

I would like to thank my parents and grandparents. They all provided me enduring love and support during my long journey in the labyrinth of study. Special thanks for my Dad, who showed me the beauty of agricultural engineering during my childhood.

Last, but not least I would like to thank my wife, Adri. There is no doubt that behind every successful man there is a great woman ... usually, his wife! ☺



# Contents

<b>Declaration of Authorship</b>	<b>iii</b>
<b>Abstract</b>	<b>vii</b>
<b>Acknowledgements</b>	<b>ix</b>
<b>1 Introduction</b>	<b>1</b>
1.1 Agricultural Machine Design . . . . .	1
1.2 Maize . . . . .	1
1.3 Research Scope and Objective . . . . .	2
<b>2 Literature Review</b>	<b>3</b>
2.1 Harvesting of Maize . . . . .	3
2.2 Experimental Studies on Agricultural Plants . . . . .	4
2.2.1 Preparation of Test Materials . . . . .	4
2.2.2 Environmental Conditions . . . . .	4
2.2.3 Physical and Morphological Properties . . . . .	5
2.2.4 Transversal Compression Tests . . . . .	5
2.2.5 Flexural Tests . . . . .	5
2.2.6 Cutting Tests . . . . .	6
2.2.7 Crop-Detachment Tests . . . . .	6
2.2.8 Crop-Collision Tests . . . . .	6
2.3 A Brief Review of Discrete Element Method . . . . .	7
2.4 DEM Studies on Agricultural Plants . . . . .	8
2.4.1 Shape Representation and Contact Models . . . . .	8
2.4.2 Calibration and Validation Methods . . . . .	9
2.4.3 Technological Simulations . . . . .	10
2.5 Conclusions and Limitations of Previous Studies . . . . .	10
<b>3 Experimental Materials and Methods</b>	<b>13</b>
3.1 Experimental Plot and Cultivation of Maize . . . . .	13
3.2 Environmental Conditions . . . . .	13
3.3 Collection and Preparation of The Test Material . . . . .	14
3.4 Physical and Morphological Characteristic of Maize . . . . .	15
3.5 Mechanical Behaviour of Maize . . . . .	18
<b>4 Experimental Results</b>	<b>21</b>
4.1 Physical Characteristic . . . . .	21
4.1.1 Maize Stalk . . . . .	21
4.1.2 Maize Ear and Shank . . . . .	22
4.2 Mechanical Behaviour . . . . .	24
4.2.1 Sectional Transversal Compression . . . . .	24
4.2.2 Local Transversal Compression . . . . .	26

4.2.3	Three-Point Bending . . . . .	29
4.2.4	Cantilever Bending . . . . .	31
4.2.5	Dynamic Cutting . . . . .	32
4.2.6	Ear-Detachment and Collision . . . . .	33
4.3	Conclusions . . . . .	35
4.3.1	Physical Characteristic of Maize . . . . .	35
4.3.2	Mechanical Behaviour of Maize . . . . .	35
<b>5</b>	<b>Numerical Simulations</b>	<b>39</b>
5.1	EDEM Software Package . . . . .	39
5.2	Model Formation . . . . .	40
5.2.1	Physical Model of The Plant . . . . .	41
5.2.2	Bonded Structure of The Plant . . . . .	44
5.2.3	Virtual Models of The Experiments . . . . .	46
5.3	Parametric Study . . . . .	47
5.3.1	Reference Models . . . . .	48
5.3.2	Bonded Contact Parameters . . . . .	49
5.3.3	Non-Bonded Contact Parameters . . . . .	51
5.3.4	Bond Fabric Parameters . . . . .	52
5.3.5	Numerical Parameters . . . . .	52
5.4	Calibration and Validation . . . . .	52
5.5	Technological Simulation of Harvesting . . . . .	54
<b>6</b>	<b>Results of The Parametric Study</b>	<b>57</b>
6.1	Reference Models . . . . .	57
6.1.1	Sectional Transversal Compression . . . . .	57
6.1.2	Three-Point Bending . . . . .	59
6.1.3	Dynamic Cutting . . . . .	59
6.1.4	Ear-Detachment and Collision . . . . .	62
6.2	Influence of Bonded Contact Parameters . . . . .	63
6.2.1	Bond Young's modulus . . . . .	63
6.2.2	Bond Poisson's ratio . . . . .	67
6.2.3	Tensile Strength of The Bonds . . . . .	67
6.2.4	Shear Strength of The Bonds . . . . .	71
6.2.5	Coefficient of Variation of The Strength Parameters . . . . .	73
6.3	Influence of Non-Bonded Contact Parameters . . . . .	75
6.3.1	Particle Young's modulus . . . . .	75
6.3.2	Particle-Particle Coefficient of Static Friction . . . . .	75
6.3.3	Particle-Geometry Coefficient of Static Friction . . . . .	76
6.3.4	Particle-Geometry Coefficient of Restitution . . . . .	78
6.4	Influence of Bond Fabric Parameters . . . . .	78
6.4.1	Contact Radius Multiplier . . . . .	78
6.4.2	Bond Radius Multiplier . . . . .	80
6.5	Influence of Numerical Parameters . . . . .	81
6.5.1	Time Step . . . . .	81
6.5.2	Global Damping . . . . .	83
6.6	Conclusions . . . . .	83

<b>7 Results of The Calibration</b>	<b>87</b>
7.1 Virtual Maize Stalk . . . . .	87
7.2 Virtual Ear and Shank . . . . .	97
7.3 Conclusions . . . . .	98
<b>8 Results of Harvesting Simulation</b>	<b>101</b>
<b>9 Conclusions and Recommendations</b>	<b>103</b>
9.1 General Conclusions . . . . .	103
9.1.1 Experimental Work . . . . .	103
9.1.2 DEM Simulations . . . . .	103
9.2 Recommendations for Future Work . . . . .	104
9.2.1 Experimental Work . . . . .	104
9.2.2 DEM Simulations . . . . .	104
<b>10 Theses</b>	<b>105</b>
<b>11 Tézisek</b>	<b>111</b>
<b>12 Összefoglalás</b>	<b>117</b>
<b>Bibliography</b>	<b>119</b>
<b>A Experimental Results</b>	<b>123</b>
<b>B Reference Models</b>	<b>129</b>
<b>C Bonded Contact Parameters</b>	<b>143</b>
<b>D Non-Bonded Contact Parameters</b>	<b>181</b>
<b>E Applied Contact Models</b>	<b>209</b>
E.1 Hertz-Mindlin Contact Model . . . . .	209
E.2 Timoshenko Beam Bonded Model . . . . .	211



# List of Figures

1.1	Parts of a maize plant . . . . .	2
2.1	Parts of a common maize header . . . . .	3
3.1	Division and major directions of maize parts . . . . .	14
3.2	Measurements on the physical characteristic . . . . .	16
3.3	Experiments on the mechanical behaviour . . . . .	19
4.1	Physical characteristic of the maize stalk . . . . .	22
4.2	Average shape and mean centre of mass of maize ears . . . . .	23
4.3	Typical force response of the internodal sections by sectional transversal compression experiment . . . . .	24
4.4	Mechanical characteristic of the internodal section by sectional transversal compression . . . . .	25
4.5	Major breaking events of internodal stalk sections during sectional transversal compression . . . . .	26
4.6	Force response characteristic by local transversal compression experiment . . . . .	27
4.7	Required compressive work characteristics by local transversal compression experiments . . . . .	28
4.8	Typical damage and breaking phenomena by local transversal compression experiment . . . . .	28
4.9	Force response characteristic by three-point bending . . . . .	29
4.10	Bending work characteristics by three-point bending . . . . .	30
4.11	Typical breakage of the samples by three-point bending experiment . . . . .	31
4.12	Results of cantilever bending experiment. . . . .	32
4.13	Results of dynamic cutting experiment. . . . .	33
4.14	Results of ear detachment experiment . . . . .	34
5.1	EDEM simulation sequence . . . . .	39
5.2	DEM geometrical model of the plant . . . . .	41
5.3	DEM geometrical model of the 4 <sup>th</sup> internodal section of a maize stalk. . . . .	43
5.4	Projected view through the central axis of a bond connecting particles A and B . .	45
5.5	DEM bond structure of the 4 <sup>th</sup> internodal section of a maize stalk. . . . .	45
5.6	Virtual model of the shank with the maize ear. . . . .	46
5.7	Virtual models of the test apparatuses. . . . .	47
5.8	Analysis of the loading direction dependency. . . . .	50
5.9	Calibration and validation method for the virtual maize plant. . . . .	53
5.10	CAD model of a common maize header . . . . .	55
5.11	Initialization of the maize plant. . . . .	55
6.1	Force response for the reference simulation cases of sectional transversal compression. . . . .	58
6.2	Number of broken bonds during the reference simulation cases of sectional transversal compression. . . . .	58

6.3	Force response for the reference simulation cases of three-point bending. . . . .	60
6.4	Number of broken bonds during the reference simulation cases of three-point bending. . . . .	60
6.5	Force response for the reference simulation cases of dynamic cutting. . . . .	61
6.6	Number of broken bonds during the reference simulation cases of dynamic cutting. . . . .	61
6.7	Reference simulation cases of ear-detachment simulation. . . . .	62
6.8	Reference simulation cases of ear-collision simulation. . . . .	63
6.9	Influence of the bond Young's modulus on the force response by sectional transversal compression. . . . .	64
6.10	Influence of the ratio between the bond Young's modulus in the core and in tangential direction of the skin on the force response by sectional transversal compression. . . . .	64
6.11	Influence of the bond Young's modulus on the force response by three-point bending. . . . .	65
6.12	Influence of the bond Young's modulus by dynamic cutting. . . . .	66
6.13	Influence of the bond Young's modulus by ear-detachment. . . . .	66
6.14	Influence of the bond tensile strength in transversal direction of the skin by sectional transversal compression. . . . .	67
6.15	Influence of the bond tensile strength the core by sectional transversal compression. . . . .	68
6.16	Influence of the tensile strength of the bonds in the core by three-point bending. . . . .	69
6.17	Influence of the tensile strength of the bonds in transversal direction of the skin by three-point bending. . . . .	69
6.18	Influence of the tensile strength of the bonds in longitudinal direction of the skin by dynamic cutting. . . . .	70
6.19	Influence of the tensile strength of the bonds in the shank by ear-detachment. . . . .	71
6.20	Influence of the shear strength of the bonds in transversal direction of the skin by three-point bending. . . . .	72
6.21	Influence of the shear strength of the bonds in longitudinal direction of the skin by dynamic cutting. . . . .	72
6.22	Influence of the coefficient of variation of the bonded strength parameters by sectional transversal compression. . . . .	73
6.23	Influence of the coefficient of variation of the bonded strength parameters by three-point bending. . . . .	74
6.24	Influence of the coefficient of variation of the bonded strength parameters by dynamic cutting. . . . .	74
6.25	Influence of the particle Young's modulus by sectional transversal compression. . . . .	75
6.26	Influence of the particle-particle coefficient of static friction by sectional transversal compression. . . . .	76
6.27	Influence of the particle-geometry coefficient of static friction by three-point bending. . . . .	77
6.28	Influence of the particle-geometry coefficient of static friction by dynamic cutting. . . . .	77
6.29	Influence of the coefficient of restitution among the maize ear and the geometry elements by ear-collision. . . . .	78
6.30	Influence of the contact radius multiplier by sectional transversal compression. . . . .	79
6.31	Influence of the contact radius multiplier by three-point bending. . . . .	79
6.32	Influence of the bond radius multiplier by sectional transversal compression. . . . .	80
6.33	Influence of the bond radius multiplier by three-point bending. . . . .	81
6.34	Influence of the time step by sectional transversal compression. . . . .	82
6.35	Influence of the time step by dynamic cutting. . . . .	82
6.36	Influence of the global damping by dynamic cutting. . . . .	83

7.1	Comparison of the physical characteristic of the virtual and the real maize stalk.	87
7.2	Comparison of the DEM predicted and experimental results by sectional transversal compression. . . . .	89
7.3	Comparison of the DEM predicted and experimental breakage by sectional transversal compression. . . . .	90
7.4	Comparison of the DEM predicted and experimental results by three-point bending. . . . .	91
7.5	Comparison of the DEM predicted and experimental breakage by three-point bending. . . . .	92
7.6	Stages of the cutting process. . . . .	93
7.7	Comparison of the DEM predicted and experimental results by dynamic cutting. . . . .	94
7.8	Comparison of the DEM predicted and experimental results by local transversal compression. . . . .	95
7.9	Comparison of the DEM predicted and experimental breakage by local transversal compression. . . . .	96
7.10	Comparison of the DEM predicted and experimental results by cantilever bending. . . . .	97
7.11	Comparison of the DEM predicted and experimental results by ear-detachment. . . . .	98
8.1	Process analysis on the stalk rollers and the chopping unit by harvesting simulation. . . . .	101
8.2	Chopped material. . . . .	102
8.3	Process analysis on the detachment. . . . .	102
10.1	Calibration and validation method for the virtual maize plant. . . . .	107
11.1	A kukoricanövény DEM modelljének kalibrálási és validálási módszere. . . . .	113
A.1	Observed maize ears. . . . .	123
A.2	Meteorological data from the experimental plot. . . . .	124
A.3	Measured force response by sectional transversal compression. . . . .	125
A.4	Measured force response by local transversal compression. . . . .	126
A.5	Measured force response by three-point bending. . . . .	127
A.6	Each measured force response by cantilever bending. . . . .	128
A.7	Each measured force response by ear-detachment. . . . .	128
B.1	Breakage during the reference simulation cases of sectional transversal compression. . . . .	130
B.2	Results of the analysis on the loading direction at the bottom position by sectional transversal compression. . . . .	131
B.3	Breakage during the analysis on the loading direction at the bottom position by sectional transversal compression. . . . .	132
B.4	Results of the analysis on the loading direction at the middle position by sectional transversal compression. . . . .	133
B.5	Breakage during the analysis on the loading direction at the middle position by sectional transversal compression. . . . .	134
B.6	Results of the analysis on the loading direction at the top position by sectional transversal compression. . . . .	135
B.7	Breakage during the analysis on the loading direction at the top position by sectional transversal compression. . . . .	136
B.8	Breakage during the reference simulation cases of three-point bending. . . . .	137
B.9	Results of the analysis on the loading direction by three-point bending. . . . .	138
B.10	Breakage during the analysis on the loading direction by three-point bending. . . . .	139

B.11 Breakage during the reference simulation cases of dynamic cutting. . . . .	140
B.12 Results of the analysis on the loading direction by dynamic cutting. . . . .	141
B.13 Breakage during the loading direction simulation cases of dynamic cutting. . . . .	142
C.1 Influence of the bond Young's modulus by sectional transversal compression. .	144
C.2 Influence of the bond Young's modulus on the breakage by sectional transversal compression. . . . .	145
C.3 Influence of the ratio between the bond Young's modulus in the core and in tangential direction of the skin by sectional transversal compression. . . . .	146
C.4 Influence of the ratio between the bond Young's modulus in the core and in tangential direction of the skin on the breakage by sectional transversal compression.	147
C.5 Influence of the Young's modulus by three-point bending. . . . .	148
C.6 Influence of the Young's modulus on the breakage by three-point bending. . . . .	149
C.7 Influence of the bond Young's modulus by dynamic cutting. . . . .	150
C.8 Influence of the bond Young's modulus on the breakage by dynamic cutting dynamic cutting. . . . .	151
C.9 Influence of the Poisson's ratio by sectional transversal compression. . . . .	152
C.10 Influence of the Poisson's ratio on the breakage by sectional transversal compression. . . . .	153
C.11 Influence of the bond Poisson's ratio by three-point bending. . . . .	154
C.12 Influence of the bond Poisson's ratio on the breakage by three-point bending. .	155
C.13 Influence of the bond Poisson's ratio by dynamic cutting. . . . .	156
C.14 Influence of the bond Poisson's ratio on the breakage by dynamic cutting dynamic cutting. . . . .	157
C.15 Influence of the tensile strength of the bond in tangential direction of the skin by sectional transversal compression. . . . .	158
C.16 Influence of the tensile strength of the bond in tangential direction of the skin on the breakage by sectional transversal compression. . . . .	159
C.17 Influence of the tensile strength of the bond in the core by sectional transversal compression. . . . .	160
C.18 Influence of the tensile strength of the bond in the core on the breakage by sectional transversal compression. . . . .	161
C.19 Influence of the tensile strength of the bonds in the core by three-point bending. .	162
C.20 Influence of the tensile strength of the bonds in the core on the breakage by three-point bending. . . . .	163
C.21 Influence of the ratio between the tensile and shear strength of the bonds in tangential direction of the skin by three-point bending. . . . .	164
C.22 Influence of the ratio between the tensile and shear strength of the bonds in tangential direction of the skin on the breakage by three-point bending. . . . .	165
C.23 Influence of the tensile strength of the bonds in longitudinal direction of the skin by dynamic cutting. . . . .	166
C.24 Influence of the tensile strength of the bonds in longitudinal direction of the skin on the breakage by dynamic cutting dynamic cutting. . . . .	167
C.25 Influence of the ratio between the tensile and shear strength of the bonds in longitudinal direction of the skin by dynamic cutting. . . . .	168
C.26 Influence of the ratio between the tensile and shear strength of the bonds in longitudinal direction of the skin on the breakage by dynamic cutting dynamic cutting. . . . .	169
C.27 Influence of the shear strength of the bonds in tangential direction of the skin by three-point bending. . . . .	170

C.28 Influence of the shear strength of the bonds in tangential direction of the skin on the breakage by three-point bending. . . . .	171
C.29 Influence of the shear strength of the bonds in longitudinal direction of the skin by dynamic cutting. . . . .	172
C.30 Influence of the shear strength of the bonds in longitudinal direction of the skin on the breakage by dynamic cutting dynamic cutting. . . . .	173
C.31 Influence of the coefficient of variation of the bonded strength parameters by sectional transversal compression. . . . .	174
C.32 Influence of the coefficient of variation of the bonded strength parameters on the breakage by sectional transversal compression. . . . .	175
C.33 Influence of the coefficient of variation of the bonded strength parameters by three-point bending. . . . .	176
C.34 Influence of the coefficient of variation of the bonded strength parameters on the breakage by three-point bending. . . . .	177
C.35 Influence of the coefficient of variation of the bonded strength parameters by dynamic cutting. . . . .	178
C.36 Influence of the coefficient of variation of the bonded strength parameters on the breakage by dynamic cutting dynamic cutting. . . . .	179
D.1 Influence of the particle Young's modulus by sectional transversal compression. . . . .	182
D.2 Influence of the particle Young's modulus on the breakage by sectional transversal compression. . . . .	183
D.3 Influence of the particle-particle coefficient of static friction by sectional transversal compression. . . . .	184
D.4 Influence of the particle-particle coefficient of static friction on the breakage by sectional transversal compression. . . . .	185
D.5 Influence of the particle-geometry coefficient of static friction by three-point bending. . . . .	186
D.6 Influence of the particle-geometry coefficient of static friction on the breakage by three-point bending. . . . .	187
D.7 Influence of the particle-geometry coefficient of static friction by dynamic cutting. . . . .	188
D.8 Influence of the the particle-geometry coefficient of static friction on the breakage by dynamic cutting dynamic cutting. . . . .	189
D.9 Influence of the coefficient of restitution by dynamic cutting. . . . .	190
D.10 Influence of the coefficient of restitution on the breakage by dynamic cutting dynamic cutting. . . . .	191
D.11 Influence of the contact radius multiplier by sectional transversal compression. . . . .	192
D.12 Influence of the contact radius multiplier on the breakage by sectional transversal compression. . . . .	193
D.13 Influence of the contact radius multiplier by three-point bending. . . . .	194
D.14 Influence of the contact radius multiplier on the breakage by three-point bending. . . . .	195
D.15 Influence of the contact radius multiplier by sectional transversal compression. . . . .	196
D.16 Influence of the contact radius multiplier on the breakage by sectional transversal compression. . . . .	197
D.17 Influence of the bond radius multiplier by three-point bending. . . . .	198
D.18 Influence of the bond radius multiplier on the breakage by three-point bending. . . . .	199
D.19 Influence of the time step by sectional transversal compression. . . . .	200
D.20 Influence of the time step on the breakage by sectional transversal compression. . . . .	201
D.21 Influence of the time step by dynamic cutting. . . . .	202
D.22 Influence of the time step on the breakage by dynamic cutting dynamic cutting. . . . .	203
D.23 Influence of the global damping by sectional transversal compression. . . . .	204

D.24 Influence of the global damping on the breakage by sectional transversal compression. . . . .	205
D.25 Influence of the global damping by dynamic cutting. . . . .	206
D.26 Influence of the global damping on the breakage by dynamic cutting dynamic cutting. . . . .	207
E.1 A two particle spring dashpot configuration. . . . .	209
E.2 Explanation for the contact and physical radii of the particles. . . . .	211
E.3 Projected view through the central axis of a bond connecting particles A and B. . . . .	212
E.4 Comparing three values for coefficient of variation of strength. . . . .	216

# List of Tables

3.1	Comparison of the environmental requirements of maize and the collected data.	14
4.1	Correlation coefficients ( $r$ ) and mean ratios ( $\phi$ ) among the analysed traits. . . . .	23
5.1	Physical properties of the virtual stalk: outer diameter ( $d^{IN}$ ); internodal length ( $L^{IN}$ ); particle diameter in the skin ( $d_p^S$ ); number of particles in the skin ( $N_p^S$ ); particle diameter range in the poly-disperse core ( $d_p^C$ ); number of particles in the core ( $N_p^C$ ); particle density ( $\rho_p$ ). . . . .	43
5.2	Initially determined X-Y coordinates of the virtual shank. . . . .	44
5.3	Length coordinates and radius of the spherical surfaces in the virtual maize ear. .	44
5.4	Bonded and non-bonded input parameters of the internodal reference model. . .	49
5.5	Bonded input parameters for the reference model of the shank with the maize ear.	49
5.6	Range of the analysed bonded parameters. . . . .	51
5.7	Range of the analysed non-bonded parameters. . . . .	52
6.1	Summary of the influence of the parameters on the mechanical behaviour and breakage of the virtual samples during sectional transversal compression. . . . .	85
6.2	Summary of the influence of the parameters on the mechanical behaviour and breakage of the virtual samples during three-point bending simulation. . . . .	85
6.3	Summary of the influence of the parameters on the mechanical behaviour and breakage of the virtual samples during dynamic cutting simulation. . . . .	86
6.4	Summary of the influence of the parameters on the mechanical behaviour and breakage of the virtual samples during ear-detachment simulation. . . . .	86
7.1	Validated bonded and non-bonded input parameters for the virtual stalk. . . . .	88
10.1	Coefficient of restitution among the maize ear and different plates. . . . .	106
10.2	Range of the analysed contact model parameters. . . . .	107
11.1	Kukoricacső ütközési tényezője különböző felületeken. . . . .	112
11.2	A paraméterérzékenység vizsgálat során elemzett paraméterek érték tartományai.	113



# List of Symbols

## Upper-case Roman symbols

<i>A</i>	Elemental area
<i>C</i>	Distance of centre of mass from the origin
<i>CI</i>	Confidence interval
<i>CI%</i>	Percentage of the confidence interval to the mean
<i>CR</i>	Measured coefficient of restitution
<i>DoP</i>	Displacement of peak force
<i>E</i>	Young's modulus
<i>F</i>	Force
<i>F<sub>0</sub></i>	Results of F-probe
<i>H</i>	Drop height
<i>L</i>	Length
<i>MC</i>	Moisture content
<i>N</i>	Particle number
<i>S</i>	Mean bond strength
<i>W</i>	Work
<i>X; Y</i>	Variables
<i>Z</i>	Student's number

## Lower-case Roman symbols

<i>d</i>	Diameter
<i>e</i>	Numerical coefficient of restitution
<i>f</i>	Degree of freedom
<i>g</i>	Gravitational acceleration ( $9.81 \text{ m} \cdot \text{s}^{-2}$ )
<i>h</i>	Bounce height
<i>k</i>	Distance of the elemental area from the origin
<i>l</i>	Length of the pendulum's swinging part
<i>m</i>	Mass
<i>n</i>	Number of the data points
<i>p</i>	Position index
<i>q; v</i>	Participants of each population
<i>r</i>	Correlation coefficient
<i>s</i>	Displacement
<i>t</i>	Student's t-distribution
<i>t<sub>0</sub>"</i>	T-value for two-sample t-test
<i>w</i>	Width

## Greek symbols

$\alpha$	Maximum angle of deflection before cutting
$\beta$	Maximum angle of deflection after cutting
$\delta$	Diameter ratio
$\Delta t$	Time step

$\zeta$	Coefficient of variation for the bond strength component
$\eta$	Contact radius multiplier
$\theta$	Static friction
$\vartheta$	Rolling friction
$\iota$	Global damping coefficient
$\kappa$	Compression rate
$\lambda$	Length ratio
$\Lambda$	Bond radius multiplier
$\mu$	Wet-mass ratio
$\nu$	Poisson's ratio
$\rho$	Density
$\sigma$	Standard deviation
$\phi$	Ratio between two parameters
$\omega$	Specific work

### Subscripts

$B$	Bond
$c$	Constant
$C$	Compressive
$crit$	Critical
$d$	Dry
$e$	Equivalent
$G$	Geometry
$m$	Maximal
$p$	Position index
$P$	Particle
$S$	Shear
$t$	Total
$T$	Tensile
$u$	Ultimate
$w$	Wet

### Superscripts

$C$	Core
$CB$	Cantilever bending
$DC$	Dynamic cutting
$IN$	Internode
$long.$	Longitudinal direction
$LC$	Local transversal compression
$mj$	Major direction
$mr$	Minor direction
$ME$	Maize-ear
$N$	Node
$S$	Skin
$SC$	Sectional transversal compression
$SH$	Shank
$tr.$	Transversal direction
$TB$	Three-point bending

*Dedicated to my son, Marci*



# 1 Introduction

## 1.1 Agricultural Machine Design

The perpetual goals of agricultural machine design and development are optimizing the energy consumption, increasing the working quality and reducing the losses of machineries. One of the most efficient analysis methods for agricultural machinery designers is the time honoured in-situ test of the latest prototypes. However, due to the seasonal characteristic of agricultural processes and products these tests are limited in time, difficult to observe in detail and often proved to be very expensive.

In typical modern machine design several computational methods are applied to analyse the interactions and phenomena in machinery during working processes instead of real experiments: finite element analysis (FEA) for structural design, computational fluid dynamics (CFD) for simulation of the interaction of liquids or gases with surface boundaries, multi-body dynamics (MBD) to study the dynamic behaviour of interconnected rigid or flexible bodies etc.

Numerical modelling of agricultural crops is becoming more common year by year. First, studies relating the mechanical behaviour of bulk crop assemblies were conducted by using the discrete element method (DEM). DEM is capable of modelling contacts and bonds among separate particles, making it an effective tool to analyse complex loading and breaking conditions of plant parts and to expand beyond the limitations of in-situ tests. Thus, researchers are turning to the modelling of fibrous agricultural materials (stalks and stems), however, due to its complex nature there is still no suitable simulation method and crop model that could predict the interactions among fibrous agricultural materials and machine parts.

## 1.2 Maize

Maize (*Zea mays* L.) is one of the most cultivated crops of the world: almost 1050 million metric tons of maize were produced in 2017 ([World of Corn](#), 2018), while it also played an important role in Hungary's agricultural industry: 6.8 million metric tons were harvested in 2017 ([Hungarian Statistical Office](#), 2018). Based on the forecast of the Food and Agriculture Organization of the United Nations ([FAO](#)), approximately 1200 million metric tons will be harvested from almost 200 million hectares in 2050 (Alexandratos and Bruinsma, [2012](#)).

The main parts of a maize plant are the root system, stalk, leaves, tassel, shank and maize ear, as shown in Figure 1.1. The stalk, the strongest part of maize plant, is constituted of nodes and internodes, both have the same skin-core (rind-pith) structure. Furthermore, there is a difference between the orientation of tissues in nodes and internodes as well: the orientation of the tissues is non-uniform while in internodes the tissues are oriented in longitudinal direction of the stalk (Robertson et al., [2015](#)). Accordingly, the biological structure of maize, especially the structure of the stalk, is suitable for our study. Consequently, maize has been chosen for the interest of the current study due to its importance in agriculture and its biological structure.

The general steps of maize production are: soil tillage, planting, fertilization, control of weeds, diseases and pests, irrigation, harvesting, drying, storing and further processes (Nagy, [2006](#)). From the previous steps, harvesting involves the most parts of the plant, moreover, it is one of the most crucial phases in maize production because the efforts of the whole growing

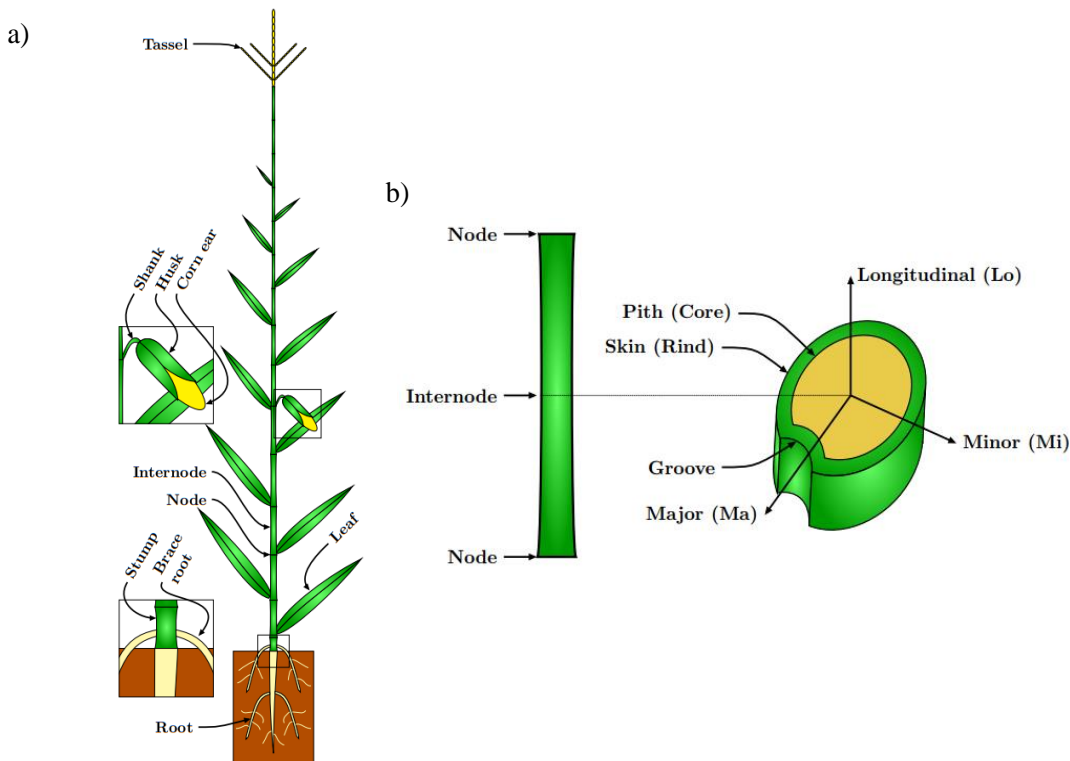


FIGURE 1.1: Parts of a maize plant: a) overview of the whole plant and b) the internodal section.

season depend on it. Several different harvesting methods exist: harvesting of maize cobs, maize kernels, maize for silage and corn-cob mix (CCM) (Nagy, 2006). The complex process of gathering of shelled maize kernels by a combine harvester is the most wide-spread method, moreover, the level of energy usage is relatively high: a common combine harvester consumes approximately 13.5 litres of fuel to harvest 1 ha maize, thus, it has been chosen for the interest of the current study.

### 1.3 Research Scope and Objective

The current project resolves to explore the suggestion that the DEM can be exploited to reproduce the mechanical behaviour and breakage of fibrous agricultural materials, such as maize plant. The primary objective of this thesis is to contribute to understanding of DEM modelling of fibrous agricultural materials and provide a model that represents the physical and mechanical existence of maize. To achieve this aim some specific objectives were defined as follows:

1. a measurement method needs to be established regarding the process of maize harvesting by a combine harvester with maize header;
2. the collected data needs to be analysed in such a way to obtain useful knowledge about the physical, morphological and mechanical properties of the harvested material for the model development;
3. a detailed DEM model of maize parts and experiments need to be created;
4. the major numerical input parameters and their influence on the DEM predicted results need to be determined;
5. a detailed DEM model of the entire plant needs to be created and validated;
6. based on the operations in a maize header, a technological simulation needs to be conducted by using the validated plant model.

## 2 Literature Review

### 2.1 Harvesting of Maize

Generally, in a combine harvester, maize is mainly processed by the maize header; only maize ears are threshed inside the machine. Hence, the current study focuses on the processes that take place in the maize header during harvesting.

Through the evolution of the maize headers, several different methods were developed to process the maize plant and gather the maize ear. Moreover, the design of the parts with the same function can be also different: e.g. several stalk roller designs exist but their function is the same. In the current study, the most popular maize header design will be considered (Figure 2.1) that consists of linear stalk rollers, chopping unit, deck plates, gathering chains, screw auger, snouts and shields.

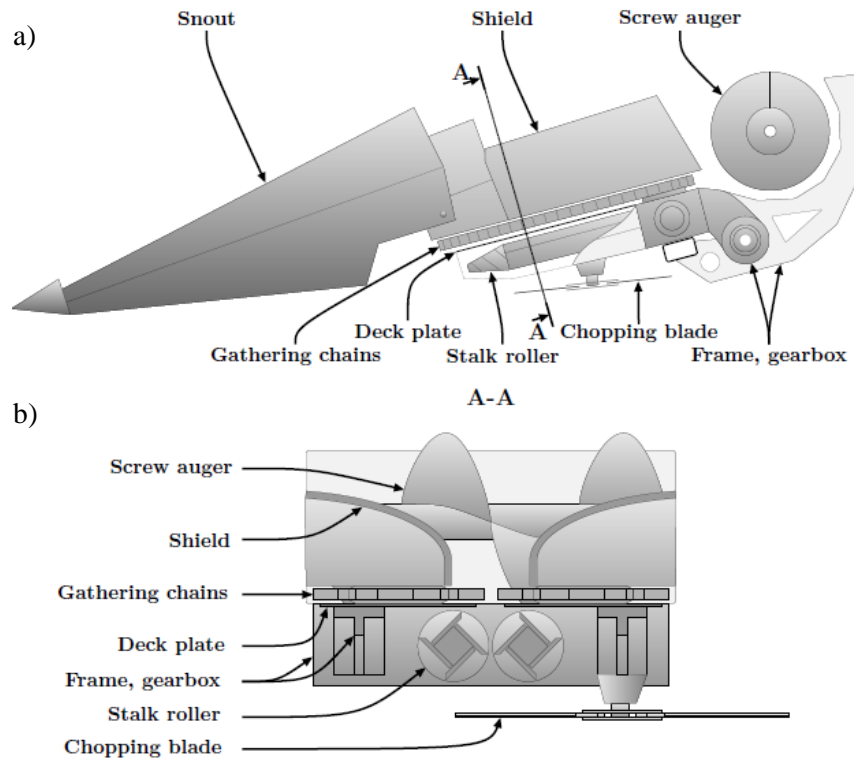


FIGURE 2.1: Parts of a common maize header: a) side view; b) middle section.

During harvesting, the whole plant is cut off by the maize head and pulled down by the stalk rollers. The maize ear is gathered by the deck plate and conveyed into the machine by the gathering chains and the screw auger while the rest of the maize plant (stalk, leaves, tassel) is chopped and spread by the chopping unit (Li et al., 2016). Accordingly, the stalk, shank and ear play the most important roles during this process; the leaves, root and tassel have negligible importance. Based on the harvesting process, the following major phenomena take place during harvesting by a combine harvester:

- **transversal compression:** the knives of rotating stalk rollers compress the maize stalk locally in its transversal direction;
- **flexural load by inertia:** the stalk is bent due to the force of inertia of the maize ear because the whole plant is accelerated by the machine in the direction of movement;
- **oscillation:** the stalk oscillates due to the interactions among the plants and flexural load from the eccentric maize ear;
- **longitudinal stretch by inertia:** the stalk and shank are stretched by the force of inertia of the maize ear because it is accelerated in the perpendicular direction to the axles of stalk rollers;
- **longitudinal stretch by gathering:** when the maize ear collides on the deck plate, a longitudinal force appears in the stalk and shank until the detachment of the maize ear;
- **collision of maize ears:** gathering chains and screw auger of the maize head convey the maize ears into the machine while they collide with them and with each other;
- **first cut:** knives of the chopping unit cut the stalk that is fixed at both ends by the stalk roller and the soil;
- **free cut:** knives of the chopping unit cut the stalk that is fixed by the stalk roller.

Based on the consideration of the importance in losses and the energy consumption of the phenomena during harvesting, our study focuses on the analysis of the following properties of maize:

- physical and morphological properties of maize stalk, shank and ear;
- mechanical behaviour of maize stalk against transversal compression load;
- mechanical behaviour of maize stalk against flexural load;
- energy requirement of dynamic cutting of maize stalks;
- mechanical behaviour of shank and ear during gathering.

## 2.2 Experimental Studies on Agricultural Plants

### 2.2.1 Preparation of Test Materials

The condition of the material under scrutiny is very important during the experiments. To prevent spoilage and to obtain comparable results, the moisture content of the specimens is usually reduced to 10-20% w.b. (Robertson et al., 2014; Robertson, Smith, and Cook, 2015; Igathinathane, Womac, and Sokhansanj, 2010) or adjusted to the determined values (e.g. 15-30-55-75% w.b.) (Ince et al., 2005; Zhong-Zhen et al., 2013). Sometimes the specimens are stored in a deep-freezer (-25°C) until the experiments take place (Igathinathane et al., 2011). In fewer studies, virgin samples were investigated (Tongdi, Yaoming, and Jin, 2011; Prasad and Gupta, 1975).

### 2.2.2 Environmental Conditions

Several studies have been conducted to analyse the impact of climate and fertilizing conditions on the crop yield (Ma and Maystadt, 2017; Di Paolo and Rinaldi, 2008), but only the effect of the harvest date on shearing force of maize stems was directly analysed (Chen et al., 2007). Indirectly, the effect of environmental parameters (solar radiation, rainfall, maximum and minimum temperatures, mean air temperature, air relative humidity, wind speed and wind direction) on mass and moisture distribution in the aboveground components of standing maize plants (Igathinathane et al., 2006) and the effect of the moisture content on the mechanical properties were separately analysed (Ince et al., 2005; Zhong-Zhen et al., 2013). For an analysis on the failure patterns of maize stalk lodging, soil type, average rainfall per month, average temperature and rainfall data were collected (Robertson et al., 2015).

### 2.2.3 Physical and Morphological Properties

To analyse the mechanical properties of a maize stalk, it is also necessary to investigate its physical and morphological properties. Most of the studies focus on the diameter (Robertson et al., 2015; Forell et al., 2015) and the structure (Huang et al., 2016; Heckwolf et al., 2015) of the stalk. Previous results show that even a small change in the size of the stalk diameter has a significant influence on its mechanical behaviour (Forell et al., 2015), while the diameter along an internodal section is relatively constant, except in the nodal region, where it slightly increases (Robertson et al., 2015). Not only the diameter, but also the number of fibre bundles of the internodal section has a significant influence on the mechanical behaviour of the stalk (Huang et al., 2016).

The effect of several morphological traits (plant height, internodal distance, internodal weight, moisture content, ear weight, ear length and cross-sectional area of the ear) on the shear strength of maize stalks were estimated by Liang and Guo, 2011. From the analysed morphological traits, ear weight and height had a closer correlation with the shear strength of the stalk.

Other physical and morphological properties were not analysed in relation to the mechanical behaviour of maize stalks, although they were analysed regarding to biomass production (Igathinathane et al., 2006). The results of this study show that the moisture content of stalks decreased significantly around the normal harvest period and reached a final stabilized moisture level. Dry matter and moisture content were affected by air temperature, reference evapotranspiration and soil temperature, but changing in other soil or environmental parameters (e.g. rainfall) did not have an effect on the measured stalk properties.

Knowledge of the physical and morphological properties of the crop is essential for harvesting. To describe the physical and morphological properties of a maize ear; the ear length, ear diameter, kernel weight per ear, cob weight, number of kernel rows per ear, number of kernels per row and number of kernels per ear were analysed in previous studies (Yu, Fu, and Yu, 2015; Homayoun, 2011). However, in case of apple and pear fruits, 3D image processing methods were also exploited advantageously to model the shape of the crop (Celik, Rennie, and Akinci, 2011; Salarikia et al., 2017).

### 2.2.4 Transversal Compression Tests

To define the mechanical behaviour and the breaking phenomena of stems and stalks against transversal compression two types of experiments can be found: compression between flat plates (sectional) and between stem-shaped plunger tools (local) (Prasad and Gupta, 1975; Robertson, Smith, and Cook, 2015; Leblicq et al., 2016b; Zhang et al., 2017). In the first case, a defined longitudinal section of a stalk, while in the second case a local area can be analysed. All the previous experiments were quasi-static because the velocity of the plungers ranged from  $2 \text{ mm min}^{-1}$  to  $70 \text{ mm min}^{-1}$ . Higher loading velocity (analysed in range of  $30\text{-}70 \text{ mm min}^{-1}$ ) results in higher resistance force against compression on the same stalk section (Zhang et al., 2017). The transversal deflection of the specimens was usually in the elastic state, which means small movements of the plunger in the range from  $0.1 \text{ mm}$  to  $0.3 \text{ mm}$ , except experiments by Zhang et al., 2017, where the displacement of the plunger was  $6 \text{ mm}$ . Results from local compression tests demonstrated that the transverse stiffness of the maize stalk is nearly constant along the internodes, but the resistance increases significantly in the region of nodes (Robertson, Smith, and Cook, 2015).

### 2.2.5 Flexural Tests

Analysis of the mechanical behaviour and the breaking phenomena of stems and stalks by a three-point bending experiment (Tongdi, Yaoming, and Jin, 2011; Robertson et al., 2014; Leblicq

et al., 2015; Robertson, Smith, and Cook, 2015; Olmedo et al., 2016; Zhang et al., 2017) is more common than transversal compression tests. The velocity of the bending tool was in the range of  $8 \text{ mm min}^{-1}$  and  $100 \text{ mm min}^{-1}$ , while the length of the span varied between 50 mm and 600 mm (Tongdi, Yaoming, and Jin, 2011; Robertson et al., 2014; Leblicq et al., 2015; Robertson, Smith, and Cook, 2015; Zhang et al., 2017). In a special experiment, the bending behaviour of wood stems against an impact load was analysed by a modified Mouton-Charpy pendulum (Olmedo et al., 2016). The effect of the internodal and the nodal location of load and the effect of span length were analysed in relation to bamboo, giant reed and maize (Robertson et al., 2014; Robertson, Smith, and Cook, 2015). The results demonstrated that when the stem is loaded on the internodal sections, the bending resistance of the maize stalks is lower by 54% and the higher span length provided less local damage in the loading area.

## 2.2.6 Cutting Tests

Cutting of stalks are involved in several agricultural processes, thus,

- energy requirement, peak force and quality of cutting;
- cross-sectional area, moisture content, dynamic coefficient of friction, orientation or alignment of maize stalks to the cutting blade;
- the design, sharpness and velocity of the blade;

were analysed in several in-situ (Chen, Gratton, and Liu, 2004; Kemper, Thorsten, and Frerichs, 2014; Azadbakht, Asl, and Zahedi, 2014) and laboratorial tests (Prasad and Gupta, 1975; O'Dogherty, 1982; Yiljep and Mohammed, 2005; Igathinathane et al., 2009; Igathinathane, Womac, and Sokhansanj, 2010; Dange, Thakare, and Rao, 2011; Igathinathane et al., 2011; Johnson et al., 2012; Kattenstroth, Harms, and Frerichs, 2012; Jia et al., 2013; Mathanker, Grift, and Hansen, 2015).

In previous studies, two types of laboratorial cutting tests were conducted: quasi-static (in range of  $25.4 \text{ mm min}^{-1}$  and  $240 \text{ mm min}^{-1}$  cutting blade velocity) and dynamic (in range of  $1.62 \text{ m s}^{-1}$  and  $18.7 \text{ m s}^{-1}$  cutting blade velocity). One of the most effective ways to carry out dynamic cutting experiments on stalks and stems is the modification of a common pendulum impact machine (Azadbakht, Asl, and Zahedi, 2014; Yiljep and Mohammed, 2005; Dange, Thakare, and Rao, 2011).

## 2.2.7 Crop-Detachment Tests

The most important part of harvesting is the gathering, when the crop is detached from the stalk or stem. Therefore, fruit detachment was investigated in several studies (Coetzee and Lombard, 2013; Torregrosa et al., 2014; He et al., 2017). However, experiments related to the detachment of maize ears from stalks could not be found by the authors. In case of fruits, the experimental apparatus usually reproduces the course (e.g. shaking of a fruit tree) of the harvesting process.

## 2.2.8 Crop-Collision Tests

To prevent losses and damage, knowledge of the mechanical behaviour of agricultural crops during collisions with each other and with parts of the machine is necessary. Several drop (Celicik, Rennie, and Akinci, 2011; Yousefi, Farsi, and Kheiralipour, 2016) and pendulum (Abedi and Ahmadi, 2013) experiments were conducted on deformation, mechanical damage and bruise of fruits during collision.

The height of the drop tests was in the range of 0.05 m and 1.2 m, while the impact energy of the pendulum tests was in the range of 0.048 J and 0.26 J. In case of drop tests, a collision

between the crop and rigid or flexible planar surface was usually recorded by a high-speed camera.

As related to grain crops, most of the studies focus on the impact of individual kernels (Jindal and Mohsenin, 1978; Zhan et al., 2013; Horabik et al., 2017) and not on the impact of crop ears. Based on the knowledge of the authors, collision test on maize ears was not conducted, but collisions usually take place during agricultural processes.

## 2.3 A Brief Review of Discrete Element Method

The discrete element method (DEM) dates back to the late 70's when this method was used to analyse the mechanical behaviour of granular assemblies (Cundall and Strack, 1979).

In DEM, the real material consists of a finite number of independent (discrete) particles (elements) that have a finite volume and density, thus the particle assembly represents the shape and mass of the subjected material. The shape of the individual particles can be polyhedron, sphere, ellipsoid or it can be a combination of the previous ones. Usually, these particles are assumed to be rigid but deformable ones are also used in several cases: rock mechanics, tunnel construction, concrete structures, etc. (Bagi, 2007; DEM Solutions, 2017).

Generally, a DEM calculation cycle consists of three stages: numerical time integration, contact detection and calculation of interaction (reaction forces, moments). In a granular assembly, each particle has six degrees of freedom, thus, two types of motion: translational and rotational. Over each time step, a numerical time integration method (e.g. Euler or Runge-Kutta) is used to calculate the particle positions and velocities from the accelerations, Equation 2.1 and 2.2:

$$x(t + \Delta t) = x(t) + v(t) \cdot \Delta t, \quad (2.1)$$

$$v(t + \Delta t) = v(t) + a(t) \cdot \Delta t, \quad (2.2)$$

where  $x(t)$  is the position,  $v(t)$  is the velocity and  $a(t)$  is the acceleration of a particle in a given time  $t$ , while  $\Delta t$  is the time step (DEM Solutions, 2017).

The translational and rotational accelerations are determined by Newton's second law, Equation 2.3 and 2.4:

$$m \cdot \frac{dv}{dt} = F, \quad (2.3)$$

$$I \cdot \frac{d\omega}{dt} = M, \quad (2.4)$$

where  $m$  is the particle mass,  $v$  is the translational velocity of the particle,  $t$  is time,  $F$  is the resultant force acting on the particle,  $I$  is the moment of inertia of the particle,  $\omega$  is the rotational velocity of the particle and  $M$  is the resultant torque acting on a particle (DEM Solutions, 2017).

The choice of a sufficiently small time step ( $\Delta t$ ) is critical to ensure the stability of the simulation. For quasi-static simulations, it is recommended to define it based on the Rayleigh time step, that is the time interval taken by the a shear wave to propagate through a solid, Equation 2.5:

$$\Delta t = \frac{\pi \cdot r}{0.1631 \cdot \nu + 0.8766} \cdot \sqrt{\frac{\rho}{G}}, \quad (2.5)$$

where  $r$  is the particle radius,  $\nu$  the particle Poisson's ratio,  $\rho$  particle density and  $G$  is the particle shear modulus. The applied time step is usually defined as a percentage of the Rayleigh time step (Rayleigh, 1885; Sheng et al., 2004; DEM Solutions, 2017).

During the contact detection, overlap among the existing particles is sought by using different algorithms depending on the number and shape of the particles. Moreover, contact detection is one of the most time consuming parts of a DEM simulation. Three main types of contact detection algorithms are widely used:

- Verlet Neighbour List;
- Link or Grid Cells;
- Lattices.

In case of the Verlet Neighbours List, an array of particles within a certain search distance (usually 2-3 particle radius) is constructed and only this array is sought for contacts. Link or Grid cells divide the simulation domain into a number of equally sized cells that are larger than a couple of particle diameters. A list is constructed of all the particles in each cell and contacts are only checked for particles within the same and neighbouring cells. The Lattice method also divides the simulation domain into a number of equally sized cells, where each one is the size of a particle (each cell can contain only one particle). Each particle is indexed in relation to a grid point and a neighbour list is created for all cells within a particle diameter. When an existing contact is found, the interaction (reaction forces, moments) is calculated based on the contact law between the particles (Bagi, 2007; DEM Solutions, 2017).

To describe the mechanical behaviour of the real material, contacts among the discrete particles can be defined as non-deformable or deformable as well. Assuming deformable contacts among the particles, there are point-like (e.g. frictional) and finite size (e.g. cemented or bonded) type of contacts. Usually, the existing contacts can break and new contacts can be formed among the particles based on the contact law (Bagi, 2007; DEM Solutions, 2017). A detailed description of the applied contact models on agricultural materials can be found in Chapter 2.4.

Nowadays, the number of DEM software is still increasing, moreover, most of the latest ones provide analysis in 3D and coupled simulations (e.g. CFD-DEM, MBD-DEM). Generally, two types of DEM codes exist: open-source codes such as **Yade** or **LIGGGHTS** and commercial codes such as **EDEM** or **PFC**.

## 2.4 DEM Studies on Agricultural Plants

DEM has been widely used to simulate the mechanical behaviour of bulk agricultural crops during different processes: discharge of silos (Coetzee and Els, 2009), threshing (Yu, Fu, and Yu, 2015), coating (Pasha et al., 2016) and drying of grains (Keppler et al., 2012) etc., but there are very few studies in relation to modelling fibrous plant parts.

To analyse the mechanical behaviour and breakage of crop stems or stalks during different agricultural processes, different DEM geometrical and mechanical models were created. The complexity of the models primarily depends on the application, the detail of the investigation and the available computational resources.

### 2.4.1 Shape Representation and Contact Models

To model the shape of stems and stalks several different DEM geometrical structures are reported but only a few of these are analysed in detail.

Different geometrical models including chain of spheres, enhanced chain of spheres, hollow structure and solid body were reported by Jünemann, Kemper, and Frerichs, 2013. In these models, a linear elastic bond is assumed among the rigid particles that can transform normal and tangential forces and torques taking into account the Young's modulus and the shear modulus.

Using cylinders or capsules as particles, a segmented virtual stem model was used to analyse the bending, compression and separation process of stems by Li et al., 2012; Lenaerts et al., 2014; Leblicq et al., 2016a; Leblicq et al., 2016b. In case of the separation process, rigid hollow cylinders were used to analyse the effect of short straws on the motion in the cleaning device by Li et al., 2012. A special bonded joint of axis-symmetrically aligned six linear spring-dampers was formed to simulate the bending behaviour of stems by Lenaerts et al., 2014. The stiffness of the springs is calculated based on the Young's modulus that determines the bending resistance of the joints in radial direction. Another set of linear spring-dampers was used to represent the elastic section of the mechanical behaviour of the stems under transversal compression. A non-linear bonded model was used to simulate the bending behaviour of stems by Leblicq et al., 2016a. In this model, the bended cross section was simulated by a rotational spring and its stiffness was variable and depended on the bending angle and the previous deformation of the stem. Another non-linear model was used to analyse interactions among stems in case of compression by Leblicq et al., 2016b. During the interaction of the stems a spring-damper system calculated the reaction forces and the stiffness of the spring depended on the actual overlap and the previous deformation of the stem.

To analyse the dynamic response of wood stems to impact and overlaid cut in disc mowers, stem models were formed by spherical particles (chain of spheres) by Kemper, Thorsten, and Frerichs, 2014; Olmedo et al., 2016. In these models, the size of all particles along the stem was uniform. A trilinear-hysteresis model was used for bonds among particles to simulate the mechanical behaviour of wood stems against impact load by Olmedo et al., 2016. Three different bond stiffness were used: one for the elastic behaviour, one for the plastic behaviour and one for the unloading behaviour after damage. A flexible bonded model was used to represent the realistic behaviour of grass stalks by Kemper, Thorsten, and Frerichs, 2014.

A DEM model was created of a bunch of grapes by Coetze and Lombard, 2013. In this model, the main and side stems were formed by spherical particles and the size of these particles are gradually decreasing from the beginning to the end of the stem to mimic its real geometry. To create a stem the particles were bonded together by using the "Linear Parallel Bond" contact model of PFC<sup>3D</sup> (Itasca Consulting Group, Inc., Minneapolis, Minnesota, US). Thus, the stems were assumed linear elastic, homogeneous and isotropic.

To develop a sensor for monitoring rice grain sieve losses in a combine harvester a special hollow structure was created of rice stems by Liang et al., 2016. In this case, the stem was one rigid multi-sphere particle that was not able to reproduce the mechanical behaviour of a real stem. One cross section of the stem consisted of 12 spherical surfaces with 1 mm of diameter, while the distance between the centres of cross sections was 0.8 mm. Thus, there was an overlap among the cross sections that provided smoother outer surface for the stem.

#### 2.4.2 Calibration and Validation Methods

To calibrate DEM models on bulk materials two calibration methods can be found: direct measurement and bulk calibration approaches (Coetze, 2017). In case of direct measurement, parameters are measured directly at particle or contact level, while in the other case the mechanical behaviour of the bulk solid is measured. These two methods were also adopted for modelling of stems and stalks because measurements on individual stems and on multiple stems could be found (Lenaerts et al., 2014; Leblicq et al., 2016b). In the first case, the interactions among stems and machine parts can be determined while in the other case interactions among individual stems and the bulk can be analysed.

### 2.4.3 Technological Simulations

However, most of the studies focused on the modelling of a specific part of the plant, some studies were related to real agricultural processes.

To analyse the destemming of grapes, the geometrical model of a rotating destemmer was imported into the DEM simulations (Coetze and Lombard, 2013). No simplifications were made on the key parts of the model, however, some of them were created by using two geometrical walls to describe the non-linear particle-wall contact. To mimic the feeding process, an initial downward velocity was added to the first particle of the main stem of each grape bunch. Afterwards, when the bunch reached a specified height inside the hopper the initial velocity was removed and the bunch fell freely under the influence of the gravitational acceleration.

To analyse the overlaid cut in a disc mower, a simplified model that involved only the main parts of the real machine was imported into the DEM simulation (Jünemann, Kemper, and Frerichs, 2013; Kemper, Thorsten, and Frerichs, 2014). Each grass stalk was placed into a cylinder that fixed them to the ground and a small field was created by using several stalks. By taking into consideration the computational time, the influence of the wind was neglected.

For analysis of the threshing process, the CAD model of a drum-type maize thresher was imported into the DEM simulation by using a boundary modelling method (Yu et al., 2011) to discretise the surfaces of the machine parts (Yu, Fu, and Yu, 2015). To reduce the computational cost, only the middle segment of the maize ear was involved into the analysis.

The grain velocity distribution in a mixed flow dryer was analysed by using only a half section and only a slice of the real dryer module to reduce the computational cost (Keppler et al., 2012). Ideal, frictionless walls were used to define the boundary of the simulation domain. At the beginning of the simulation, the dryer was filled with particles by using the dropping method.

## 2.5 Conclusions and Limitations of Previous Studies

Based on the literature review, several studies on the physical and morphological properties, transversal compression, three-point bending and cutting of maize stalks were conducted but no studies related to the maize ear detachment and collision was found. The previous studies were carried out on different maize varieties from different parts of the world in different growing seasons. On the other hand, experiments were usually conducted on dried or deep-frozen samples and, therefore, the condition of these samples was not related to the harvested material. Furthermore, the mechanical behaviour of samples was estimated through small deformation loading cases, while large deformation of samples occurs during harvesting by a combine harvester with a maize head.

It is common knowledge that the environmental conditions during the different growing stages of maize have a significant effect on the properties of the fully developed plant, but only a few studies provided detailed meteorological data about the experimental plot regarding the actual growing season. The effect of reducing the moisture content or freezing on the mechanical behaviour are not known and, moreover, in the real processes, mainly virgin plants with 60-80% w.b. moisture content are involved. Thus, the analysis of virgin plants is evident in order to obtain results related to the real agricultural process. The diameter, length, mass and moisture content of each internodal section of the stalk and the position, shape, diameter, length and mass of the maize ear play the most important role during harvesting. Therefore, these properties must be measured and observed during the harvesting period when they are stabilized.

To the knowledge of the author, no study has been conducted to analyse the mechanical behaviour of stalks or stems against transversal compression with large plunger displacement,

however the stalks and stems are significantly compressed between the stalk rollers of a common maize header. Consequently, it is practical to conduct transversal compression experiments on maize stalks with large deformation and high plunger velocity. In case of harvesting, flexural loads with small span length are more common and, therefore, it is practical to use a shorter span length for the bending experiment. Furthermore, the likelihood of loading on an internodal section of the stalk is higher than on the nodal section. Therefore, the experiments need to be conducted on the internodal region of the stalk.

The primary purpose of the previously described DEM models was to simulate the response of stems in a special loading case: bending, compression, impact load or collision between a stem and a flat plate. Thus, most of them cannot predict a detailed mechanical behaviour and breakage of stems during the complex loading situation of maize harvesting. Furthermore, the previous DEM models about stems and stalks were less detailed to analyse effectively the working quality of agricultural process.

Consequently, the following hypotheses are drawn regarding the experiments and the DEM model based on the literature review:

- a measurement method, that consists of laboratorial and in-situ experiments, can provide the necessary knowledge about the physical, morphological and mechanical properties of maize plant regarding harvesting;
- clear relationship can be determined between the physical and morphological properties of the plant;
- clear relationship can be determined between the physical properties of the morphological element and its mechanical behaviour;
- DEM is capable to create a detailed model of maize to analyse the complex process of harvesting;
- input parameters that have a significant influence on the response of the model can be determined;
- a calibration method can be established to determine the input parameters of the model;
- the validated DEM model can be exploited to analyse the process of maize harvesting.



# 3 Experimental Materials and Methods

## 3.1 Experimental Plot and Cultivation of Maize

Maize, variety Sufavor FAO360 ([Saaten-Union Hungária Ltd, Hungary](#)), was planted in the central region of Hungary (location:  $47^{\circ}44' N$ ;  $19^{\circ}36' E$ , 149 m a.s.l.) on 15 April 2016. The plant density was 70,000 pieces  $ha^{-1}$  and the distance between the rows and plants was 0.75 m and 0.2 m, respectively. On the same day, the experimental plot, approximately 100 rows width and 500 plants long, was appointed in the middle of the non-irrigated field after taking into consideration its geographical properties for a homogeneous experimental plot.

As to the cultivation of the plants, they were sprayed against diseases and pests on 21 May 2016 and mechanical weed control was carried out on 7-8 June 2016. Ears were harvested on 26-27 October 2016. The average moisture content of the threshed maize kernels was 19.7% w.b. and the yield was 8,800  $kg ha^{-1}$ .

## 3.2 Environmental Conditions

Daily meteorological data were collected from the nearest meteorological station to the experimental plot by the Hungarian National Meteorological Service ([OMSZ](#)). Soil samples were uniformly collected once from the experimental plot right after planting and the analysis of soil pH was conducted (Hungarian standard MSZ-08-0206-2:1978 Paragraph 2.1.).

Basic environmental properties: solar radiation; rainfall; maximum, minimum and mean air temperatures; soil temperature at depth of 0.1 m; soil pH; were compared with the basic requirements of maize ([Nagy, 2006](#)) to determine the appropriateness of the environmental conditions, see below:

- **Soil I.** - pH;
- **Rainfall I.** - Total amount;
- **Rainfall II.** – During flowering and grain filling stages in July and August;
- **Solar radiation I.** - Total amount;
- **Solar radiation II.** – During kernel development and maturation stages in August and September;
- **Temperature I.** – Soil temperature in depth of 0.1 m at planting;
- **Temperature II.** - Soil temperature in depth of 0.1 m during germination stages in April and May;
- **Temperature III.** – Mean air temperature during flowering and grain filling stages in July and August;
- **Temperature IV.** – Mean air temperature during kernel development and maturation stages in August and September;
- **Temperature V.** – Mean air temperature to avoid forced kernel maturation in September.

Based on the general environmental requirements of maize all the measured data were close to the ideal, except Rainfall II. which was only 200.4 mm instead of the ideal 300 mm during flowering and grain filling stages in July and August, as shown in Table 3.1. All the collected meteorological data is shown in Figure A.2.

TABLE 3.1: Comparison of the environmental requirements of maize and the collected data.

Property	Requirement (Nagy, 2006)	Measured
Soil I.	6 - 7.2	6.67
Rainfall I.	450 - 500 mm	438.5 mm
Rainfall II.	300 mm	200.4 mm
Solar radiation I.	900 h	1626.9 h
Solar radiation II.	360 h	568 h
Temperature I.	> -2°C	min. 9.3°C
Temperature II.	> 10 - 12°C	min. 11.4°C
Temperature III.	> 24 - 26°C	July: 22.3°C; August: 20.5°C
Temperature IV.	> 15°C	August: 20.5°C; September: 18°C
Temperature V.	> -1°C	min. 11.3°C

### 3.3 Collection and Preparation of The Test Material

To determine the actual condition of maize in relation to harvesting, all the observations and experiments were carried out during the harvesting days on 26-27 October 2016.

For all tests, healthy plants without any observable damage, disease or mutation were systematically selected to provide uniform sample collection. In-situ experiments and observations were conducted on virgin samples at the experimental plot. For the laboratorial tests, plants were cut off right above the soil surface, and the leaves and tassel were carefully removed to secure the virginity of the samples. By using maize stalks, bunches were created and transported to the laboratory.

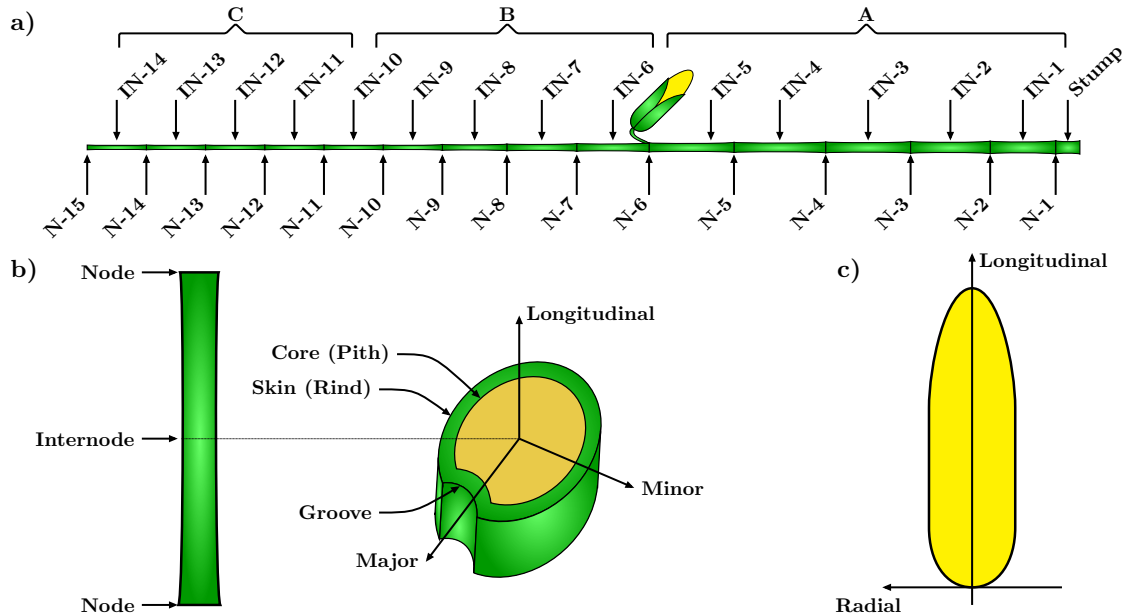


FIGURE 3.1: Division and major directions of maize parts: a) division of the maize stalk (N: node; IN: internode); b) major directions of an internodal section and structure of a cross-sectional area; c) major directions of a maize ear.

First, the nodes and internodes (internodal sections) of each stalk were continuously numbered and marked by a position index ( $p$ ), as shown in Figure 3.1(a). The stump, where the brace root joins to the stalk, was excluded from the measurement because this part does not come into contact with the maize head. Three sections of the maize stalk were defined: A, B

and C. Section A contains the first five internodal sections, the shank and the maize ear. Section B consists of another five internodal sections above the maize ear, while Section C consists the rest of the stalk.

To make the experiments uniform, the main axes of the internodes and the maize ears were defined, as shown in Figure 3.1(b) and (c). Figure 3.1(b) shows the general skin-core structure, the shape of an internodal cross-sectional area and the main axes of an internode: longitudinal, major and minor. In case of maize ears, two axes: longitudinal and radial were also defined because an axis-symmetric property was assumed, as shown in Figure 3.1(c).

Based on the experiments, the stalks were cut into smaller samples by a band saw and stored in hermetically sealed plastic bags until the tests. By the previously described collection and preparation method, samples were measured within 6-8 hours after their cutting at the experimental plot. Therefore, the properties of the stalks remained close to its harvesting condition.

### 3.4 Physical and Morphological Characteristic of Maize

At the **experimental plot**, a general observation on the structure of maize was carried out by using 100 virgin maize plants. On 20 maize plants, the location of the maize ears was observed and its centre of mass was estimated from the soil surface and from the centre of the stalk by using a measuring tape (accuracy 1 mm), as shown in Figure 3.2(a)(b).

In the **laboratory**, the minor and major dimensions of nodal and internodal cross-sections were measured on 10 stalks by a digital calliper (accuracy 0.01 mm), as shown in Figure 3.2(c). Along the internodal sections, the equivalent diameter was assumed constant (Robertson et al., 2015). Thus, the minor and major dimensions were measured in one cross-section near to the middle of the section. Distance between two nodes (length of internodes) was also measured on 10 stalks by using a measuring tape (accuracy 1 mm), as shown in Figure 3.2(e).

The complex cross-sectional shape of the real internode (Figure 3.1 (b)) and node was approximated by a circular cross-section. A similar method was used to calculate the cross-sectional area, lateral surface and total volume of the internodal samples that were simplified as tapered elliptical cylinders by Igathinathane et al., 2006. The equivalent diameter was calculated by using the width of the real cross-section in the major and minor directions by Equation 3.1:

$$d_{ep}^{IN/N} = \frac{w_p^{mj} + w_p^{mr}}{2}, \quad (3.1)$$

where  $d_{ep}^{IN/N}$  (mm) is the equivalent diameter of the  $p^{th}$  internode ( $IN$ ) or node ( $N$ ),  $w_p^{mj}$  (mm) is the measured width of the real cross-section in its major direction,  $w_p^{mr}$  (mm) is the measured width of the real cross-section in its minor direction.

For each stalk, all the equivalent diameters were specified by the equivalent diameter of the first node by Equation 3.2:

$$\delta_p^{IN/N} = \frac{d_{ep}^{IN/N}}{d_{e1}^N}, \quad (3.2)$$

where  $\delta_p^{IN/N}$  (-) is the equivalent diameter ratio of the  $p^{th}$  internode ( $IN$ ) or node ( $N$ ),  $d_{ep}^{IN/N}$  (mm) is the equivalent diameter of the  $p^{th}$  internode ( $IN$ ) or node ( $N$ ),  $d_{e1}^N$  (mm) is the equivalent diameter of the  $1^{st}$  node.

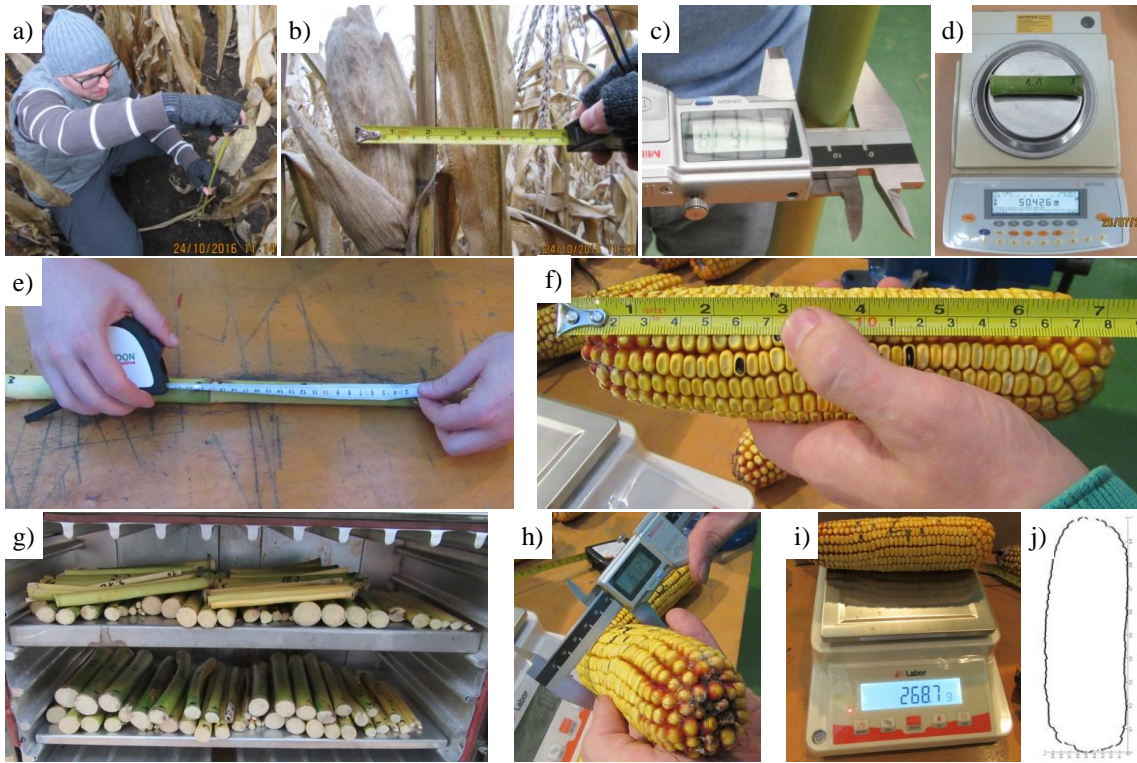


FIGURE 3.2: Experiments on the physical characteristic: a) estimating the ear's centre of mass from the soil surface; b) estimating the ear's centre of mass from the stalk; c) measuring the major and minor dimensions in an internodal cross-section; d) measuring the internodal wet-mass; e) measuring the internodal length; f) measuring the length of a maize ear; g) samples in the dryer; h) measuring the diameter of a maize ear; i) measuring the mass of a maize ear (kernel and cob); j) profile of a maize ear.

The measured length of the internodes were also specified by the total length of the stalk, see Equation 3.3:

$$\lambda_p = \frac{L_p}{L_t}, \quad (3.3)$$

where  $\lambda_p$  (-) is the length ratio and  $L_p$  (mm) is the length of the  $p^{th}$  internode, while  $L_t$  (mm) is the total length of the stalk.

Ten stalks were cut into internodal sections by a bandsaw and their wet-mass was measured by a digital balance (accuracy 0.01 g), as shown in Figure 3.2(d). Afterwards, the same samples were placed into a drying oven (Figure 3.2(g)) on 102°C and the internodal dry-mass was also measured after 24 hours according to Igathinathane et al., 2006.

Each measured wet-mass was also specified by the total wet-mass of the stalk, see Equation 3.4:

$$\mu_{w,p} = \frac{m_{w,p}}{m_{w,t}}, \quad (3.4)$$

where  $\mu_{w,p}$  (-) is the wet-mass ratio and  $m_{w,p}$  (g) is the wet-mass of the  $p^{th}$  internode, while  $m_{w,t}$  (g) is the total wet-mass of the stalk.

The moisture content of the internode was calculated by Equation 3.5:

$$MC_p = \frac{m_{w,p} - m_{d,p}}{m_{w,p}} \cdot 100, \quad (3.5)$$

where  $MC_p$  (%) is the moisture content,  $m_{w,p}$  (g) is the wet-mass and  $m_{d,p}$  (g) is the dry-mass of the  $p^{th}$  internode.

The diameter and length of the shank and maize ears (Figure 3.2(h) & (f)) were measured on 20 maize ears by a digital calliper (accuracy 0.01 mm) and measuring tape (accuracy 1 mm), respectively (Yu, Fu, and Yu, 2015). The diameter of the ears was measured in one point in the middle section of the ear, where it is nearly constant (Yu, Fu, and Yu, 2015). The total mass (kernels and cob) was measured on 20 samples by a digital balance (accuracy 0.01 g), as shown in Figure 3.2(i).

An image, parallel to the longitudinal axis of the ear, was taken in front of a white background. Afterwards, the background was completely removed by an image processing software. In the next step, the pictures were transformed into binary images with luminance factor 0.95, so the profile of the images (shape of ears) could be easily estimated, as shown in Figure 3.2(j). After the detection of the boundaries of ears, the projected diameter and length data were specified by the main diameter and the total length to compare the shape of maize ears with different sizes. Thus, an average ear-shape could be formulated. In this process, an axis-symmetric property of the maize ear was assumed.

By using the processed images about the ear, the centre of mass of the maize ear was calculated based on the equation of first moment of area:

$$C = \frac{\sum_{i=1}^n k_i \cdot A_i}{\sum_{i=1}^n A_i}, \quad (3.6)$$

where  $C$  (mm) is the distance of the centre of mass of the maize ear from the origin,  $k$  (mm) is the distance of the elemental area from the origin,  $A$  ( $\text{mm}^2$ ) is the size of the elemental area.

To determine the relationship among the morphological traits (equivalent diameter of the 1<sup>st</sup> node ( $d_{e1}^N$ ); diameter and length of the shank ( $d^{SH}$  and  $L^{SH}$ ); diameter, length and mass of the maize ear ( $d^{ME}$ ,  $L^{ME}$  and  $m^{ME}$ )) correlation and comparative analysis were carried out. The radius of the confidence interval ( $CI$ ) was determined at 5% ( $P=0.05$ ) significance level by Equation 3.7:

$$CI = Z \cdot \frac{\sigma_X}{\sqrt{f}}, \quad (3.7)$$

where  $Z$  is the Student's number at 5% ( $P=0.05$ ) significance level,  $\sigma_X$  is the standard deviation of variable  $X$  and  $f$  is the degree of freedom. The percentage of the confidence interval to the mean value ( $CI\%$ ) was calculated by Equation 3.8:

$$CI\% = \frac{CI}{\bar{X}} \quad (3.8)$$

The correlation coefficient between two variables ( $r_{X,Y}$ ) was calculated by Equation 3.9:

$$r_{X,Y} = \frac{\sum_{i=1}^n (X_i - \bar{X}) \cdot (Y_i - \bar{Y})}{\sqrt{\sum_{i=1}^n (X_i - \bar{X})^2} \cdot \sqrt{\sum_{i=1}^n (Y_i - \bar{Y})^2}}, \quad (3.9)$$

where  $X_i$  and  $Y_i$  are the measured variables,  $\bar{X}$  and  $\bar{Y}$  are the mean of variables  $X$  and  $Y$ , while  $n$  is the sample size. The Student's t-distribution ( $t$ ) was calculated as follows by Equation 3.10:

$$t = r_{X,Y} \cdot \sqrt{\frac{f - 2}{1 - r_{X,Y}^2}} \quad (3.10)$$

Some results showed that there is an exact ratio between two parameters. Therefore, during

a comparative analysis, a mean ratio ( $\phi_{X,Y}$ ) between the chosen parameters ( $X, Y$ ) was calculated by Equation 3.11:

$$\phi_{X,Y} = \frac{\sum_{i=1}^n \frac{X}{Y}}{n}, \quad (3.11)$$

where  $n$  is the number of parameter pairs. During the evaluation of the correlation and the comparative analysis, the following governing principles were taken into consideration:

- a **strong correlation** is assumed if the correlation coefficient is above 0.75 ( $|r| \geq 0.75$ ) and Student's t-distribution is above 1.734 ( $t \geq 1.734, n = 18, P=0.05$ );
- a **moderate correlation** is assumed if the correlation coefficient is in the range of 0.5 and 0.75 ( $0.75 > |r| \geq 0.5$ ) and Student's t-distribution is above 1.734 ( $t \geq 1.734, n = 18, P=0.05$ );
- a **weak correlation** is assumed if the correlation coefficient is in the range of 0.25 and 0.5 ( $0.5 > |r| \geq 0.25$ ) and Student's t-distribution is above 1.734 ( $t \geq 1.734, n = 18, P=0.05$ );
- a **correlation is not assumed** if the correlation coefficient is in the range of 0.25 and 0.0 ( $0.25 > |r| \geq 0.0$ );
- the **ratio** between two parameters is **strong** if the percentile confidence interval ( $CI\%$ ) is under 5% ( $CI\% \leq 5\%$ );
- the **ratio** between two parameters is **moderate** if the percentile confidence interval ( $CI\%$ ) is in the range of 10% and 5% ( $5\% < CI\% \leq 10\%$ );
- the **ratio** between two parameters is **weak** if the percentile confidence interval ( $CI\%$ ) is in the range of 15% and 10% ( $10\% < CI\% \leq 15\%$ ).

### 3.5 Mechanical Behaviour of Maize

Generally, all the mechanical experiments in the current study focused on the internodal sections of the stalk because the likelihood of loading on an internodal section of the stalk is higher than on the nodal section (Igathinathane et al., 2011), moreover, previous studies justified that the physical and mechanical properties are roughly the same along the internodal region of the stalk (Robertson et al., 2014; Robertson et al., 2015).

Before the experiments, the minor ( $w_p^{mr}$ ) and major ( $w_p^{mj}$ ) width of the internodal cross-section were measured on each sample by using a digital calliper (accuracy 0.01 mm). During all the experiments, the minor axis of the internodes (Figure 3.1 (b)) was the direction of load and force-displacement data were collected at 100 Hz by the universal testing machine (Zwick Z020 and Z250 test frame with a 5000-N load cell), while high-resolution videos were recorded on each sample with 30 frames per second. Afterwards, the recorded videos and force-displacement curves were analysed in detail to determine the mechanical behaviour of the samples. Finally, the work requirement of each process was calculated by using Equation 3.12:

$$W = \sum_{i=1}^n \frac{F_i + F_{i+1}}{2} \cdot (s_{i+1} - s_i), \quad (3.12)$$

where  $W$  (J) is the required work,  $F$  (N) is the force response at any instant,  $s$  (m) is the displacement of the plunger at any instant and  $n$  (-) is the number of measured data points.

Two types of **transversal compression** tests; sectional transversal compression between flat plates (Figure 3.3(a)) and local transversal compression between a flat plate and an edge (Figure 3.3(b)); were conducted on each internode of 10 maize stalks with deformation velocity of 300  $\text{mm min}^{-1}$ . For the sectional transversal compression test, samples of 50 mm length were cut from the middle section of internodes, while the local tests were conducted on the middle of internodes.

First, the plunger approached the sample with velocity of 10  $\text{mm min}^{-1}$  until reaching a preload. The value of the preload was 2 N for the sectional transversal and 5 N for the local

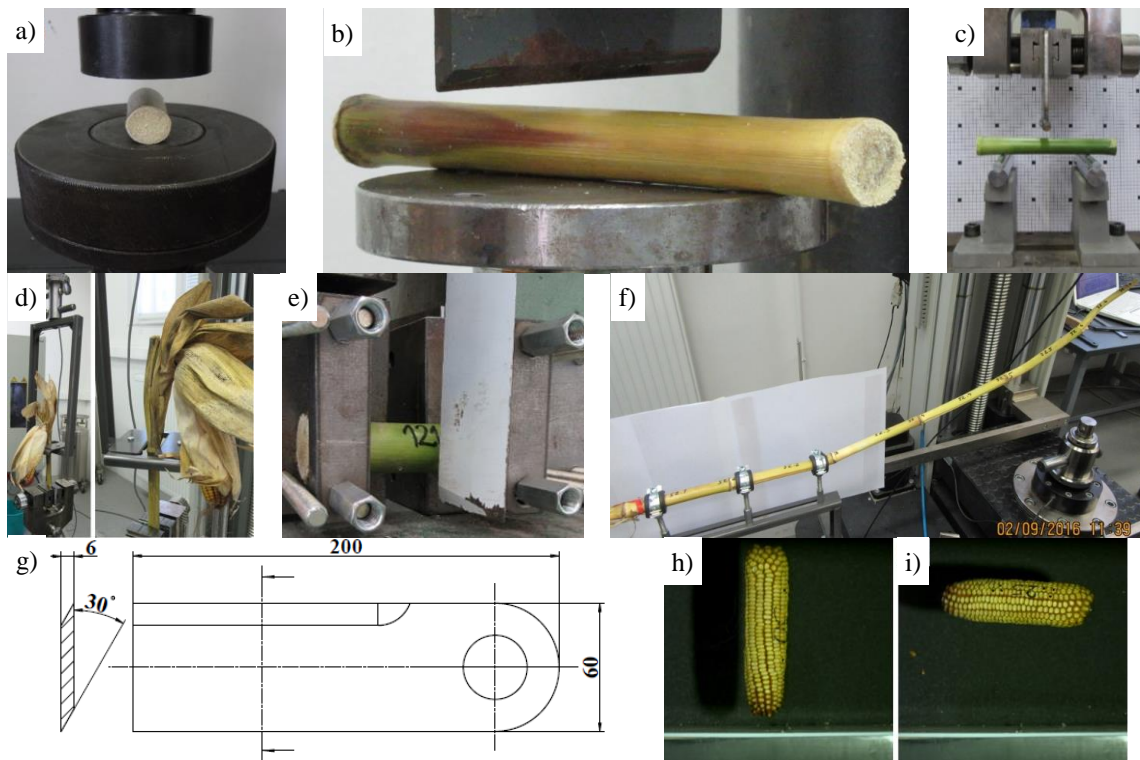


FIGURE 3.3: Experiments on the mechanical behaviour: a) sectional transversal compression; b) local transversal compression; c) three-point bending; d) ear detachment; e) fixtures and cutting blade for dynamic cutting; f) cantilever bending; g) design of the cutting blade (all dimensions in mm); h) collision of ears in longitudinal direction; i) collision of ears in radial direction.

transversal compression tests, respectively. For all the investigated internodes, the applied preloads provided full-contact among the plungers and both sides of the sample. The minor width of the sample was stored after the preload and the compression was carried out until 0.75 of compression rate of the samples that was calculated by Equation 3.13:

$$\kappa = \frac{s}{w_p^{mr}}, \quad (3.13)$$

where  $\kappa$  (-) is the compression rate,  $s$  (mm) is the displacement of the plunger at any instant and  $w_p^{mr}$  (mm) is the width of the pre-loaded cross-section in its minor direction.

**Three-point bending** experiments on each internode of 10 maize stalks were conducted with a deformation speed of  $300 \text{ mm min}^{-1}$ , while the bending tool and the supports had a cylindrical shape with a diameter of 10 mm, as shown in Figure 3.3(c). In contrast to the results of previous studies (Robertson et al., 2014; Robertson, Smith, and Cook, 2015), the span length of 100 mm has been chosen and the samples were loaded in the middle of the internodal sections. This adjustment on the span length resulted in a loading case similar to the phenomenon taking place during harvesting. First, the bending tool approached the sample with a velocity of  $10 \text{ mm min}^{-1}$  until reaching a preload of 2 N. In each case, the displacement of the bending tool was 30 mm.

**Cantilever bending** experiments on the stalk Section A (see Figure 3.1(f)) under the maize ear were conducted with a deformation speed of  $300 \text{ mm min}^{-1}$  by using 20 samples. The bending tool had a cylindrical shape with a diameter of 10 mm and the stalk was fixed by three clamps in such a way the 3<sup>rd</sup> node was in the axis of the bending moment, as shown in 3.3(f). Based on the results of previous studies (Robertson et al., 2014; Robertson, Smith, and Cook, 2015), the span length of 600 mm has been chosen, however, the sample was loaded in

the middle of the 6<sup>th</sup> internodal section. First, the bending tool approached the sample with a velocity of 10 mm min<sup>-1</sup> until reaching a preload of 2 N. In each case, the displacement of the bending tool was 200 mm.

For the **dynamic cutting** experiments, a pendulum impact machine was modified by replacing the hammer with a cutting blade unit (Figure 3.3(g)) in such a way that the gap between the blade and supports was approximately 6 mm on both sides (Figure 3.3(e)). The cutting test was carried out on each internode of 10 maize stalks.

Without causing local deformation, the sample was fixed at both ends. The pendulum started from the same position each time that resulted in a cutting velocity of 3.5 m s<sup>-1</sup>. The reversal angle was visualised and recorded with a scale. Based on the recorded data, the required dynamic cutting work ( $W^{DC}$ ) was calculated by Equation 3.14.

$$W^{DC} = m \cdot g \cdot l \cdot (\cos \beta - \cos \alpha), \quad (3.14)$$

where  $m$  (kg) is the mass of the swinging part,  $g$  (m s<sup>-2</sup>) is the gravitational acceleration,  $l$  (m) is the distance of the centre of the gravity of the swinging part from the pivot point of the pendulum,  $\beta$  (°) is the maximum angle of deflection on the pendulum after the cutting and  $\alpha$  (°) is the maximum angle of deflection on the pendulum before the cutting. For further analysis, the calculated, required cutting work ( $W^{DC}$ ) was specified by the cross-sectional area of the internode, by Equation 3.15.

$$\omega^{DC} = \frac{W^{DC}}{\left(\frac{d_{ep}^{IN}}{4}\right)^2 \cdot \pi}, \quad (3.15)$$

where  $\omega^{DC}$  (J mm<sup>-2</sup>) is the specific required dynamic cutting work and  $d_{ep}^{IN}$  (mm) is the equivalent diameter of the internode in position  $p$ .

For the **ear-detachment** experiment, a special apparatus was developed based on the process of maize harvesting and the general design of deck plates in a maize header, as shown in Figure 3.3(d). The stalk section with the maize ear was fixed in a clamp while the cross head of the universal testing machine with the apparatus moved upwards with a velocity of 600 mm min<sup>-1</sup>. The gap between the deck plates was 25 mm in each case. Before the experiment, the diameter of the shank was measured by a digital calliper (accuracy 0.01 mm). Separately, 10 tests were carried out for standing (SME) and for hanging maize ears (HME).

Through the **ear-collision** experiment, the coefficient of restitution among maize ears and steel (S235, EN 10027) and plastic (Polyethylene, PE) sheets were measured in longitudinal (Figure 3.3(h)) and radial (Figure 3.3(i)) directions of the maize ear. Before the experiment, the diameter, mass and length of the investigated maize ears were measured, and the estimated centre of mass was marked on each sample.

During the experiment, 10 samples were dropped onto the sheets (size 500x500 mm, thickness of the plastic: 5 mm; thickness of the steel: 1 mm) from a 1-metre height and the collision was detected with 1,000 frames per second by a high-speed camera in each case. Based on the recorded frames, the height of the first bounce was estimated. Afterwards, the coefficient of restitution (CR [-]) was calculated based on the drop height ( $H$  [mm]) and the estimated bounce height ( $h$  [mm]) by Equation 3.16.

$$CR = \sqrt{\frac{h}{H}} \quad (3.16)$$

# 4 Experimental Results

All the results are reported in the form given by Equation 4.1:

$$\bar{X} \pm CI(CI\%) \quad (4.1)$$

On the figures, error bars also represent the confidence interval ( $CI$ ) at 5% significance level ( $P=0.05$ ).

## 4.1 Physical Characteristic

### 4.1.1 Maize Stalk

According to the in-situ observation on 100 plants, the upper part of the stalk was broken or completely missing in 93% of the samples. To provide comparable results, measurements on the first ten internodes and nodes (Section A and B) will be presented.

The measured mean equivalent diameter of the 1<sup>st</sup> node ( $\bar{d}_{e1}^N$ ) was  $28.5 \pm 1.4$  (4.9) mm. The distribution of the mean nodal and internodal equivalent diameter ratio ( $\delta_p^{IN/N}$  [-]) along the maize stalk (Figure 4.1(a)) showed a strong correlation ( $r=0.99$ ,  $r=0.98$ ) with position indices ( $p$  [-]), that can be described by Equation 4.2 - 4.5:

$$\delta_{p=1-6}^N = -0.0593 \cdot p + 1.0602 \quad (R^2 = 0.99), \quad (4.2)$$

$$\delta_{p=7-10}^N = -0.0829 \cdot p + 1.1782 \quad (R^2 = 0.99), \quad (4.3)$$

$$\delta_{p=1-5}^{IN} = -0.0594 \cdot p + 0.8673 \quad (R^2 = 0.98), \quad (4.4)$$

$$\delta_{p=6-10}^{IN} = -0.0632 \cdot p + 0.8640 \quad (R^2 = 0.99). \quad (4.5)$$

For the nodes, the inflection point of the bi-linear characteristic is situated at the 6<sup>th</sup> nodal position index (where the maize ear is situated), while, for the internodes it is situated at the 5<sup>th</sup> internodal position index (right below the maize ear). The gradient of decreasing the nodal and the internodal equivalent diameter ratios below the position of the maize ear were nearly the same: -0.0593 and -0.0594, respectively. However, above the position of the maize ear, the decreasing gradient of the nodal ratios was higher (-0.0829) than the decreasing gradient of the internodal ratio (-0.0632).

The measured mean total length of the first ten internodes was  $1510 \pm 128$  (8.5) mm. Three sections could be determined on the length ratio distribution along the maize stalk, as shown in Figure 4.1(b): the length ratio linearly increases between the 1<sup>st</sup> and the 4<sup>th</sup> internodes, where it reaches the maximum value; afterwards, it starts to linearly decrease until reaching a constant value at the 9<sup>th</sup> internode. The relationship between the internodal length ratios ( $\lambda_p$  [-]) and the position indices ( $p$  [-]) can be described by Equations 4.6 - 4.8:

$$\lambda_{p=1-4} = 0.0118 \cdot p + 0.0711 \quad (R^2 = 0.97), \quad (4.6)$$

$$\lambda_{p=5-8} = -0.0051 \cdot p + 0.1371 \quad (R^2 = 0.99), \quad (4.7)$$

$$\lambda_{p=9-10} = 0.09081. \quad (4.8)$$

The measured mean wet-mass of the first ten internodes was  $191.7 \pm 38.5$  (20.1) g. The wet-mass ratio of internodes significantly decreases from the 1<sup>st</sup> to the 5<sup>th</sup> internode where the gradient of decreasing drops, as shown in Figure 4.1(c). The relationship between internodal wet-mass ratios ( $\mu_{w,p}$  [-]) and position indices ( $p$  [-]) is described by Equation 4.9 - 4.10:

$$\mu_{w,p=1-5} = -0.0360 \cdot p + 0.2786 \quad (R^2 = 0.99), \quad (4.9)$$

$$\mu_{w,p=6-10} = -0.0135 \cdot p + 0.1375 \quad (R^2 = 0.96). \quad (4.10)$$

The mean moisture content of the internodes (MC [%]) linearly decreases from the 1<sup>st</sup> to the 8<sup>th</sup> internode where it starts to decrease more significantly, as shown in Figure 4.1(d). Below the maize ear, the mean moisture content of internodes was 67% w.b.

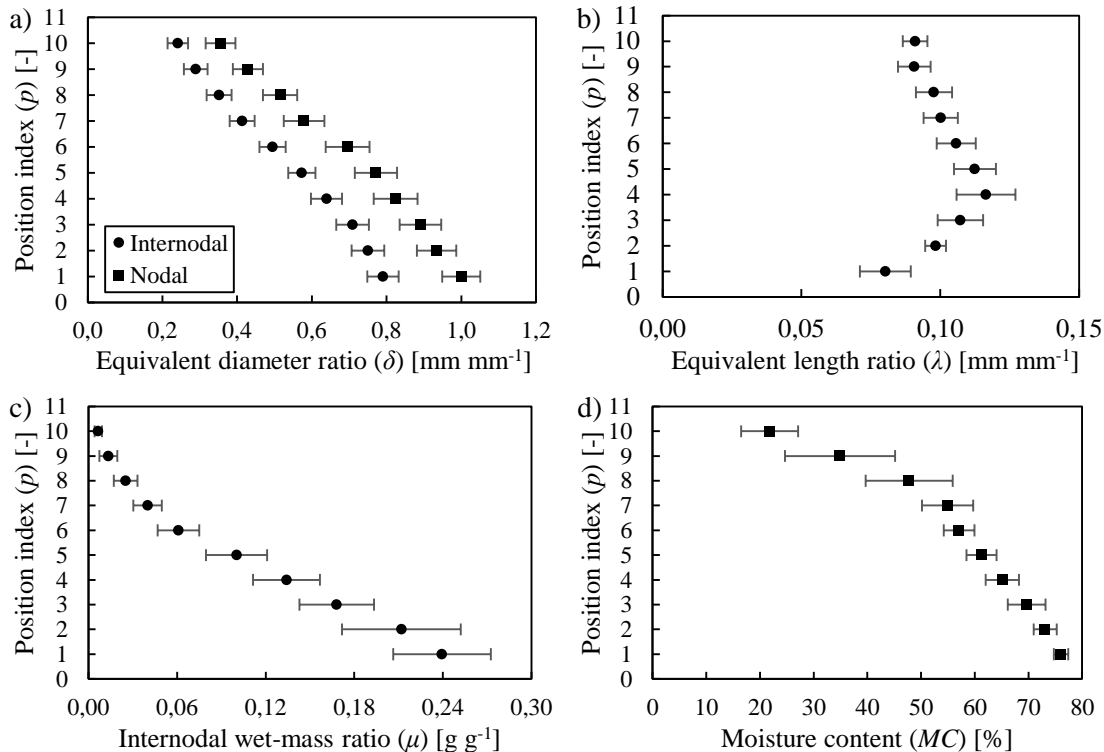


FIGURE 4.1: Physical characteristic of the maize stalk: a) equivalent diameter ratio, b) length ratio, c) wet-mass ratio and d) moisture content distribution on the maize stalk.

#### 4.1.2 Maize Ear and Shank

According to the in-situ structural observation on 100 plants, each plant had two ears: a fully developed and a rudimentary one. Hence, the results will be explained in relation to the fully developed maize ear and its shank.

Generally, the fully developed maize ear was situated beside the 6<sup>th</sup> internode. However, two different positions were observed: hanging (HME) and standing (SME). In the first case, the shank of the ear was buckled, thus, it was not able to hold the mass of the ear. According to our observation, 59% of the ears were in the hanging position.

The calculated mean distance of the centre of mass (CM) from the soil surface was  $93 \pm 5.0$  (5.2) cm and  $108.2 \pm 4.5$  (4.2) cm for HME and for SME, respectively. The calculated mean distance of CM from the stalk was  $10.0 \pm 1.0$  (10.0) cm and  $5.6 \pm 0.5$  (8.9) cm for HME and

SME, respectively. The measured mean diameter and length of the shank was  $10.6 \pm 0.4$  (3.6) mm and  $115.8 \pm 15.7$  (13.6) mm, respectively.

TABLE 4.1: Correlation coefficients ( $r$ ) and mean ratios ( $\phi$ ) among the analysed traits.

Trait	Relation	$d_{e1}^N$	$d^{ME}$	$L^{ME}$	$m^{ME}$	$d^{SH}$	$L^{SH}$
$d_{e1}^N$	$r(t)$	1					
	$\phi(CI\%)$	1					
$d^{ME}$	$r(t)$	0.17 (0.72)	1				
	$\phi(CI\%)$	1.94 (5.1)	1				
$L^{ME}$	$r(t)$	0.49 (2.41)	0.24 (1.05)	1			
	$\phi(CI\%)$	6.88 (5.4)	3.50 (3.2)	1			
$m^{ME}$	$r(t)$	0.53 (2.63)	0.61 (3.28)	0.88 (7.72)	1		
	$\phi(CI\%)$	8.54 (7.1)	4.43 (6.8)	1.24 (4.2)	1		
$d^{SH}$	$r(t)$	-0.22 (-0.97)	-0.16 (-0.69)	0.22 (0.95)	0.01 (0.05)	1	
	$\phi(CI\%)$	0.43 (7.0)	0.22 (4.3)	0.06 (5.9)	0.05 (9.8)	1	
$L^{SH}$	$r(t)$	0.16 (0.70)	0.13 (0.54)	0.66 (3.73)	0.56 (2.88)	0.46 (2.23)	1
	$\phi(CI\%)$	4.70 (13.9)	2.43 (13.6)	0.68 (10.9)	0.55 (11.5)	10.92 (12.3)	1

The results of the comparative and the correlation analysis are shown in Table 4.1. A strong correlation among the equivalent diameter of the first node ( $d_{e1}^N$ ) and the other morphological properties were not found, but the mean ratio between the equivalent diameter of the first node ( $d_{e1}^N$ ) and the diameter of the maize ear ( $d^{ME}$ ) had the smallest percentile radius of  $CI\%$  (5.1%). A moderate correlation ( $r=0.61$ ,  $t=3.28$ ) was found between the diameter of maize ears ( $d^{ME}$ ) and the mass of maize ears ( $m^{ME}$ ), while, the mean ratio between the diameter of maize ears ( $d^{ME}$ ) and the diameter of shanks ( $d^{SH}$ ) had the smallest  $CI\%$  (4.3%). The ratio between the diameter ( $d^{ME}$ ) and length ( $L^{ME}$ ) of maize ears also had a small  $CI\%$  (3.2%). A strong correlation ( $r = 0.88$ ,  $t=7.72$ ) was found between the length ( $L^{ME}$ ) and mass ( $m^{ME}$ ) of maize ears. However, the mean ratio between these properties also had the smallest  $CI\%$  (4.2%). A moderate correlation was found between the length of shanks ( $L^{SH}$ ) and the maize ears ( $L^{ME}$ ), but the ratio between these parameters was weak.

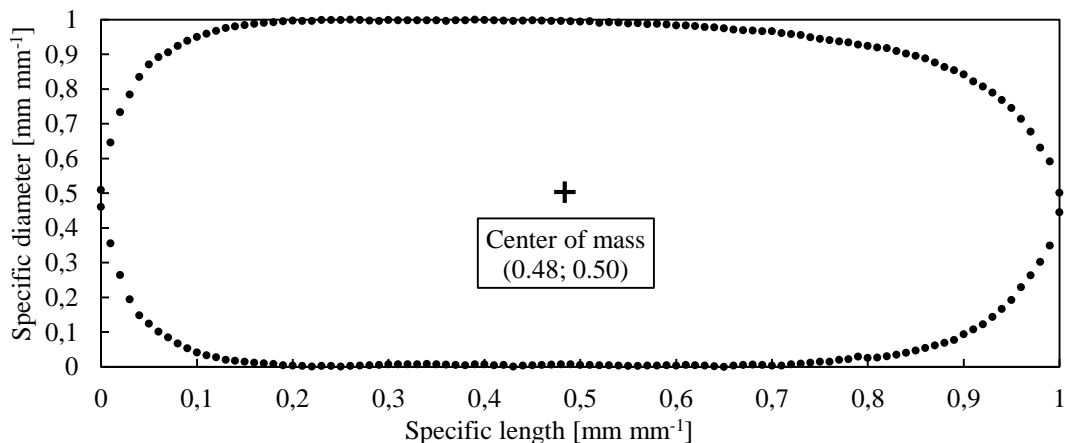


FIGURE 4.2: Average shape and mean centre of mass of maize ears.

The measured mean diameter, mean length and mass of the maize ear was  $47.6 \pm 0.9$  (1.8) mm,  $169.8 \pm 8.7$  (5.1) mm and  $211.2 \pm 16.0$  (7.6) g, respectively. The average shape of the maize ear is shown in Figure 4.2, where three sections were determined: the bottom section in the range of 0–0.2 specific length, where the shank joins to the ear and the diameter increases

significantly until reaching a constant value; the middle section in the range of 0.2–0.6 specific length, where the diameter of the ear is nearly constant; the top section in the range of 0.6–1.0, where the diameter smoothly decreases to the tip of the ear. The mean value of the centre of mass in longitudinal and radial directions was  $0.50 \pm 0.005$  (1.0) and  $0.48 \pm 0.004$  (0.8), respectively. All the observed maize ears are presented in Figure A.1.

## 4.2 Mechanical Behaviour

### 4.2.1 Sectional Transversal Compression

The typical phases of the force response were determined for each internodal section, as shown in Figure 4.3. All the measured characteristics are shown in Figure A.3.

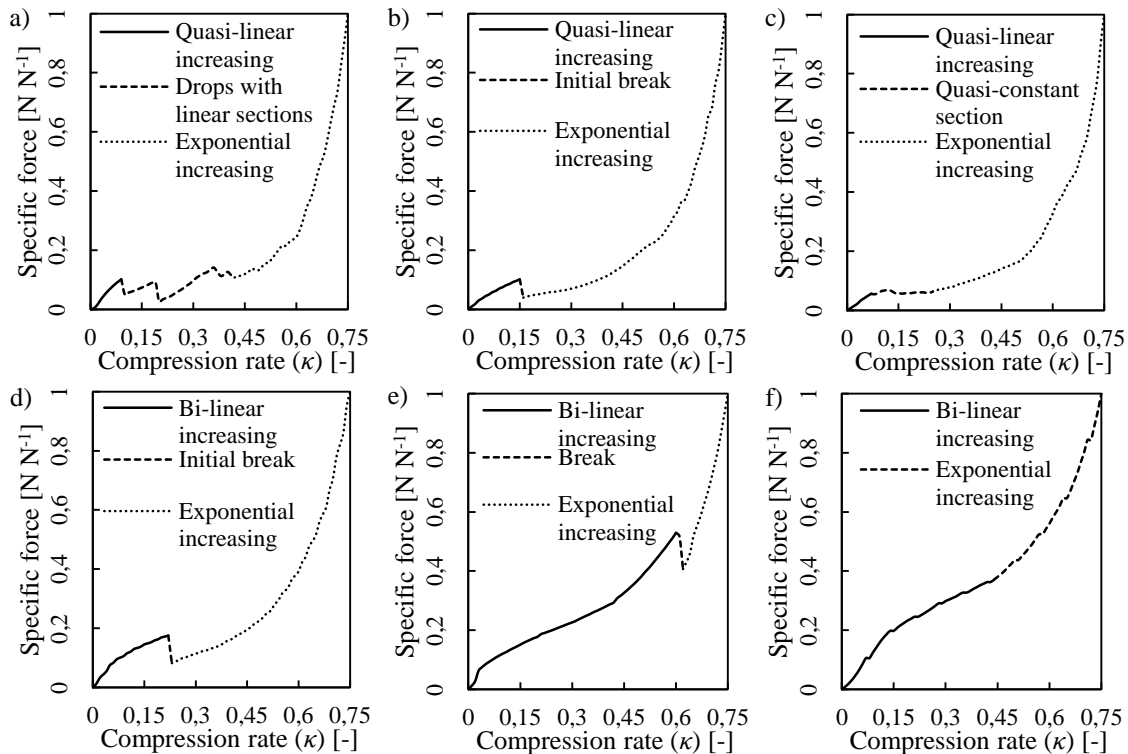


FIGURE 4.3: Typical force response of the internodal sections by sectional transversal compression experiment: a) typical force response of the 1<sup>st</sup>; b) the 2<sup>nd</sup>, 3<sup>rd</sup>, 4<sup>th</sup>, 5<sup>th</sup> and 7<sup>th</sup>; c) the 6<sup>th</sup>; d) the 8<sup>th</sup>; e) the 9<sup>th</sup> and f) the 10<sup>th</sup> internodal stalk sections.

In case of the 1<sup>st</sup> internode, the force response was divided into three typical phases (Figure 4.3(a)): quasi-linear increasing; drops with linear sections and exponential increasing in the range of compression rate 0 - 0.075; 0.075 – 0.3 and 0.3 - 0.75, respectively. For the internodal positions from the 2<sup>nd</sup> to the 5<sup>th</sup> and the 7<sup>th</sup>, the force response was made up of the same phases (Figure 4.3(b)): quasi-linear increasing; initial break and exponential increasing. However, the range of these phases was different for internodes in different positions, as shown in Figure 4.4(a). Only in case of the 6<sup>th</sup> internode, the quasi-linear increasing phase was followed by a quasi-constant phase in the range of 0.2–0.3 compression rate, as shown in Figure 4.3(c). The typical characteristics of the 8<sup>th</sup> and 9<sup>th</sup> internodes consist of the same phases (Figure 4.3(d) & (e)): bi-linear increasing; initial break and exponential increasing. However, the range of these phases was different for the different positions of internodes. In both cases, an initial linear increasing phase was observed between a 0 and 0.05 compression rate, which was followed by another linear increasing with a lower gradient in the range of a 0.05–0.225 compression rate for

the 8<sup>th</sup> internode and in the range of a 0.05–0.4 compression rate for the 9<sup>th</sup> internode. The break occurred in the range of a 0.225–0.55 compression rate for the 8<sup>th</sup> internode and in the range of a 0.4–0.75 compression rate for the 9<sup>th</sup> internode. The exponential increasing phase could be observed over a 0.55 compression rate for the 8<sup>th</sup> internode and over a 0.4 compression rate for the 9<sup>th</sup> internode. In case of the 10<sup>th</sup> internode, the force response was divided into a bilinear increasing and an exponential increasing phase, in the range of 0–0.1, 0.1–0.5 and 0.5–0.75 compression rate, as shown in Figure 4.3(f).

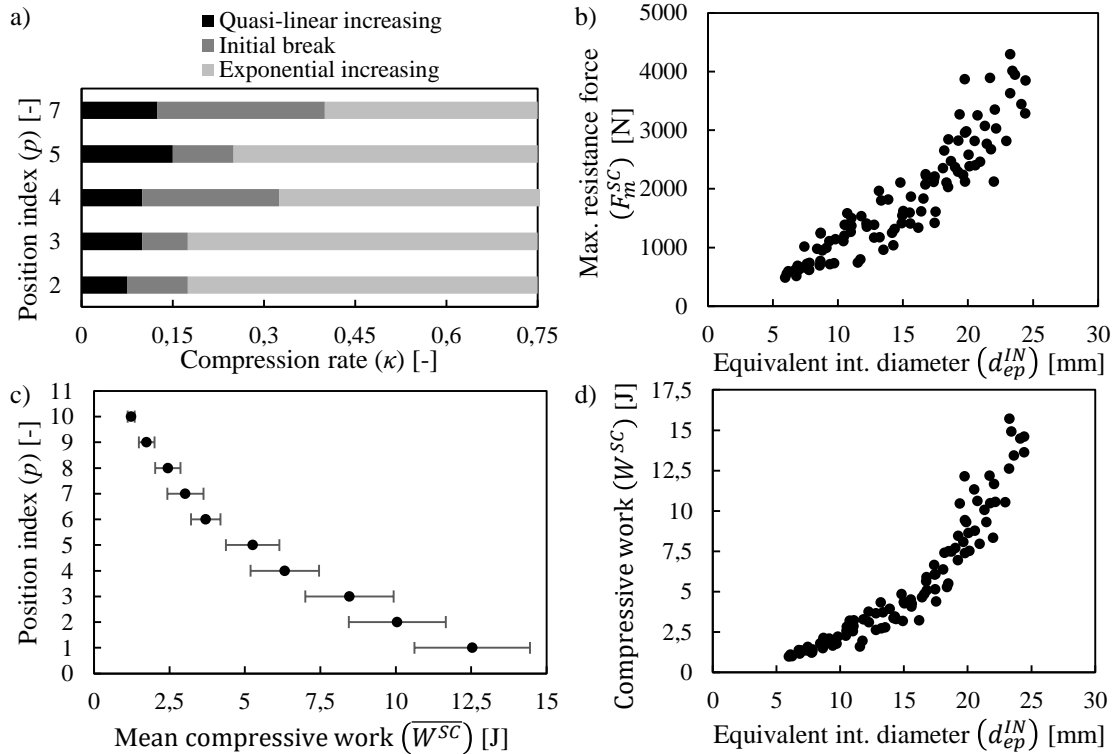


FIGURE 4.4: Mechanical characteristic of the internodal section by sectional transversal compression: a) length of the typical force response phases of the 2<sup>nd</sup>, 3<sup>rd</sup>, 4<sup>th</sup>, 5<sup>th</sup> and 7<sup>th</sup> internodes; b) relationship among the maximal compressive force and the equivalent internodal diameter; c) mean compressive work distribution on the maize stalk and d) relationship among the compressive work and the equivalent internodal diameter.

Through an analysis of the maximal compressive force at 0.75 compression rate ( $F_m^{SC}$  [N]) and the equivalent diameter of internodes ( $d_{ep}^{IN}$  [mm]), a strong correlation ( $r = 0.92$ ) was found, as shown in Figure 4.4(b), and an exponential relation was determined, see Equation 4.11.

$$F_m^{SC} = 360.98 \cdot e^{0.099 \cdot d_{ep}^{IN}} \quad (R^2 = 0.87) \quad (4.11)$$

The mean compressive work distribution on the maize stalks is shown in Figure 4.4(c). The results proved that the mean compressive work significantly decreases to the 6<sup>th</sup> internode where the slope of the decreasing drops. The required compressive work on the 1<sup>st</sup> internode (12.53 J) was approximately 10 times higher than on the 10<sup>th</sup> internode (1.23 J), moreover, the first five internodes provided 77.8% (42.6 J) of the total required compressive work (54.8 J) on an average stalk.

By the analysis of the compressive work ( $W^{SC}$  [J]) and the internodal equivalent diameter ( $d_{ep}^{IN}$  [mm]), a strong correlation ( $r = 0.93$ ) was found, as shown in Figure 4.4(d), and an

exponential relation was determined, see Equation 4.12.

$$W^{SC} = 0.506 \cdot e^{0.1402 \cdot d_{ep}^{IN}} \quad (R^2 = 0.95) \quad (4.12)$$

During the analysis of the recorded videos, five major breaking events could be observed: ovalisation, vertical break of the core, vertical break of the skin, horizontal breaks of the skin and flattening. Moreover, most of them were related to the measured force response, as shown in Figure 4.5. At the beginning of the compression, the sample was ovalised without any observable damage or break in its structure. This phenomenon was related to the initial-quasi linear increasing section on force-compression rate curves. After that, a straight vertical break appeared in the core of the sample that was related to the initial break phase on the force-compression rate curves. The vertical break of the core propagated to the skin and it also broke in the vertical direction. By this phenomenon, the sample was broken into two separated parts. However, the effect of this phenomenon on the force response was not observable. On both sides of the skin, small breaks appeared in the horizontal direction. Usually, these breaks propagated to the boundary between the skin and the core. This phenomenon resulted in the small drops in the exponentially increasing section of force-compression rate curves. After the structural collapse of the skin, the core had a more significant effect on the mechanical behaviour of the internodal section against transversal compression. During flattening, the vertical break in the middle disappeared, while, the breaks on the sides opened up. Usually, a large amount of liquid flowed out from the sample.

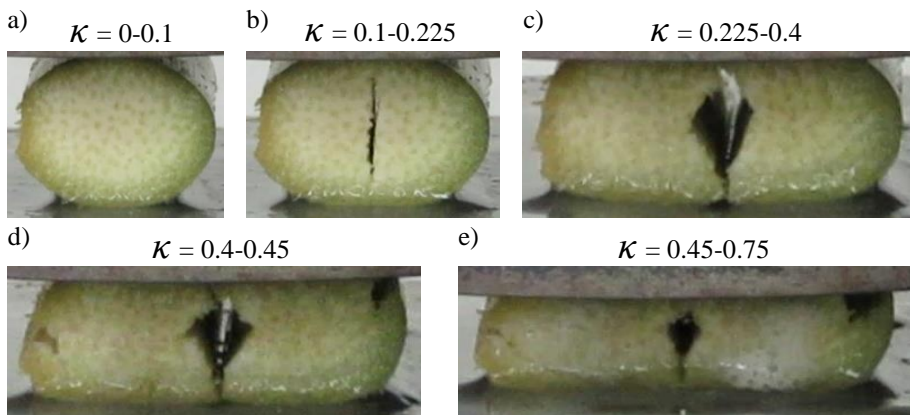


FIGURE 4.5: Major breaking events of internodal stalk sections during sectional transversal compression: a) ovalisation; b) vertical break of the core; c) vertical break of the skin; d) horizontal breaks of the skin; e) flattening.

#### 4.2.2 Local Transversal Compression

The determined typical phases of the force response were the initial bilinear increasing with an inflection point; the constant and the exponential increasing section in range of 0–0.3; 0.3–0.45 and 0.45–0.75 compression rate, respectively (Figure 4.6(a)). All the measured characteristics are shown in Figure A.4.

Figure 4.6(b) shows the mean maximal ( $\overline{F_m^{LC}}$  [N]) and mean constant force ( $\overline{F_c^{LC}}$  [N]) values for each internodal section. The mean maximal compressive force of the 1<sup>st</sup> internode (967.24 N) was 12.2 times higher than the mean maximal force of the 10<sup>th</sup> internode (79.18 N), while, the mean constant force of the 1<sup>st</sup> internode (340.34 N) was 6.5 times higher than the mean constant force of the 10<sup>th</sup> internode (52.62 N). Strong correlation was found among the position indices ( $p$  [-]), the mean constant ( $r=-0.94$ ) and the mean maximal ( $r=-0.92$ ) forces. These relations can

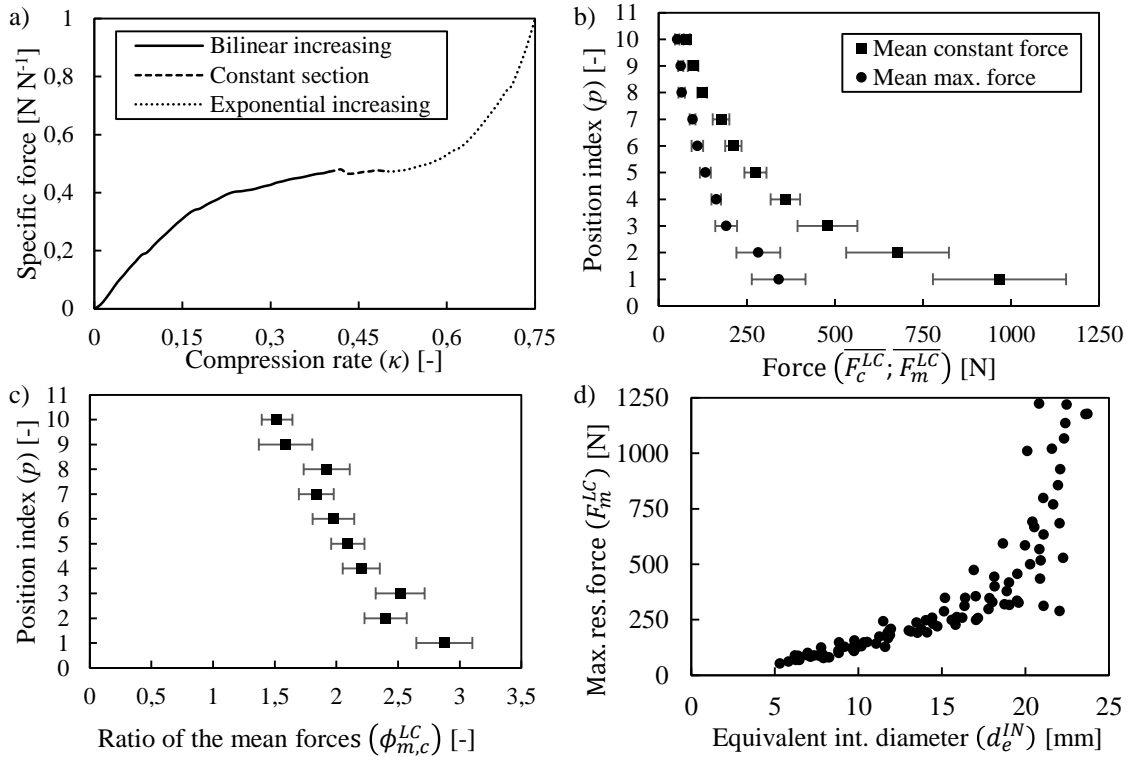


FIGURE 4.6: Force response characteristic by local transversal compression experiment: a) typical phases of the force response; b) mean maximal and constant forces; c) distribution of the ratio of the mean maximal and constant force on a maize stalk; d) relationship among the maximum compressive force and the equivalent internodal diameter.

be determined by Equation 4.13 - 4.14:

$$\overline{F_c^{LC}} = 393.6 \cdot e^{-0.209 \cdot p} \quad (R^2 = 0.97) \quad (4.13)$$

$$\overline{F_m^{LC}} = 1147.2 \cdot e^{-0.274 \cdot p} \quad (R^2 = 0.99) \quad (4.14)$$

Moreover, a strong correlation ( $r=-0.96$ ) was also found between the ratios of the mean maximal and the mean constant forces ( $\phi_{m,c}^{LC}$  [-]) and positions indices ( $p$  [-]), as shown in Figure 4.6(c). This relation can be defined by Equation 4.15:

$$\phi_{m,c}^{LC} = -0.1338 \cdot p + 2.8279 \quad (R^2 = 0.93) \quad (4.15)$$

By the further analysis of the maximal compressive force ( $F_m^{LC}$  [N]) and the equivalent diameter of the internodes ( $d_{ep}^{IN}$  [mm]), a strong correlation ( $r = 0.82$ ) was found, as shown in Figure 4.6(d), and an exponential relation was determined, see Equation 4.16.

$$F_m^{LC} = 30.657 \cdot e^{0.1432 \cdot d_{ep}^{IN}} \quad (R^2 = 0.91) \quad (4.16)$$

The required mean compressive work ( $\overline{W^{LC}}$  [N]) distribution on maize stalks is shown in Figure 4.7(a). The results proved that it significantly decreases from the bottom to the top sections of the stalk, while the mean required compressive work on the 1<sup>st</sup> internode (6.35 J) was 31.75 times higher than on the 10<sup>th</sup> internode (0.20 J). Moreover, the first five internodes provided 86.7% (17.1 J) of the total required compressive work (19.7 J) on an average stalk.

By the analysis of the required compressive work ( $W^{LC}$  [N]) and the internodal equivalent diameter ( $d_{ep}^{IN}$  [mm]), a strong correlation ( $r = 0.83$ ) was found, as shown in Figure 4.7(b), and

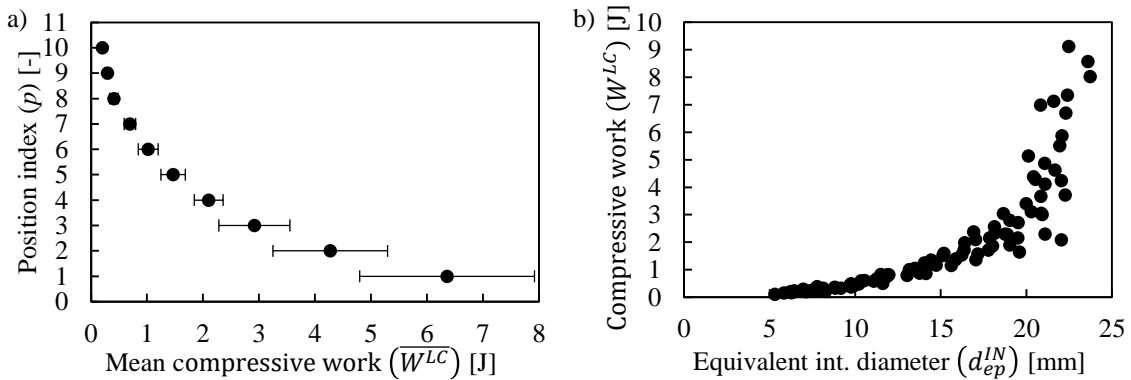


FIGURE 4.7: Required compressive work characteristics by local transversal compression experiments: a) mean required compressive work distribution on a maize stalk; b) relationship among the compressive work and the equivalent internodal diameter.

an exponential relation was determined, see Equation 4.17.

$$W^{LC} = 0.058 \cdot e^{0.2031 \cdot d_{ep}^{IN}} \quad (R^2 = 0.96) \quad (4.17)$$

Based on the recorded videos, the damage and breaking phenomena took place close to the plunger tool, where the cross-section was buckled and longitudinal breaks appeared locally, as shown in Figure 4.8. First, a complex bending and transverse compression deformation was observed that relates to the initial bi-linear increasing phase of the force response. In the quasi-constant phase of the typical characteristic, internal fracture was assumed, while complex tissue compression was assumed during the exponential increasing phase. After the experiment, residual deformation and two flat triangular surfaces (so called diamond (Leblicq et al., 2015)) on the top of the specimen were observed in the region of compression, as shown in Figure 4.8(b). In some cases, mainly for the upper and drier internodal parts, the plunger cut through the top fibres of the samples.

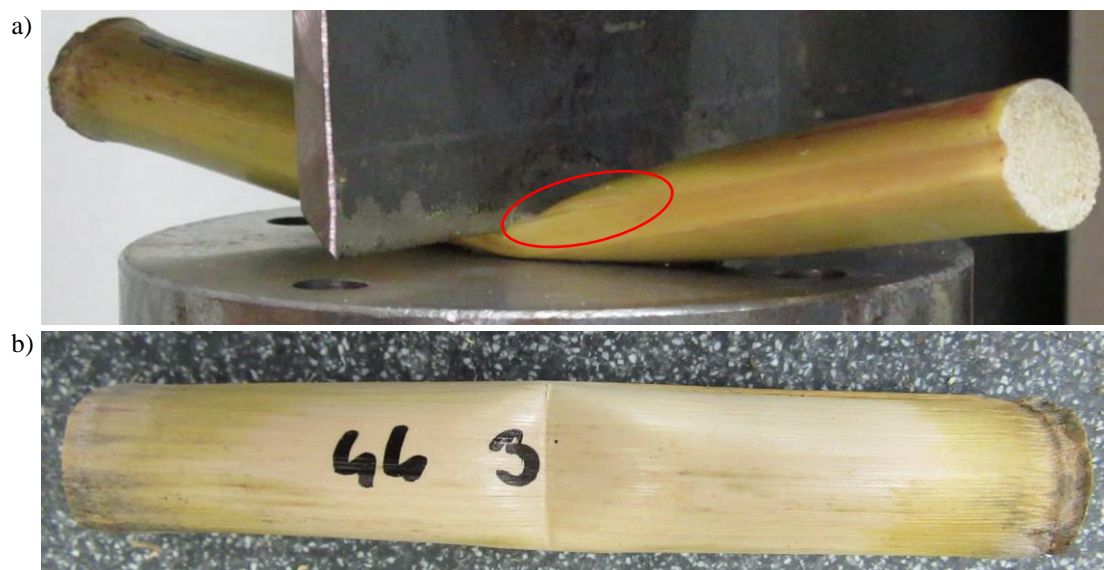


FIGURE 4.8: Typical damage and breaking phenomena by local transversal compression experiment: a) longitudinal breaks under the plunger (marked by red ellipse); b) residual deformation.

### 4.2.3 Three-Point Bending

The bending characteristic was divided into four typical phases: an elastic phase where the resistance force increases linearly; a plastic phase where the force response reaches its maximum; the phase of the structural collapse (buckling) where the resistance force decreases until reaching an ultimate value and the sliding phase where the resistance force remains constant, as shown in Figure 4.9(a). All the measured characteristics are shown in Figure A.5.

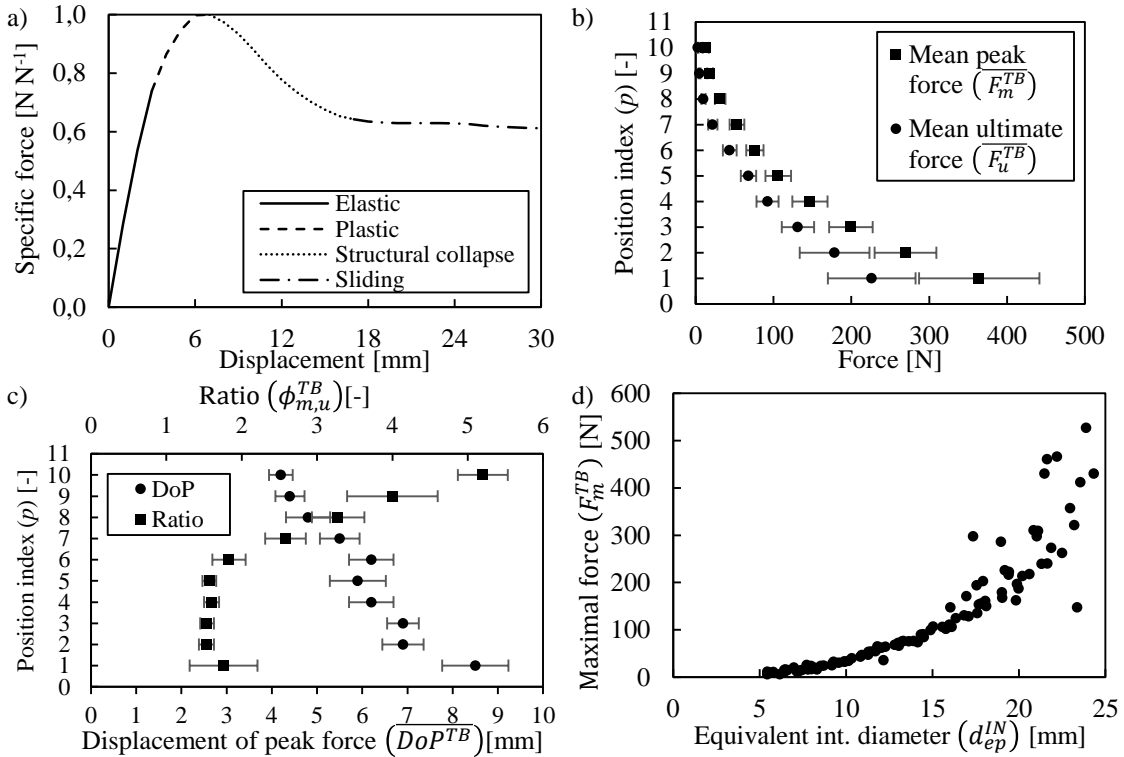


FIGURE 4.9: Force response characteristic by three-point bending: a) typical phases of the force response; b) distribution of mean maximal and mean ultimate and c) distribution of the mean displacement of the peak force and the mean ratio between the maximal and the ultimate forces on a maize stalk; d) relationship among the maximal forces and the equivalent diameter of internodes.

Figure 4.9(b) shows the mean maximal ( $\bar{F}_m^{TB}$  [N]) and mean ultimate ( $\bar{F}_u^{TB}$  [N]) force values for each internodal section. The mean peak force of the 1<sup>st</sup> internode (364.24 N) was 28.5 times higher than the mean peak force of the 10<sup>th</sup> internode (12.78 N), while, the mean ultimate force of the 1<sup>st</sup> internode (226.15 N) was 88.3 times higher than the mean ultimate force of the 10<sup>th</sup> internode (2.56 N). Strong correlation was found among the position indices ( $p$ ), the mean peak ( $r=-0.94$ ) and the mean ultimate ( $r=-0.95$ ) forces that were described by Equation 4.18 - 4.19:

$$\bar{F}_m^{TB} = 612.75 \cdot e^{-0.373 \cdot p} \quad (R^2 = 0.96) \quad (4.18)$$

$$\bar{F}_u^{TB} = -106.2 \cdot \ln(p) + 238.19 \quad (R^2 = 0.99) \quad (4.19)$$

The mean displacement of the plunger where the peak (maximal) force appears (mean displacement of peak force,  $\bar{D}oP^{TB}$  [mm]) and the mean ratio ( $\phi_{m,u}^{TB}$  [-]) between the peak and the ultimate forces are shown in Figure 4.9(c). A strong correlation ( $r=-0.96$ ) was found between the  $\bar{D}oP^{TB}$  and the position indices ( $p$  [-]) of the stalk and a linear relation was defined by Equation 4.20:

$$\bar{D}oP^{TB} = -0.4152 \cdot p + 8.2333 \quad (R^2 = 0.92) \quad (4.20)$$

The mean ratio among the peak and the ultimate forces ( $\phi_{m,u}^{TB}$  [-]) was divided into two sections: under and above the position of the maize ear. Under the maize ear it was nearly constant, while above the maize ear it increased linearly. These relations were determined by Equation 4.21 - 4.22:

$$\phi_{m,u(p=1-6)}^{TB} = 1.6383 \quad (4.21)$$

$$\phi_{m,u(p=7-10)}^{TB} = 0.8160 \cdot p - 3.1500 \quad (R^2 = 0.99) \quad (4.22)$$

By the further analysis of the maximal force ( $F_m^{TB}$  [N]) and the equivalent diameter of the internode ( $d_{ep}^{IN}$  [mm]), a strong correlation ( $r = 0.89$ ) was found, as shown in Figure 4.9(d), and an exponential relation was determined, see Equation 4.23.

$$F_m^{TB} = 0.0818 \cdot e^{2.6432 \cdot d_{ep}^{IN}} \quad (R^2 = 0.96) \quad (4.23)$$

The mean required bending work ( $\bar{W}^{TB}$  [J]) distribution on maize stalks is shown in Figure 4.10(a). The results show that the mean required bending work decreases significantly from the bottom to the top sections of the stalk. Moreover, the mean required bending work on the 1<sup>st</sup> internode (7.94 J) was 53 times higher than on the 10<sup>th</sup> internode (0.15 J), and the first five internodes provided 87.4% (23.62 J) of the total required bending work (27.04 J) on each stalk.

By the analysis of the required bending work ( $W^{TB}$  [J]) and the internodal equivalent diameter ( $d_{ep}^{IN}$  [mm]), a strong correlation ( $r = 0.89$ ) was found, as shown in Figure 4.10(b), and an exponential relation was determined, see Equation 4.24.

$$W^{TB} = 0.0459 \cdot e^{0.2376 \cdot d_{ep}^{IN}} \quad (R^2 = 0.94) \quad (4.24)$$

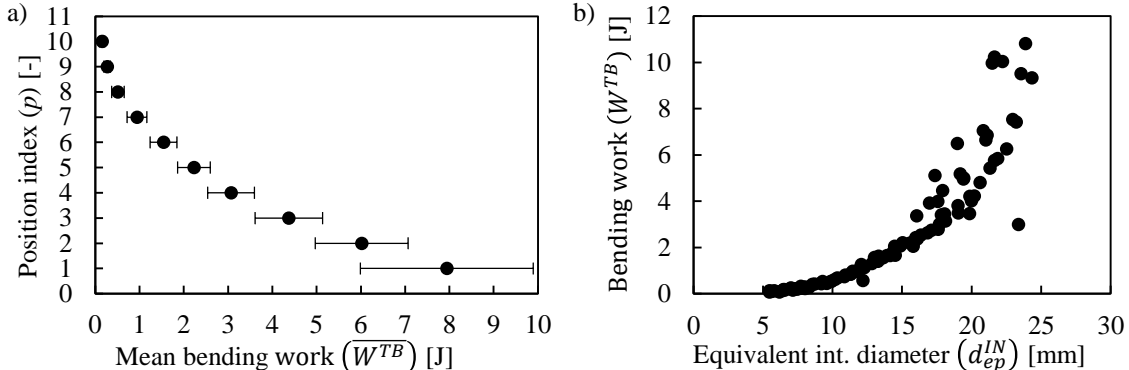


FIGURE 4.10: Bending work characteristics by three-point bending: a) mean bending work distribution on a maize stalk; b) relationship among the bending work and the equivalent internodal diameter.

The breakage of the samples were analysed based on high-resolution records, as shown in Figure 4.11. The following major phenomena could be observed: ovalisation (flattening), structural collapse (buckling), sliding and residual deformation. These phenomena were also related to the typical sections of resistance force – displacement curves of three-point bending experiment. At the beginning of the bending, the cross-section under the bending tool was ovalised without any observable damage or break in the skin structure. This phenomenon took place in a small area near to the bending tool and resulted in a flattened and ovalised cross-section, but real bending displacement did not occur rather than transversal deformation. This phenomenon related to the elastic section of the resistance force – displacement curve. The structure became unstable in the bending area and longitudinal breaks appeared that resulted in a plastic-hinge (structural collapse) under the bending tool. These breaks usually propagated to the ends of the specimen. This phenomenon related to the structural collapse section of

the resistance force – displacement curves. At the end of the process, the sample slid on the supports while it provided constant resistance against bending. After the experiments, the cross-sections in the bending area had residual deformation. In case of drier samples, usually with smaller cross-sectional area, the significance of the residual deformation was higher.

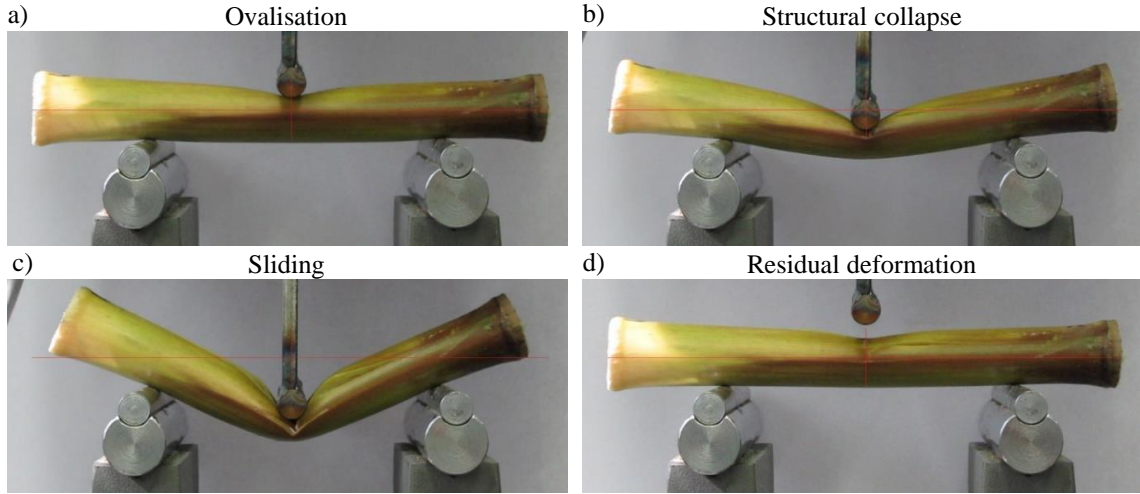


FIGURE 4.11: Typical breakage of the samples by three-point bending experiment: a) ovalisation (flattening); b) structural collapse; c) sliding; d) residual deformation.

#### 4.2.4 Cantilever Bending

The bending characteristic was also divided into four typical phases: an initial elastic phase where the resistance force increases linearly; a plastic phase where the force-displacement curve reaches its maximum; the phase of the structural collapse (buckling) where resistance force suddenly drops to an ultimate value and the plastic joint phase where the resistance force remains approximately constant, as shown in Figure 4.12(a). Based on the analysis of the peak and ultimate forces, a ratio ( $\phi_{m,u}^{CB}$  [-]) was defined that varied between 0.08 and 0.27 (-), while its mean value was  $0.1727 \pm 0.033$  (19.0). All the measured results are presented in Figure A.6.

The displacement of the plunger where the maximal force appears (displacement of peak force,  $DoP^{CB}$  [mm]) varied between 106.6 and 158.7 mm. A strong correlation ( $r=-0.93$ ) was found between the  $DoP^{CB}$  and the equivalent diameter of the 1<sup>st</sup> node of the stalk ( $d_{e1}^N$  [mm]), as shown in Figure 4.12(b), and a linear relation was defined, see Equation 4.25:

$$DoP^{CB} = -11.956 \cdot d_{e1}^N + 464.51 \quad (R^2 = 0.86) \quad (4.25)$$

The maximal force ( $F_m^{CB}$ ) varied between 13 and 24 N, moreover, a strong correlation ( $r=0.86$ ) was found between the maximal force and the equivalent diameter of the 1<sup>st</sup> node of the stalk ( $d_{e1}^N$  [mm]), as shown in Figure 4.12(c), and a linear relation was defined in the range of 25-30 mm equivalent diameter by Equation 4.26:

$$F_m^{CB} = 1.8668 \cdot d_{e1}^N - 32.738 \quad (R^2 = 0.75) \quad (4.26)$$

The breakage of the samples was analysed based on high-resolution records, as shown in Figure 4.12(d)(e). In each case a buckled, creased breakage occurred close to the 3<sup>rd</sup> (fixed) node that was oriented parallel to the axis of the applied bending moment, moreover, the breakage results in the structural collapse section of the typical curve (see Figure 4.12(a)). The distance of the breakage from the 3<sup>rd</sup> node was ranged between 9 and 36 mm, moreover, its mean value was  $22.3 \pm 2.4$  (10.7) mm based on 20 observed samples.

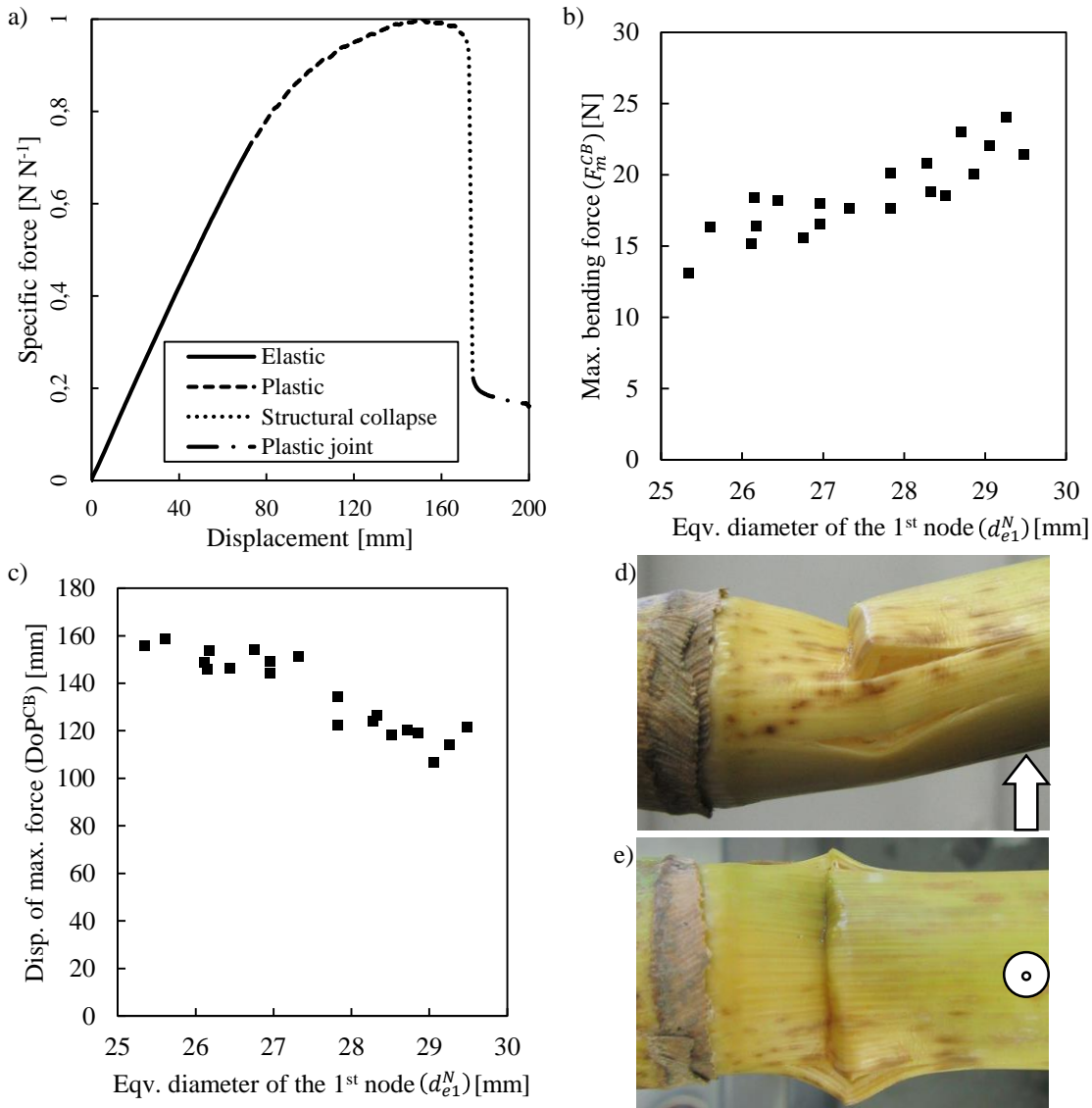


FIGURE 4.12: Results of cantilever bending experiment: a) typical sections of the force response; b) relationship between the displacement of the peak force and the equivalent diameter of the 1<sup>st</sup> node; c) relationship among the peak force and the equivalent diameter of the 1<sup>st</sup> node; breakage of the stalk from d) side and e) top view (the movement direction of the bending tool is marked by the arrows).

#### 4.2.5 Dynamic Cutting

The mean dynamic cutting work distribution on the stalk is shown in Figure 4.13(a). The mean required dynamic cutting work of the internode ( $W^{DC}$  [J]) decreased as the position index ( $p$  [-]) increased, but two different stages were observable. After the 5<sup>th</sup> internode, a significant drop was observed on the characteristic while the grades of decreasing were nearly the same. Moreover, the CI ( $P=0.05$ ) of results under the 5<sup>th</sup> internode was significantly higher than herein above. Thus, the uncertainty of these results is higher. The mean required cutting work on the 1<sup>st</sup> internode (21.13 J) was 7 times higher than on the 10<sup>th</sup> internode (3.02 J). Moreover, the first five internodes provided 78.8% (90.4 J) of the total required cutting work (114.7 J) on an average stalk.

The mean specific dynamic cutting work ( $\omega^{DC}$  [ $J \text{ mm}^{-2}$ ]) vs. the position of the internode ( $p$  [-]) on the stalk is shown in Figure 4.13(b). The mean values were nearly the same for the

first two internodes but after that it increased until reaching the 5<sup>th</sup> internode, where a significant drop could also be observed. Above the 6<sup>th</sup> internode the mean specific required dynamic cutting work increased linearly. For these values, the level of uncertainty is lower for the internodes under the 5<sup>th</sup>, but the level of uncertainty is relatively higher for the internodes above the 5<sup>th</sup>.

Damage and breaking of samples were analysed after the cutting process of the experiments, as shown in Figure 4.13(c)(d). A significant break perpendicular to the cutting direction was observed. The surface of the cut was perfectly straight, however, usually a rim of fibres could be observed on the side where the cutting blade left the sample.

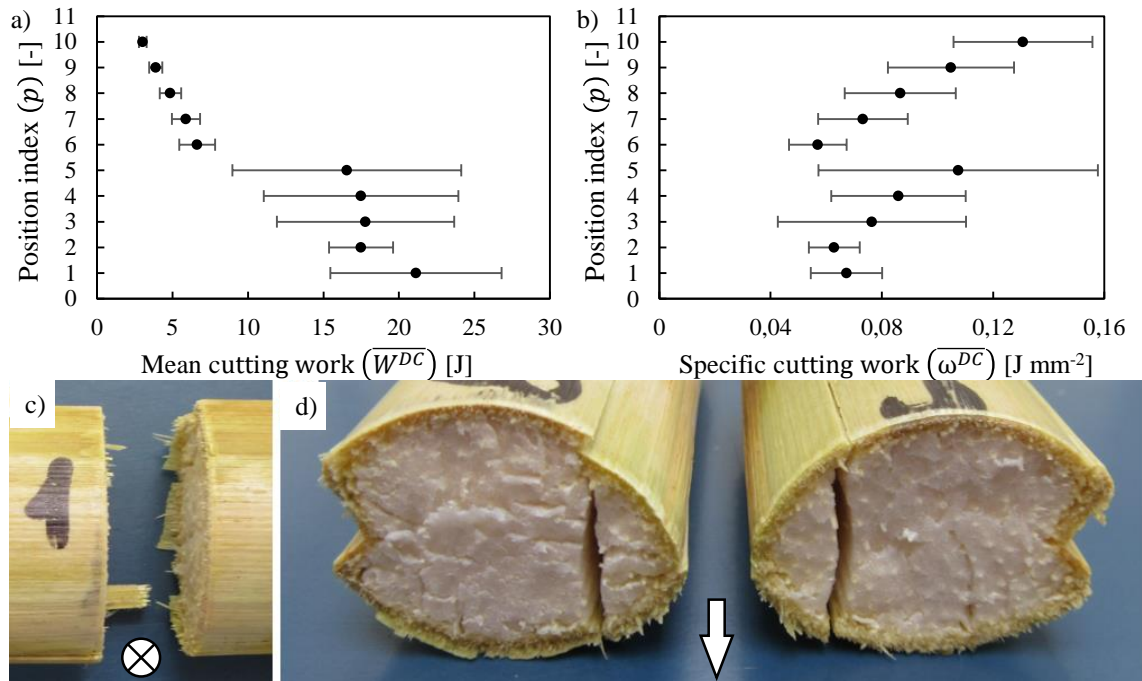


FIGURE 4.13: Results of dynamic cutting experiment: a) mean cutting work distribution and b) mean specific cutting work distribution on a maize stalk; c) rim of fibres on the side where the cutting blade left the sample (the direction of cut is perpendicular to the view); d) breaks in the cross-section perpendicular to the direction of cut (the direction of cut is roughly parallel to the view).

#### 4.2.6 Ear-Detachment and Collision

In case of the ear-detachment experiment, the typical force response consisted of two major sections, as shown in Figure 4.14(a). First, a lifting (hanging ears) or sliding (standing ears) section was observed, when the experimental apparatus lifted the maize ear or slid on the surface of stalk but the shank did not provide any resistance. This was followed by the detachment section, when the shank started to stretch and the recorded force response increased significantly until the ultimate detachment force (breaking of the joint between the shank and ear). After the detachment, the residual parts of the plant, shank and husk provided a negligible load on the apparatus and, therefore, this part of the measured curve is not presented here. The length of the sections depended on the actual position of the sample in the grip. All the results are presented in Figure A.7.

Figure 4.14(b) shows the measured ear-detachment forces that were separately analysed on hanging and standing maize ears by using 10-10 samples, respectively. For hanging and standing ears, the mean ear detachment force was  $441.6 \pm 93.0$  (21.0) N and  $473.0 \pm 88.1$  (18.6) N, respectively. The confidence intervals overlap each other, thus, a two-sample t-test was

carried out on the independent data. The standard deviation of measured data was different for hanging (130.0 N) and standing maize ears (123.2 N), so F-probe was calculated by Equation 4.27.

$$F_0 = \frac{\sigma_X^2}{\sigma_Y^2}, \quad (4.27)$$

where  $F_0$  is the result of F-probe,  $\sigma_X$  is the standard deviation of X values and  $\sigma_Y$  is the standard deviation of Y values. The result of F-probe of the two populations was  $F_0=1.11$ , while, the critical value of  $F$  at the 5% significance level ( $P=0.05$ ) is 2.98. Accordingly, the difference between the standard deviations is not significant because  $F_0 < F_{crit}$  and a two-sample t-test can be calculated.

The t-value was calculated by Equation 4.28:

$$t''_0 = \frac{\bar{X} - \bar{Y}}{\sqrt{(q-1) \cdot \sigma_X^2 + (v-1) \cdot \sigma_Y^2}} \cdot \sqrt{\frac{q \cdot v \cdot (q+v-2)}{q+v}}, \quad (4.28)$$

where  $t''_0$  is the calculated t-value for the two-sample t-test,  $\bar{X}$  and  $\bar{Y}$  are the mean of X and Y values,  $q$  and  $v$  are the number of participants of each population and  $\sigma_X$  and  $\sigma_Y$  are the standard deviations of the X and Y values. Thus, the calculated t-value was 0.554, while the critical t-value is 2.101 for the two-tailed test with a degree of freedom of 18. Accordingly, the difference between the mean detachment force values of hanging and standing maize ears is not significant because the calculated t-value is smaller than the critical,  $t''_0 < t_{crit}$ .

After taking into consideration our results, it is suggested to use a mean value for the ear-detachment force regardless of the position of maize ears. Thus, the calculated mean ear-detachment force is  $457.3 \pm 58.2$  N (12.7). Based on our observation during the ear detachment experiments, the joint between the shank and maize ear broke, except 2 samples when the break appeared in the middle section of the shank.

Based on the analysed data, the mean coefficient of restitution was  $0.34 \pm 0.04$  (13.0) on the steel plate and  $0.41 \pm 0.09$  (22.2) on the plastic plate in the axial direction of the maize ear. In the radial direction of the maize ear, the mean coefficient of restitution was  $0.34 \pm 0.05$  (15.1) on the steel plate and  $0.42 \pm 0.03$  (8.3) on the plastic plate. The recorded videos showed that more maize kernels broke away from the maize ear in case of experiments on steel plates and in the axial direction of the ear.

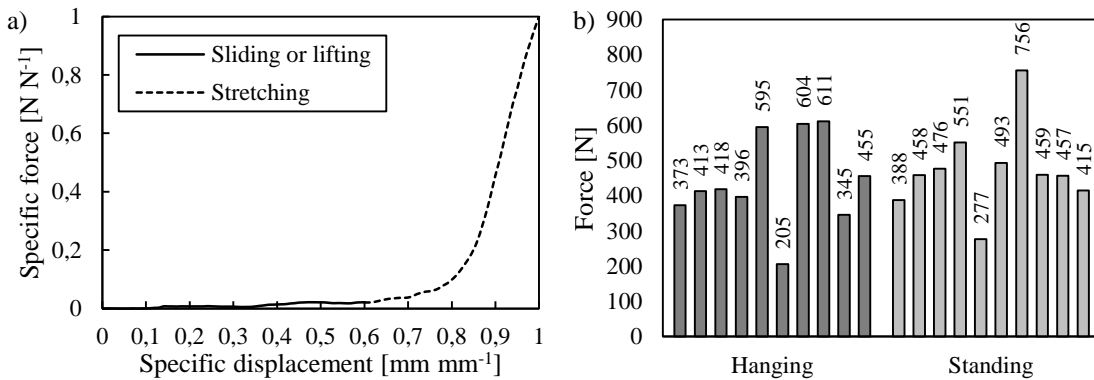


FIGURE 4.14: Results of ear detachment experiment: a) typical force response; b) measured ear detachment forces of hanging and standing maize ears.

## 4.3 Conclusions

### 4.3.1 Physical Characteristic of Maize

The bi-linear decreasing of the mean equivalent **diameter ratios** from the bottom to the top of the stalk (Figure 4.1(a)) proves that the natural stalk-structure forms two beams of uniform strength: the first section with lower decreasing grade aims to support the maize ear and the above parts of the stalk; while the second part with a higher decreasing grade aims to support the tassel. The results of previous studies show the same linear relation among the equivalent diameter of the internodes and their positions on maize stalks (Robertson et al., 2015; Igathinathane et al., 2006; Huang et al., 2016) and on sorghum stalks (Bakeer et al., 2013). However, in case of the sorghum samples, the diameter of the internodes in the upper part of the stalk was nearly uniform.

The results on the equivalent **length ratios** show that the length of the internode increases up to the 4<sup>th</sup> internode but after that it decreases to the 9<sup>th</sup> internode where it becomes uniform (Figure 4.1(b)). A similar characteristic was determined in relation to sorghum stalks by Bakeer et al., 2013, where the length of the internodes increased up to the 8<sup>th</sup> internode and after that it started to decrease to the 15<sup>th</sup> internode where it became uniform.

The **wet-mass** of the internodes linearly decreases from the bottom to the top of the stalk (Figure 4.1(c)). This mass distribution characteristic was also reported by Igathinathane et al., 2006. The sum of the wet-mass ratios of the first five internodes is 0.85. Therefore, the total wet-mass of internodes in stalk Section 'A' is more significant.

The lower **moisture content** in the upper parts (Figure 4.1(d)) results in more brittle behaviour against external loading, this is the reason for the broken or missing upper parts of the stalks that were observed at the experimental plot. Below the 5<sup>th</sup> internode the mean moisture content of the internodes was in the range of 65-76% w.b. that corresponds with results (64-75% w.b.) by Tongdi, Yaoming, and Jin, 2011. Moreover, this distribution of moisture content on maize stalks was also reported by Igathinathane et al., 2006.

In our study, the measured **maize ear** heights of HME and SME ( $93 \pm 5.0$  (5.2) cm and  $108.2 \pm 4.5$  (4.2) cm) are in the range of 50-110 cm that was reported by Tongdi, Yaoming, and Jin, 2011. Based on the correlation and comparative analysis of the physical traits of the maize ear and the shank, a strong correlation was found between the mean equivalent diameter of the first node and the mean diameter of the maize ear; among the mean diameter, the mean length and the mean mass of the maize ear; and among the mean diameter and the mean length of the shank and the mean diameter and the mean length of the maize ear (Table 4.1). The defined sections of an ideal maize ear (bottom, middle and top sections) were also reported by Yu, Fu, and Yu, 2015.

### 4.3.2 Mechanical Behaviour of Maize

The typical phases of the force response were defined for the internodal sections under scrutiny (Figure 4.3) by **sectional transversal compression** experiment. For the 2<sup>nd</sup>, 3<sup>rd</sup>, 4<sup>th</sup>, 5<sup>th</sup>, 7<sup>th</sup> and 8<sup>th</sup> internodal sections nearly the same characteristic with an initial increasing, significant break and an exponential increasing phase could be defined (Figure 4.3(b) and (d)). The significant break occurs because of the plastic deformation of the soft core without a fracture during the increasing section (Niklas, 1992). After the cell walls in the core reach their limit of strength they start to rupture in a chain reaction and the resistance drops. For the 1<sup>st</sup> internode, the initial increasing phase was followed by a phase with multiple drops after linear increasing segments (Figure 4.3(a)). That implies the presence of more woody fibres and higher lignin content which results in a more elastic mechanical behaviour of the fibres (Niklas, 1992). In case of the 6<sup>th</sup> internode, a quasi-constant phase appears between the initial linear and exponential increasing

phases (Figure 4.3(c)). The reason for this special characteristic might be the proportionally deeper longitudinal groove along the 6<sup>th</sup> internode because of the presence of the maize ear that results in a special crescent-shape in the cross-section. The compression rate range of the significant break is continuously changing from the lower compression rate to the higher (Figure 4.3(b)(d)(e) and Figure 4.4(a)), until it disappears in case of the 10<sup>th</sup> internode (Figure 4.3(f)). The reason behind this can be the lower plasticity of the core that results in continuous fracture propagation in the core instead of micro-structural reorganisations without a fracture (Niklas, 1992).

By the **local transversal compression** experiment, the typical force responses were close to uniform for all the investigated internodal samples (Figure 4.6(a)). At the beginning of the loading complex bending and transversal compression, deformation is observable in the skin until a plastic hinge under the loading edge occurs. This is the beginning of the quasi-constant phase and the load starts to relocate to the core from the skin.

The typical phases (Figure 4.9(a)) of the force response (elastic; plastic; structural collapse (buckling) and sliding phase) by **three-point bending** experiment correspond with the results of previous studies (Tongdi, Yaoming, and Jin, 2011; Zhong-Zhen et al., 2013; Leblicq et al., 2015; Zhang et al., 2017). The range of the mean peak force (146.62–364.24 N) and the mean displacement range of the peak force (6.2–8.5 mm) on the internodal phases 1<sup>st</sup> – 4<sup>th</sup> correspond with results of previous studies (190.54 – 314.36 N; 4.31–10.16 mm) (Tongdi, Yaoming, and Jin, 2011). According to the results, the displacement range of peak force is smaller as the internodal position index is higher. Thus, the peak force is reached earlier in the case of internodes with a smaller cross-sectional area.

The determined phases (Figure 4.12(a)) of the force response of **cantilever bending** (elastic; plastic; structural collapse (buckling) and plastic joint) also correspond with the results of previous studies on the flexural behaviour of stalks and stems (Tongdi, Yaoming, and Jin, 2011; Zhong-Zhen et al., 2013; Leblicq et al., 2015; Zhang et al., 2017). However, in case of three-point bending experiments on stalks and stems the structural collapse phase took place gradually, not suddenly. After the buckling of the skin the flexural resistance of the stalk drops to approximately one-fifth of its initial flexural resistance which implies that the skin is the main supporting material (Huang et al., 2016).

In case of the quasi-static tests, the first stage of **cutting** is a compression stage (Igathinathane, Womac, and Sokhansanj, 2010) where the resistance force reaches its peak. The observed vertical break on the tested samples (Figure 4.13(d)) indicates that the first stage of the dynamic cut is also transversal compression. Moreover, the presence of a rim of fibres on the side where the cutting blade left the sample proves that the final cut of the internode (Igathinathane, Womac, and Sokhansanj, 2010) did not take place perfectly in the case of the dynamic cutting because of the additional bending effect.

In case of the **transversal compression** experiments, the maximal force at a 0.75 compression rate decreases from the bottom to the top of the maize stalk (Figure 4.4(b) and 4.6(d)). This relation corresponds with the result by Zhang et al., 2017.

During the **three-point bending** experiments, the peak bending force significantly increases (Figure 4.9(b)) from the top to the bottom of the stalk; a similar observation was reported in previous studies on maize stalks (Huang et al., 2016; Zhang et al., 2017), whereas the equivalent diameter increases slightly from the top to the bottom of the stalk (Figure 4.1(a)). Moreover, the peak bending force also slightly increases (Figure 4.12(b)) as the equivalent diameter of the 1<sup>st</sup> node increases in case of the **cantilever bending**; a similar observation was reported in previous studies on maize stalks (Huang et al., 2016; Zhang et al., 2017). This relationship can be explained by two theories: first, the relation between the diameter and the second moment of inertia of a cross section is on the fourth grade; second, the number of fibre bundles in the epidermis and cortex increases significantly from the top to the bottom of the stalk. Thus, the bending resistance of the bottom sections is higher than in the top sections (Huang et al., 2016).

By taking into consideration the fact that the bending load on an internodal section results in significant transverse deformation instead of bending (Robertson et al., 2014) the number of fibre bundles has more influence on the initial bending resistance.

For the **local transversal compression** experiment, the mean maximal (at a 0.75 compression rate) and mean constant forces (during the quasi-constant phase) show a significant decrease from the bottom to the top of plant (Figure 4.9(b)), while the ratio between these forces also decreases in the same direction (Figure 4.9(b)). This relation can be explained by the decreasing level of the flexibility of the skin. In case of a more flexible skin that can deform locally under the loading edge without a fracture, the core supports the skin locally, while, in case of a less flexible skin, the external load is distributed on a larger longitudinal section of the core.

In case of the **three-point bending** experiment, the determined ratio between the peak and ultimate forces demonstrates the flexibility of the samples: in a more flexible maize stalk, the structural collapse under the bending tool does not lead to the rupture of the fibres, so they can support more of the structure against subsequent loads. It is general knowledge that the flexibility of the stalks depends on the moisture content. This explains why this ratio significantly increases above the position of the maize ear (Figure 4.9(c)) where the moisture content of the stalk decreases significantly as well (Figure 4.1(d)). The reason behind the quasi-constant ratio values for internodal sections under the maize ear can be explained by the lower influence of moisture content decreasing: the difference between the moisture content of the 1<sup>st</sup> and the 6<sup>th</sup> internode is 17.7% w.b., while this difference between the 6<sup>th</sup> and 10<sup>th</sup> internode is 35.3% w.b. Based on our results, the internodal sections with lower moisture content than approximately 60% w.b. behave in a more brittle way. Furthermore, as the equivalent diameter of the 1<sup>st</sup> node increases the displacement of the peak force decreases (Figure 4.12(c)) during the **cantilever bending** tests, thus, the structural collapse of the thinner stalk takes place later and the elastic phase is longer. This implies the higher plasticity of the thinner stalks which indicates that their moisture content is higher based on the results provided by Zhong-Zhen et al., 2013.

The mean compressive, bending and cutting work of the internodal sections decreases significantly from the bottom to the top of the stalk (Figure 4.4(c), 4.7(a), 4.10(a) and 4.13(a)) in each experiment. Based on the current results, the compressive, bending and cutting work of the internodal sections under the maize ear (Section A) provides the majority (77.8%, 86.7%, 87.4% and 78.8%) of the total compressive, bending and cutting work on an average maize stalk. Therefore, the significance of these parts is higher than the upper parts of the stalk from the point of view of the energy consumption during processing. Taking into consideration that the higher position of the internode results in lower moisture content, this finding is contrary to the previous results on the bending energy absorption of maize straws because the previous results show less total energy absorption by higher moisture content (Zhong-Zhen et al., 2013).

The mean **cutting** work distribution on the maize stalk shows a significant drop above the 5<sup>th</sup> internode (Figure 4.13(a)), but the specific mean required cutting work distribution on the maize stalk shows two separated and increasing sections under and above the maize ear (Figure 4.13(b)). By taking into consideration the mechanical behaviour of the upper stalk parts during three-point bending and local transversal compression experiments, this phenomenon can be explained by the flexibility of the skin. Both experiments show that the less flexible skin provides a more significant elastic resistance against external loads. Therefore, in case of the upper parts, the initial compression stage before cutting is smaller, while the additional bending effect is more significant. Based on our observations, the bending effect results in the rupture of the fibres of the skin instead of cutting, and the rupture requires more energy (Huang et al., 2016) and that explains the distribution of the mean specific cutting work (Figure 4.13(b)). However, this phenomenon results in a higher specific work requirement of the internode, skin and core cutting phase which do not take place perfectly, so the required cutting work is relatively lower for those internodes (Figure 4.13(a)).

Generally, the observed breakage of the specimens explains the characteristics of force response in each experiment. In case of the **local transversal compression**, the appearance of the flat triangular surfaces on the top of the specimen (so-called “diamond-shape”) was also reported by Lebllicq et al., 2015, while, the phenomenon of ovalisation and buckling was described based on **three-point bending** experiments on wheat (*Triticum L.*) and barley (*Hordeum vulgare L.*) stems (Lebllicq et al., 2015). Buckled and creased cross-section was also reported in relation to maize stalk lodging (Robertson et al., 2015). Their results on maize stalks show that 89% of the failures are in 40 mm from the node that corresponds with our observation where all the failures took place between 9 and 36 mm from the 3<sup>rd</sup> node in case of **cantilever bending**. In the structural collapse phase of the bending experiments, crack propagation in the longitudinal direction of the internode was also noted by Tongdi, Yaoming, and Jin, 2011.

Significant transverse internodal deformation under the bending tool (in the bending area) before the structural collapse was also observed by Robertson et al., 2014. Based on the current results, the core prevents the inward buckling of the skin tissue before reaching the peak force (Robertson et al., 2014), but inward buckling of the skin tissue usually takes place during the structural collapse phase. Otherwise, the results of previous experiments on wheat, barley (Lebllicq et al., 2015) and maize (Robertson et al., 2014) and the results from the three-point bending experiment in the current study indicate that the core contributes to the compression and bending resistance of maize stems after the structural collapse of the skin.

However, the shank of the hanging maize ears is buckled the results of the **detachment force measurement** demonstrate that there is no significant difference between the required detachment force of standing and hanging maize ears. Thus, the longitudinal mechanical properties of the shank are more important than the condition of the buckled cross-section during ear-detachment.

Based on the results of the **collision tests**, there is no significant difference between the longitudinal and radial drop cases on the same type of plates. Thus, the contact area has no significant effect on the coefficient of restitution.

# 5 Numerical Simulations

Generally, the DEM model of a maize plant was formed based on the physical, morphological and mechanical characteristics of the real plant presented in Chapter 4. Particles were bonded together using the Timoshenko Beam Bond Model (TBBM) (Brown, Chen, and Ooi, 2014). The influence of the bonded, non-bonded, bond-fabric and the numerical model parameters on the DEM simulated mechanical behaviour of the model was analysed by using a virtual representation of each laboratory experiment. To find an optimal set of the model parameters an optimization loop was determined based on the observed qualitative and measured quantitative characteristics of the investigated samples. Finally, a technological simulation of maize harvesting was carried out by using the simplified CAD model of a maize header row unit. The DEM model of the maize stalk and the experiments were created and analysed in the commercial DEM software **EDEM®** (DEM Solutions Ltd, Edinburgh, Scotland, UK), while the CAD models of the apparatus and the row unit were created in the commercial CAD software **CATIA®** (Dassault Systèmes, Vélizy-Villacoublay, France).

## 5.1 EDEM Software Package

A brief review of the discrete element method was provided in Chapter 2.3, thus, only specific details regarding the applied **EDEM®** Software Package are discussed here.

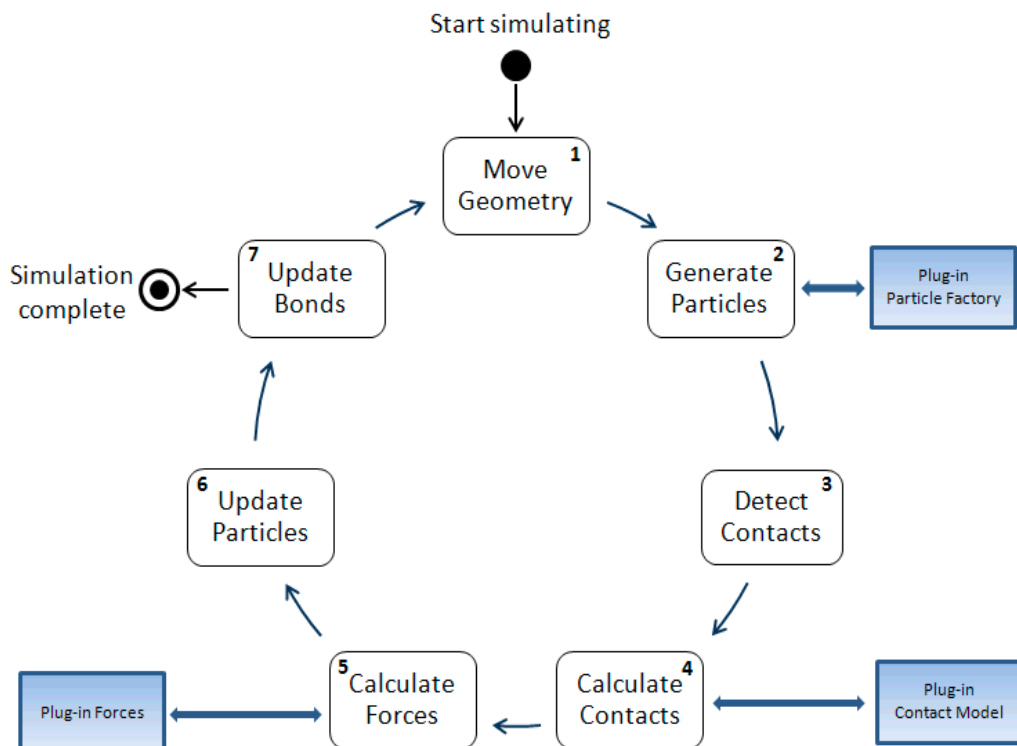


FIGURE 5.1: EDEM simulation sequence (DEM Solutions, 2017).

The simulation sequence consists of seven steps: move geometry, generate particles, detect contacts, calculate contacts, calculate forces, update particles and update bonds, as shown in Figure 5.1.

The movement of the geometrical elements can be defined by rigid (e.g. a fixed rotational velocity regardless the external forces on the element) or flexible motion laws (e.g. coupling with a third party multi-body dynamics software when the motion is calculated with respect of the external forces on the element).

Particles can be generated by built-in and custom made factories by using the particle position, initial velocity, scaling factor, orientation.

**EDEM®** uses a hybrid contact detection algorithm that is a combination of the Lattice and the Link or Grid cells methods (see Chapter 2.3). The user defines the size of the grid in the recommended range of 2-4 radius of the smallest particle. At a value of 2 this is the Lattice method, while at values larger than 3-4 it become the Link or Grid cell method.

There are two different contact model chains: one for particle-to-particle contacts and one for particle-to-geometry contacts. Each contact model in the chain is executed in order from top to bottom, irrespective of whether it is a custom made or built-in model. In the next step, the calculated forces (contact or external from a field or boundary condition) are applied to each particle in the system.

The last steps of the sequence are updating the particles and bonds, if they are formed among the particles.

**EDEM®** automatically estimates the critical Rayleigh time step based on the particle properties (see Chapter 2.3), however, it can be overwritten by the user. Three numerical time integration methods are applied in EDEM: Euler, Position Verlet and Velocity Verlet. In this study the Explicit Euler Method was applied based on the recommendations of the user manual for bonded structures (DEM Solutions, 2017).

## 5.2 Model Formation

During the model formation of the **virtual maize stalk** the first ten internodal sections were considered based on the presented in-situ observations of Chapter 4.1.1. Moreover, the mechanical characteristics of the stalk indicate the consideration of two different DEM models because the first five internodal sections provided the majority of the biomass (Figure 4.2), even more, the processing of the same internodal sections required approximately 80% of the total compressive, bending and cutting work along the stalk (Figure 4.4(c); 4.7(a); 4.10(a) and 4.13(a)). The cross-section of the real internodal section has an elliptical shape, moreover, usually a groove runs along it on the side of the leaf, as shown in Figure 1.1(b). In practice, the direction of the interaction among the plant and the machine parts can be in any orientation of the stalk, however, it is not certainly predictable. The cross-sectional area of the stalk is continuously decreasing from the bottom to the top of the stalk (Figure 4.1(a)), thus, it is subtly decreasing along the internodal section as well. However, a previous study showed that this decrement of the cross-sectional area is negligible along an internodal section in practice (Robertson et al., 2015). Thus, in the current study a simplified model was formed of the real internodal section by using the following assumptions: the shape of the internodal cross-section is perfectly circular and the size of the internodal cross-section is permanent along the internodal section. The mechanical structure of an internodal cross-section can be divided into a soft inner core and a stiffer outer skin ("medulla - epidermis plus cortex" or "core – rind" structure as biologists refer to this), as shown in Figure 3.1(b). Both in the skin and in the core, fibre bundles run along the internodal section, however, the number of fibre bundles are higher in the skin than in the core and their mechanical properties are significantly stronger, thus, the

skin provides the main mechanical resistance against external loads during elastic deformations (Huang et al., 2016). However, the core governs the mechanical behaviour after buckling or breaking of the skin (Leblanc et al., 2015), thus, it is not negligible for a detailed analysis. The mechanical properties of the internodal section in transverse direction are different than in the longitudinal direction, thus, during the model formation a transversely isotropic mechanical behaviour will be assumed for the structure of the maize stalk.

During the model formation of the **virtual maize ear with the shank**, hanging maize ear position was considered based on the presented in-situ observations of Chapter 4.1.2. The husk, the kernels and the cob were formed as one geometrical unit, hence they will be referred as maize ear, that was assumed to be perfectly axis-symmetric. The complex mechanical structure that involves the stalk, the shank, the husk and the cob was simplified to an elementary joint that is provided by the shank between the stalk and the maize ear.

### 5.2.1 Physical Model of The Plant

During the model formation a complex solid-, solid-, hollow- and chain of spheres geometrical structures were used to create each parts of the virtual plant. Based on the importance and role of maize parts during harvesting, their geometrical structure is more or less detailed, as shown on Figure 5.2.

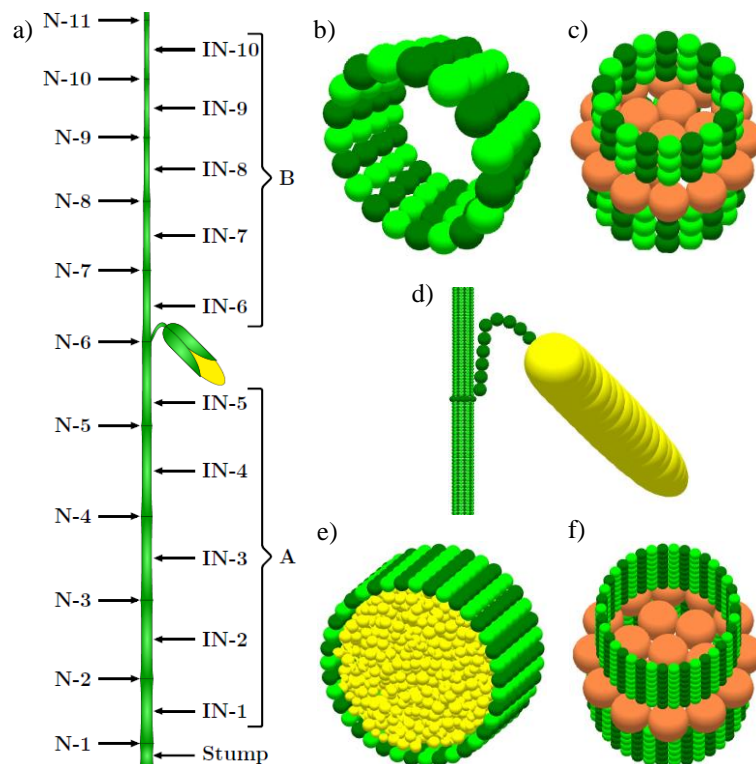


FIGURE 5.2: Geometrical model of the plant: a) division of the plant; b) hollow internodal structure and c) solid nodal structure in Section B; d) chain of spheres structure for the shank and cluster of spherical surfaces for the maize ear; e) complex solid internodal structure and f) solid nodal structure in Section A (note that the yellow core is not visualized here).

From the 1<sup>st</sup> to the 11<sup>th</sup>, nodes were modelled by a solid geometrical structure in which one circular layer was created by using 19 particles: 12 in the outer circle, 6 in the middle circle and 1 in the centre, as shown in Figure 5.2(c) and (f). This model provides higher resistance against external loading near the nodes.

From the 1<sup>st</sup> to the 5<sup>th</sup>, internodes were modelled by a complex solid geometrical structure. In a cross section of the internode, an outer circular layer was created by using 38 particles for the skin and it was filled by a randomly generated poly-disperse structure that represents the core, as shown in Figure 5.2(e). For creating the core particles with high-density, a collective rearrangement algorithm was used (Labra and Onate, 2009). This model provides a good possibility to analyse the typical failure modes (buckling and ovalisation) of internodes. Otherwise, internodes were modelled by hollow geometrical structure that consists of 18 particles in each circular layer between the 6<sup>th</sup> and 10<sup>th</sup>, as shown in Figure 5.2(b). This model can precisely predict the mechanical behaviour of the real stalk parts during the elastic deformation stages but after the breakage of the skin its accuracy is decreasing.

The shape of the shank was formed for carrying a hanging maize ear by using chain of spheres model, as shown in Figure 5.2(d). It is impossible to model this broken condition of the shank so a curved shape with unbroken bonds was created. The geometrical model of the maize ear is one particle that is formed by several spherical surfaces, as shown in Figure 5.2(d). This detailed maize ear model provides a good possibility to analyse its interactions with the parts of the machine.

Figure 5.3 shows the complex solid geometrical structure of the 4<sup>th</sup> internodal section that was inspired by the real fibrous mechanical structure (skin-core) of a maize stalk. To reproduce this structure five different particle types were defined: particle types P41 and P42 form the skin; particle types P40 and P50 form the nodes and particle type P43 forms the core. In the skin, types P41 and P42 form a special composition: each cross-section contains 38 particles, 19 P41 particles and 19 P42 particles alternately. Thus, longitudinal fibres can be formed by aligning the cross-sectional layers. In the nodes, a solid cross-section is formed by using 19 particles of types P40 and P50 respectively. Finally, the inner volume is made up by using randomly generated particles type P43 with porosity of 60% and the diameter of the core particles shows a normal (Gaussian) distribution. By using a non-structured particle distribution in the core, the disadvantages of the well-structured skin can be compensated, namely: the influence of the artificially created breaking planes of the skin on the breakage of the internodal section and the dependency of the loading direction can be reduced. The stalk parts in Section B were formed by following the same logic, however, 18 particles were used to form the skin in a cross-sectional layer and the poly-disperse core was neglected.

The physical properties of each virtual internodal section were determined based on the averaged results of the measurements on real internodal sections (4.1.1). During the calculations an average plant was assumed with equivalent first node diameter ( $d_{e1}^N$ ) of 28.5 mm, total length ( $L_t$ ) of 1510 mm and total wet-mass ( $m_{w,t}$ ) of 192 g, moreover, the experimentally determined relationships (Equation 4.2 - 4.10) among the physical properties and morphological elements were used to calculate the physical properties of the stalk. The calculated physical properties of the nodal and internodal sections are shown in Table 5.1.

The shank consists of 10 spherical particles with diameter of 10.5 mm, based on the results of Chapter 4.1.2. The position of the particles were determined in such a way to form a special curved shape, that was observed during the field tests (4.1.2). Table 5.2 shows the initially determined X-Y coordinates of the particles in the shank. The rest of the physical parameters of the shank were similar to the physical properties of the 6<sup>th</sup> internodal section.

The geometrical model of the maize ear is one particle in which the previously described ideal shape of the maize ear (Figure 4.3) was approached by 23 spherical surfaces, supposing that the maize ears are axi-symmetric, as shown in Figure 5.6. The major diameter of the virtual maize ear was 47.5 mm and the ratio between the major diameter and the length was 3.5, based on the results of Chapter 4.1.2. The length coordinates and the radius of the particles are shown in Table 5.3. The density of the maize ear particle was  $930 \text{ kg m}^{-3}$ , thus its mass was 214.6 g. The maize ear with the shank was situated beside the 6<sup>th</sup> internodal section (Figure 5.6(a)) in

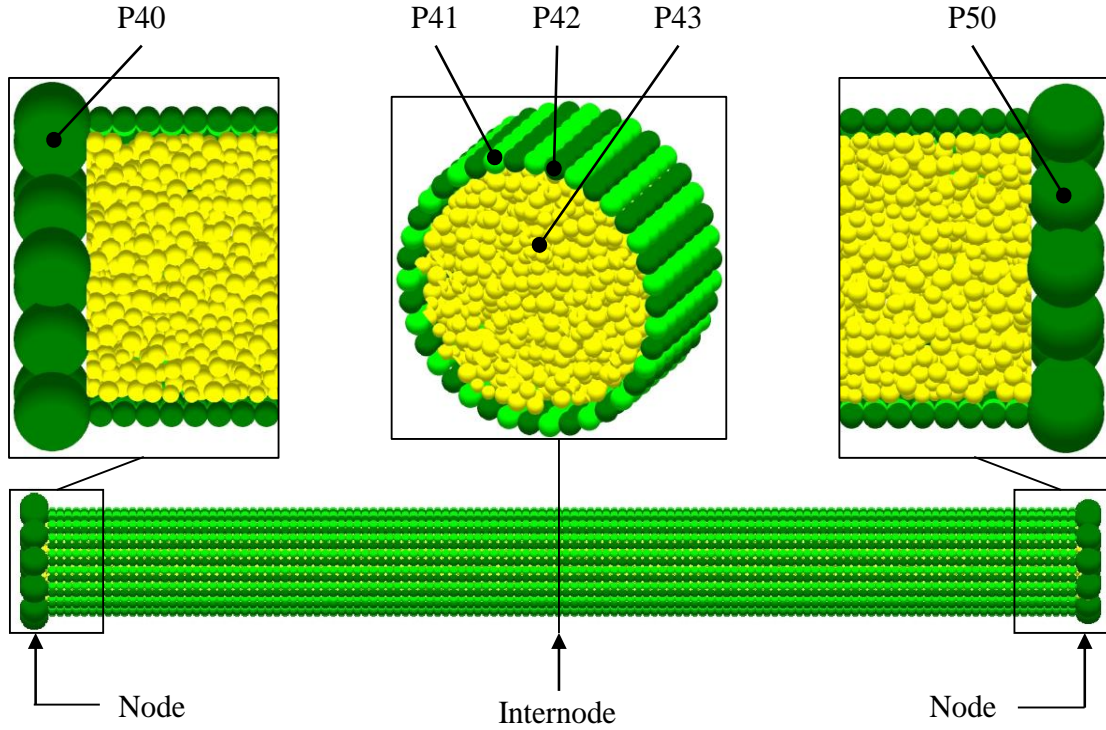


FIGURE 5.3: DEM geometrical model of the 4<sup>th</sup> internodal section of a maize stalk.

TABLE 5.1: Physical properties of the virtual stalk: outer diameter ( $d^{IN}$ ); internodal length ( $L^{IN}$ ); particle diameter in the skin ( $d_P^S$ ); number of particles in the skin ( $N_P^S$ ); particle diameter range in the poly-disperse core ( $d_P^C$ ); number of particles in the core ( $N_P^C$ ); particle density ( $\rho_P$ ).

Stalk part	$d^{IN}$ [mm]	$L^{IN}$ [mm]	$d_P^S$ [mm]	$N_P^S$ [-]	$d_P^C$ [mm]	$N_P^C$ [-]	$\rho_P$ [ $\text{kg m}^{-3}$ ]
IN-1	23.60	135.0	1.8	2850	1.2 - 1.6	11632	1586
IN-2	20.98	164.8	1.6	3914	1.0 - 1.4	17749	1477
IN-3	19.66	178.5	1.5	4522	0.9 - 1.3	21778	1264
IN-4	18.35	179.2	1.4	4864	0.8 - 1.2	25475	1134
IN-5	15.73	170.4	1.2	5396	0.6 - 1.0	34092	1181
IN-6	14.19	155.4	2.1	1332	-	-	1656
IN-7	12.17	136.8	1.8	1368	-	-	1684
IN-8	10.14	121.5	1.5	1458	-	-	1713
IN-9	8.11	109.2	1.2	1638	-	-	1598
IN-10	6.76	106.0	1.0	1890	-	-	1164
N-1	29.18	6.0	6.0	12	6.0	7	1586
N-2	27.24	5.6	5.6	12	5.6	7	1477
N-3	24.80	5.1	5.1	12	5.1	7	1264
N-4	22.86	4.7	4.7	12	4.7	7	1134
N-5	20.91	4.3	4.3	12	4.3	7	1181
N-6	18.97	3.9	3.9	12	3.9	7	1656
N-7	16.54	3.4	3.4	12	3.4	7	1684
N-8	14.59	3.0	3.0	12	3.0	7	1713
N-9	12.65	2.6	2.6	12	2.6	7	1598
N-10	10.70	2.2	2.2	12	2.2	7	1164

TABLE 5.2: Initially determined X-Y coordinates of the virtual shank.

Particle ID	X-coordinate [mm]	Y-coordinate [mm]
#1	0.872	9.962
#2	1.743	19.924
#3	2.615	29.886
#4	3.486	39.848
#5	4.602	50.329
#6	13.493	54.905
#7	23.308	52.989
#8	31.667	47.500
#9	38.739	40.429
#10	42.273	36.893

such a way that its centre of the mass was 93.99 cm and 9.42 cm from the virtual soil surface and the centre of the stalk, respectively.

TABLE 5.3: Length coordinates and radius of the spherical surfaces in the virtual maize ear.

Surface	Length coord. [mm]	Radius [mm]	Surface	Length coord. [mm]	Radius [mm]
#1	22.15	22.06	#13	97.05	23.11
#2	26.15	23.06	#14	105.21	22.74
#3	28.12	23.20	#15	115.00	22.19
#4	32.36	23.54	#16	120.94	21.44
#5	33.77	23.63	#17	130.37	20.33
#6	40.58	23.70	#18	132.25	20.27
#7	50.55	23.70	#19	138.27	19.04
#8	56.99	23.67	#20	142.80	17.60
#9	65.01	23.73	#21	145.56	16.34
#10	74.38	23.66	#22	149.09	14.63
#11	81.57	23.54	#23	152.56	12.10
#12	88.94	23.34			

### 5.2.2 Bonded Structure of The Plant

After taking into consideration the existing DEM bonded models the Timoshenko Beam Bond Model (EDEM®), DEM Solutions Ltd, Edinburgh, UK) was chosen for this study (Brown, Chen, and Ooi, 2014) because the Timoshenko beam theory takes into account the shear deformation that is essential for analysis on short, stubby beams, moreover, this bonded model enables a stochastic variation for the strength parameters that reflects the natural diversification of the real material.

In this model a virtual beam element is formed between two spherical particles (Figure 5.4) that can transfer forces and moments between them. Based on the displacements and rotations of the bonded particles the reaction forces and moments of the virtual beam element are calculated using the Timoshenko beam theory. Moreover, the maximum compressive, tensile and shear stress are calculated for each bond based on its actual loads. A bond fails when one of the maximum stresses exceeds the predefined corresponding strength. The strength of each bond is defined by assuming a Gaussian strength distribution in the model, thus, a mean strength and a stochastic variation are required. If a bond fails, the bonded contact between the particles

is removed and cannot be reintroduced. Afterwards, the interaction between the particles is determined by the Hertz-Mindlin contact model (Johnson, 1987). All the details and governing equations of the contact models can be found in Appendix E.

To define the mechanical behaviour of the bonded model the following bonded properties need to be defined: Young's modulus ( $E_B$ , [Pa]); Poisson's ratio ( $\nu_B$ , [-]); mean compressive, tensile and shear strength ( $S_C$ ,  $S_T$ ,  $S_S$ , [Pa]); coefficients of variation for the compressive, tensile and shear strength ( $\zeta_C$ ,  $\zeta_T$ ,  $\zeta_S$ , [-]) and a bond radius multiplier ( $\Lambda$ , [-]).

Figure 5.5 shows the bond structure of the 4<sup>th</sup> internodal section of the virtual maize stalk. To ensure the transversely isotropic mechanical behaviour of the model, different bonded parameters were used in the bonds that are oriented in different directions. In the skin, bonds among the specially composed particles P41-P41 and P42-P42 provide the mechanical behaviour in longitudinal direction, while, bonds among the particles P41-P42 provide the mechanical behaviour in transversal direction. In the core, the bonds among the randomly generated particles P43-P43 provide an isotropic mechanical behaviour, while, the bonds among the particles P43-P41 and the P43-P42 provide the contact among the skin and core in transversal direction. Bonds among the nodal particles P40-P40 and P50-P50 provide the mechanical behaviour of the node in transversal direction, while, bonds among the particles P40-P43, P40-P41, P40-42, P50-P43, P50-P41 and P50-42 provide the contact among the nodes, the skin and the core. The bonded structure of the stalk parts in Section B were formed by following the same logic but without the poly-disperse core.

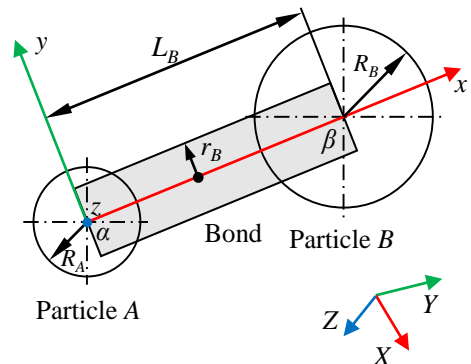


FIGURE 5.4: Projected view through the central axis of a bond connecting particles A and B (redrawn from Brown, Chen, and Ooi, 2014).

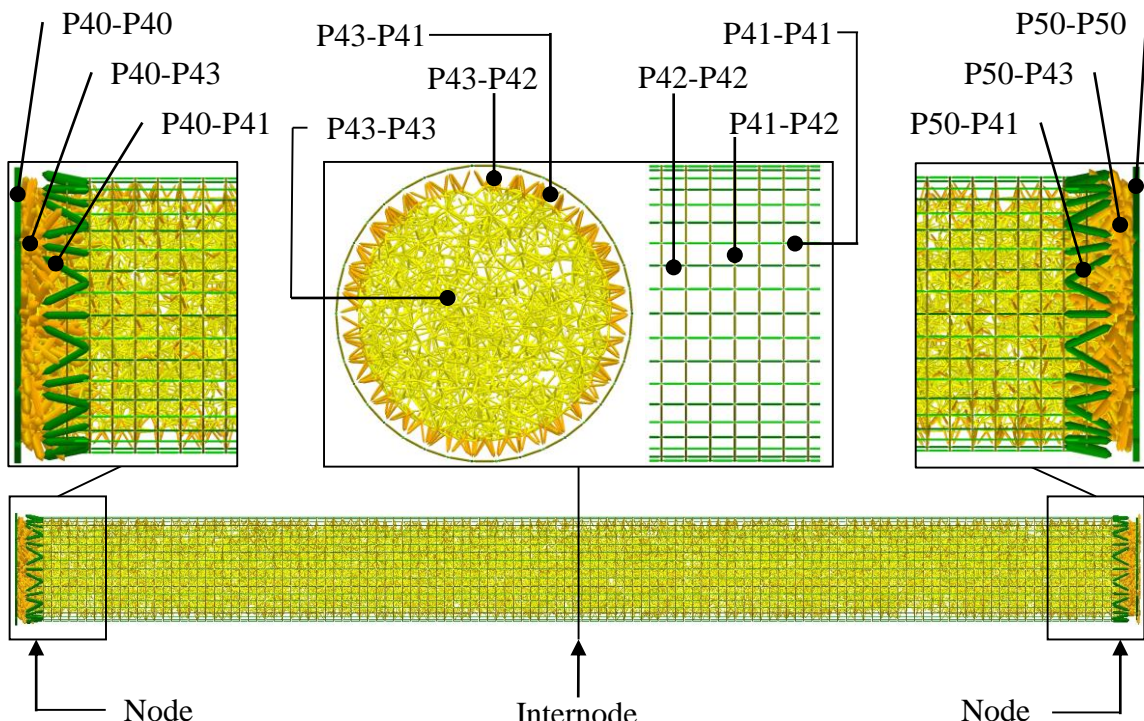


FIGURE 5.5: DEM bond structure of the 4<sup>th</sup> internodal section of a maize stalk.

As to the bonded structure of the shank with the maize ear, it is necessary to note that it is impossible to model the real, broken condition of the shank so a curved shape with unbroken bonds among the particles was modelled, as shown in Figure 5.6(b). In this model there is only one type of bond among the particles along the axial direction of the shank, thus its mechanical behaviour in transversal direction is provided by the stiffness of the particles. The shank ensures the contact between the stalk and the ear thus bonds among the particles of the stalk and the shank were also formed. Needless to say that another bond is needed between the free-end of the shank and the maize ear.

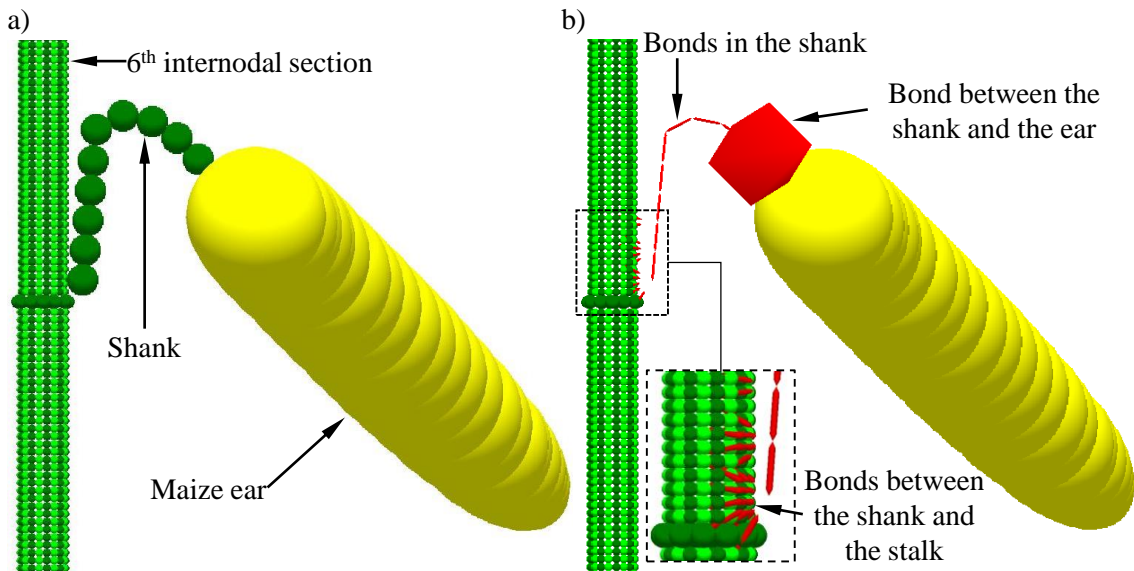


FIGURE 5.6: Virtual model of the shank with the maize ear: a) DEM geometrical model; b) DEM bonded structure.

### 5.2.3 Virtual Models of The Experiments

For all numerical simulations of the experiments, idealised models of the real apparatus were utilised, in which the major dimensions and boundary conditions of the apparatus were the same, as shown in Figure 5.7. In case of the sectional transversal compression, the top and bottom plungers were modelled by two flat planes (Figure 5.7(a)), while the real geometry of the edge-plunger was used with a flat plane for the bottom-plunger for the local sectional compression simulations (Figure 5.7(b)). For the three-point bending simulation, three cylinders represent the bending tool and the supports in the virtual experiment (Figure 5.7(c)). In case of the simulation of the dynamic cutting experiment, the geometry of the real cutting blade was used with four flat planes instead of the real support that is made up of steel sheets (Figure 5.7(e)). For the ear-detachment simulation, the CAD geometrical model of the real test apparatus was imported into the software without any modifications (Figure 5.7(d)). In case of the ear-collision simulation, only a steel and a plastic sheet were modelled based on the material properties of the real ones (Figure 5.7(f)). For the cantilever bending simulation, the CAD geometrical model of the real supports and the bending tool were used without any modification (Figure 5.7(g)).

The motion of all parts of the virtual apparatus were the same as in the real experiments, except the dynamic cutting simulation, in which it was assumed that the cutting blade moves in a straight line with constant speed instead of the reality where it moves in a circular line. For the quasi-static simulations (compression, ear-detachment and bending tests) and for the

dynamic simulations (dynamic cutting and ear-collision tests) the save interval was 100Hz and 50000Hz, respectively.

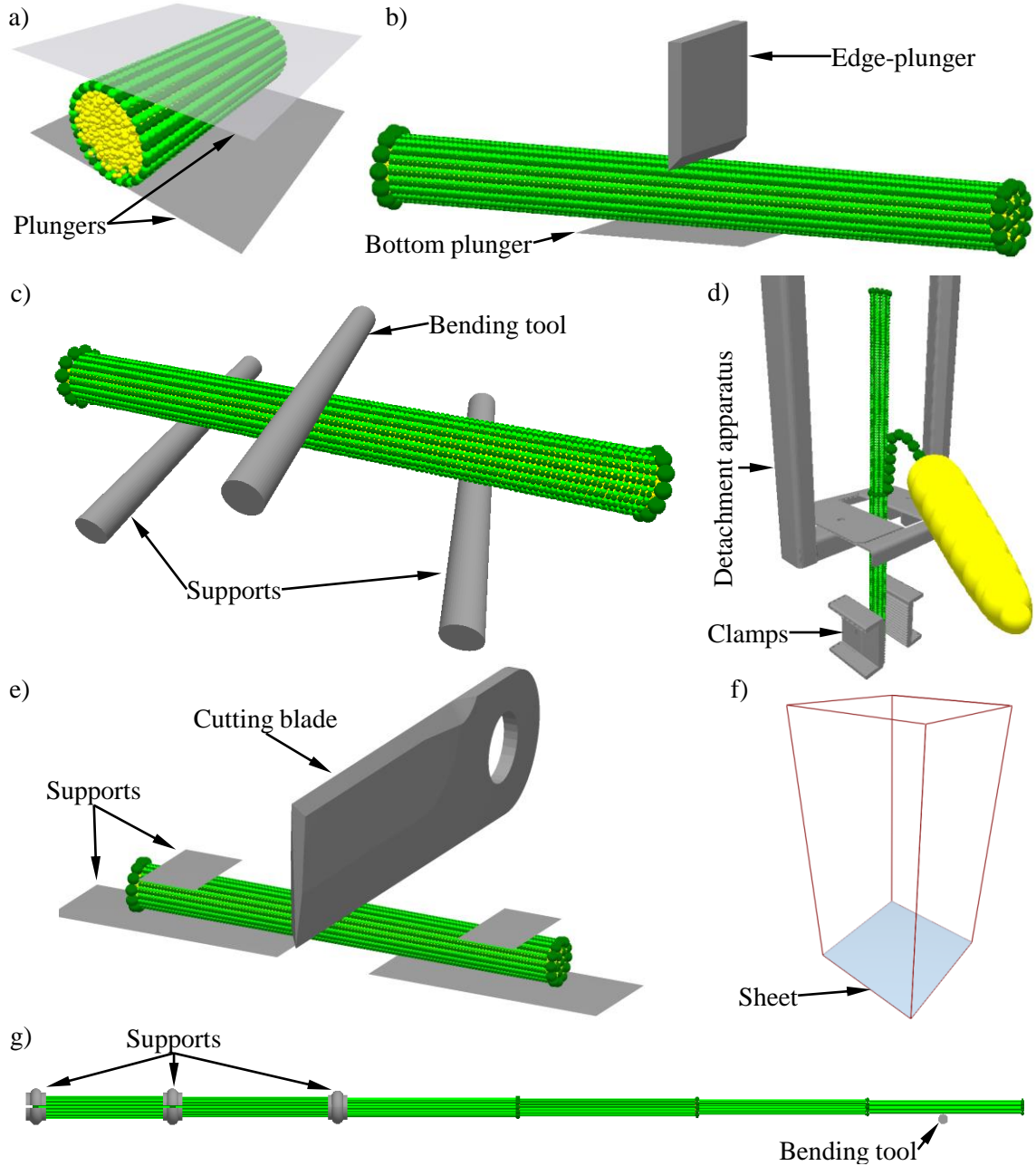


FIGURE 5.7: Virtual models of the test apparatuses: a) sectional transversal compression; b) local transversal compression; c) three-point bending; d) ear-detachment; e) dynamic cutting; f) ear-collision; g) cantilever bending.

### 5.3 Parametric Study

A detailed parametric study was conducted to determine the influence of the main bonded, non-bonded, bond-fabric and numerical parameters on the mechanical behaviour and breakage of the plant parts by using the sectional transversal compression, three-point bending, dynamic cutting, ear-detachment and ear-collision simulations.

To reduce the number of the bonded parameters being considered the following assumptions were made based on the natural behaviour of the plant fibres and based on the observations during the experiments:

1. the bonds cannot fail by compressive load, because flexible natural plant fibres buckle under axial compressive load instead of rupture;
2. the bonds in the core cannot fail by shear load, because this failure mode is not typical for randomly generated poly-disperse structure;
3. the bonds in the core, and between the core and the skin have the same bonded properties;
4. the bonds between the nodal and the internodal particles cannot fail and their stiffness is equal to the stiffness of the longitudinal fibres of the next internodal section;
5. the bonds between the shank and the stalk, and along the shank cannot fail because this type of failure was not observed among field conditions;
6. the detachment takes place by the failure of the bond between the shank and the maize ear based on the results of Chapter 4.2.6;
7. the bond between the shank and the maize ear fails by pure tensile load as it is expected during the real detachment process;
8. the value of the Poisson's ratio ( $\nu_B$ ) is the same for all the bonds;
9. the value of the coefficient of variation ( $\zeta_{C-T-S}$ ) is the same for all the bonds;
10. the value of the bond radius multiplier ( $\Lambda$ ) is the same for all the bonds;
11. the non-bonded contact parameters are the same for all the particle types, except the Young's modulus of the skin ( $E_p^S$ ) and core ( $E_p^C$ ) particles.

Moreover, only those numerical parameters were analysed which are expected to have the greatest impact on the mechanical behaviour and breakage of the sample during the actual type of simulation, for instance the influence of the particle-geometry coefficient of restitution ( $e_{P-G}$ ) was explored by only the dynamic cutting and ear-collision simulations because it is not expected that it has an effect on the quasi-static simulations.

The influences of the input parameters were analysed separately by using the virtual model of the 4<sup>th</sup> internodal section for the compression, bending and cutting tests, a stalk section from the 1<sup>st</sup> to the 6<sup>th</sup> internode for the cantilever bending, the 5<sup>th</sup> and the 6<sup>th</sup> internodal sections with the shank and the ear for the ear-detachment and a single maize ear for the ear-collision tests. The analysis was univariate, thus, only the analysed parameter was changed, while the others were the same in each simulation case. During the parametric study the physical parameters (geometrical structure; number, size and density of the particles) and the bonded structure were not changed. For all the simulations the only external loading on the specimen came from the displacement of the plunger, bending or cutting tool, except for the ear-collision simulation where the gravity accelerates the maize ear before the collision, thus it was set to  $9.81 \text{ m s}^{-2}$ .

Generally, the influence of the parameters were evaluated through quantitative (overall force response; peak, ultimate or detachment forces; displacement of the peak force; cutting work; bounce height; number of broken bonds) and qualitative (deformation of the samples; overall breakage of the skin and core; breakage of the loaded cross-section; resulted cutting surface; deformation of the shank) results, however, the applied method depends on the simulation.

### 5.3.1 Reference Models

At the beginning of the parametric study a reference model was determined to define a basic set of parameters and analyse the predictive capabilities of the model through sectional transversal compression, three-point bending and dynamic cutting simulations on the virtual 4<sup>th</sup> internodal section, and the ear-detachment and collision simulations.

Five simulations were carried out by using the same bonded and non-bonded parameters (Table 5.4) to analyse the similarity of the predicted results. In each simulation the critical time

step ( $\Delta t_{crit}$ ) was set to 8.5e-8 s that was calculated based on the approximate solution of a mass spring system with one degree of freedom by using the largest bond stiffness component, the smallest particle mass and the safety factor of 0.1 (Brown, Chen, and Ooi, 2014). The applied non-viscous damping coefficient ( $\iota$ ) was 0.5 for all the simulations (Brown, Chen, and Ooi, 2014).

TABLE 5.4: Bonded and non-bonded input parameters of the internodal reference model.

Bonds	$E_B$ [MPa]	$\nu_B$ [-]	$S_T$ [MPa]	$\zeta_T$ [-]	$S_S$ [MPa]	$\zeta_S$ [-]	$\Lambda$ [-]
Skin, long.	4000	0.2	500	0.1	100	0.1	1.0
Skin, tr.	1200	0.2	50	0.1	10	0.1	1.0
Core	4	0.2	4	0.1	-	-	1.0
Non-bonded parameter		Description					
							Value
	$E_P$		Particle Young's modulus [MPa]				270
	$\nu_P$		Particle Poisson's ratio [-]				0.35
	$\theta_{P-P}$		Particle-particle static friction [-]				0.3
	$\theta_{P-G}$		Particle-geometry static friction [-]				0.9
	$\vartheta_{P-P}$		Particle-particle rolling friction [-]				0.01
	$\vartheta_{P-G}$		Particle-geometry rolling friction [-]				0.01
	$e_{P-P}$		Particle-particle restitution [-]				0.05
	$e_{P-G}$		Particle-geometry restitution [-]				0.8

The poly-disperse core was created to reduce the loading direction dependency of the well-structured skin (Chapter 5.2.1). Thus, the virtual 4<sup>th</sup> internodal section of the stalk was loaded in three different locations (at the bottom, middle and top of the internodal section) and in four different directions ( $0^\circ - 45^\circ - 90^\circ - 135^\circ$ ) by the sectional transversal compression simulation, as shown in Figure 5.8(a) and (c). Moreover, it was also tested in four different directions ( $0^\circ - 45^\circ - 90^\circ - 135^\circ$ ) by the three-point bending simulation. By using the dynamic cutting simulation, that is expected to be the most sensitive about the loading location relating to the particles in the skin, the influence of the load on a particle and between two particles was also analysed, as shown on Figure 5.8(b).

The bonded model parameters for the reference model of the shank with the maize ear is presented in Table 5.5. Based on the experimental results of Chapter 4.2.6, the detachment is expected between the shank and the maize ear, thus, the tensile strength between the shank and the maize ear was set to 45 MPa while the rest of the strength parameters were not considered. The non-bonded parameters were the same as they are presented in Table 5.4.

TABLE 5.5: Bonded input parameters for the reference model of the shank with the maize ear.

Bonds	$E_B$ [MPa]	$\nu_B$ [-]	$S_T$ [MPa]	$\zeta_T$ [-]	$\Lambda$ [-]
Stalk - Shank	4000	0.2	-	-	1.0
Shank	400	0.2	-	-	1.0
Shank - Maize ear	400	0.2	45	0.0	1.0

### 5.3.2 Bonded Contact Parameters

The bonded contact parameters characterise the mechanical behaviour and breakage of the bonded contacts. In case of all the simulations it is expected that the stiffness parameters of the bonds (bond Young's modulus ( $E_B$ ) and Poisson's ratio( $\nu_B$ )) governs the mechanical behaviour

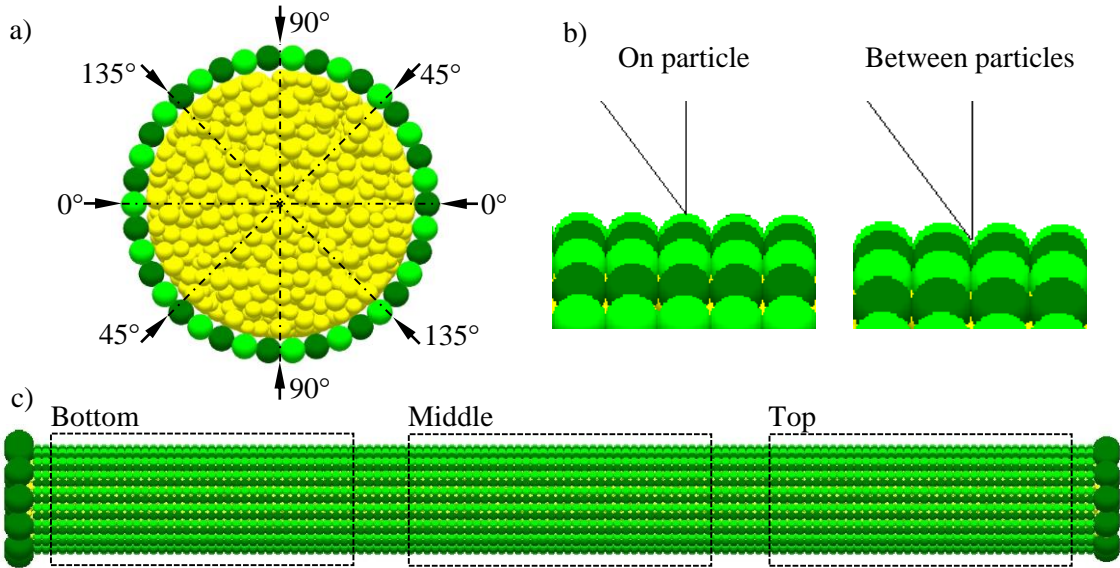


FIGURE 5.8: Analysis of the loading direction dependency: a) loading in four different directions; b) loading on a particle and between two particles; c) loading at three different locations.

of the virtual samples at the beginning of the loading. As the loading continues more and more bonds reach their strength limit, typically in the skin of the virtual sample, that is characterized by the bond mean compressive ( $S_C$ ), tensile ( $S_T$ ), shear ( $S_S$ ) stress and their coefficient of variation (CoV) ( $\zeta_C; \zeta_T; \zeta_S$ ). This means that the initial mechanical behaviour of the samples will be predominantly influenced by the bonded contact parameters. The bonded stiffness and strength parameters that were analysed by sectional transversal compression, three point bending, dynamic cutting and ear-detachment simulations are presented in Table 5.6.

In case of **sectional transversal compression**, an exact ratio among the Young's modulus of the tangential skin and core bonds were assumed thus they were varied in such way to keep this ratio of 300 during the first five cases. Afterwards, this ratio was modified in the range of 100-600 in such way to keep the Young's modulus of the transversal skin bonds ( $E_B^{S,tr.}$ ) of 1200 MPa. The influence of the Poisson's ratio ( $\nu_B$ ) was analysed in the range of 0.0-0.4. The influence of the mean tensile strength ( $S_T$ ) was analysed in two steps. First, the tensile strength of the transversal bonds of the skin ( $S_T^{S,tr.}$ ) was modified in the range of 10-100 MPa, afterwards, the tensile strength of the core bonds ( $S_T^C$ ) was modified in the range of 1-8 MPa. Finally, the influence of the coefficient of variation ( $\zeta$ ) was analysed in the range of 0.0-0.9.

Through **three-point bending**, the influence of the Young's modulus of the longitudinal bonds of the skin ( $E_B^{S,long.}$ ) was analysed in the range of 2000-6000 MPa, while, the influence of the Poisson's ratio ( $\nu_B$ ) was analysed in the range of 0.0-0.5. The first analysed strength parameter was the mean tensile strength of the core ( $S_T^C$ ), its influence was analysed in the range of 1-8 MPa. Second, the influence of the mean tensile strength of the bond in transversal direction of the skin ( $S_T^{S,tr.}$ ) was analysed in the range of 10-100 MPa. Third, the influence of the mean shear strength of the bond in transversal direction of the skin ( $S_S^{S,tr.}$ ) was analysed in the range of 5-15 MPa. Finally, the influence of the coefficient of variation ( $\zeta$ ) was analysed in the range of 0.0-0.9.

The bonded stiffness parameters, that were analysed by **dynamic cutting** simulations, are the same as they were during the three-point bending simulations, however, the analysed bonded parameters were different. First, the influence of the mean tensile strength of the bonds in longitudinal direction of the skin ( $S_T^{S,long.}$ ) was analysed in the range of 100-1000 MPa. Afterwards, the influence of the mean shear strength of the longitudinal bonds in the skin ( $S_S^{S,long.}$ )

was analysed in the range of 5-15 MPa. Finally, the influence of the coefficient of variation ( $\zeta$ ) was analysed in the range of 0.0-0.9.

In case of the **ear-detachment** simulation, the influence of the bond Young's modulus ( $E_B^{SH}$ ) was analysed in the range of 200-600 MPa, while, the influence of the tensile strength of the bond between the shank and maize ear ( $S_T^{SH-ME}$ ) was analysed in the range of 20-60 MPa.

TABLE 5.6: Range of the analysed bonded parameters.

Bonded parameters					
Bonds	$E_B [MPa]$	$\nu_B [-]$	$S_T [MPa]$	$S_S [MPa]$	$\zeta [-]$
Skin, long.	2000-6000 ♣ ♦	0.1-0.4 ♣ ♪ ♦	100-1000 ♦	10-100 ♦	0.1-0.9 ♣ ♪ ♦
Skin, tr.	600-1800 ♣	0.1-0.4 ♣ ♪ ♦	10-100 ♣ ♪ ♦	5-15 ♣	0.1-0.9 ♣ ♪ ♦
Core	2-6 ♣	0.1-0.4 ♣ ♪ ♦	1-8 ♣ ♪	-	0.1-0.9 ♣ ♪ ♦
Shank & Maize ear	200-600 ♦	-	20-60 ♦	-	-

Analysed by ♣ transversal compression; ♠ three-point bending; ♦ dynamic cutting;  
♦ ear-detachment and ◎ ear-collision.

### 5.3.3 Non-Bonded Contact Parameters

The non-bonded contact parameters characterise the mechanical behaviour of the contacts among the particles that were not initially bonded together or the bond already failed between them, moreover, these parameters also characterise the mechanical behaviour of the contacts among the particles and geometry elements.

The analysed non-bonded contact parameters are shown in Table 5.7. In case of the sectional transversal compression simulations it is expected that the Young's modulus of the particles ( $E_P$ ) and the coefficient of static friction among the particles ( $\theta_{P-P}$ ) have a significant effect on the final stage of the compression. Thus, the Young's modulus of the particles ( $E_P$ ) was analysed in the range of 67.5-540 MPa, while the Poisson's ratio of the particles ( $\nu_P$ ) was 0.35 in each case. The coefficient of static friction of the particles ( $\theta_{P-P}$ ) was separately analysed in the range of 0.1-0.9. In case of the three-point bending simulation it is expected that the coefficient of static friction among the particles and geometry elements ( $\theta_{P-G}$ ) has a significant effect on the final stage (sliding, Figure 4.11) of bending, thus it was analysed in the range of 0.1-0.9. In case of the dynamic cutting it is expected that the coefficient of static friction among the particles and geometry elements ( $\theta_{P-G}$ ) and the coefficient of restitution among the particles and geometry elements ( $e_{P-G}$ ) have a significant effect on the required cutting work, thus they were analysed in the range of 0.1-0.9 and 0.2-1.0, respectively. The coefficient of restitution among the particles and geometry elements ( $e_{P-G}$ ) was also analysed through the special case of the collision between the maize ear and a plastic or steel sheet. Based on the contact law of the Hertz-Mindlin model (Johnson, 1987), the coefficient of restitution, the stiffness, the equivalent mass and relative velocity influence the damping force calculation. The Young's modulus and the density of the steel and polyethylene sheets are well-determined material properties: 200 GPa and  $7850 \text{ kg} \cdot \text{m}^{-3}$  for steel and 0.7 GPa and  $950 \text{ kg} \cdot \text{m}^{-3}$  for polyethylene, respectively. The Young's modulus of the maize ear was chosen for 27 GPa, that is 100 times higher than the Young's modulus of the stalk particles. The relative velocity is determined by the gravitational acceleration and the drop height, thus they are also determined by the experimental method (Chapter 3.5). Consequently, the coefficient of restitution ( $e_{P-G}^{ME}$ ) is the only parameter that is not determined, thus it was analysed in the range of 0.5-0.9.

As to the rest of the non-bonded parameters, the coefficient of rolling friction among the particles ( $\vartheta_{P-P}$ ) and among the particles and geometry elements ( $\vartheta_{P-G}$ ) was chosen for 0.01, while the coefficient of restitution among the particles ( $e_{P-P}$ ) was 0.05.

TABLE 5.7: Range of the analysed non-bonded parameters.

Parameter	Description	Range
$E_p$	Particle Young's modulus [MPa]	67.5-540 ♣
$\theta_{P-P}$	Particle-particle static friction [-]	0.1-0.9 ♣
$\theta_{P-G}$	Particle-geometry static friction [-]	0.1-0.9 ♠ ♦
$e_{P-G}$	Particle-geometry restitution for the stalk particles [-]	0.2-1.0 ♦
$e_{P-G}^{ME}$	Particle-geometry restitution for the maize ear [-]	0.5-0.9 ⊙

Analysed by ♣ transversal compression; ♠ three-point bending; ♦ dynamic cutting;  
 ♠ ear-detachment and ⊙ ear-collision.

### 5.3.4 Bond Fabric Parameters

The bond fabric parameters, contact radius multiplier ( $\eta$ ) and bond radius multiplier ( $\Lambda$ ), are used for the initialisation of the bonds among the particles. The contact radius multiplier ( $\eta$ ) affect the number, while the bond radius multiplier ( $\Lambda$ ) affects the stiffness of the initialised bonds.

Both parameters were analysed through the sectional transversal compression and three-point bending simulations. By increasing the value of the contact radius multiplier ( $\eta$ ), overlap is formed among more and more particle pairs (Brown, Chen, and Ooi, 2014). In a well-structured bond system bonds can be formed between particles that are not necessarily in direct contact because of the high value of the contact radius multiplier ( $\eta$ ). Based on some pre-test on the 4<sup>th</sup> internodal section of the stalk (Chapter 5.2.2), the upper limit of the contact radius multiplier ( $\eta$ ) was determined:  $\eta_m = 1.4$ . Above this value, cross-bonds appear among the particles of the longitudinal fibres, thus the transversely isotropic mechanical behaviour cannot be ensured. Consequently, the influence of the contact radius multiplier ( $\eta$ ) was analysed in the range of 1.05-1.25 in which it really affects the number of the bonds in the poly-disperse core. The bond radius multiplier ( $\Lambda$ ) was analysed in the range of 0.2-1.0 for all the bonds.

### 5.3.5 Numerical Parameters

The numerical parameters, time step ( $\Delta t$ ) and global damping ( $\iota$ ), ensures the numerical stability of the models. Thus, it is expected that they have a negligible effect on the results when their value are selected carefully.

By the consideration of the safety factor of 0.1, the calculated critical time step ( $\Delta t_{crit}$ ) was 8.5e-8 s for the 4<sup>th</sup> internodal section (Chapter 5.3.1). Based on some pre-tests, the highest value of the time step ( $\Delta t$ ), that results in a stable solution, is 32e-8 s because the tangential bonds in the skin have pre-maturely failed regardless of the loading stage by using the time step ( $\Delta t$ ) of 33e-8 s. Through the sectional transversal compression and the dynamic cutting simulations, the influence of the time step ( $\Delta t$ ) and the global damping ( $\iota$ ) was analysed from 1.5e-8 s to 32e-8 s and in the range of 0.1-0.9, respectively.

## 5.4 Calibration and Validation

During the calibration and validation process the results of the previously conducted parametric study were exploited. To find an optimal set of parameters for the model of each maize part a calibration and validation method was established, as shown in Figure 5.9. From point of view of the plant, the calibration and validation method was divided into three main parts: numerical parameters for the internodal sections, for the stalk and for the shank with maize ear.

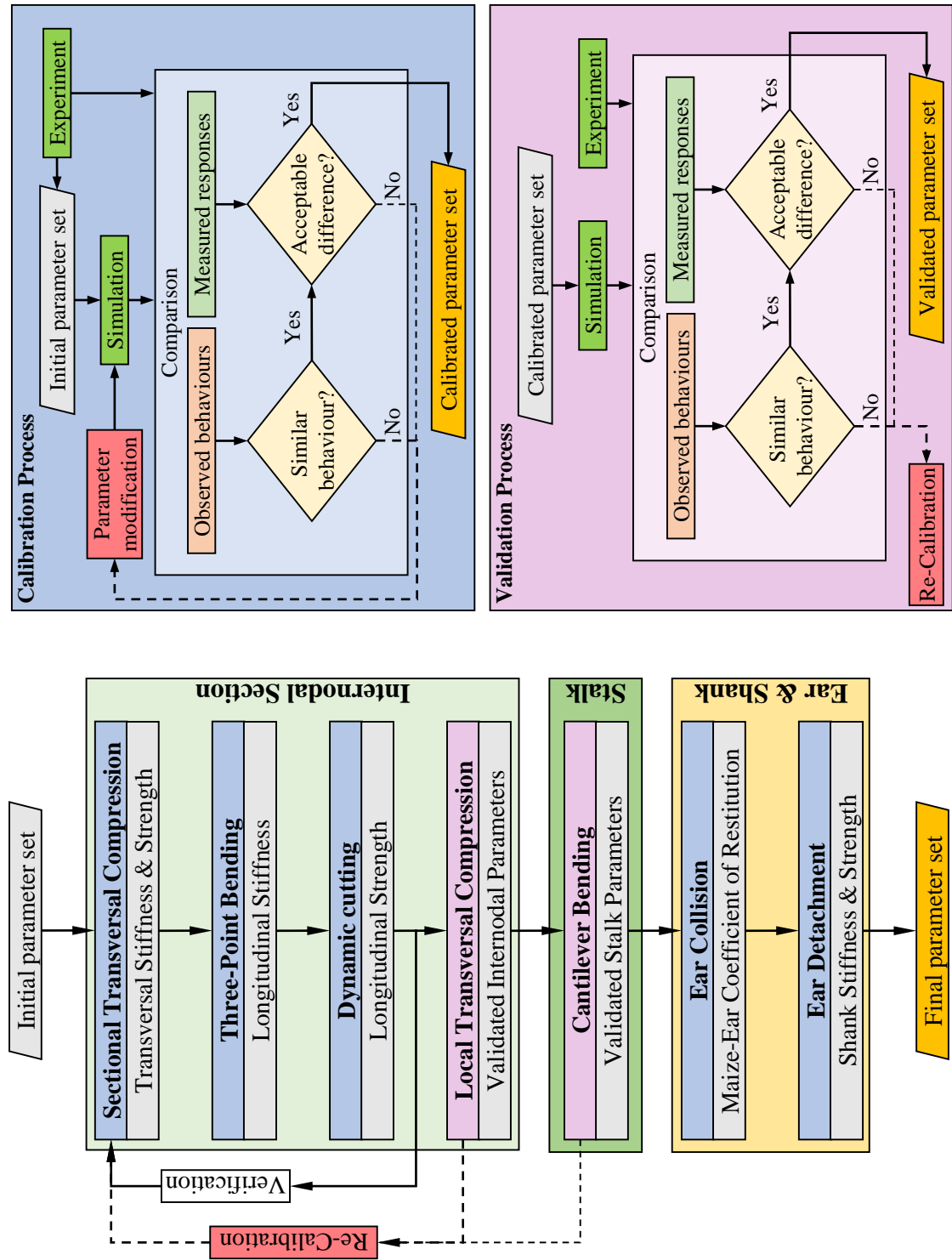


FIGURE 5.9: Calibration and validation method for the virtual maize plant.

In case of the internodal sections, the sectional transversal compression, three-point bending, dynamic cutting and local transversal compression simulations were conducted to find an optimal set of parameters for the internodal section that is subjected to a complex loading case during harvesting. Thus, the parameters needed to be optimised to work concurrently and provide the best overall DEM predicted behaviour. After the determination of the internodal model parameters, a cantilever bending simulation was carried out to validate the overall flexural behaviour of the stalk section under the maize ear. During these steps the following assumptions were considered:

- the influence of the longitudinal bonded parameters on the simulation of sectional transversal compression is negligible because the skin behaved rigidly in this direction during the experiments;
- the longitudinal fibres in the skin do not break during the simulation of sectional transversal compression and three-point bending experiment because they did not break neither during the experiments.

For the virtual shank with maize ear, the coefficient of restitution of the maize ear was determined by the ear-collision simulation in which it was assumed that the shape of the virtual maize ear does not affect the collision. The stiffness and strength parameters of the shank were determined by the ear-detachment simulation. In this step the following assumptions are considered: the DEM predicted mechanical behaviour and breakage of the 5<sup>th</sup> and the 6<sup>th</sup> internodal sections are verified in the previous steps and the longitudinal fibres in the shank do not break during the simulation.

In case of each step, the quantitative (measured diagrams & parameters) and qualitative (image-based observations) results of the experiments were compared with the same DEM predicted results to calibrate and verify the input parameters. For the quantitative results, an acceptance criterion of 30% difference between the experimental and numerical results was defined because of the high level of diversification of living materials. For the qualitative results, the similarity of the experimental and numerical results was the acceptance criterion.

For the upper internodal sections of the stalk, that were modelled by the hollow structure (Figure 5.2), the compressive, bending or cutting work was in the focus of the calibration and validation process because a detailed force response or breakage of the sample can not be reproduced by this simplified model. Moreover, the numerical parameters were defined in such a way to reproduce the exponential increasing section of the force response against the compression load because the likelihood of this type of external load on the upper stalk parts is much higher than bending with large deformation during the real process of harvesting. From this reason, the force response of the virtual sample against the bending load was verified until 5 mm of plunger displacement.

## 5.5 Technological Simulation of Harvesting

Based on observations of 13 commercial maize headers the CAD geometry of a common maize header unit was designed in the commercial CAD software **CATIA®**, as shown in Figure 5.10. Each part of the unit was designed based on the dimensions and parts of a real machine, however, the entire design is not identical with any of them. Afterwards, the CAD model was imported into the discrete element software **EDEM®**, where its kinematics was also determined based on real operation parameters of a maize header; thus, the forward velocity of the unit was  $2 \text{ m s}^{-1}$ ; the speed of the gathering chains was  $4 \text{ m s}^{-1}$ ; the rotational speed of the stalk rollers and chopping unit were 400 rpm and 3500 rpm, respectively.

As to the initialization of the plant, the bottom section of the stalk (stump) was placed into a cylindrical-conical geometrical support, as shown in Figure 5.11(a). The outer diameter of

the stump section was 30 mm that perfectly fitted in the cylindrical geometry, moreover, a downward force of 8.77 N was applied onto each particle that resulted in a total downward force of 5000 N. The conical part of the support limited the flexural deformation of the stump that reflects the real behaviour of the soil-root interaction. Thus, the movement of the stump was restricted.

In this simulation, gravitational acceleration ( $g=9.81 \text{ m s}^{-2}$ ) was also applied. From this reason, the DEM model needed some time to reach an equilibrium before starting the harvesting process, thus, the following criteria was defined: the system reached its equilibrium when the magnitude velocity of the maize ear is permanently lower than  $1\text{e-}3 \text{ m s}^{-1}$ . The maize ear means a huge eccentric load on the stalk, thus, its velocity worthily reflects the damping of the system, as shown in Figure 5.11(b). Based on the previous consideration, the system reached its equilibrium around 0.15 sec simulation time where the magnitude velocity of the maize ear oscillated around  $4.6\text{e-}4 \text{ m s}^{-1}$  with an amplitude of  $1.6\text{e-}4 \text{ m s}^{-1}$ . Moreover, the oscillation also showed a decreasing characteristic between 0.15 and 0.25 sec simulation time. By taking into consideration that the real plants are not in equilibrium on the field because of the pre-interactions among them and the row divider, moreover, the movements of the parts in the maize header are much quicker, 0.25 sec simulation time was defined as the beginning of the harvesting process because the actual movements of the maize ear are negligible.

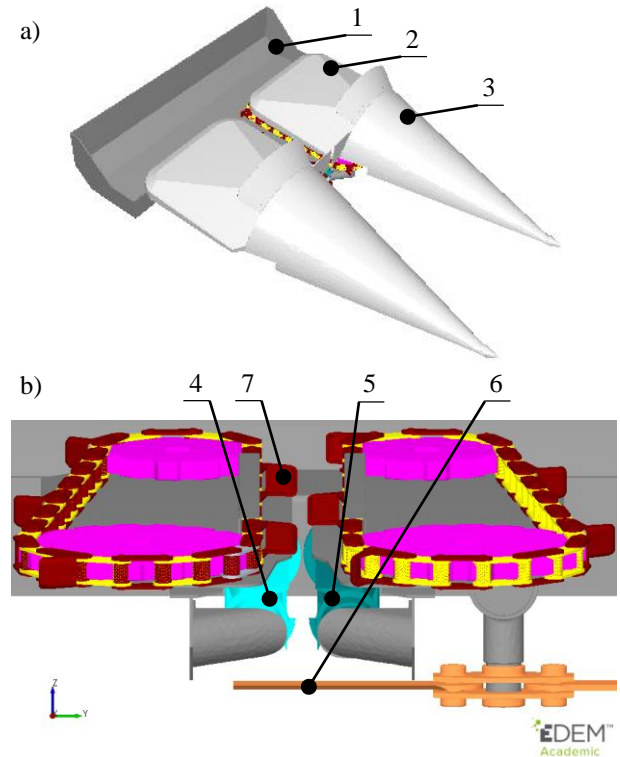


FIGURE 5.10: CAD model of a common maize header: 1. gathering box; 2. hood; 3. row divider; 4. right stalk roller; 5. left stalk roller; 6. chopping blade; 7. gathering chains.

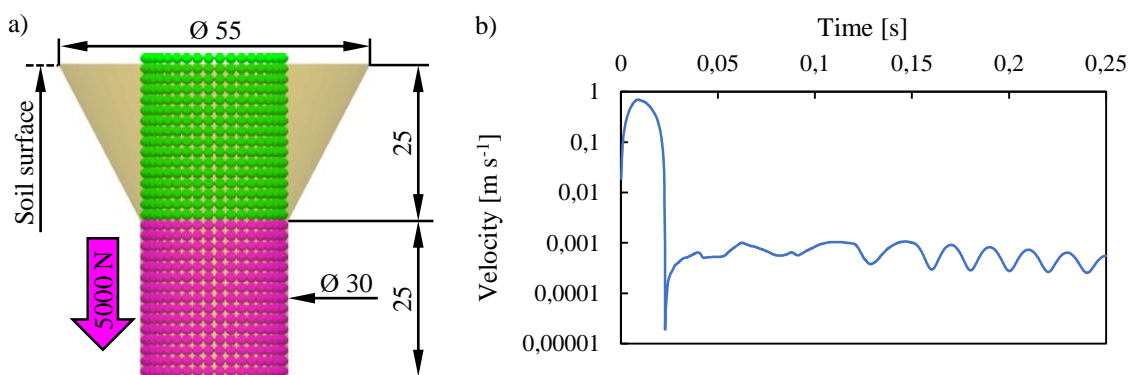


FIGURE 5.11: Initialization of the maize plant: a) soil-root model; b) magnitude velocity of the maize ear on logarithmic scale.



# 6 Results of The Parametric Study

## 6.1 Reference Models

### 6.1.1 Sectional Transversal Compression

Generally, the force response of the internodal section during the five simulation cases were similar, as shown in Figure 6.1(a). Three phases were determined: initial linear increasing up to 0.1 compression rate, several drops between 0.1 and 0.25 compression rate and exponential increasing between 0.25 and 0.75 compression rate. In Figure 6.1(b), it can be seen that there is a small difference among the results between 0.1 and 0.25 compression rate where the initial breakage of the skin takes place. Except the cases of Run 2 and Run 5, four major breaking events could be observed that took place approximately at 0.1, 0.15, 0.24 and 0.25 compression rate, respectively (Figure 6.1(c)). In case of Run 2 and 5, the first two breaks appeared at the same time. The mean compressive force of the five simulation cases was 3163 N at 0.75 compression rate.

For further analysis of the breakage, the development of the broken bonds was also compared, as shown in Figure 6.2. All characteristics of broken bonds showed an increasing trend except the number of the skin bonds in longitudinal direction that remained constant because none of the longitudinal fibres broke (Figure 6.2(a)). All drops of the resistance force curve were related to the major breakage events (when more than one bond broke suddenly) of the skin bonds in tangential direction (Figure 6.2(b)), thus, the strength of the sample mainly depended on these bonds. However, the initial four major breakage events of the skin in tangential direction resulted in additional breakage events among the bonds between the skin and the core (Figure 6.2(c)), thus, the initial breakage of the skin was affected by the strength of these bonds as well. The number of the bonds in the core (Figure 6.2(d)) increased linearly until 0.35 of compression rate, where it started to increase more sharply until the end of the compression. Therefore, the core was proved to be the major supporting material during the range of 0.35-0.75 compression rate. Finally, the evolution of the breakage was compared through an image-based comparison for each simulation cases and significant differences were not found, as shown in Figure B.1.

During the analysis on the influence of the loading direction significant differences were not found. At each position (bottom, middle, top) and loading direction ( $0^\circ - 45^\circ - 90^\circ - 135^\circ$ ), the force responses showed the same characteristic (Figure B.2 *bottom*; B.4 *middle*; B.6 *top*), moreover, the number of the broken bonds has the same trend in each case (Figure B.2 *bottom*; B.4 *middle*; B.6 *top*). Finally, the breakage of the virtual specimens was similar in each simulation case according to an image-based comparison (Figure B.3 *bottom*; B.5 *middle*; B.7 *top*).

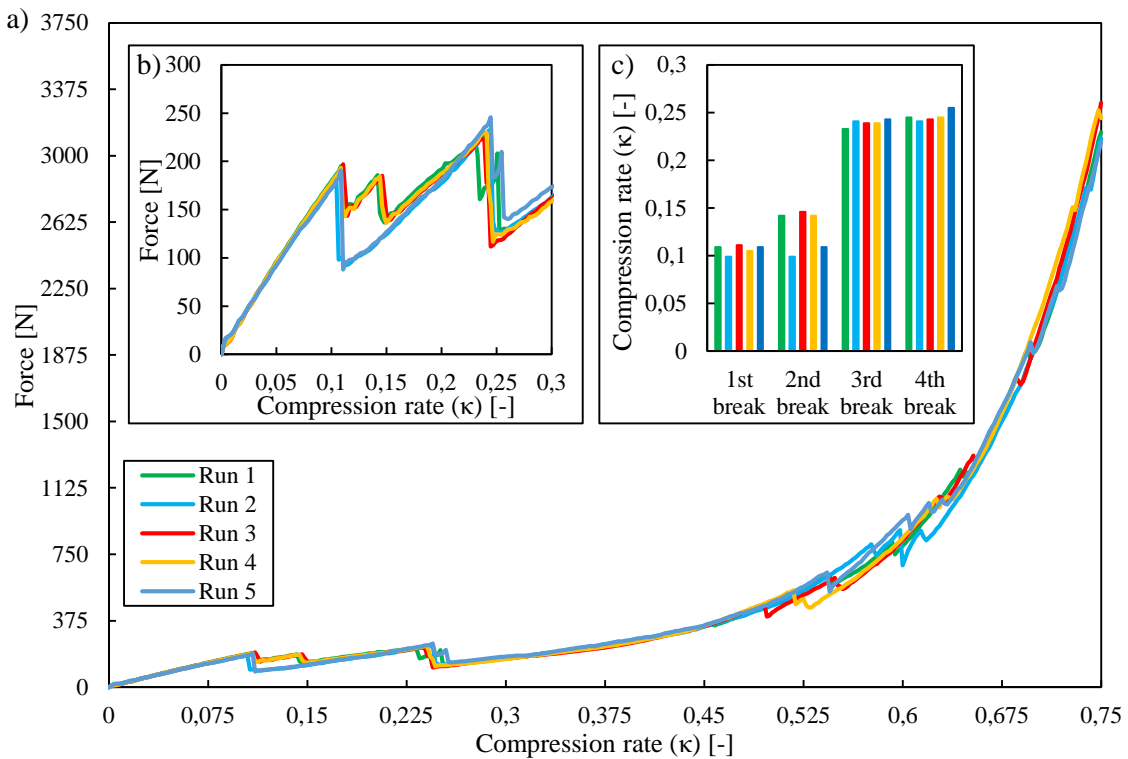


FIGURE 6.1: Force response for the reference simulation cases of sectional transversal compression:  
a) overall force-compression rate characteristics; b) force-compression rate characteristics in range of 0-0.3 compression rate; c) major break events in tangential direction of the skin.

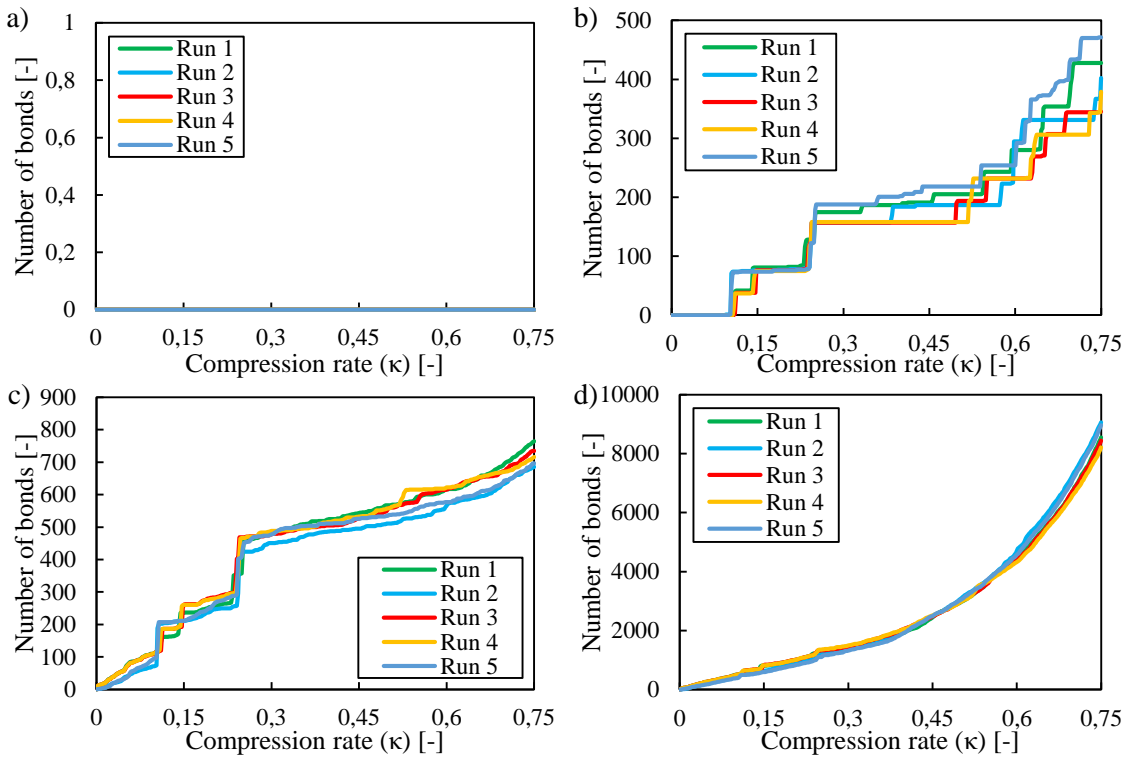


FIGURE 6.2: Number of broken bonds during the reference simulation cases of sectional transversal compression: a) broken bonds of the skin in longitudinal direction; b) broken bonds of the skin in tangential direction; c) broken bonds between the skin and the core; d) broken bonds in the core.

### 6.1.2 Three-Point Bending

Figure 6.3(a) shows the force response of the internodal section during the five reference simulation cases. At the beginning of the bending process the resistance force increased linearly until reaching the first break in the skin. After this, the grade of increase dropped, however, this section was constituted of short linear increasing sections and large drops. The characteristic reached its peak ( $F_m^{TB}$ ) at around 6 mm of displacement ( $DoP^{TB}$ ) (Figure 6.3(c)) where it fell within 180-210 N (Figure 6.3(b)). Afterwards, the force response started to decrease, however, this section is governed by several major drops between displacement of 10 and 15 mm. This is followed by some further small breaks before the plateau region where the ultimate force ( $F_u^{TB}$ ) fell within 125-140 N (Figure 6.3(b)). Finally, the force response increased slightly until the end of the bending process because of the continuously increasing displacement of the un-broken longitudinal fibres in the skin.

The number of broken bonds for all types increased while the displacement increased with exception of the skin bonds in longitudinal direction (Figure 6.4(a)) because none of the longitudinal fibres broke. All the major drops of the resistance force curve were related to one of the major breakage events of the skin bonds in tangential direction (Figure 6.4(b)), thus, these bonds have a significant effect on the characteristic of the resistance force. The effect of the breakage between the skin and core, and in the core was minimal because the majority of the bonds remained bonded until the end of the bending process (Figure 6.4(c)(d)). Finally, the deformation of the bended cross-section and the longitudinal break propagation in longitudinal direction of the skin were also compared and significant differences were not found, as shown in Figure B.8

During the analysis on the influence of the loading direction significant differences were not found. At each loading direction ( $0^\circ - 45^\circ - 90^\circ - 135^\circ$ ), the force responses showed the same characteristic (Figure B.9(a)(b)(c)), moreover, the number of the broken bonds also had the same characteristic (Figure B.10(d)(e)(f)(g)). Furthermore, the breakage of the virtual specimens was similar for each simulation case according to the image-based comparison (Figure B.10).

### 6.1.3 Dynamic Cutting

In the case of the **dynamic cutting**, the force response the internodal section was similar in each reference case, as shown in Figure 6.5(a). At the beginning the force response increased until approximately 15 mm of cutting blade displacement (initial compression phase), where a small drop was observable (phase of initial cut of the skin). Afterwards, it also increased until reaching its maximal value ( $F_m^{DC}$ ) around displacement of 24 mm (phase of skin and core cut). After its peak, a sudden drop appeared (phase of final cut of the skin) and the ultimate force ( $F_u^{DC}$ ) started to decrease gradually until reaching zero around displacement of 100 mm.

The peak ( $F_m^{DC}$ ) (Figure 6.5(b)) and ultimate force ( $F_u^{DC}$ ) (Figure 6.5(c)) fell within 1345-1613 N and 36-61 N, respectively. The length of the stages of cut were close to similar in each simulation case, as shown in Figure 6.5(d). Based on the force responses, the calculated dynamic cutting work fell within 16.26-17.09 J. Finally, the breakage of the virtual specimens was similar for each simulation case based on an image-based comparison, as shown in Figure B.11.

During the analysis on the influence of the loading on a particle and between two particles, significant differences were not found. At each loading case, the force response showed the same characteristic (Figure B.12(a)(b)(c)(d), moreover, the number of the broken bonds also showed the same characteristic (Figure B.12(e)(f)(g)(h)). Furthermore, the breakage of the virtual specimens was similar for each simulation case according to the image-based comparison (Figure B.13).

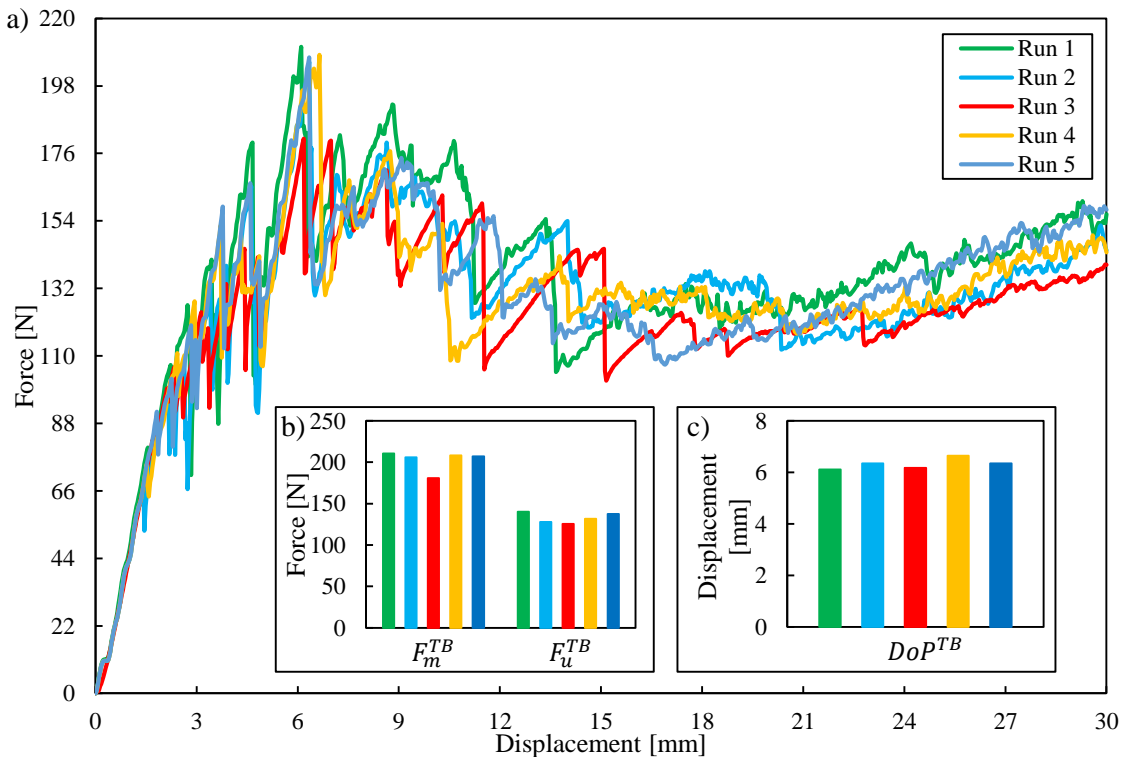


FIGURE 6.3: Force response for the reference simulation cases of three-point bending: a) overall force-displacement characteristics; b) range of the peak and the ultimate forces; c) range of the displacement of peak forces (DoP).

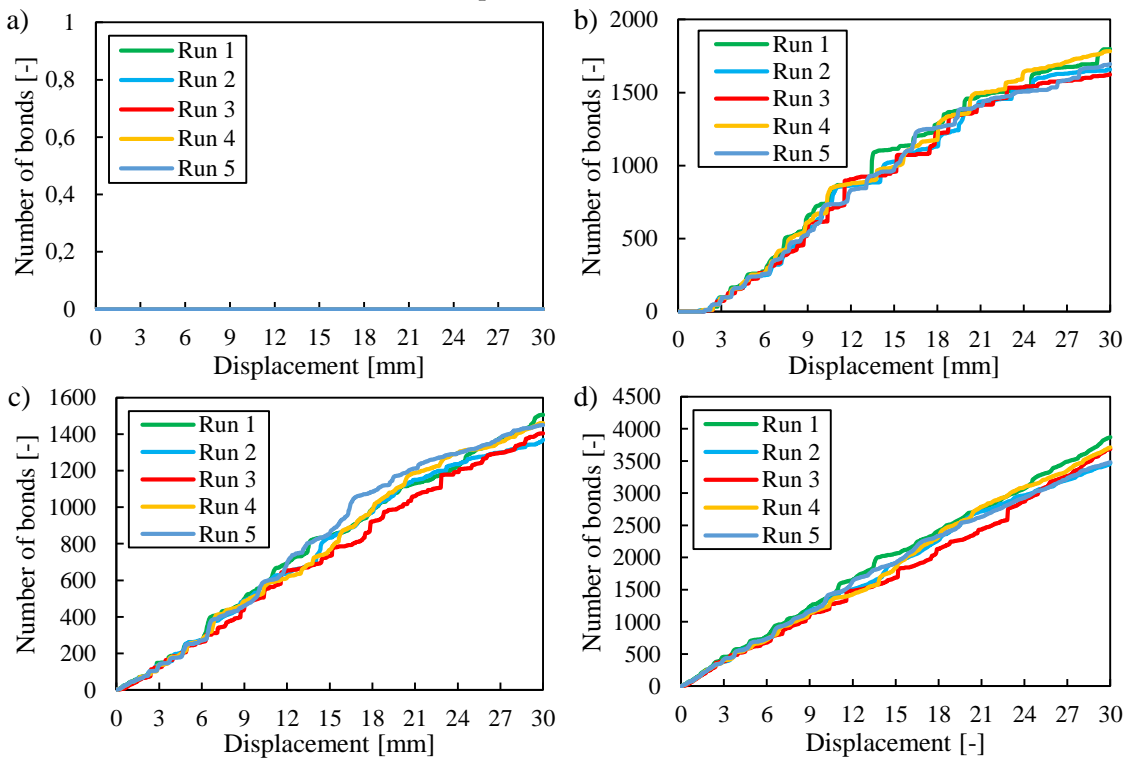


FIGURE 6.4: Number of broken bonds during the reference simulation cases of three-point bending: a) broken bonds of the skin in longitudinal direction; b) broken bonds of the skin in tangential direction; c) broken bonds between the skin and the core; d) broken bonds in the core.

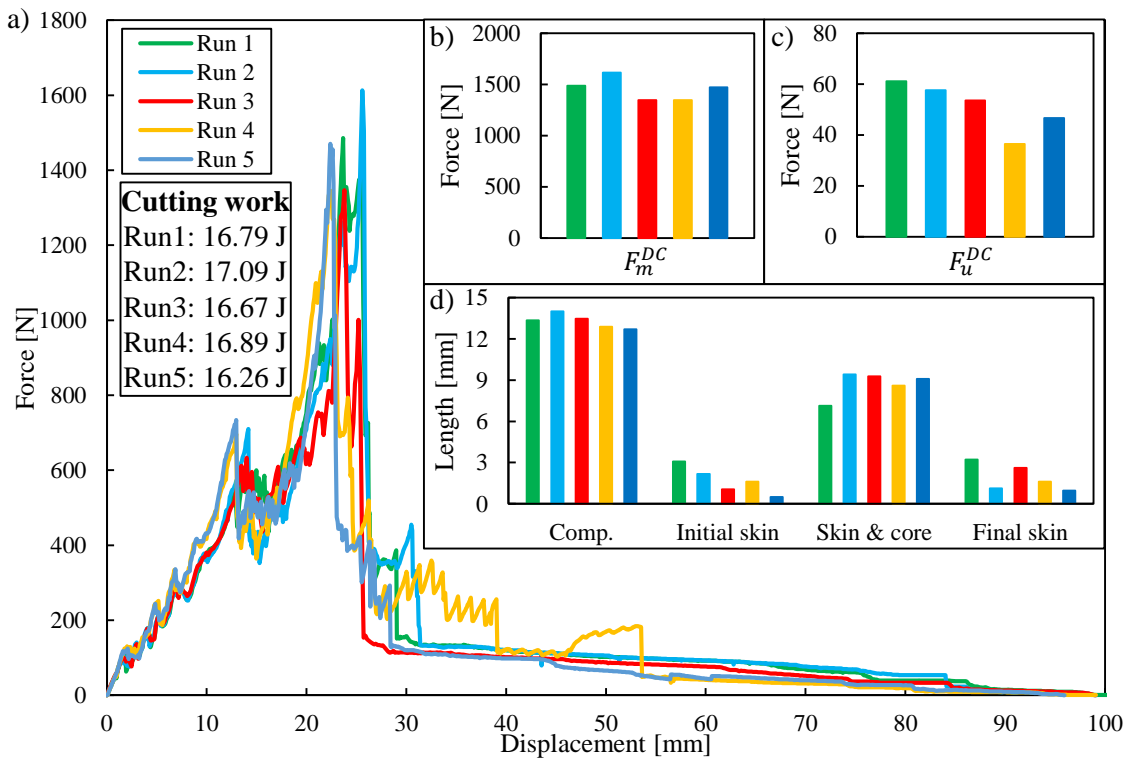


FIGURE 6.5: Force response for the reference simulation cases of dynamic cutting: a) overall force-displacement characteristics; b) range of the peak forces; c) range of the ultimate forces; d) length of the stages of cut.

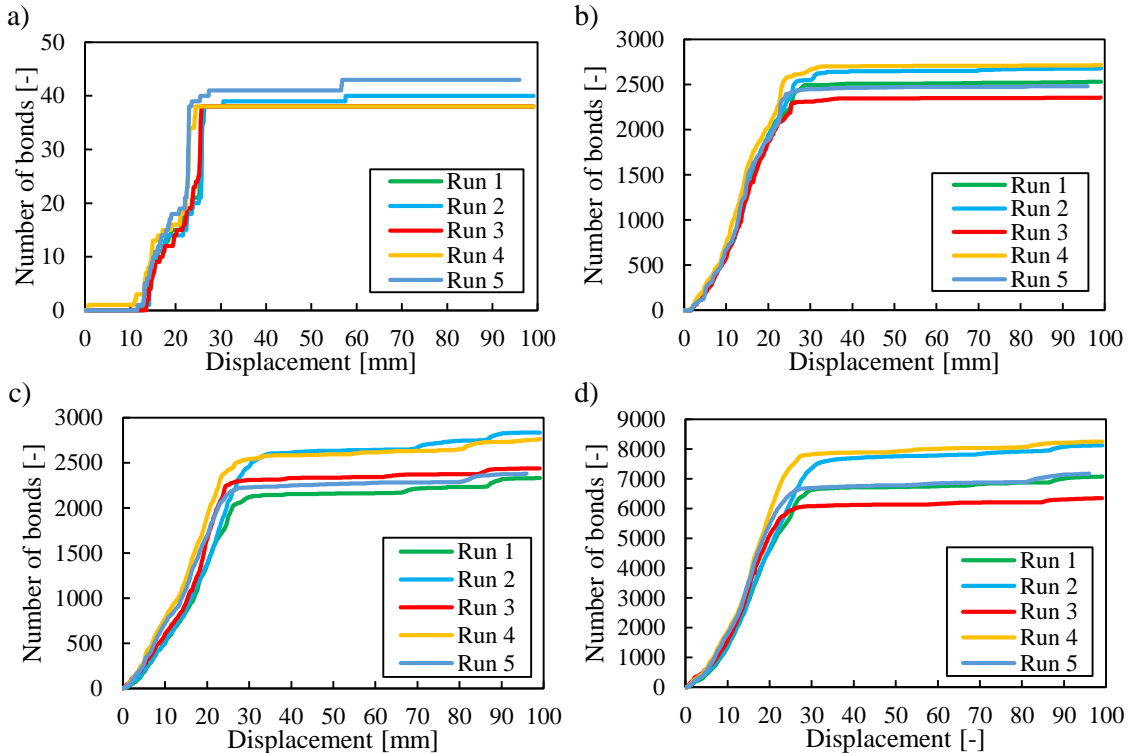


FIGURE 6.6: Number of broken bonds during the reference simulation cases of dynamic cutting: a) broken bonds of the skin in longitudinal direction; b) broken bonds of the skin in tangential direction; c) broken bonds between the skin and the core; d) broken bonds in the core.

### 6.1.4 Ear-Detachment and Collision

Figure 6.7 shows the force response of the five reference simulation cases of the **ear-detachment**. Generally, the force responses were similar (Figure 6.7(a)), while the detachment force fell into the range of 455.3–457.5 N (Figure 6.7(b)) and the displacement of the detachment was between 118.8 and 119.4 mm (Figure 6.7(c)). Three typical sections were determined:

- a lifting section between 10 and 80 mm displacement when the maize ear lays on the front plate of the detachment apparatus (Figure 6.7(d)) and the force response increases linearly;
- a sliding section between 80 and 100 mm displacement when the maize ear slides to the side plates of the detachment apparatus (Figure 6.7(d)) and the force response oscillates around a gradually increasing mean value;
- stretching section between 100 and 120 mm displacement when the shank is stretched (Figure 6.7(d)) and the force response increases sharply until the detachment.

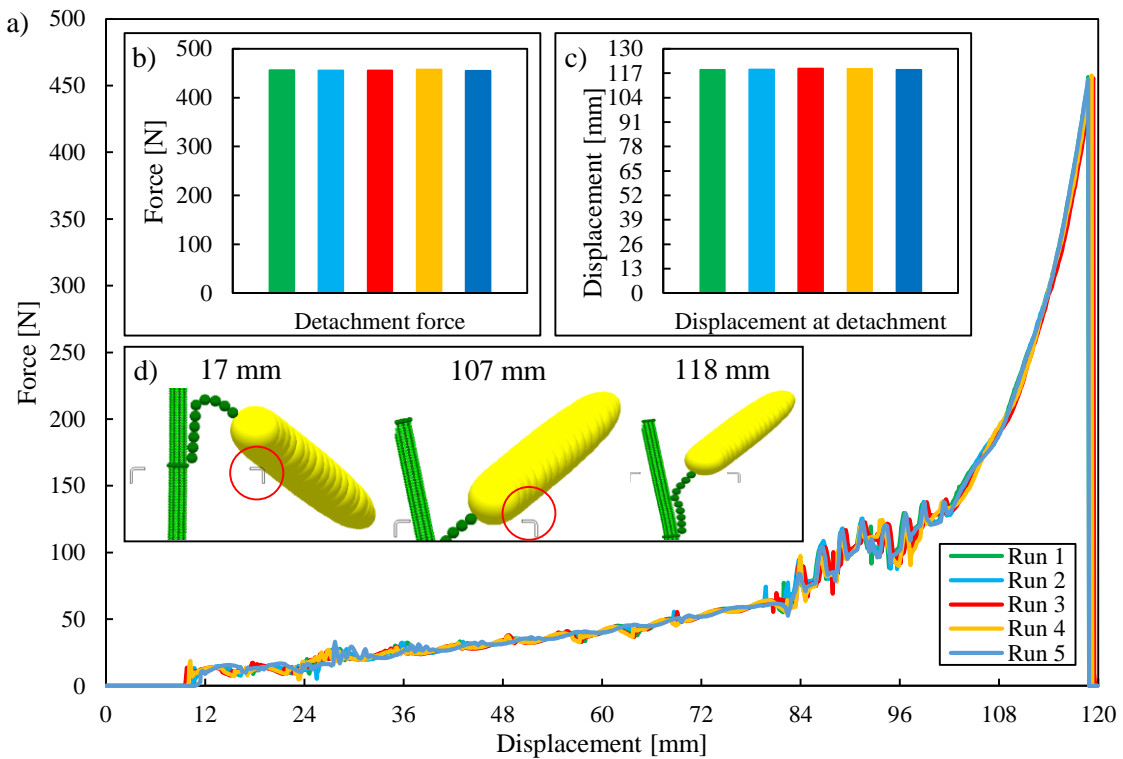


FIGURE 6.7: Reference simulation cases of ear-detachment simulation: a) overall force-displacement characteristic; b) detachment force distribution; c) distribution of the displacement at detachment; d) position of the maize ear at 17, 107 and 118 mm displacement.

Figure 6.8 shows the course of the ear-collision simulation. Obviously, the resulted bounce height-time characteristics were exactly the same by using the same parameter set because the coefficient of variation of the bonds ( $\zeta$ ) does not influence the collision between a single particle and a geometrical element. Thus, one characteristic is presented for steel and plastic sheets in Figure 6.8(a). At the beginning, the gravity accelerated the maize ear until the first collision (II.). Because of the different stiffness of the steel and plastic sheets, the bounce height of the first bounce was also different (III.). Afterwards, a second collision (IV.) took place that results in a smaller bounce height (V.). The bouncing stages were visualized in Figure 6.8(b). After the collisions (II. and IV.), the orientation of the maize ear was not changed.

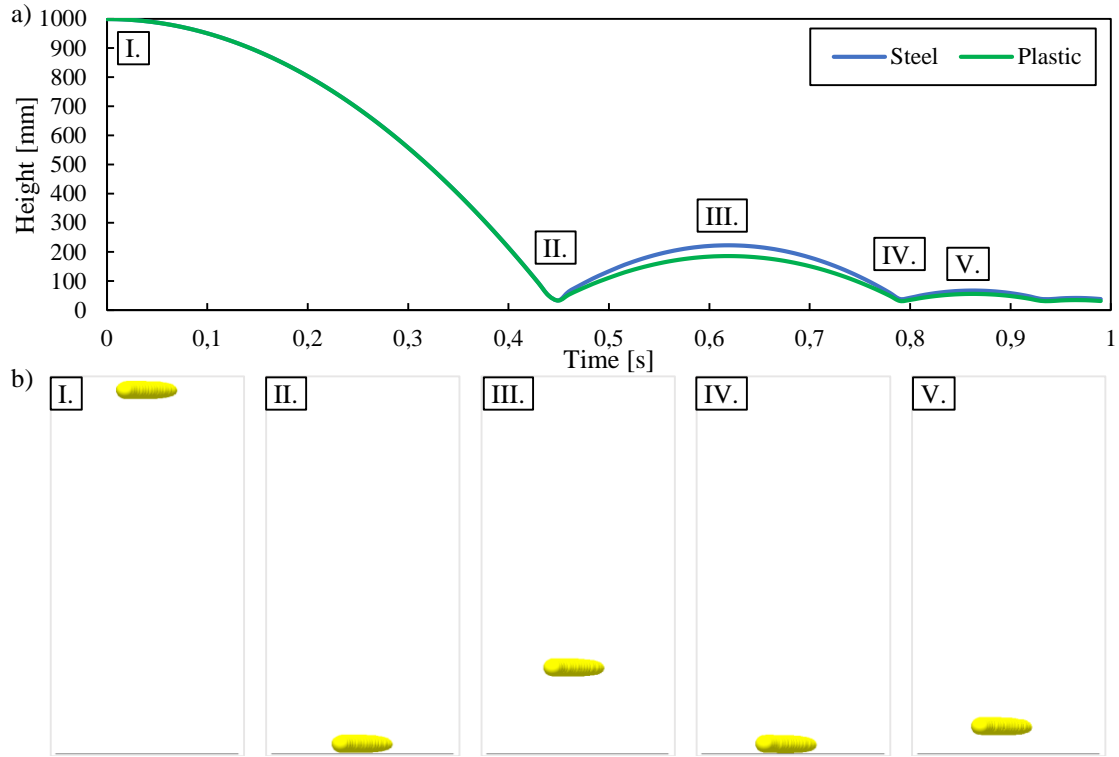


FIGURE 6.8: Reference simulation cases of ear-collision simulation: a) bounce height characteristic for steel and plastic plates; b) bouncing of maize ear.

## 6.2 Influence of Bonded Contact Parameters

### 6.2.1 Bond Young's modulus

In the case of **sectional transversal compression**, the increasing of the Young's modulus of the bonds ( $E_B$ ) led to the increase of the initial transversal stiffness of the virtual specimen, moreover, by using the same strength parameters it also resulted in earlier breakage of the skin, as shown in Figure 6.9(b). In the exponential section where the core is the main supporting material, the higher parameters also caused stiffer behaviour, as shown in Figure 6.9(a). Through the image-based comparison, the softer Young's moduli led to a more ovalised shape before the first break of the skin, as shown in Figure 6.9(c). All the results are presented in Figure C.1 and C.2.

The increasing of the ratio between the bond Young's modulus in the core and in transversal direction of the skin ( $\phi_{E_B}^{S,C}$ ) led to a stiffer core, thus, the resistance of the virtual sample during the exponential increasing phase was also higher (Figure 6.10(a)), while the significance of the third and fourth break in the skin was lower (Figure 6.10(b)). In the case of Ratio 100, the third and the fourth break disappeared, only a fine decrease was observable in this region of the curve. Significant difference among the breakage of the virtual samples was not observable through the image-based comparison, as shown in Figure C.4. All the results are presented in Figure C.3 and C.4.

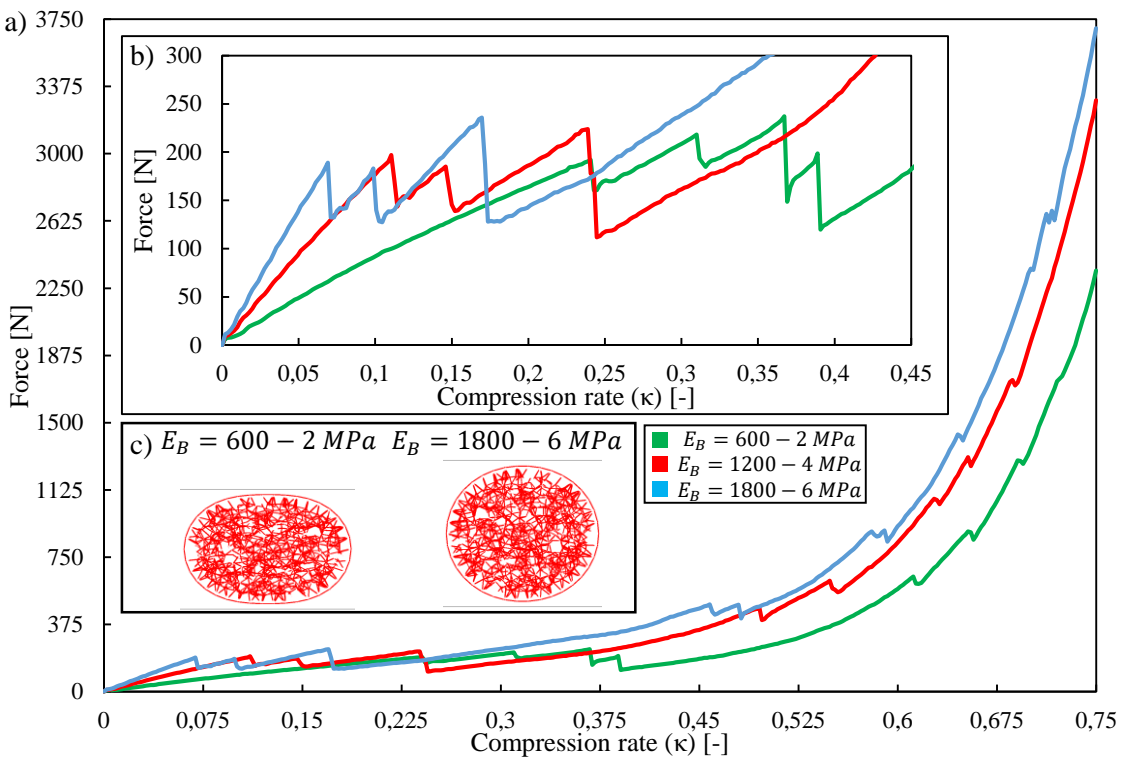


FIGURE 6.9: Influence of the bond Young's modulus on the force response by sectional transversal compression: a) overall force-compression rate characteristic; b) force-compression rate characteristics in range of 0-0.3 compression rate; c) shape of the samples at the end of the ovalisation stage.

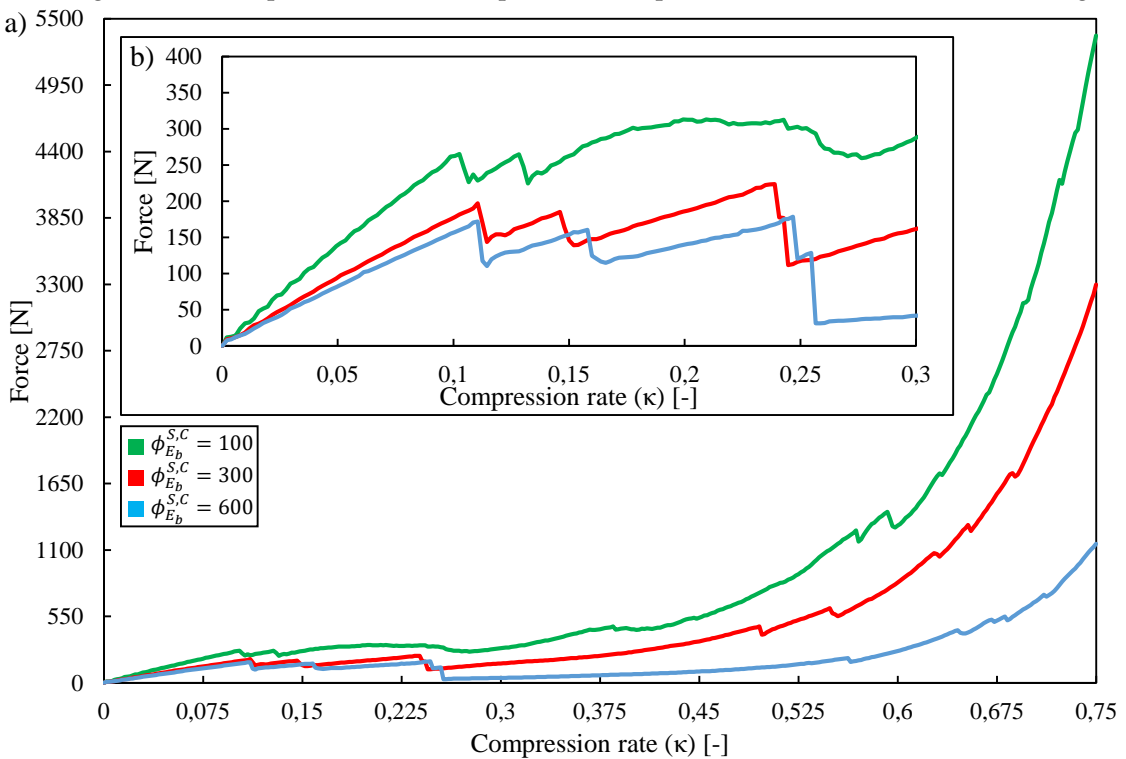


FIGURE 6.10: Influence of the ratio between the bond Young's modulus in the core and in tangential direction of the skin on the force response by sectional transversal compression: a) overall force-compression rate characteristic; b) force-compression rate characteristics in range of 0-0.3 compression rate.

In the case of **three-point bending**, the increasing of the Young's modulus of the longitudinal bonds ( $E_B^{S, long.}$ ) led to a higher resistance against bending (Figure 6.11(a)), that resulted in higher peak ( $F_m^{TB}$ ) and ultimate ( $F_u^{TB}$ ) forces as well (Figure 6.11(b)). The displacement of the peak force ( $DoP^{TB}$ ) slightly decreased as the stiffness increased, as shown in Figure 6.11(c). The softer skin in longitudinal direction led to less extensive damage zone under the bending tool, moreover, the longitudinal breaks did not propagate to the nodal particles, as shown in Figure 6.11(d). All the results are presented in Figure C.5 and C.6.

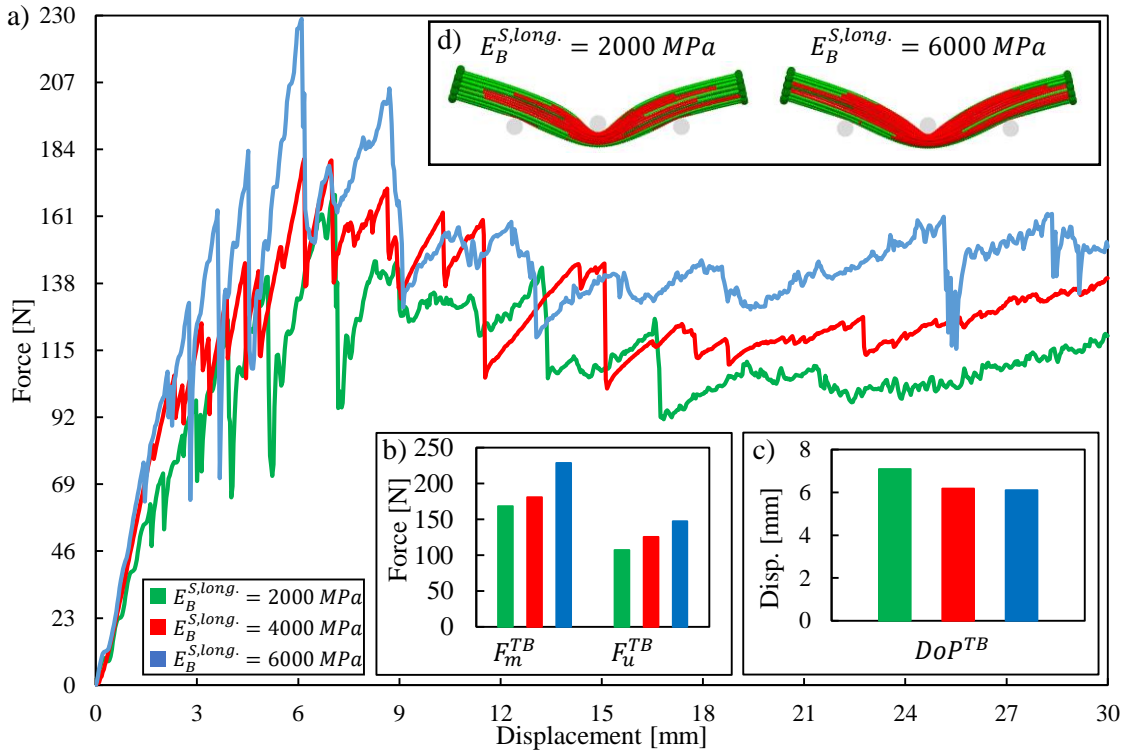


FIGURE 6.11: Influence of the bond Young's modulus on the force response by three-point bending: a) overall force-displacement characteristic; b) the range of peak and ultimate forces; c) displacement range of the peak force; d) longitudinal breaks in the skin.

In the case of **dynamic cutting**, the increasing of the Young's modulus of the longitudinal bonds ( $E_B^{S, long.}$ ) led to smaller force response (Figure 6.12(a)), that resulted in smaller peak forces ( $F_m^{DC}$ ) as well (Figure 6.12(b)). However, it did not affect the ultimate force ( $F_u^{DC}$ ), as shown in Figure 6.12(c). As to the length of the stages of cut, significant relationship between the increasing Young's modulus and the compression stage was observed: lower Young's modulus resulted in a longer compression stage (Figure 6.12(d)). The overall required cutting work of the process decreased while the Young's modulus of the longitudinal fibres increased. When the Young's modulus of longitudinal fibres was 6000 MPa, a perfectly straight cutting surface was observed, while the lowest Young's modulus (2000 MPa) resulted in a serrated cutting surface, as shown in Figure 6.12(e). All the results are presented in Figure C.7 and C.8.

In the case of **ear-detachment**, the bond Young's modulus in the shank ( $E_B^{SH}$ ) had a significant effect on the force response, as shown in Figure 6.13. For the stiffer bonds of the shank, the characteristic of the force response presented a sharper increasing in its each stages (Figure 6.13(a)), that led to detachment at lower displacement (Figure 6.13(c)), however, the detachment force was not affected (Figure 6.13(b)). In the sliding section between 80 and 100 mm displacement, the oscillation of the force response was lower in case of lower values of Young's modulus. The lower bond stiffness also led to straighter shank, and less bended stalk sections right before the detachment, as shown in Figure 6.13(d).

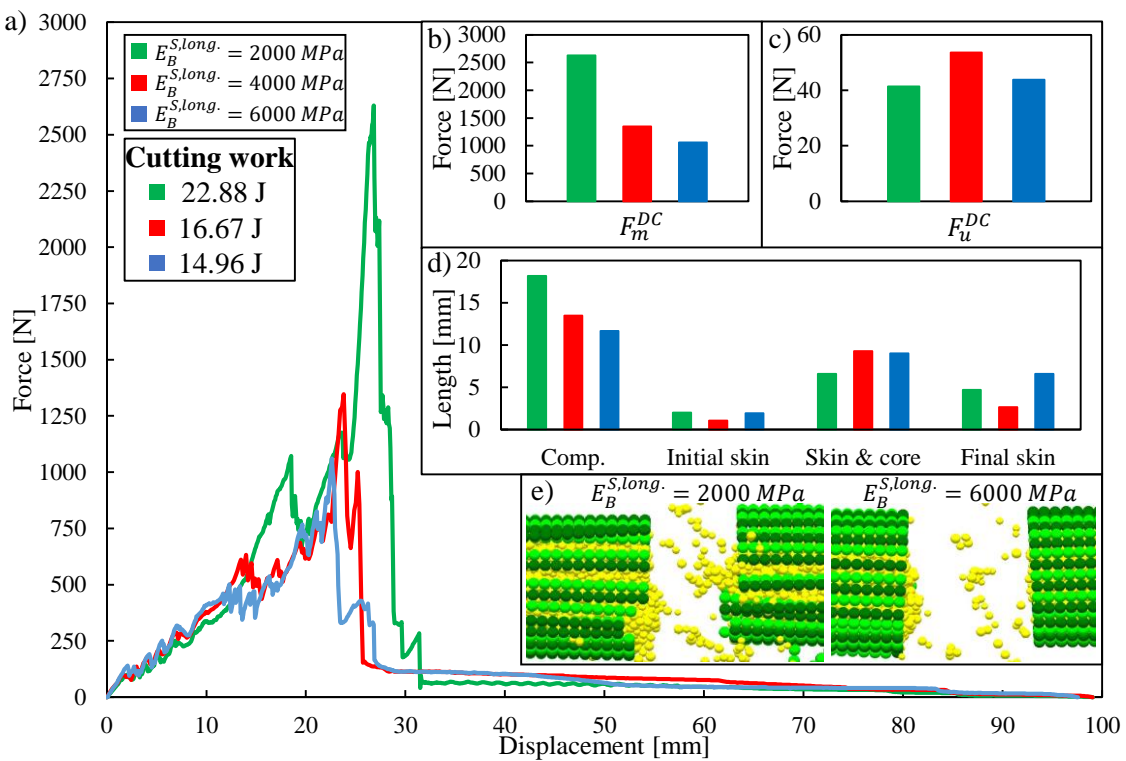


FIGURE 6.12: Influence of the bond Young's modulus by dynamic cutting: a) overall force-displacement characteristics; b) range of the peak forces; c) range of the ultimate forces; d) length of the stages of cut; e) resulted cutting surface .

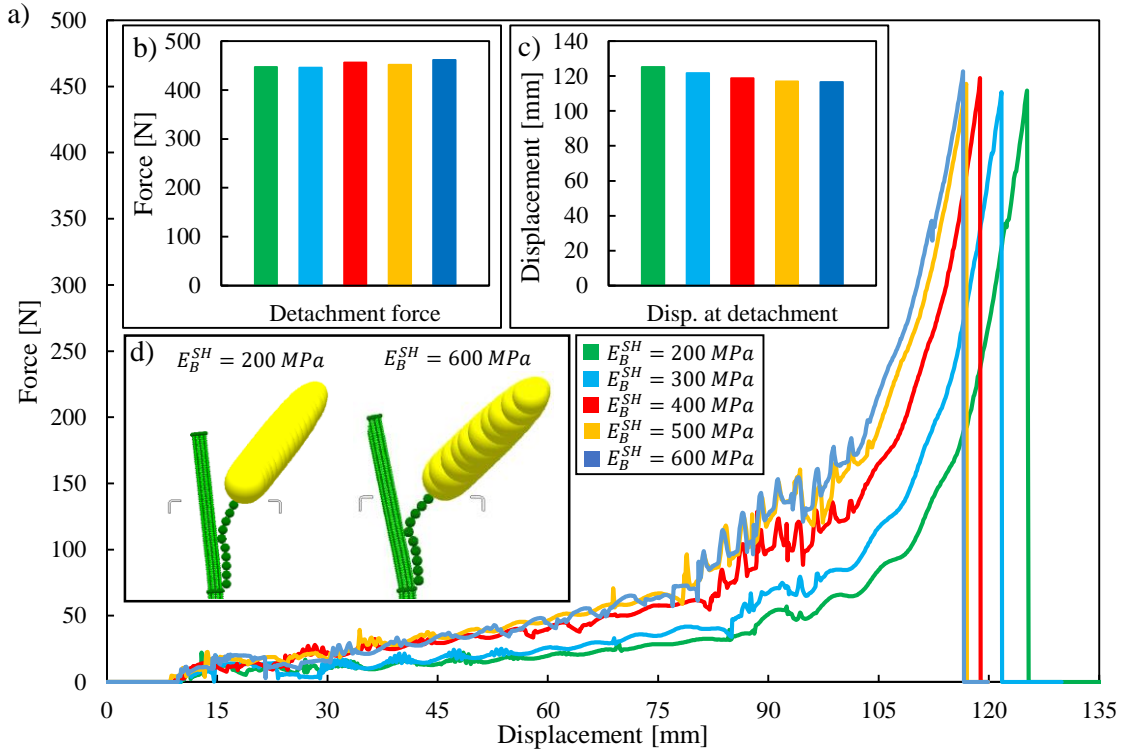


FIGURE 6.13: Influence of the bond Young's modulus by ear-detachment: a) overall force-displacement characteristics; b) range of the detachment forces; c) range of the displacement at detachment; d) shape of the shank right before the detachment.

### 6.2.2 Bond Poisson's ratio

By the analysis of the bond Poisson's ratio in the range of 0.1-0.4, significant influence on the force response, number of broken bonds and breakage of the virtual samples were not found in the case of the sectional transversal compression (Figure C.9, C.10), three-point bending (Figure C.11, C.12) and dynamic cutting (Figure C.13, C.14) simulations.

### 6.2.3 Tensile Strength of The Bonds

In the case of **sectional transversal compression**, the increasing of the tensile strength of the bonds in transversal direction of the skin ( $S_T^{S,tr.}$ ) led to breakage of the skin at higher compression rate that resulted in higher local forces at the beginning of the compression process, as shown in Figure 6.14(b). It also affected slightly the exponential increasing phase of the force response (Figure 6.14(a)). Through the image-based comparison, the higher parameters led to an extended damage zone around the first, second, third and fourth breaks, as shown in Figure 6.14(c). All the results are presented in Figure C.15 and C.16.

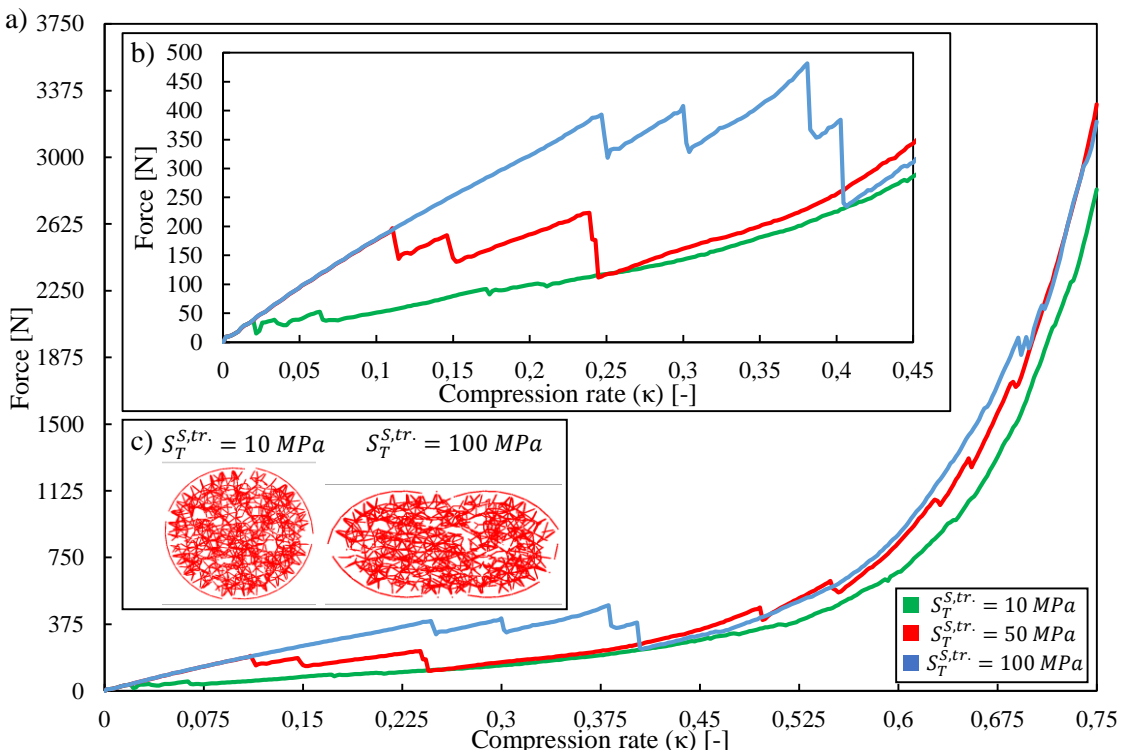


FIGURE 6.14: Influence of the bond tensile strength in tangential direction of the skin by sectional transversal compression: a) overall force-compression rate characteristic; b) force-compression rate characteristics in range of 0-0.45 compression rate; c) shape of the samples after the fourth break of the skin.

The increasing of the tensile strength of the bonds in the core ( $S_T^C$ ) led to a stiffer mechanical behaviour during the exponential increasing phase of the force response (Figure 6.15), however, the lowest ( $S_T = 1 \text{ MPa}$ ) and the highest ( $S_T = 8 \text{ MPa}$ ) tensile strength parameters also affected the force response between the second and the third break of the skin (Figure 6.15(b)). Through the image-based comparison, the lower parameters led to more broken bonds in the core, moreover, the width of the virtual samples was higher at the end of the compression process, as shown in Figure 6.15(c). All the results are presented in Figure C.17 and C.18.

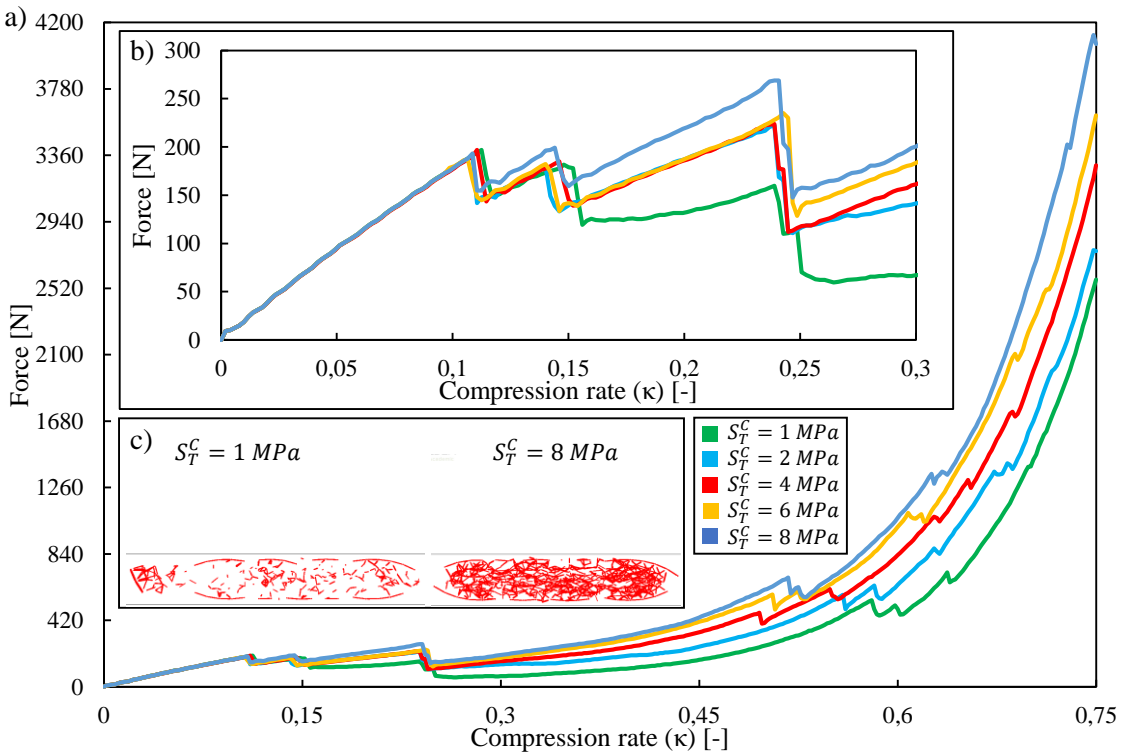


FIGURE 6.15: Influence of the bond tensile strength of the core by sectional transversal compression:  
a) overall force-compression rate characteristic; b) force-compression rate characteristics in range of  
0-0.3 compression rate; c) shape of the samples at the end of the compression process.

In the case of **three-point bending**, the increasing of the tensile strength of the bonds in the core ( $S_T^C$ ) did not affect the overall force response of the virtual sample (Figure 6.16(a)), however, the ultimate force ( $F_u^{TB}$ ) slightly increased (Figure 6.16(b)). The peak force ( $F_m^{TB}$ ) and the displacement of the peak force ( $DoP^{TB}$ ) were not influenced (Figure 6.16(b)(c)). Through the image-based comparison, the lower parameters led to a more flattened cross-section under the bending tool at the end of the compression process, as shown in Figure 6.16(d). All the results are presented in Figure C.19 and C.20.

The increasing of the tensile strength of the bonds in transversal direction of the skin ( $S_T^{S,tr.}$ ) did not affect the overall force response except the case when it was 10 MPa, as shown in Figure 6.17(a). In this case the typical stages of the force response were not observable because after the first breaks a linear increasing section took place between 3 and 30 mm displacement. The higher strength resulted in higher peak forces ( $F_m^{TB}$ ), however, the ultimate force ( $F_u^{TB}$ ) was not affected (Figure 6.17(b)). The tensile strength of 10 MPa resulted in the highest displacement of the peak force ( $DoP^{TB}$ ) because of its unusual characteristic, however, overall relationship between the increasing tensile strength and the displacement of the peak forces ( $DoP^{TB}$ ) could not be observable, as shown in Figure 6.17(c). Through the image-based comparison, the lower parameters led to more longitudinal breaks along the internodal section, as shown in Figure 6.17(d). All the results are presented in Figure C.21 and C.22.

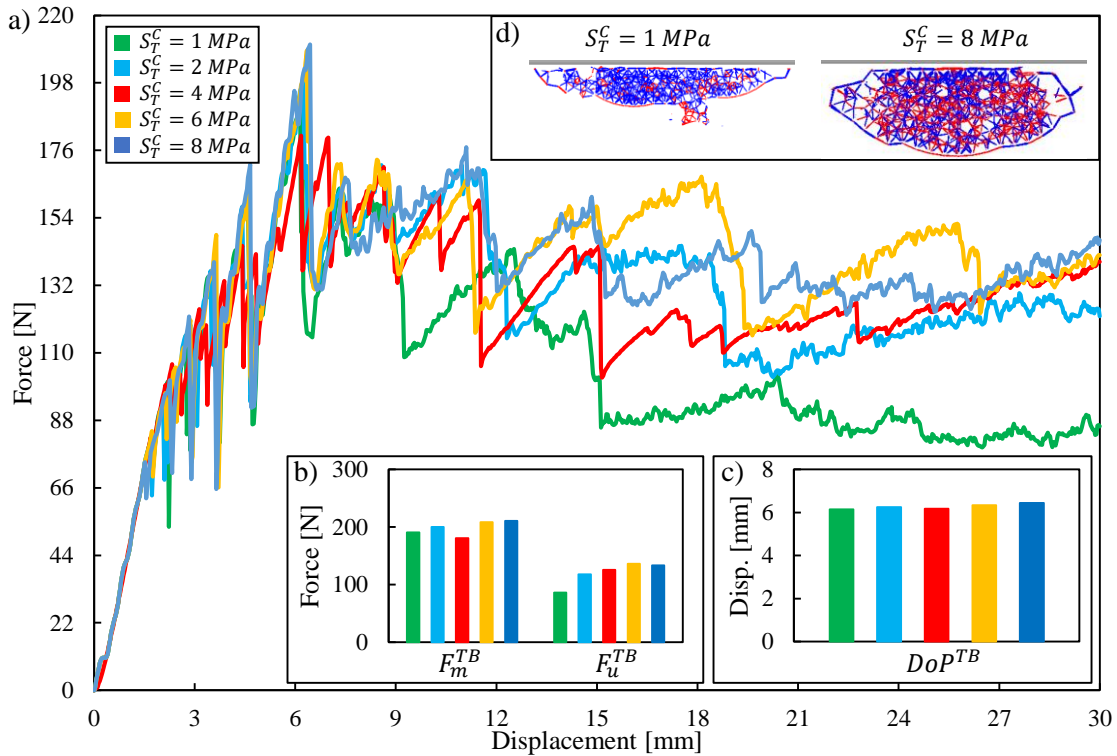


FIGURE 6.16: Influence of the tensile strength of the bonds in the core by three-point bending: a) overall force-displacement characteristic; b) the range of peak and ultimate forces; c) displacement range of the peak force; d) deformation of the bended cross-section at displacement of 27 mm.

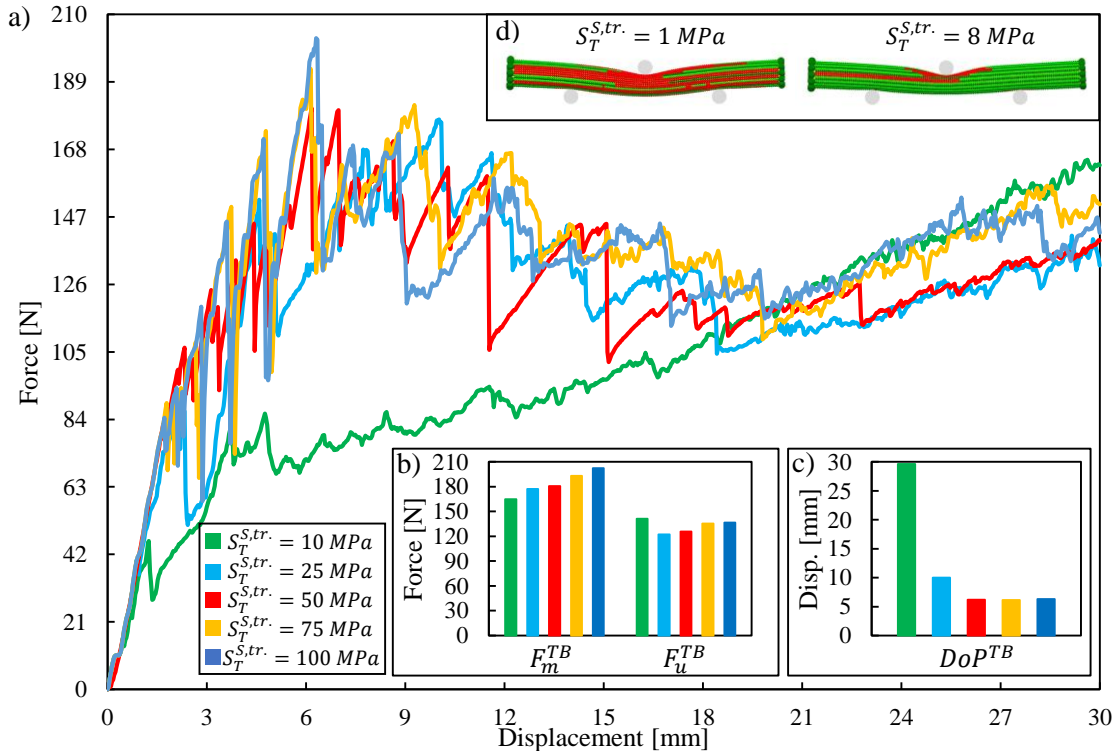


FIGURE 6.17: Influence of the tensile strength of the bonds in transversal direction of the skin by three-point bending: a) overall force-displacement characteristic; b) range of the peak and ultimate forces; c) displacement range of the peak force; d) longitudinal breaks at displacement of 9 mm.

In the case of **dynamic cutting**, the increasing of the tensile strength of the bonds in longitudinal direction of the skin ( $S_T^{S, long.}$ ) led to different force responses (Figure 6.18(a)), where the peak and ultimate forces show a significant increasing by using higher values of the tensile strength (Figure 6.18(b)(c)). Obviously, the higher peak ( $F_m^{DC}$ ) and ultimate ( $F_u^{DC}$ ) forces resulted in higher required cutting work. The length of the compression and final skin cut stages of the cutting process also increased by using higher values of the tensile strength, as shown in Figure 6.18(d). Through the image-based comparison, the lower parameters led to more breaks in longitudinal direction, thus, a large part, that consists of skin and core particles, was broken out from the virtual sample. Contrary to this, the higher tensile strength parameters resulted in more individually ruptured fibres in the skin, as shown in Figure 6.18(e). All the results are presented in Figure C.23 and C.24.

The different tensile strength of the bonds in transversal direction of the skin ( $S_T^{S, tr.}$ ) did not result in any significant changes of the force response and breakage of the virtual samples, as shown in Figure C.25 and C.26.

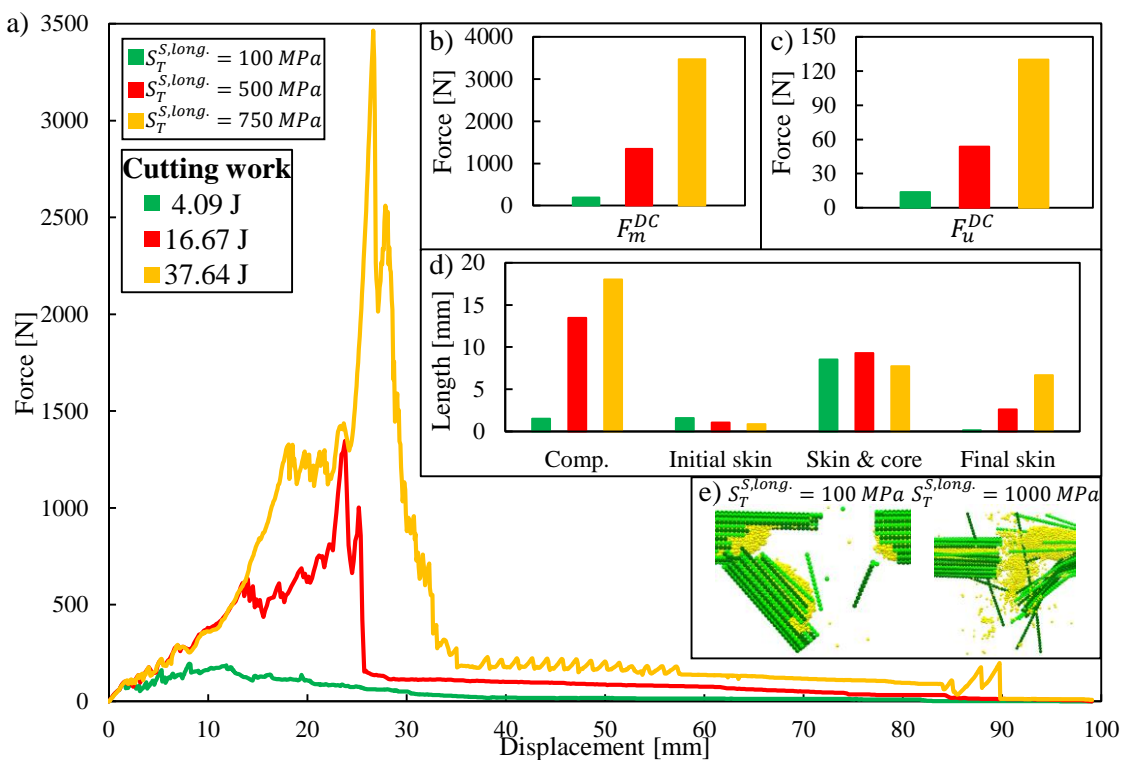


FIGURE 6.18: Influence of the tensile strength of the bonds in longitudinal direction of the skin by dynamic cutting: a) overall force-displacement characteristics; b) range of the peak forces; c) range of the ultimate forces; d) length of the stages of cut; e) resulted cutting surface.

In the case of **ear-detachment**, the tensile strength of the bonds in the shank ( $S_T^{SH}$ ) had a significant influence on the ear-detachment, however, the overall force response showed the same characteristic in each case, as shown in Figure 6.19(a). As the tensile strength decreased, the detachment force decreased as well (Figure 6.19(b)), moreover, it also resulted in slightly lower displacement at detachment (Figure 6.19(c)). The relationship between the detachment force ( $F^D$ ) and the bond tensile strength was described in the range of  $S_T = 20 - 60 \text{ MPa}$  by Equation 6.1:

$$F^D = 0.1042 \cdot S_T^2 + 2.9236 \cdot S_T + 117.43 \quad (R^2 = 0.99) \quad (6.1)$$

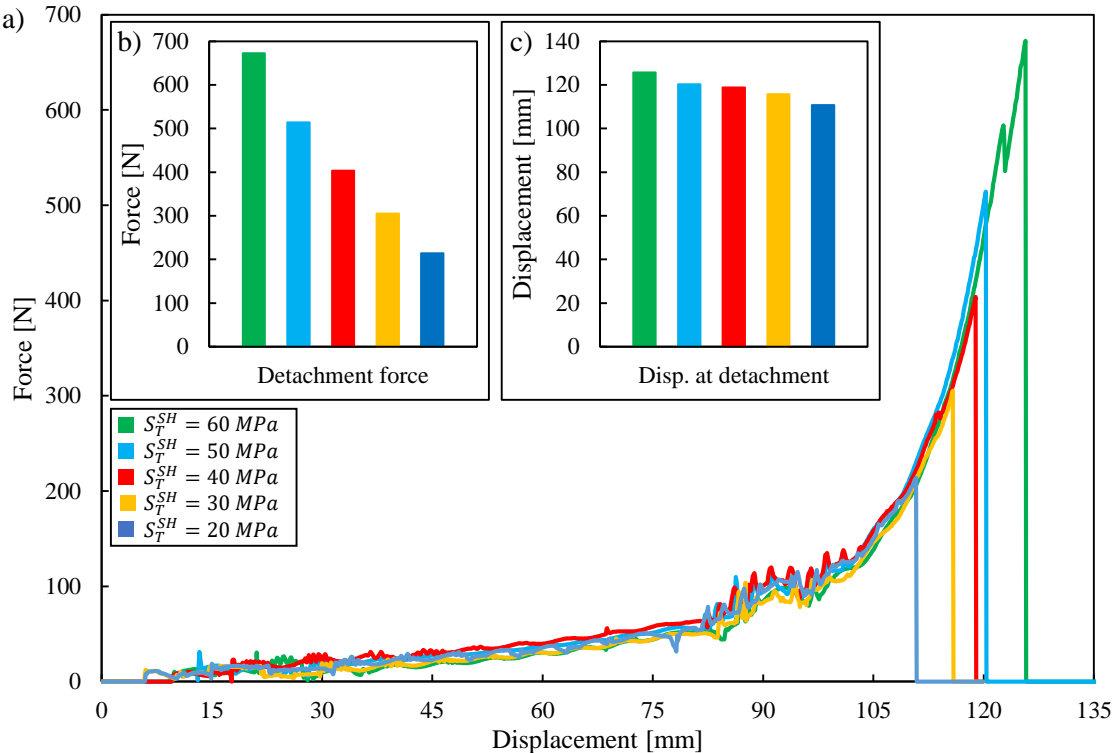


FIGURE 6.19: Influence of the tensile strength of the bonds in the shank by ear-detachment: a) overall force-displacement characteristics; b) range of the detachment forces; c) range of the displacement at detachment.

#### 6.2.4 Shear Strength of The Bonds

In the case of **three-point bending**, the increasing of the shear strength of the bonds in transversal direction of the skin ( $S_S^{S,tr.}$ ) led to different force response characteristics, as shown in Figure 6.20(a). In case of the lowest value of the shear strength, the final increasing of the force response governed the characteristic that resulted in a peak force ( $F_m^{TB}$ ) at the displacement of approx. 26 mm (Figure 6.20(c)). The force decreasing after the peak seems to be less significant in case of the highest shear strength value. The peak ( $F_m^{TB}$ ) and ultimate ( $F_u^{TB}$ ) forces also increased as the shear strength increased, as shown in Figure 6.20(b). Through the image-based comparison, the lower values of the shear strength resulted in an extended damage zone that propagated to the nodal particles. Contrary to this, the majority of the longitudinal breaks were localized around the bending tool in case of the highest shear strength, as shown in Figure 6.20(d). All the results are presented in Figure C.27 and C.28.

In the case of **dynamic cutting**, the increasing of the shear strength of the bonds in longitudinal direction of the skin ( $S_S^{S,long.}$ ) led to slightly higher required cutting work, while, the force response of the samples were quite similar, as shown in Figure 6.21(a). Relationship among the peak ( $F_m^{DC}$ ) and ultimate ( $F_u^{DC}$ ) forces and the increasing shear strength was not observable (Figure 6.21(b)(c)). Significant difference among the length of the stages of the cut was not observed (Figure 6.21(e)). Through the image-based comparison, the higher shear strength led to a more jagged rupture instead of a clean cut, as shown in Figure 6.21(e). All the results are presented in Figure C.29 and C.30.

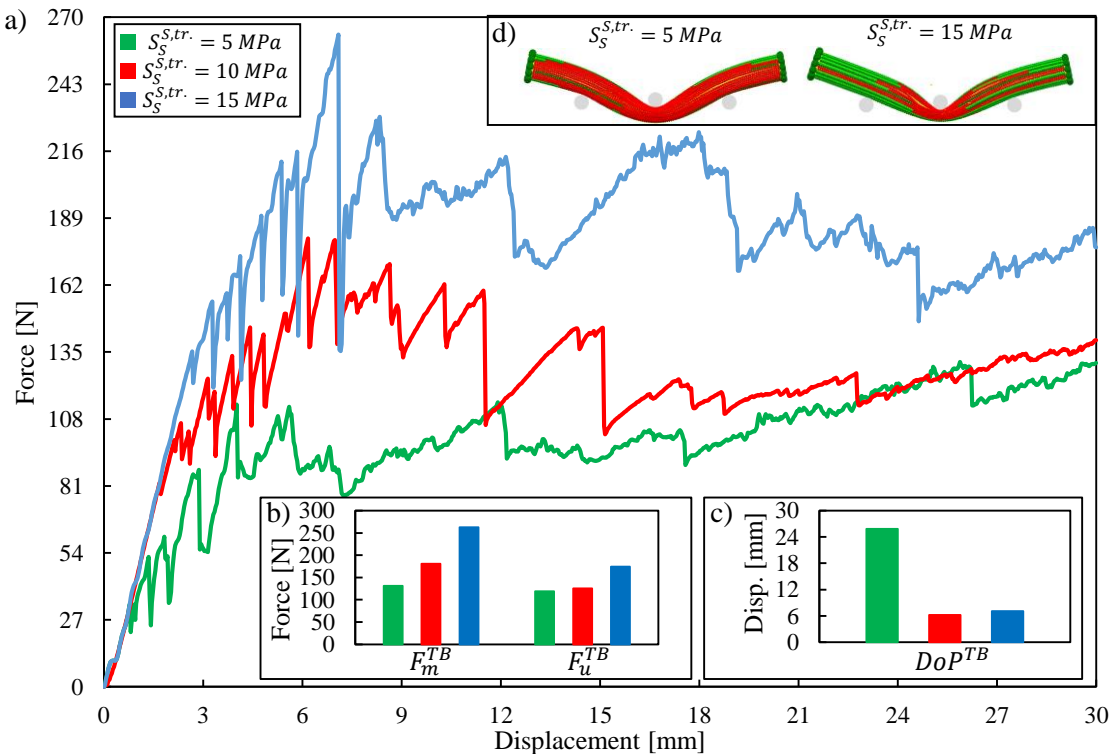


FIGURE 6.20: Influence of the shear strength of the bonds in transversal direction of the skin by three-point bending: a) overall force-displacement characteristic; b) the range of peak and ultimate forces; c) displacement range of the peak force; d) longitudinal crack propagation at displacement of 27 mm.

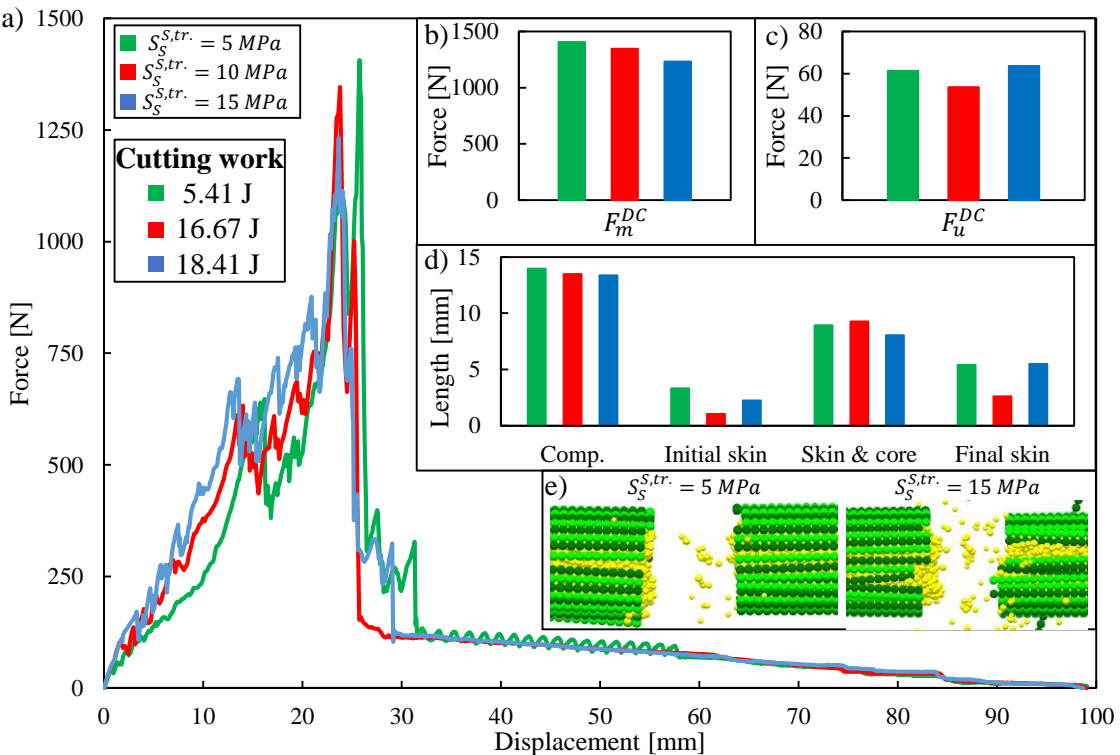


FIGURE 6.21: Influence of the shear strength of the bonds in longitudinal direction of the skin by dynamic cutting: a) overall force-displacement characteristics; b) range of the peak forces; c) range of the ultimate forces; d) length of the stages of cut; e) resulted cutting surface.

### 6.2.5 Coefficient of Variation of The Strength Parameters

In the case of **sectional transversal compression**, the coefficient of variation of the strength parameters ( $\zeta$ ) had a smaller influence on the overall force-compression rate characteristic, as shown in Figure 6.22(a). However, its increasing had a significant effect on the initial breaks of the skin (Figure 6.22(b)), since, the higher values resulted in smoother breaks in transversal direction of the skin at the beginning of the compression. Two significant breaks were observed in the case of coefficient of variation of 0.0 when all the strength parameters were the same, while several smaller breaks appear by using a value of 0.9. Through the image-based comparison, significant differences were not found. All the results are presented in Figure C.31 and C.32.

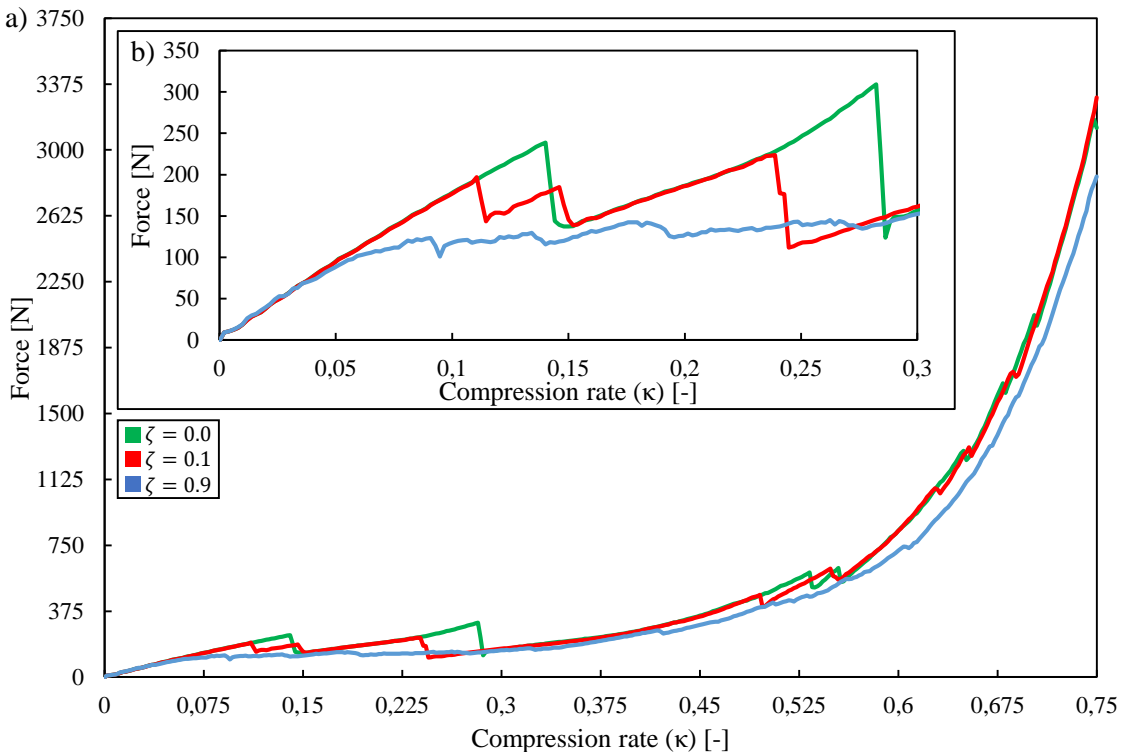


FIGURE 6.22: Influence of the coefficient of variation of the bonded strength parameters by sectional transversal compression: a) overall force-compression rate characteristic; b) force-compression rate characteristics in range of 0-0.3 compression rate.

In the case of **three-point bending**, the increasing of the coefficient of variation of the strength parameters ( $\zeta$ ) resulted in a flatter force-displacement characteristic around the peak force ( $F_m^{TB}$ ), as shown in Figure 6.23(a). In parallel with this, the peak force ( $F_m^{TB}$ ) also decreased while the ultimate force ( $F_u^{TB}$ ) and the displacement of the peak force ( $DoP^{TB}$ ) were not affected (6.23(b)(c)). Through the image-based comparison, the higher values of CoV caused more longitudinal breaks along the internodal section at the beginning of the bending process, however, most of them was evolved between two individual particles, as shown in Figure 6.23(d). All the results are presented in Figure C.33 and C.34.

In the case of **dynamic cutting**, the coefficient of variation of the strength parameters ( $\zeta$ ) had a significant influence on the overall force-displacement characteristic, as shown in Figure 6.24(a). The peak ( $F_m^{DC}$ ) and ultimate ( $F_u^{DC}$ ) forces decreased as the CoV increased (Figure 6.24(b)(c)). The length of the initial compression section decreased, while the length of the skin & core and the final skin cut increased by the increasing of the CoV, as shown in 6.24(d). Through the image-based comparison, the lower CoVs resulted in a more straight cutting surface, while the higher values caused an extensive damage zone around the path of the cutting

blade, as shown in Figure 6.24(e). All the results are presented in Figure C.35 and C.36.

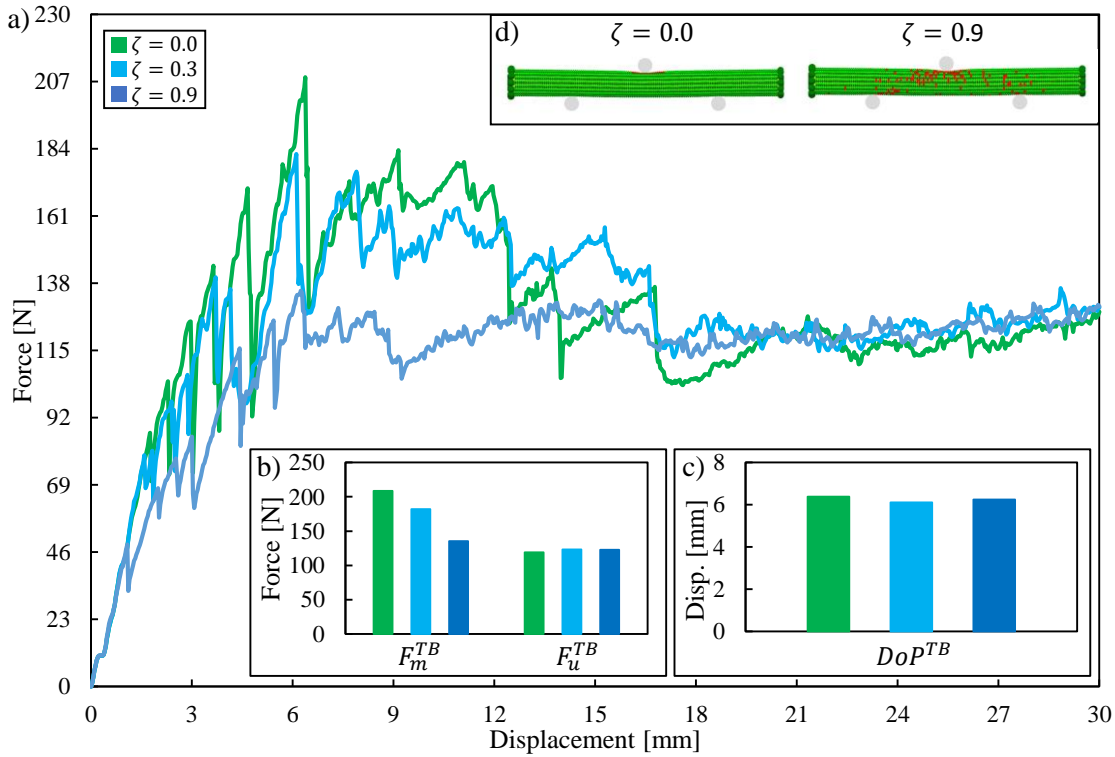


FIGURE 6.23: Influence of the coefficient of variation of the bonded strength parameters by three-point bending: a) overall force-displacement characteristic; b) the range of peak and ultimate forces; c) displacement range of the peak force; d) longitudinal crack propagation at displacement of 3 mm.

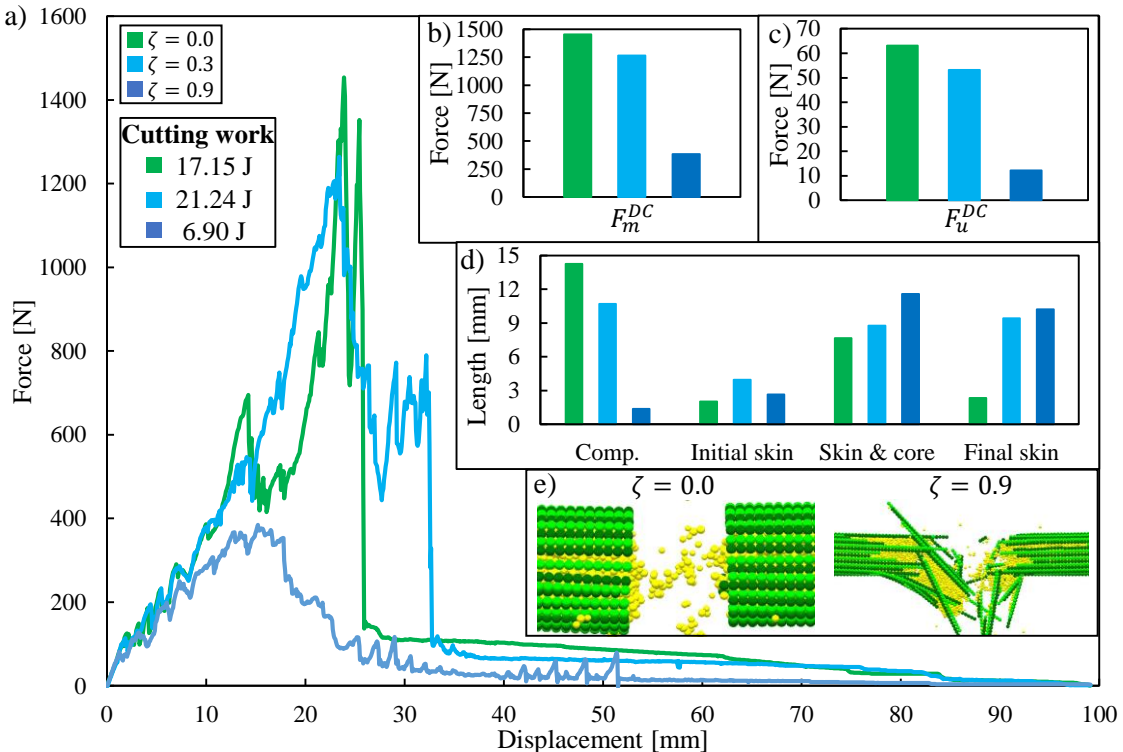


FIGURE 6.24: Influence of the coefficient of variation of the bonded strength parameters by dynamic cutting: a) overall force-displacement characteristics; b) range of the peak forces; c) range of the ultimate forces; d) length of the stages of cut; e) resulted cutting surface.

## 6.3 Influence of Non-Bonded Contact Parameters

### 6.3.1 Particle Young's modulus

In the case of the **sectional transversal compression** simulation, the increasing of the particle Young's modulus ( $E_B$ ) had a significant effect on the exponential increasing section of the force-compression rate characteristic, as shown in Figure 6.25(a). At the beginning of the compression process, the stiffness and breakage of the sample were not affected by the particle Young's modulus, as shown in Figure 6.25(b)(c). Above 0.375 compression rate, the higher values resulted in a sharper increasing of the force response, thus, the resistance force at 0.75 compression rate increased from 2689 N to 4139 N. Through the image-based comparison, significant differences were not observed. All the results are presented in Figure D.1 and D.2.

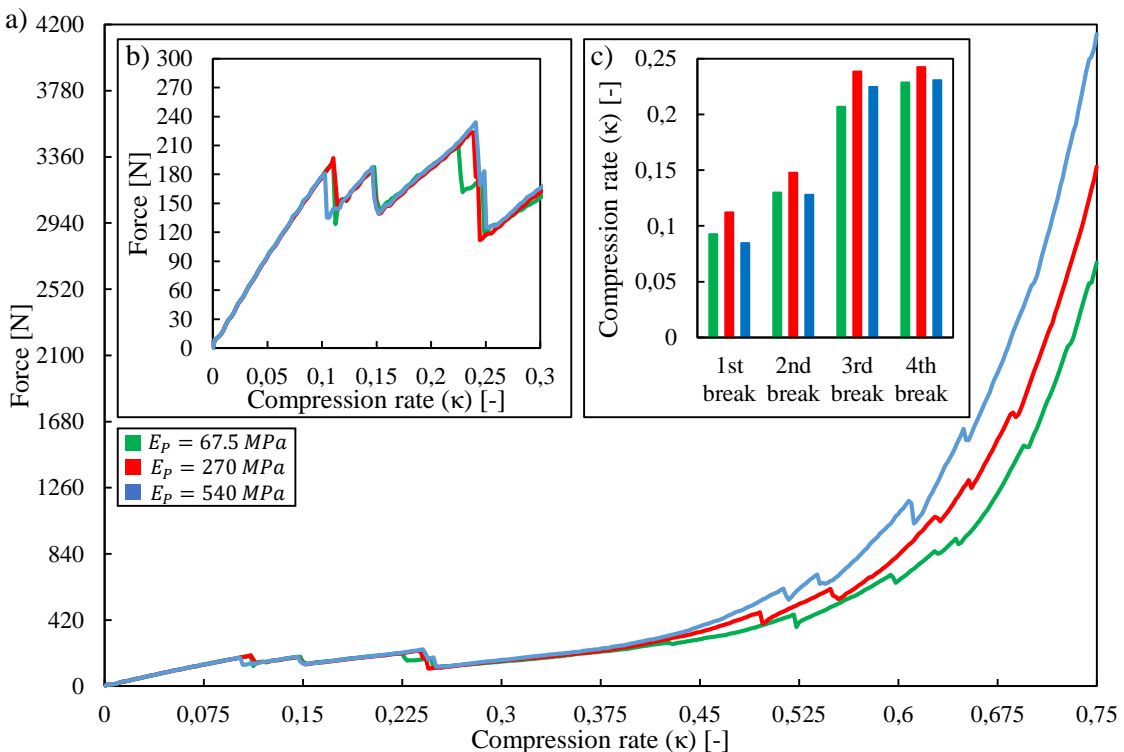


FIGURE 6.25: Influence of the particle Young's modulus by sectional transversal compression: a) overall force-compression rate characteristic; b) force-compression rate characteristics in range of 0-0.3 compression rate; c) major break events in tangential direction of the skin.

### 6.3.2 Particle-Particle Coefficient of Static Friction

The influence of the coefficient of static friction among the particles was analysed by the **sectional transversal compression** simulation. The increasing of the particle-particle coefficient of static friction ( $\theta_{P-P}$ ) had a significant effect on the exponential increasing phase of the force-compression rate characteristic, as shown in Figure 6.26(a). At the beginning of the compression process, the stiffness and breakage of the sample were not affected by the particle-particle coefficient of static friction, as shown in Figure 6.26(b)(c). Above 0.3 compression rate, the higher values resulted in a sharper increasing of the force response, thus, the resistance force at 0.75 compression rate increased from 2127 N to 7199 N. However, significant difference between the characteristics resulted by the values of 0.7 and 0.9 could not be observed. Through the image-based comparison, significant differences were not observed. All the results are presented in Figure D.3 and D.4.

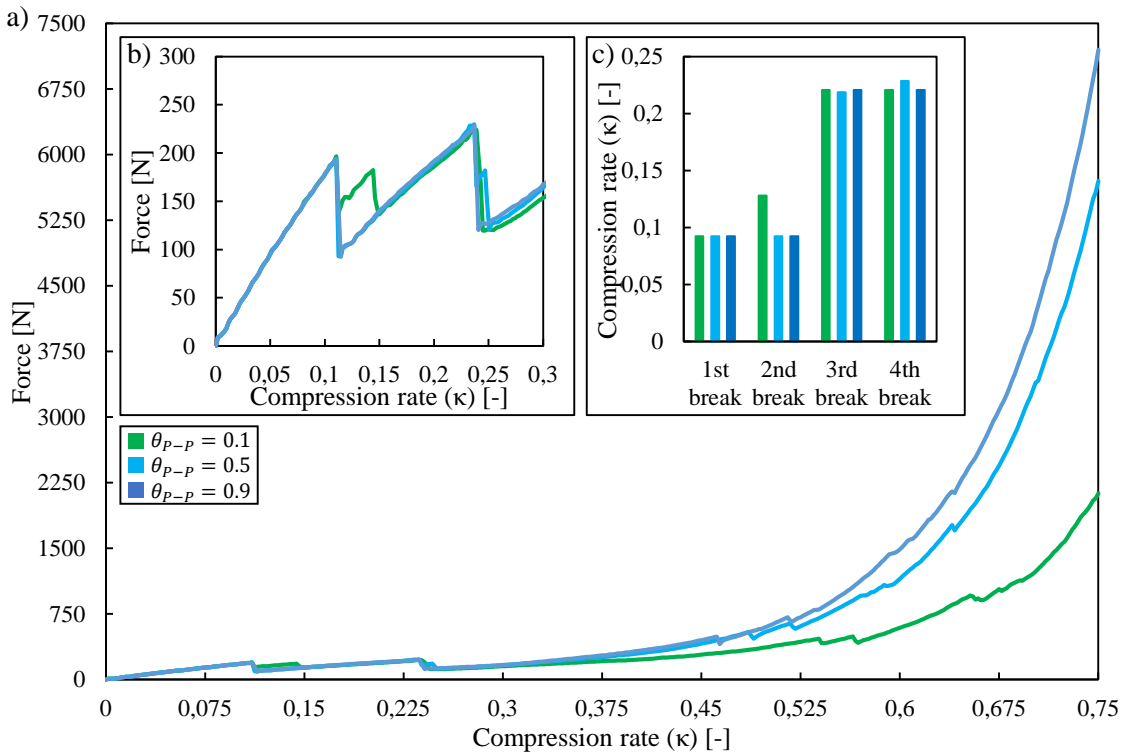


FIGURE 6.26: Influence of the particle-particle coefficient of static friction by sectional transversal compression: a) overall force-compression rate characteristics; b) force-compression rate characteristics in range of 0-0.3 compression rate; c) major break events in tangential direction of the skin.

### 6.3.3 Particle-Geometry Coefficient of Static Friction

In the case of **three-point bending**, the coefficient of static friction among the particles and geometry elements ( $\theta_{P-G}$ ) had a significant influence on the sliding section of the force-displacement characteristic, as shown in Figure 6.27(a). As the value of the static friction increased, the ultimate force ( $F_u^{TB}$ ) also increased while the peak force ( $F_m^{TB}$ ) and its displacement ( $DoP^{TB}$ ) were not affected (Figure 6.27(b)(c)). Through the image-based comparison, significant differences were not observed. All the results are presented in Figure D.5 and D.6.

In the case of **dynamic cutting**, the coefficient of static friction among the particles and geometry elements ( $\theta_{P-G}$ ) had also a significant influence on the sliding section of the force-displacement characteristic, as shown in Figure 6.28(b). As the value of the static friction increased, the ultimate force also increased (Figure 6.28(c)) while the peak force ( $F_m^{DC}$ ) and the length of cutting stages were not affected (Figure 6.28(b)(d)). Due to the higher ultimate forces ( $F_u^{DC}$ ), the resulted cutting energy also slightly increased from 13.41 J to 16.67 J. Significant differences during the image-based comparison could not be observed, however, the resulted cutting surface is clearer in case of the higher parameters, as shown in Figure 6.28(e). All the results are presented in Figure D.7 and D.8.

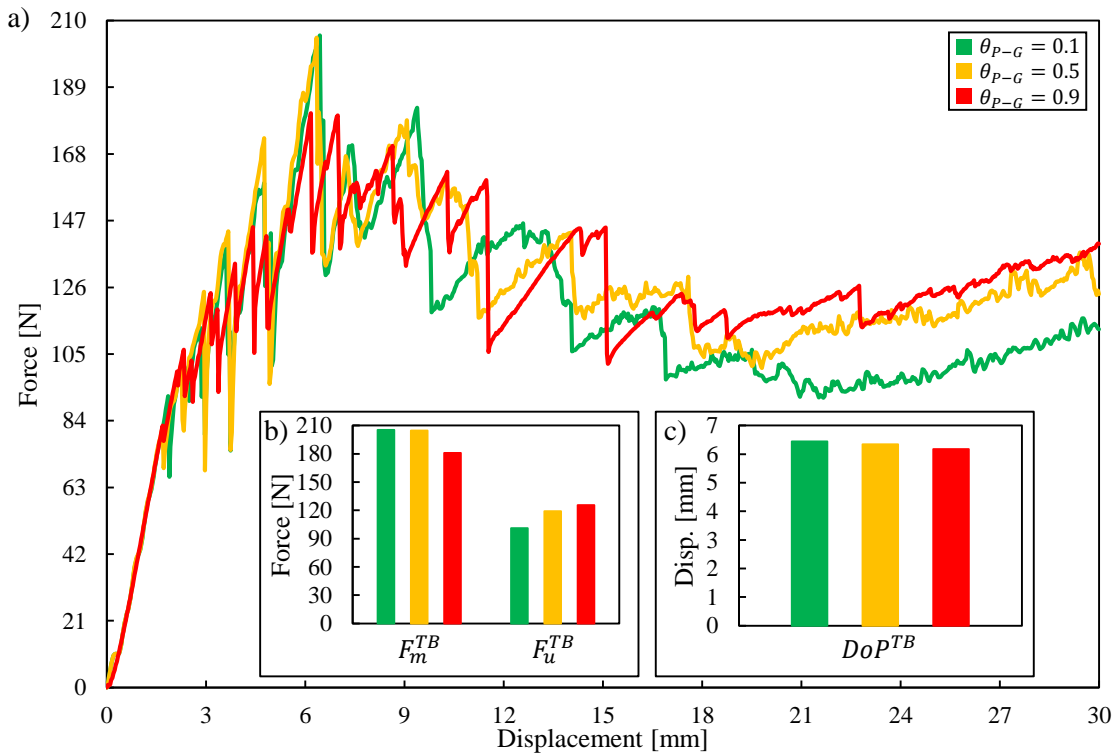


FIGURE 6.27: Influence of the particle-geometry coefficient of static friction by three-point bending:  
a) overall force-displacement characteristic; b) the range of peak and ultimate forces; c) displacement range of the peak force.

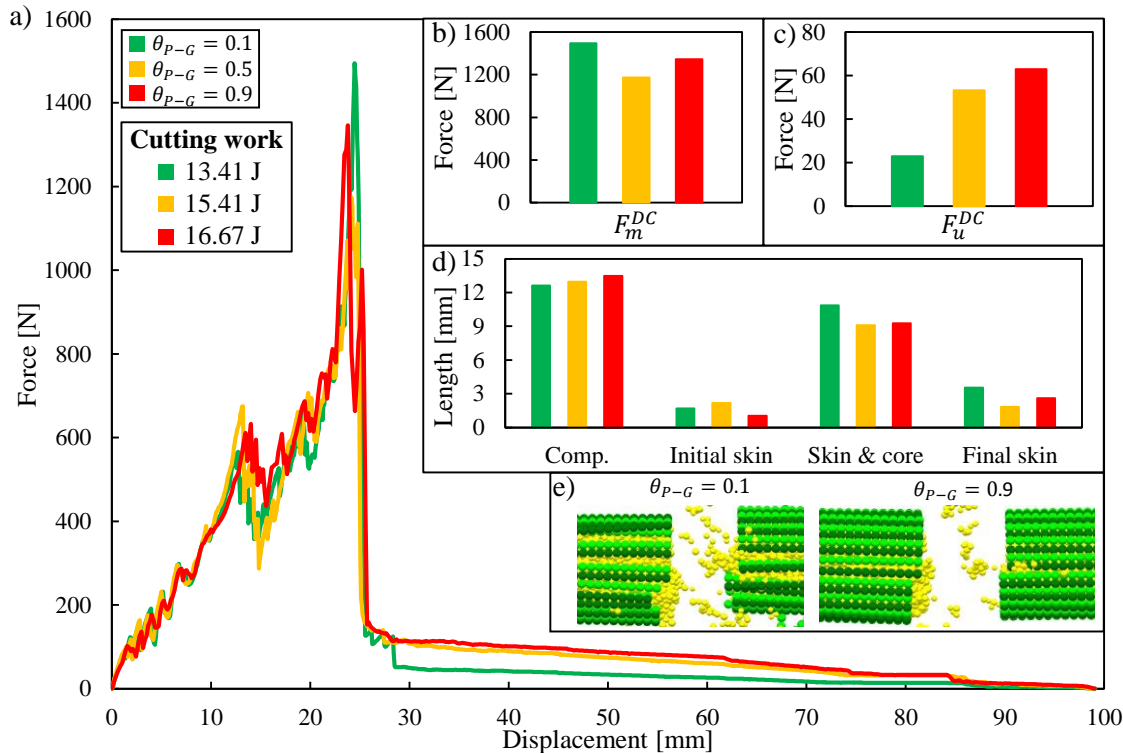


FIGURE 6.28: Influence of the particle-geometry coefficient of static friction by dynamic cutting:  
a) overall force-displacement characteristics; b) range of the peak forces; c) range of the ultimate forces;  
d) length of the stages of cut; e) resulted cutting surface.

### 6.3.4 Particle-Geometry Coefficient of Restitution

By the analysis of the coefficient of restitution among the particles and geometry ( $e_{P-G}$ ) elements in the range of 0.2-1.0, significant influence on the force response, number of broken bonds and breakage of the virtual samples were not found in case of the **dynamic cutting** simulation, as shown in Figure D.9, D.10).

In the case of **ear-collision**, the coefficient of restitution ( $e_{P-G}^{ME}$ ) had a significant influence on the collision between the maize ear and the sheets, as shown in Figure 6.29. The higher coefficient of restitution led to higher bounce heights in case of the steel and the plastic sheet as well. The relationship between the bounce height ( $H$ ) and the coefficient of restitution ( $e_{P-G}^{ME}$ ) was described by Equation 6.2 and 6.3 for steel and plastic sheet respectively:

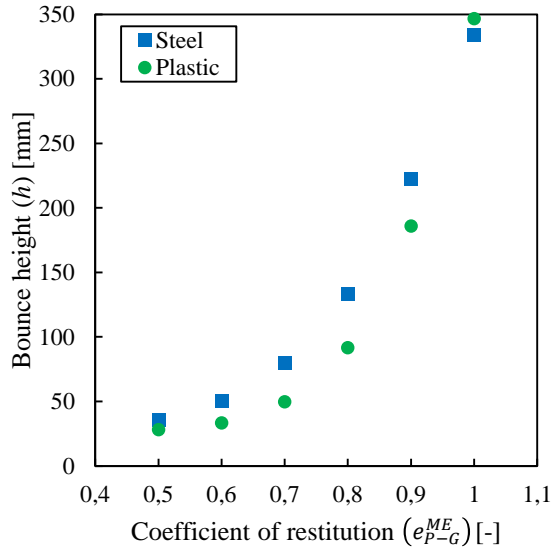


FIGURE 6.29: Influence of the coefficient of restitution among the maize ear and the geometry elements by ear-collision.

$$H^{Steel} = 1284.1 \cdot (e_{P-G}^{ME})^2 - 1336.5 \cdot (e_{P-G}^{ME}) + 385.14 \quad (R^2 = 0.99) \quad (6.2)$$

$$H^{Plastic} = 3303.5 \cdot (e_{P-G}^{ME})^3 - 5489 \cdot (e_{P-G}^{ME})^2 + 3090 \cdot (e_{P-G}^{ME}) - 557.66 \quad (R^2 = 1.0) \quad (6.3)$$

## 6.4 Influence of Bond Fabric Parameters

### 6.4.1 Contact Radius Multiplier

In the case of **sectional transversal compression**, the contact radius multiplier ( $\eta$ ) had a significant effect on the force response during the exponential increasing section, as shown in Figure 6.30(a). As the contact radius multiplier decreased, the drop after the breakage of the skin increased. Moreover, the increasing section started at higher compression rate, however, it increased sharper over 0.6 compression rate and resulted in slightly higher maximal compressive force at 0.75 compression rate. The breakage of the skin was not affected significantly, however, the stiffness of the sample slightly increased as the contact radius multiplier increased, as shown in Figure 6.30(b). Furthermore, the average number of bonds per particle linearly increased as the contact radius multiplier increased (Figure 6.30(c)). The relationship between the average number of bonds per particle ( $N_B^0$ ) and the contact radius multiplier was described by Equation 6.4.

$$N_B^0 = 12.16 \cdot \eta - 9 \quad (R^2 = 0.99) \quad (6.4)$$

Significant differences during the image-based comparison could not be observed, however, less remaining bond was observed between the core and the skin, as shown in Figure 6.30(d). All the results are presented in Figure D.11 and D.12.

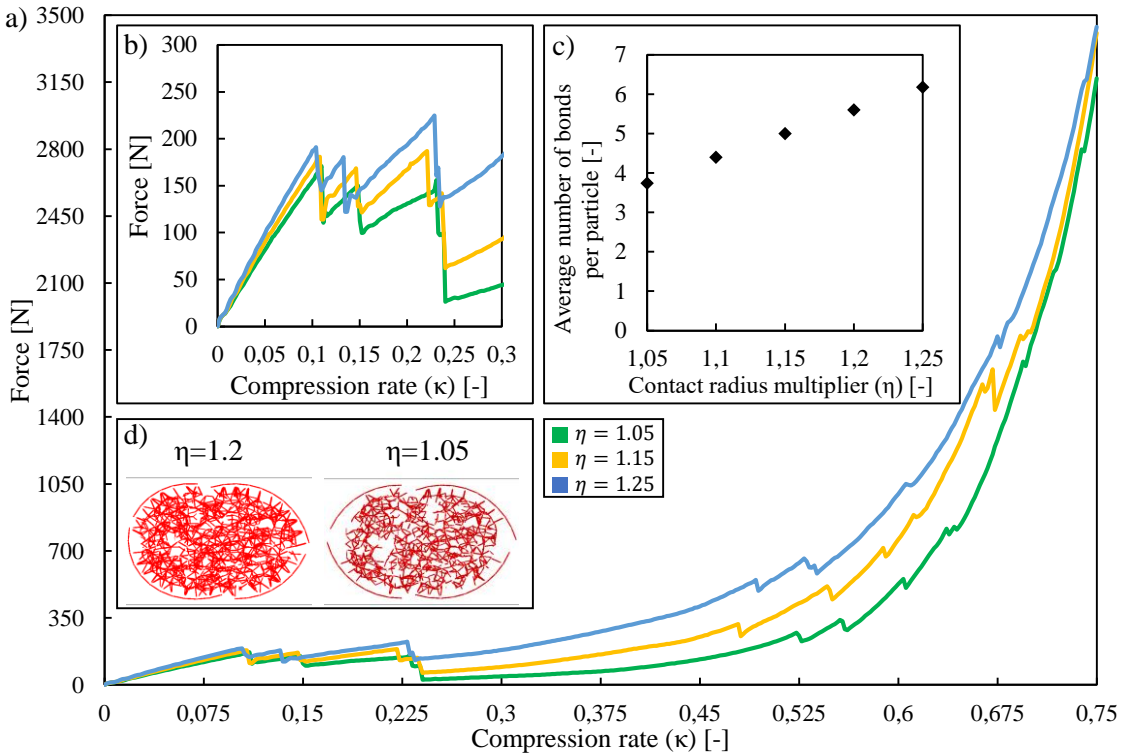


FIGURE 6.30: Influence of the contact radius multiplier by sectional transversal compression: a) overall force-compression rate characteristic; b) force-compression rate characteristics in range of 0-0.3 compression rate; c) average number of bonds per particle; d) bonded structure of samples after the fourth break of the skin.

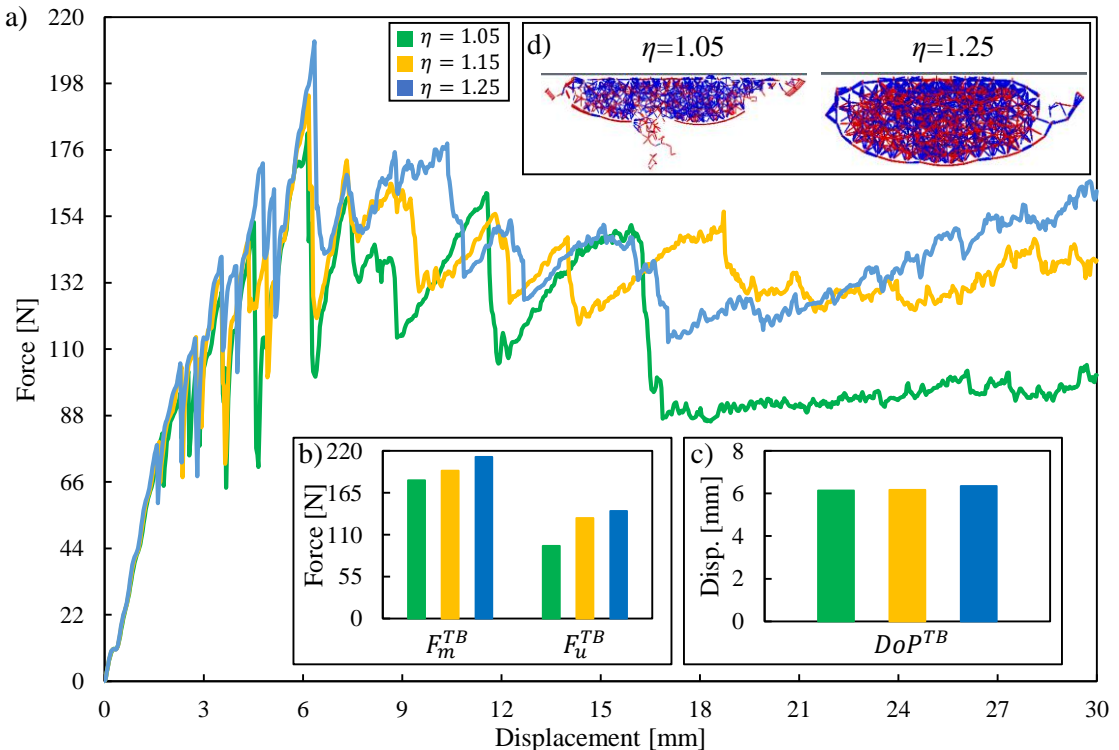


FIGURE 6.31: Influence of the contact radius multiplier by three-point bending: a) overall force-displacement characteristic; b) the range of peak and ultimate forces; c) displacement range of the peak force; d) shape of the bended cross section at displacement of 27 mm.

In the case of **three-point bending**, the contact radius multiplier ( $\eta$ ) had a significant effect on force response after the structural collapse (over 15 mm displacement), as shown in Figure 6.31(a). As the contact radius multiplier increased, the peak ( $F_m^{TB}$ ) and ultimate ( $F_u^{TB}$ ) forces also increased (Figure 6.31(b)), while the displacement of the peak force ( $D_oP^{TB}$ ) was not affected (Figure 6.31(c)). Through the image-based comparison, more flat bended cross-section and more damaged skin structure were observed by the decreasing of the contact radius multiplier, as shown in Figure 6.31(d). All the results are presented in Figure D.13 and D.14.

#### 6.4.2 Bond Radius Multiplier

In the case of **sectional transversal compression**, the bond radius multiplier ( $\Lambda$ ) had a significant effect on the overall force response, as shown in Figure 6.32(a). The decreasing bond radius multiplier resulted in a softer material (Figure 6.32(b)), thus, the breakage of the bonds took place in the skin at higher displacement by using the same strength parameters, as shown in Figure 6.32(c). Furthermore, the lower values resulted in a more ovalised shape before the first break of the skin, as shown in Figure 6.32(d). All the results are presented in Figure D.15 and D.16.

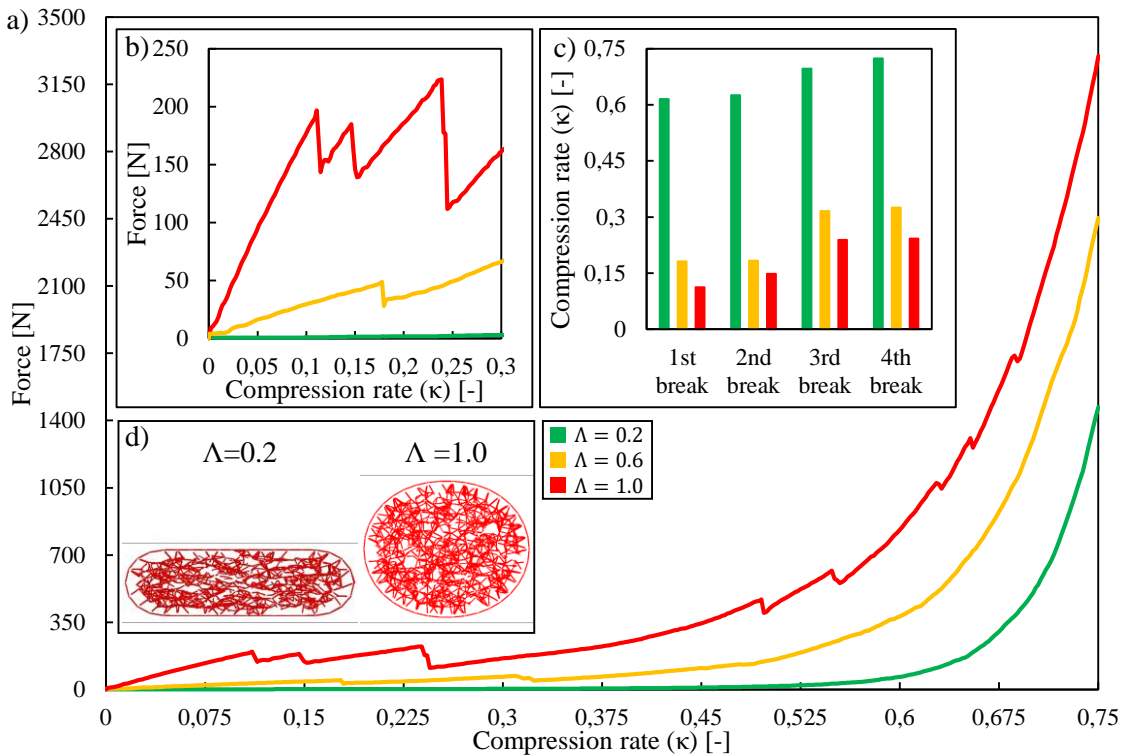


FIGURE 6.32: Influence of the bond radius multiplier by sectional transversal compression: a) overall force-compression rate characteristic; b) force-compression rate characteristics in range of 0-0.3 compression rate; c) breakage of the skin; d) ovalised shape.

In the case of **three-point bending**, the bond radius multiplier ( $\Lambda$ ) also had a significant effect on the overall force response, as shown in Figure 6.33(a). The decreasing bond radius multiplier resulted in a softer material, thus, the peak ( $F_m^{TB}$ ) and ultimate ( $F_u^{TB}$ ) forces increased by using higher multipliers, as shown in Figure 6.33(b). The lower values resulted in a smaller differences between the peak and ultimate forces, moreover, the zone of the peak force has totally disappeared in case of the bond radius multiplier of 0.4, as shown in Figure 6.33(a)(c). In case of the softer materials, the longitudinal crack propagation was less extended along the

internodal section, while the bended cross-section opened up on the side of the bending tool, as shown in Figure 6.33(d). All the results are presented in Figure D.17 and D.18.

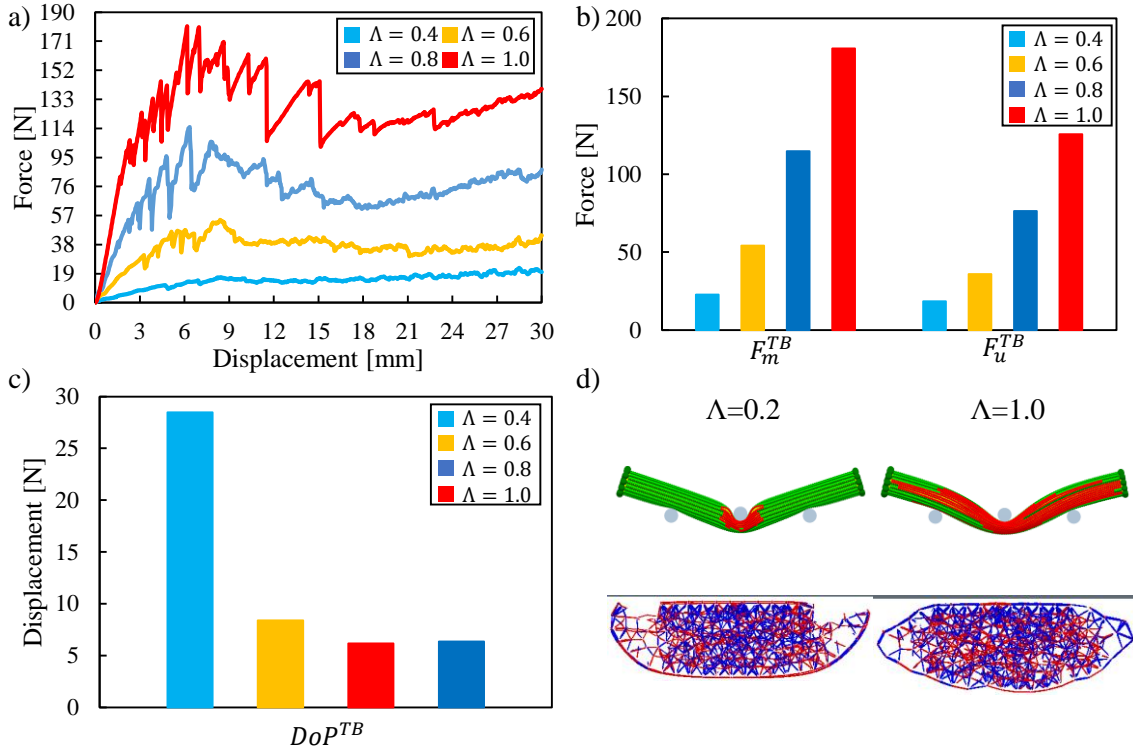


FIGURE 6.33: Influence of the bond radius multiplier by three-point bending: a) overall force-displacement characteristic; b) the range of peak and ultimate forces; c) displacement range of the peak force; d) shape of the bended cross section at displacement of 27 mm.

## 6.5 Influence of Numerical Parameters

### 6.5.1 Time Step

In the case of **sectional transversal compression**, only the highest time step ( $\Delta t = 32e - 8 \text{ s}$ ) resulted in a different overall force response, as shown in Figure 6.34(a). In this case, the exponential increasing section showed higher force response between 0.25 and 0.55 compression rate. Afterwards, the increasing of the force response was moderate. The initial stiffness and the breakage of the samples were not affected by the time step ( $\Delta t$ ), as shown in Figure 6.34(b)(c). At the end of the compression, almost all of the tangential bonds of the skin were broken, moreover, less remaining bonds could be observed in the core as well, as shown in Figure 6.34(d). All the results are presented in Figure D.19 and D.20.

In the case of **dynamic cutting**, the highest time step ( $\Delta t = 32e - 8 \text{ s}$ ) also resulted in a different force response, as shown in Figure 6.35(a). In this case, the peak force ( $F_m^{DC}$ ), the ultimate force ( $F_u^{DC}$ ) and the cutting work were also higher than in the other cases (Figure 6.35(b)(c)), however, the length of the stages of the cut were not affected by the time step (Figure 6.35(d)). In the case of the time step of  $32e - 8 \text{ s}$ , some particles from the free end of the already cut longitudinal fibres penetrated through the geometry of the cutting blade (Figure 6.35(e)), thus, it tore a large part of the skin out. All the results are presented in Figure D.21 and D.22.

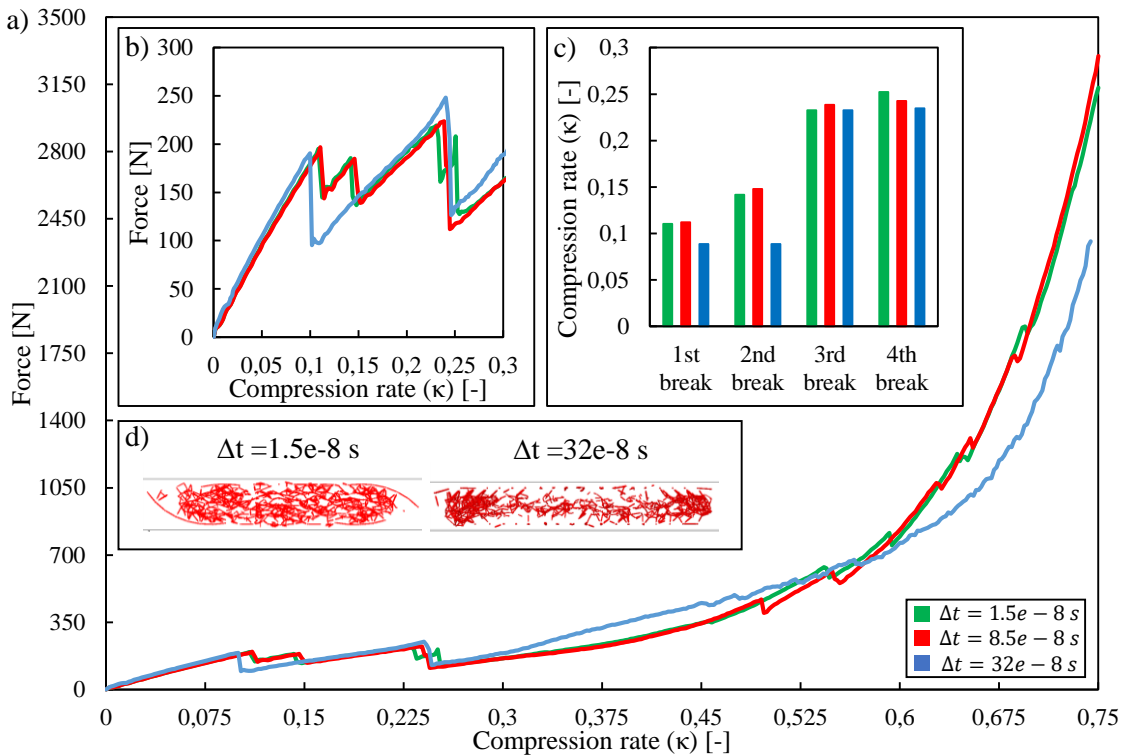


FIGURE 6.34: Influence of the time step by sectional transversal compression: a) overall force-compression rate characteristic; b) force-compression rate characteristics in range of 0-0.3 compression rate; c) breakage of the skin; d) compressed shape.

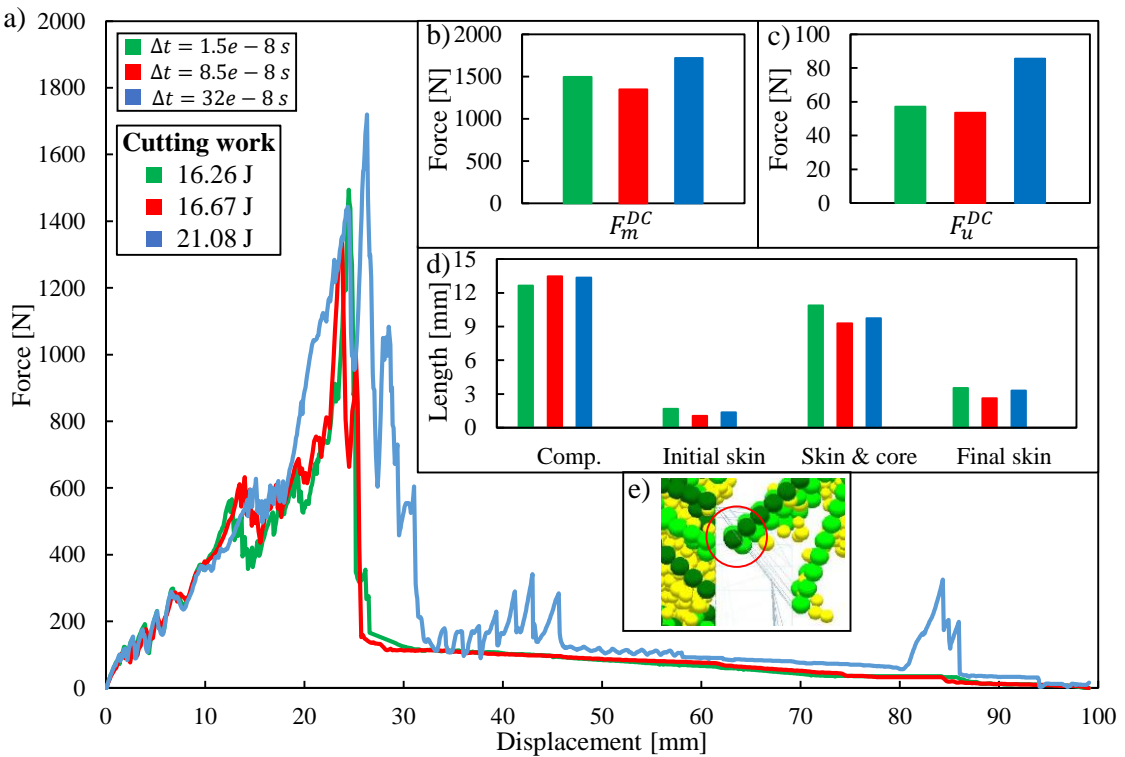


FIGURE 6.35: Influence of the time step by dynamic cutting: a) overall force-displacement characteristics; b) range of the peak forces; c) range of the ultimate forces; d) length of the stages of cut; e) particle penetration (the penetrated particles are marked by red circle).

### 6.5.2 Global Damping

By the analysis of the global damping ( $\iota$ ) in the range of 0.1-0.9, significant influence on the force response, number of broken bonds and breakage of the virtual samples were not found in case of the **sectional transversal compression**, as shown in Figure D.23, D.24).

In the case of **dynamic cutting**, the global damping ( $\iota$ ) of 0.9 resulted in a different force response, however, significant difference were not found among the rest of the results, as shown in Figure 6.36(a). The calculated force response characteristic, peak force ( $F_m^{DC}$ ), ultimate force ( $F_u^{DC}$ ) and cutting work were higher in case of global damping of 0.9 (Figure 6.36(b)(c)), however, only the length of the final skin cut was significantly longer than the others (see Figure 6.36(d)). Through the image-based analysis, significant differences were not found. All the results are presented in Figure D.25 and D.26.

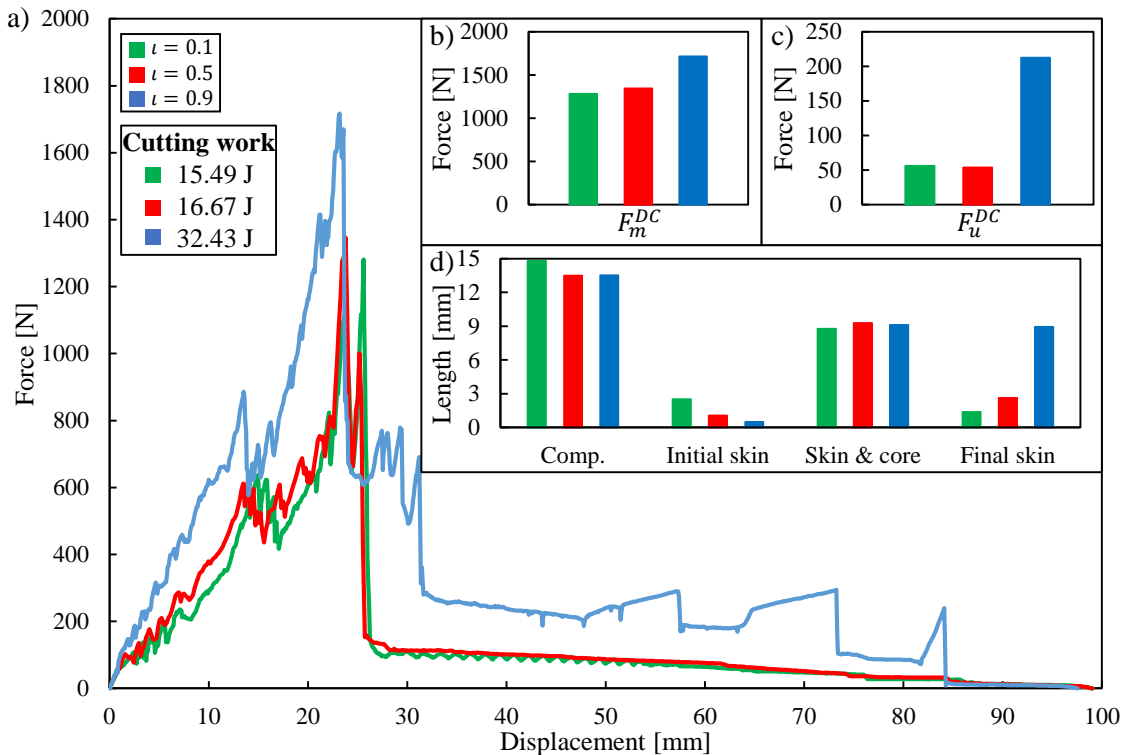


FIGURE 6.36: Influence of the global damping by dynamic cutting: a) overall force-displacement characteristics; b) range of the peak forces; c) range of the ultimate forces; d) length of the stages of cut.

## 6.6 Conclusions

During five simulations on each reference model, the reliability of the model was justified because there were no significant differences among the force response and breakage of the reference models despite of the applied coefficient of variation of 0.1. Moreover, the loading direction and loading position do not have a significant influence on the results. Thus, the model is suitable for further analysis, moreover, it provides the same response regardless the loading direction or position which is crucial during the technological simulations.

Due to the complexity of the model there are many parameters that could have an effect on its mechanical behaviour and breakage. During the parametric study, the parameters that have the most significant effect were determined for each simulation case. Generally, these parameters are the followings:

- the bond Young's modulus ( $E_B$ );
- the bond mean tensile strength ( $S_T$ );
- the bond mean shear strength ( $S_S$ );
- the coefficient of variation of the mean strength parameters ( $\zeta$ );
- the bond radius multiplier ( $\Lambda$ );
- the particle Young's modulus ( $E_P$ );
- the particle-particle coefficient of static friction ( $\mu_{P-P}$ );
- the particle-geometry coefficient of restitution of the maize ear ( $e_{P-G}^{ME}$ );
- the particle contact radius multiplier ( $\eta$ ).

Contrary to this, some of the analysed parameters have no influence or only its excessive value has an influence on the mechanical behaviour and breakage of the virtual samples. These parameters are the followings:

- the bond Poisson's ratio ( $\nu_B$ );
- particle-geometry coefficient of restitution of the internodal stalk section ( $e_{P-G}$ );
- time step ( $\Delta t$ );
- global damping ( $\iota$ ).

In the bonded model, the Poisson's ratio ( $\nu_B$ ) describes the relationship between the Young's modulus ( $E_B$ ) and the shear modulus ( $G_B$ ) of the virtual beam among the particles (Brown, Chen, and Ooi, 2014). Accordingly, the shear deformation of the bonds is negligible because the Poisson's ratio ( $\nu_B$ ) does not affect the behaviour of the model.

The particle-geometry coefficient of restitution ( $e_{P-G}$ ) describes the ratio of the final to initial relative velocity of the particles after their collision with a geometry element. According to the results, collisions among the particles and geometry elements of the cutting blade during dynamic cutting has a negligible effect on the cutting process.

As it was expected, the well-chosen set of numerical parameters results in stable solutions, thus, only the highest time step ( $\Delta t = 32e - 8 \text{ s}$ ) and global damping ( $\iota = 0.9$ ) resulted in different solutions. Obviously, the model was unstable in both cases. Consequently, it is suggested that a safety factor of 0.1 or less for the time step and a global damping of 0.5 should be used for the rest of the current study.

The effect of each parameter on the response of the virtual specimen during **sectional transversal compression** simulation is shown in Table 6.1. The increasing of the Young's modulus of the bonds ( $E_b$ ) in tangential direction of the skin leads to an increase of the initial transversal stiffness of the internodal stalk section. The increasing of the Young's modulus ( $E_b$ ), the mean tensile strength ( $S_T$ ) or the contact radius multiplier ( $\lambda$ ) of the bonds in the core causes strong increase in the stiffness of the internodal stalk section at larger compression rate, where the skin is no longer carrying the applied load. In this region of compression rate many of the bonds are broken, so the non-linear increase also arise from the non-linear Hertz-Mindlin contact among the un-bonded particles, thus, the particle Young's modulus ( $E_P$ ) and the particle-particle coefficient of static friction ( $\mu_{P-P}$ ) have a significant influence during this section.

The higher values of the mean tensile strength of the bonds ( $S_T$ ) in tangential direction of the skin causes that the breakage takes place at higher compression rate, while, the increasing of its coefficient of variation ( $\zeta_T$ ) results in a smoother breakage. The increasing ratio between the Young's modulus of the bonds ( $E_b$ ) in tangential direction of the skin and in the core results in a more significant drop at the characteristic after the breakage of the skin. Hence, a ratio of 300 is suggested to use, that results in a drop at the characteristic that was experienced during the measurements.

The breakage of the skin is mainly related to the mean tensile strength of the bonds ( $S_T$ ) between the skin and the core: when the mean tensile strength ( $S_T$ ) is too high, the phenomenon of the skin breakage does not take place, because the skin cannot detach from the core.

TABLE 6.1: Summary of the influence of the parameters on the mechanical behaviour and breakage of the virtual samples during sectional transversal compression.

Input parameter	Initial stiffness	Skin breakage	Core breakage	Exponential increasing	Ultimate force
$E_B$	↑	↑	×	↑	↑
$\phi_{E_B}^{S,C}$	↑	↑	×	↑	↑
$S_T^{S,tr.}$	×	↓	×	×	×
$S_T^C$	×	×	↓	↑	↑
$\zeta$	×	↑	×	×	×
$E_P$	×	×	×	↑	↑
$\theta_{P-P}$	×	×	×	↑	↑
$\Lambda$	↑	×	↑	↑	×
$\eta$	↑	↑	↑	↑	↑

Where ↑, ↓, ↔ and × indicates an increase, decrease, influence and no influence, respectively.

The effect of each parameter on the response of the **three-point bending** simulation is shown in Table 6.2. The increasing of the Young's modulus of the bonds ( $E_b$ ) in longitudinal direction of the skin results in the increasing of the initial stiffness of the internodal stalk section, while it also causes higher peak and ultimate forces at lower displacement. The mean tensile strength of the bonds ( $S_T$ ) between the skin and the core has a significant influence on the buckling effect under the bending tool, thus, the ultimate force also increases. The peak force also increases with the increasing of the mean tensile strength ( $S_T$ ) of the bonds in tangential direction of the skin. Increasing of the mean shear strength ( $S_S$ ) of the skin in its tangential direction causes longer initial elastic section on the curve, thus, higher peak and ultimate forces. Contrary to this, the peak force zone decreases while the coefficient of variation is increasing, moreover, it disappeared at the highest value of CoV. Increasing of the particle-geometry coefficient of static friction ( $\mu_{P-G}$ ) also results in a higher ultimate force.

TABLE 6.2: Summary of the influence of the parameters on the mechanical behaviour and breakage of the virtual samples during three-point bending simulation.

Input parameter	Initial stiffness	Peak force	Displacement of peak force	Ultimate force	Longitudinal breaks	Breakage of the cross-section
$E_B^{S,long.}$	↑	↑	↓	↑	↑	×
$S_T^C$	×	×	×	↑	×	↔
$S_T^{S,tr.}$	×	↑	×	×	↓	×
$S_S^{S,tr.}$	×	↑	×	↑	↓	×
$\zeta$	×	↓	×	×	↔	×
$\theta_{P-G}$	×	×	×	↑	×	×
$\Lambda$	×	↑	×	↑	×	↔
$\eta$	↑	↑	×	↑	↑	↔

Where ↑, ↓, ↔ and × indicates an increase, decrease, influence and no influence, respectively.

The length of the longitudinal breaks among the fibres in the skin is shorter if the the mean shear and tensile strength of the skin are higher or the bond radius multiplier or the bond Young's modulus is lower that results in a softer material. In the case of higher coefficient

of variation, the characteristic of the longitudinal break propagation is different because of the randomly appeared local breakage zones along the internodal section. The bended cross-section is more cohesive when the mean tensile strength or the contact radius multiplier of the core is higher.

In the case of **dynamic cutting**, the bonded parameters of the skin in longitudinal direction have a significant influence, as shown in Table 6.3. By increasing the Young's modulus ( $E_b$ ) in the longitudinal direction of the skin, the additional bending effect at the beginning of the cutting process is decreasing, thus, the initial cutting of the skin takes place earlier because of the earlier rupture of the fibres. The increasing of the mean tensile strength ( $S_T$ ) of the skin in longitudinal direction results in increasing required cutting work, but also a more jagged final cut surface because some of the fibres of the skin do not rupture in the path of the cutting blade. The quality of the final cut surface is mainly related to the mean shear strength ( $S_S$ ) of the longitudinal fibres in the skin: higher mean shear strength ( $S_S$ ) leads to a more jagged rupture instead of a clean cut, while it also results in higher required cutting work. Hence, a ratio of 5 between the mean tensile and shear strength ( $S_T, S_S$ ) of the skin in longitudinal direction is considered to use, that results in the most similar cutting surface as it was observed during the experiments. The higher particle-geometry coefficient of variation ( $\mu_{P-G}$ ) results in higher ultimate force while the cutting blade passes through the already cut internodal sections, thus, it also causes higher cutting work.

TABLE 6.3: Summary of the influence of the parameters on the mechanical behaviour and breakage of the virtual samples during dynamic cutting simulation.

Input parameter	Length of cutting stages	Peak force	Ultimate force	Cutting work	Resulted cutting surface
$E_B^{S, long.}$	$\leftrightarrow$	$\downarrow$	$\times$	$\downarrow$	$\leftrightarrow$
$S_T^{S, long.}$	$\leftrightarrow$	$\uparrow$	$\uparrow$	$\uparrow$	$\leftrightarrow$
$S_S^{S, long.}$	$\times$	$\downarrow$	$\times$	$\uparrow$	$\leftrightarrow$
$\zeta$	$\leftrightarrow$	$\downarrow$	$\downarrow$	$\downarrow$	$\leftrightarrow$
$\theta_{P-G}$	$\times$	$\times$	$\uparrow$	$\uparrow$	$\leftrightarrow$

Where  $\uparrow, \downarrow, \leftrightarrow$  and  $\times$  indicates an increase, decrease, influence and no influence, respectively.

In the case of the **ear-detachment**, the higher values of the bond Young's modulus resulted in higher stiffness of the shank, thus, the displacement took place earlier and its deformed shape was also straighter. The detachment force and its displacement were higher as the tensile strength of the bond between the shank and maize ear was higher. The **collision** among the maize ear and geometry elements is strongly related to the particle-geometry coefficient of restitution.

TABLE 6.4: Summary of the influence of the parameters on the mechanical behaviour and breakage of the virtual samples during ear-detachment simulation.

Input parameter	Stiffness of the shank	Deformation of the shank	Detachment force	Displacement at detachment
$E_B^{SH}$	$\uparrow$	$\leftrightarrow$	$\times$	$\downarrow$
$S_T^{SH\&ME}$	$\times$	$\times$	$\uparrow$	$\uparrow$

Where  $\uparrow, \downarrow, \leftrightarrow$  and  $\times$  indicates an increase, decrease, influence and no influence, respectively.

# 7 Results of The Calibration

## 7.1 Virtual Maize Stalk

Figure 7.1 presents the physical characteristics of the real and the virtual maize stalk. The distribution of the internodal and nodal diameter ratio showed a good agreement with the experimentally determined values (Figure 7.1(a)). The characteristic of the length ratio distribution was similar to the measured one, however, the length ratio of the internodal part above the maize ear showed higher difference (Figure 7.1(b)). Contrary to this, the internodal mass ratio showed exactly the same distribution that was determined for the real maize stalk (Figure 7.1(c)).

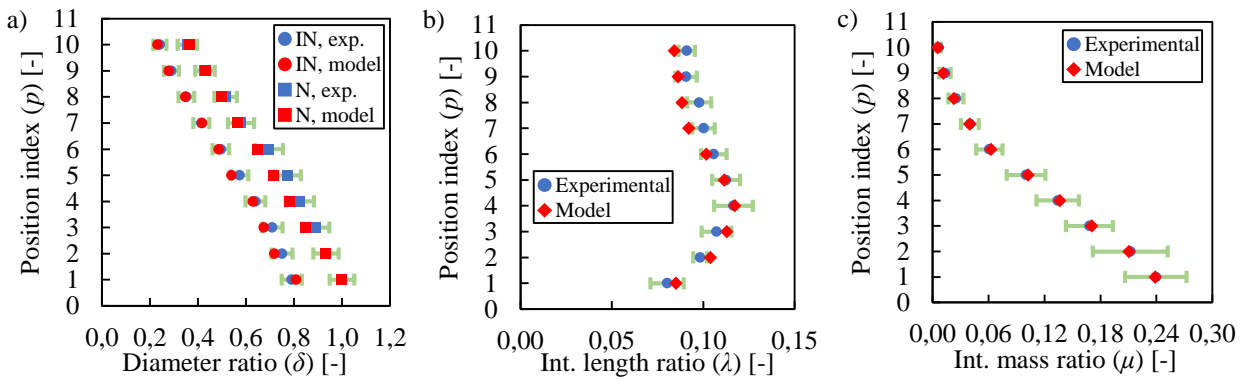


FIGURE 7.1: Comparison of the physical characteristic of the virtual and the real maize stalk: distribution of the internodal and nodal diameter ratio (a), internodal length ratio (b) and internodal mass ratio (c).

The internodal input parameters defined by the optimization cycle (Figure 5.9) are shown in Table 7.1, while, the Young's modulus ( $E_B$ ) was chosen to 4000 MPa and the strength properties were determined for numerically infinite (1e15 Pa) for all the bonds relating the nodal particles based on the considerations described in Chapter 5.3. The rest of the input parameters, that are not discussed here, were the same as in Table 5.4. As it was expected, the experimentally determined force response and breakage of the samples could be reproduced by the modification of the key parameters as the Young's modulus of the particles and bonds ( $E_P; E_B$ ), and the bonded mean tensile and shear strength ( $S_T; S_S$ ).

Figure 7.2 presents the comparison of the DEM predicted and experimental results by **sectional transversal compression**. In each case, the numerically determined force response was in a good agreement with the measured one, however, the difference was higher for the internodal sections above the maize ear. At the beginning of the compression, multiple drops on the numerical force response of the 1<sup>st</sup> internodal section (Figure 7.2(a)) perfectly represented the typical force response of the real sample, while, the rest of the curve also agreed well with the measured one. In case of the 2<sup>nd</sup>, 3<sup>rd</sup>, 4<sup>th</sup>, 5<sup>th</sup> internodal sections (Figure 7.2(a-e)), the overall DEM force response coincided well with the measured one, however, two drops governed the initial numerical response contrary to the experimental results where only one initial drop was observed. The DEM overall force response of the internodal sections (the 6<sup>th</sup>, 7<sup>th</sup>, 8<sup>th</sup>, 9<sup>th</sup>, 10<sup>th</sup>)

TABLE 7.1: Validated bonded and non-bonded input parameters for the virtual stalk.

IN	Part	$E_P [MPa]$	$E_B [MPa]$	$S_T [MPa]$	$S_S [MPa]$
$1^{st}$	Skin L.	270	4000	250	50
	Skin, tr.	270	1800	70	14
	Core	350	6	4	-
$2^{nd}$	Skin L.	270	4000	250	50
	Skin, tr.	270	1500	60	12
	Core	270	6	4	-
$3^{rd}$	Skin L.	270	4000	500	100
	Skin, tr.	270	1200	50	10
	Core	270	4	3	-
$4^{th}$	Skin L.	270	4000	500	100
	Skin, tr.	270	1200	50	10
	Core	200	4	3	-
$5^{th}$	Skin L.	270	4000	600	120
	Skin, tr.	270	1200	50	10
	Core	135	7	5	-
$6^{th}$	Skin L.	270	4000	135	27
	Skin, tr.	270	80	65	-
$7^{th}$	Skin L.	270	4000	150	30
	Skin, tr.	270	80	65	-
$8^{th}$	Skin L.	270	4000	150	30
	Skin, tr.	270	80	65	-
$9^{th}$	Skin L.	270	4000	175	35
	Skin, tr.	270	120	85	-
$10^{th}$	Skin L.	270	4000	200	40
	Skin, tr.	270	160	100	-

above the maize ear (Figure 7.2(f-j)) also was in a good agreement with the measured characteristic, however, the details (e.g. the initial drop) could not be reproduced by the simplified model. Beyond the force response, the compressive work is also a crucial factor, thus, the compressive work distribution on the virtual maize stalk (Figure 7.2(k)) and relationship between the compressive work and the internodal diameter (Figure 7.2(l)) were also compared. The distribution of the compressive work on the virtual maize stalk showed the same characteristic as it was experimentally determined, moreover, the relationship between the compressive work and the internodal diameter fell within the experimentally determined results.

Figure 7.3 shows the typical DEM predicted and experimental breakage of the samples in the range of 0.0 - 0.75 compression rate ( $\kappa$ ). The initial ovalisation (flattening of the circular cross-section into an oval shape by (Leblcq et al., 2015)) of the sample had finished around 0.1 compression rate before the first break at the top side of the skin appeared at 0.11 compression rate. This break caused the first drop on the resistance force curve. After a short deformation stage, the second break at the bottom of the skin appeared that results in the second drop of the resistance force curve at 0.14 compression rate. The third and the fourth break of the skin appeared close to each other, within approximately 0.01 compression rate. Hence, the core carried the majority of the external load. However, during the rest of the process, breaks in the skin

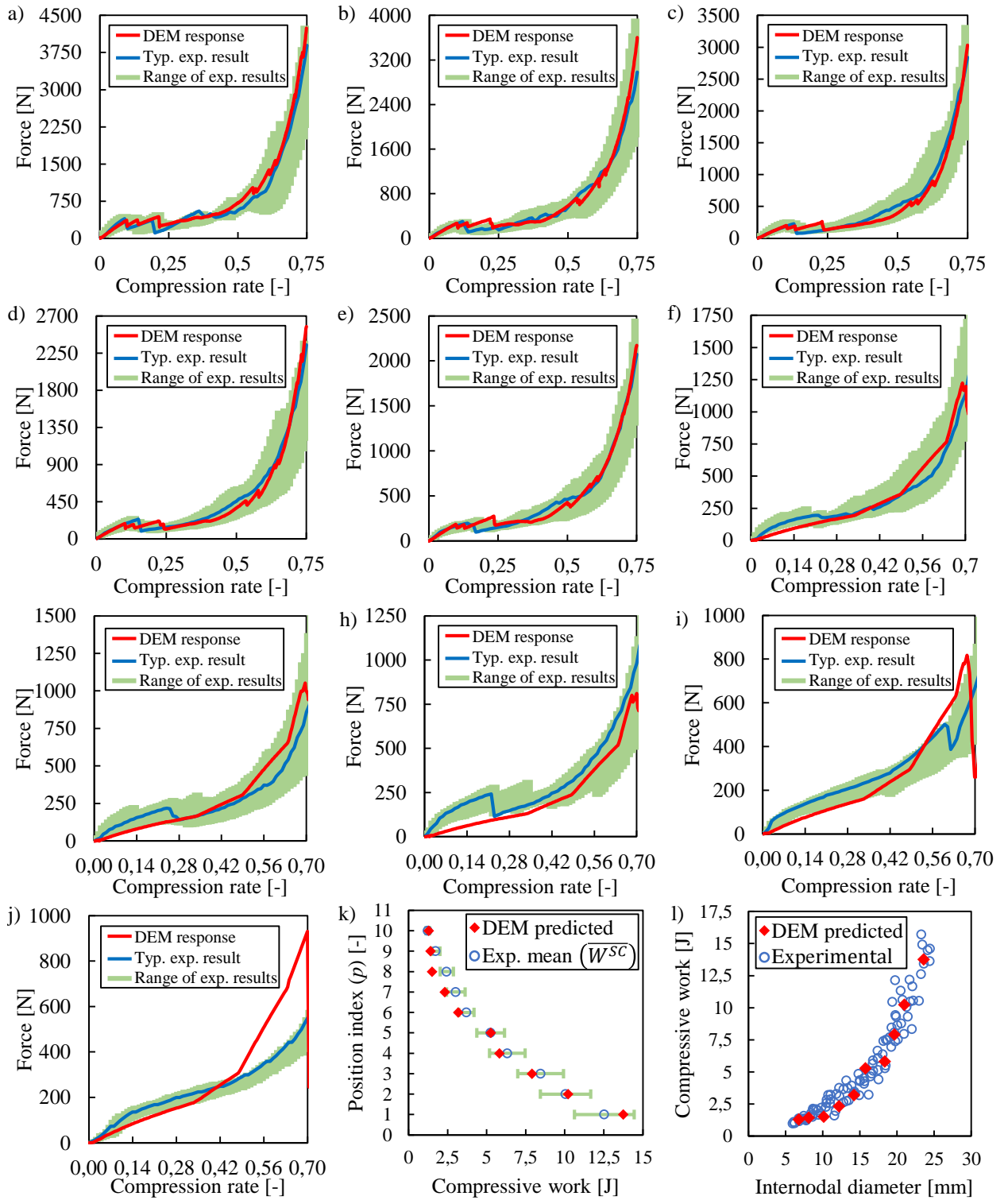


FIGURE 7.2: Comparison on the DEM predicted and experimental results by sectional transversal compression: force response of the 1<sup>st</sup> (a), 2<sup>nd</sup> (b), 3<sup>rd</sup> (c), 4<sup>th</sup> (d), 5<sup>th</sup> (e), 6<sup>th</sup> (f), 7<sup>th</sup> (g), 8<sup>th</sup> (h), 9<sup>th</sup> (i), 10<sup>th</sup> (j) internodal section; k) compression work distribution on the stalk and l) compressive work vs internodal diameter.

caused small drops during the exponential increasing section as significant re-arrangement may occur due to the sudden reduction in confinement. Finally, in the end of the process the skin was broken into narrow segments that consists of two or three longitudinal fibres.

Comparing the DEM and experimental results in case of the 4<sup>th</sup> internodal section (Figure 7.3(a)), the initial vertical break was not clearly visible in the DEM results. As the compression continues the breakage of the skin took place in a similar manner, however, the breakage of the skin appeared earlier in case of the model. Finally, the fully compressed DEM samples were quite similar to the experimental specimens. To reproduce the force response with the simplified structure of the internodal sections above the maize ear, the breakage of the skin took place around 0.7 compression rate with one break in the left and right side of the virtual specimen (Figure 7.3(b)).

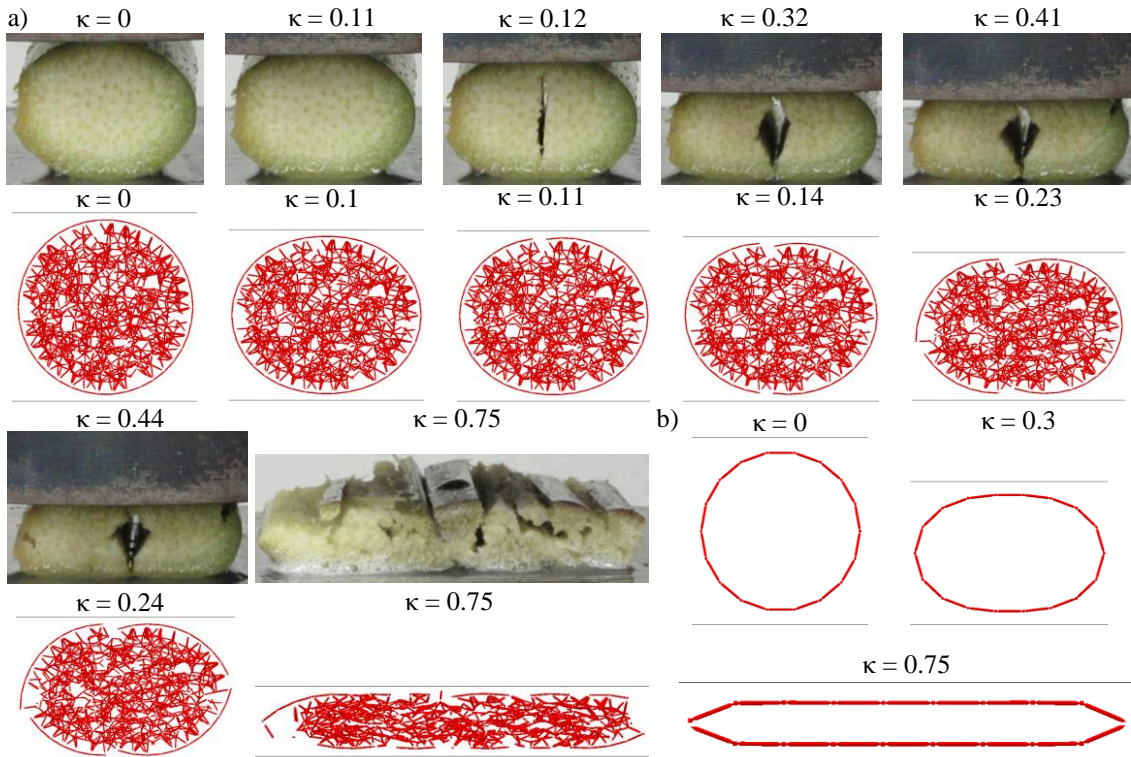


FIGURE 7.3: Comparison of the DEM predicted and experimental breakage by sectional transversal compression: breakage of the 4<sup>th</sup> (a) and the 6<sup>th</sup> (b) internodal section.

Figure 7.4 presents the comparison of the DEM predicted and experimental results by **three-point bending**. In each case, the DEM force response showed good agreement with the measured one during the initial elastic section. Before reaching the peak force the grade of increasing dropped in case of the internodal sections under the maize ear (Figure 7.4(a-e)), however, this section was constituted of short linear increasing sections and large drops. After reaching the peak force the resistance force started to decrease, however, this section was governed some significant drops relating to breaking of the skin in transversal direction. This was followed by some further small breaks before the plateau region. Finally, the resistance force increased slightly until the end of the bending process, because of the continuously increasing displacement of the un-broken longitudinal fibres in the skin. These sections could not be reproduced by the simplified model of the internodal sections above the maize ear as shown in Figure 7.4(f-j). Beyond the force response, the bending work is also a crucial factor, thus, the bending work distribution on the virtual maize stalk (Figure 7.4(k)) and relationship between the compressive work and the internodal diameter (Figure 7.4(l)) were also compared for the internodal sections under the maize ear. The distribution of the bending work on the virtual maize stalk showed the same characteristic as it was experimentally determined, moreover, the relationship between the bending work and the internodal diameter fell within the experimentally determined results.

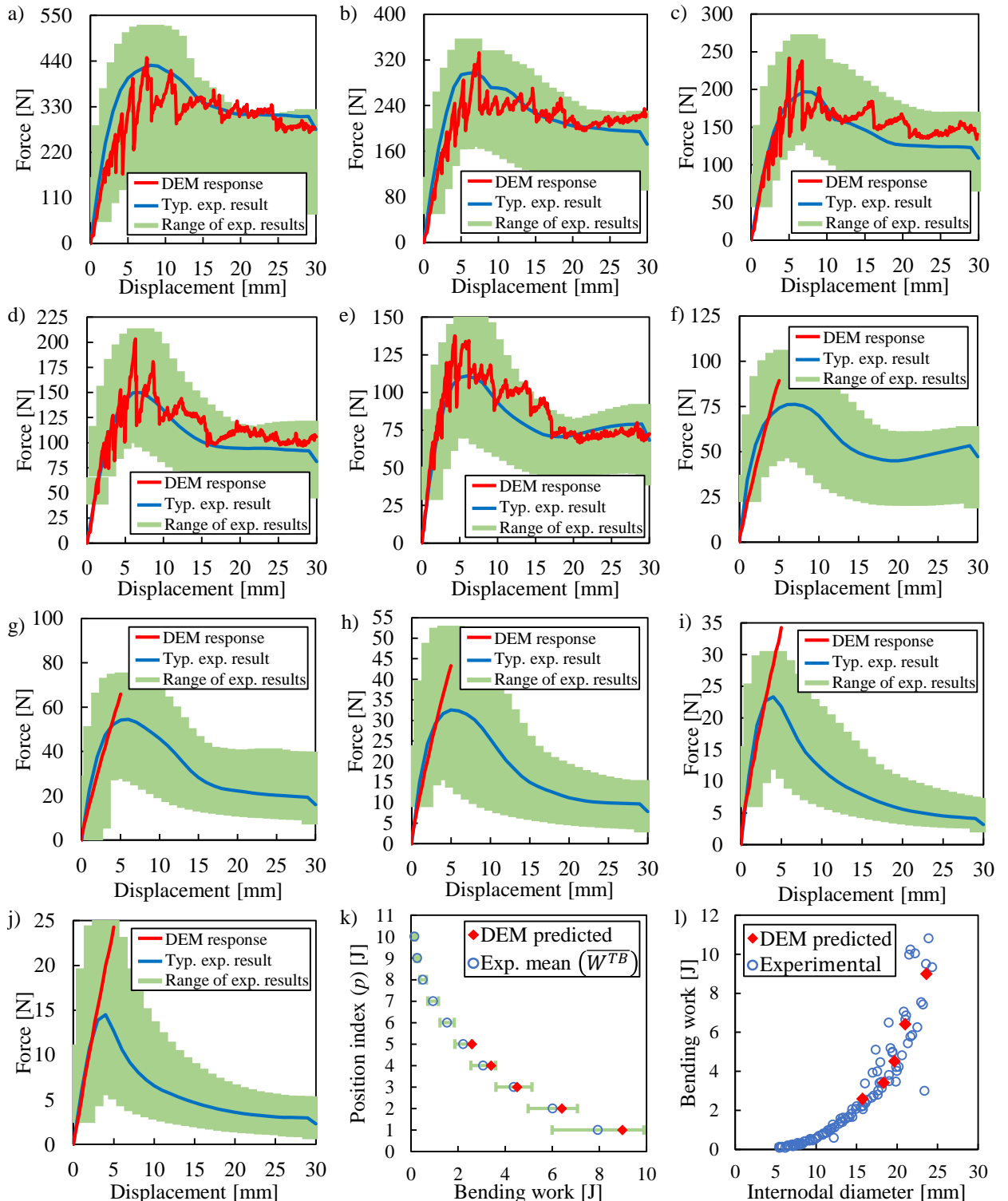


FIGURE 7.4: Comparison on the DEM predicted and experimental results by three-point bending: force response of the 1<sup>st</sup> (a), 2<sup>nd</sup> (b), 3<sup>rd</sup> (c), 4<sup>th</sup> (d), 5<sup>th</sup> (e), 6<sup>th</sup> (f), 7<sup>th</sup> (g), 8<sup>th</sup> (h), 9<sup>th</sup> (i), 10<sup>th</sup> (j) internodal section; k) bending work distribution on the stalk and l) bending work vs internodal diameter.

The DEM predicted and the experimental breakage and deformation of the internodal section was also compared at 0-6-15-24-30 mm displacements, as shown in Figure 7.5. Generally, the deformed shape of the virtual internodal section was similar to the observations on the real

specimen through the bending process. Between 0 mm and 15 mm displacement the deformation of the virtual sample under the bending tool (in the bending zone) is in a good agreement with deformation of the real specimen. In case of both specimen, the compressive deformation in the bending zone was more significant than the bending deformation at the beginning of the process. Afterwards, around 15 mm displacement the cross-section under the bending tool became unstable and a structural collapse (buckling: complete local flattening of the cross-section defined by (Leblanc et al., 2015)) took place that resulted in a V-shape forming in the bending zone. This phenomenon did not occur during the simulation, thus the DEM simulated bending zone remained U-shaped until the end of the bending process. At 30 mm displacement the difference between the V-and U-shape was highlighted on Figure 7.5(b). Here, it is also observable that the transverse deformation of the cross-section of the real specimen was higher than the transverse deformation of the virtual specimen, moreover, the top fibres of the internodal section were involved into the structural collapse, while the fibres on the bottom side remain U-shaped. In case of the virtual specimen, the top and bottom fibres remained U shaped as well.

The propagation of the longitudinal cracks of the skin of the real and the virtual specimen during three-point bending are highlighted on Figure 7.5 for comparison. In case of the real specimen the first crack appeared around 15 mm displacement, while the virtual specimen showed significant breaks around 6 mm displacement. This difference between the real and the virtual specimens was observable during the entire process, thus, the virtual specimen had an extensive longitudinal crack system at the end of the bending.

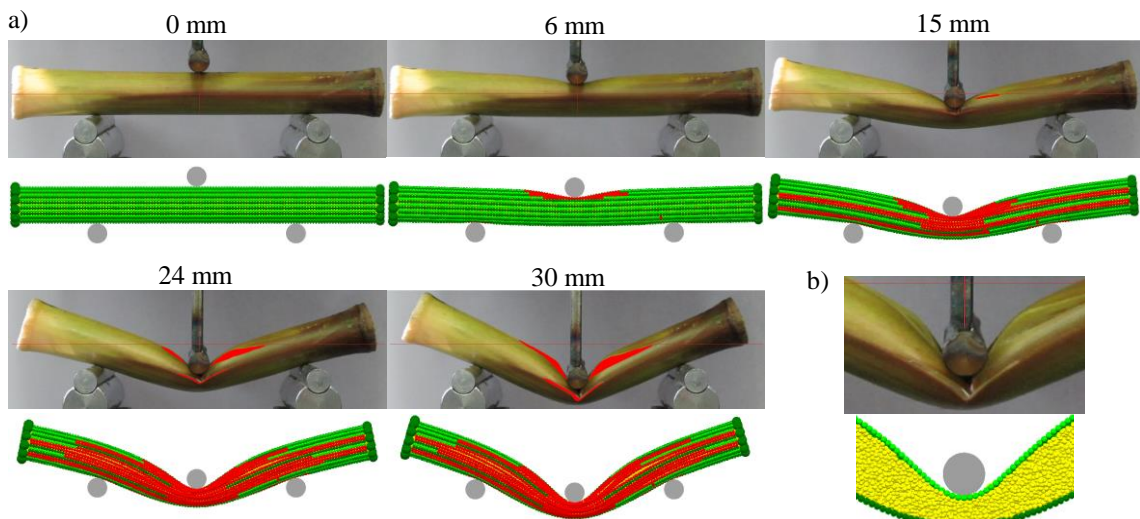


FIGURE 7.5: Comparison of the DEM predicted and experimental breakage by three-point bending:  
a) longitudinal break propagation and b) buckling under the bending tool in case of the 4<sup>th</sup> internodal section.

The total DEM **dynamic cutting** process, from the first to the last contact between the cutting blade and the virtual sample, lasted until 95 mm of displacement of the leading blade edge, however, the crucial phases took place before approximately 25 mm of displacement. As it was expected, the rupture of the longitudinal fibres had the most significant influence on the force response, as shown in Figure 7.6(a).

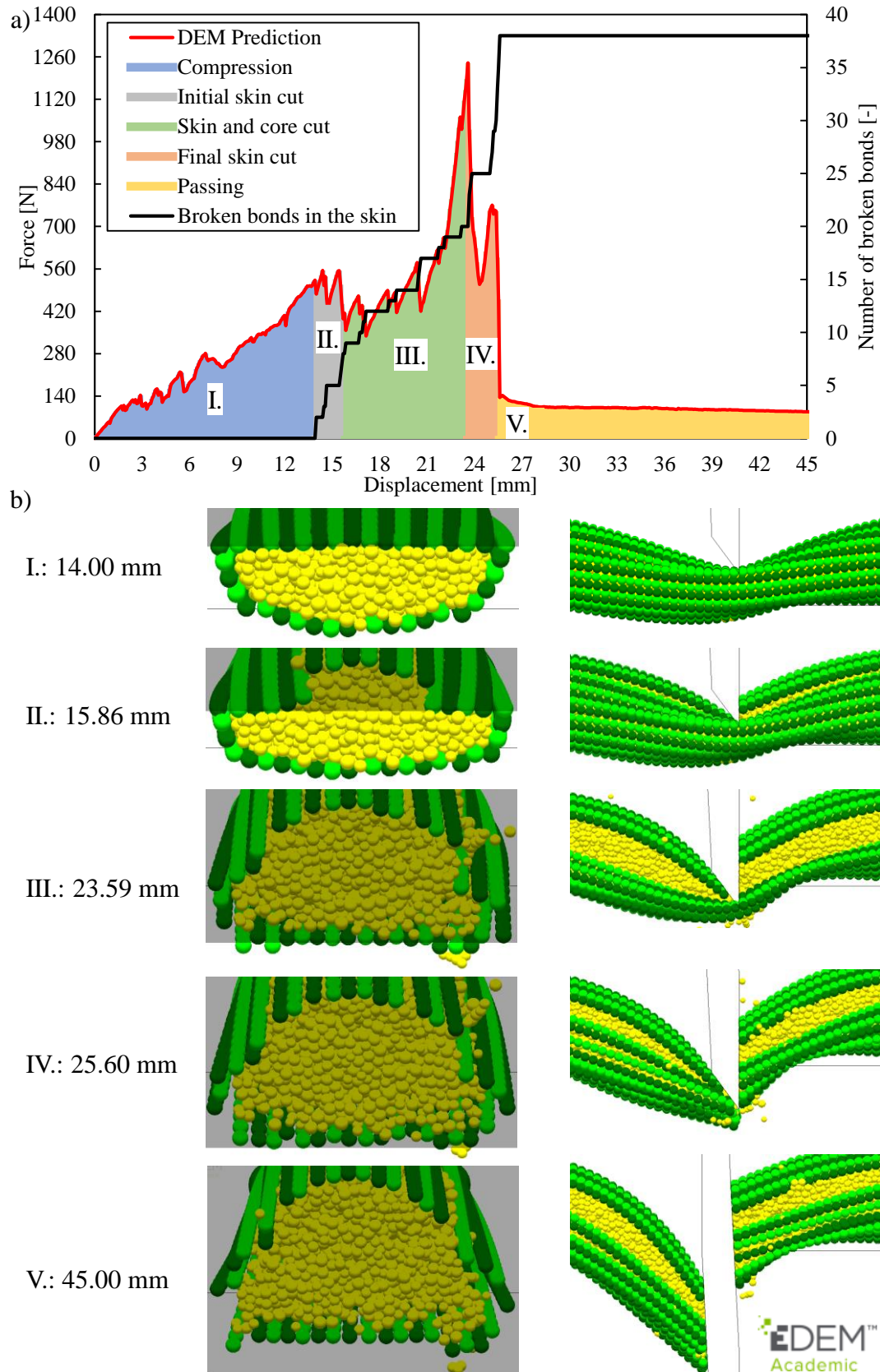


FIGURE 7.6: Stages of the cutting process: a) plot of the resistance force characteristic and the number of broken bonds in longitudinal direction of the skin; b) stages of dynamic cutting visualized by particles in the plane of cutting (left) and side view of the cutting process (right).

Based on these characteristics the cutting process can be divided into five different stages:

- I **Compression stage** (before 14.00 mm displacement), when the internodal cross-section is flattening under the cutting blade without rupture of the longitudinal fibres (Figure 7.6(b) I.) and the resistance force is gradually increasing (Figure 7.6(a));
- II **Initial cut of the skin** (between 14.00 mm and 15.86 mm displacement), when 9 longitudinal fibres on the top side of the cross-section are ruptured (Figure 7.6(b) II.) while the resistance force is decreasing (Figure 7.6(a));
- III **Cut of the skin and core** (between 15.86 mm and 23.59 mm displacement), when the lateral fibres of the skin and the core are cut off (Figure 7.6(b) III.) while the resistance force reaches its peak (Figure 7.6(a));
- IV **Final cut of the skin** (between 23.59 mm and 25.60 mm displacement), when the rest of the fibres on the bottom side of the cross-section are ruptured (Figure 7.6(b) IV.) and the resistance force sharply drops (Figure 7.6(a));
- V **Passing through of the cutting blade** (between 25.60 mm and 95 mm displacement), when the cut has been done because the leading edge left the sample, thus it was separated into two parts (Figure 7.6(b) V.) and resistance force is decreasing as the cutting blade passing through the sample and the number of contacts between the blade and the sample decreases (Figure 7.6(a)).

Figure 7.7(a) shows the cutting work distribution on the maize. The DEM predicted distribution showed good agreement with the measured results: all the numerically determined values fell close to the outcomes of the experiments.

A comparison of the resulted cutting surfaces and breakage are shown on Figure 7.7(b)(c). In case of the real specimens the cutting surface was usually straight, however, a rim of fibres was observable on the side where the cutting blade left the specimen. These properties were also observable for the DEM simulated cutting surface, (Figure 7.7(b)). Breaks in the core (parallel to the cutting direction) and longitudinal breaks in skin (perpendicular to the cutting direction) occurred on the real specimen, while breaks in the core were not observable on the virtual specimen due to the fidelity of the core representation and the zone of the longitudinal breaks was more extensive than on the real specimen, see on Figure 7.7(c). Moreover, the damage of the bonds between the core and the skin was more significant in the zone of cutting, thus, some of the fibres were totally detached from the core here.

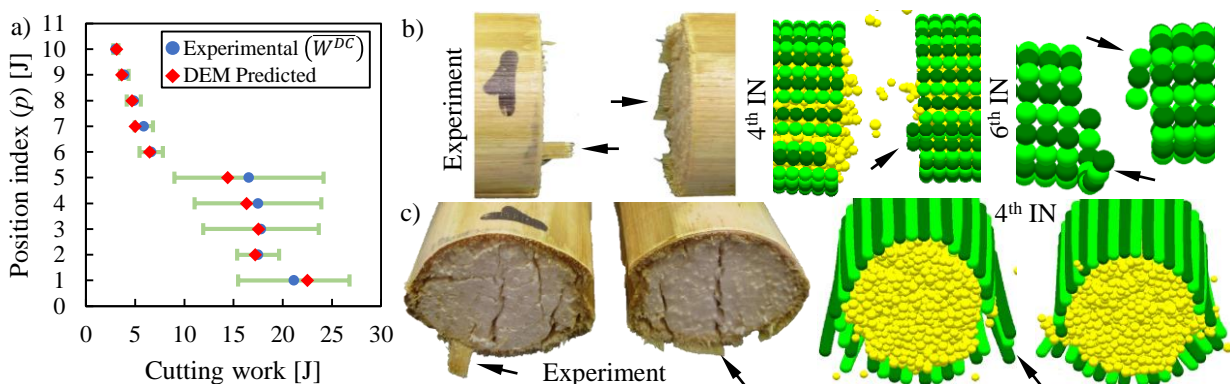


FIGURE 7.7: Comparison of the DEM predicted and experimental results by dynamic cutting: a) distribution of the cutting work; b) side and c) front view of the cutting surface (rim of fibres is marked by black arrow).

Figure 7.8 presents the comparison of the DEM predicted and experimental results by **local transversal compression**. In case of the internodal sections under the maize ear the force response showed good agreement with experimentally determined one, as shown in Figure 7.8(a-e). The DEM predicted force characteristic coincides well with the typical force responses

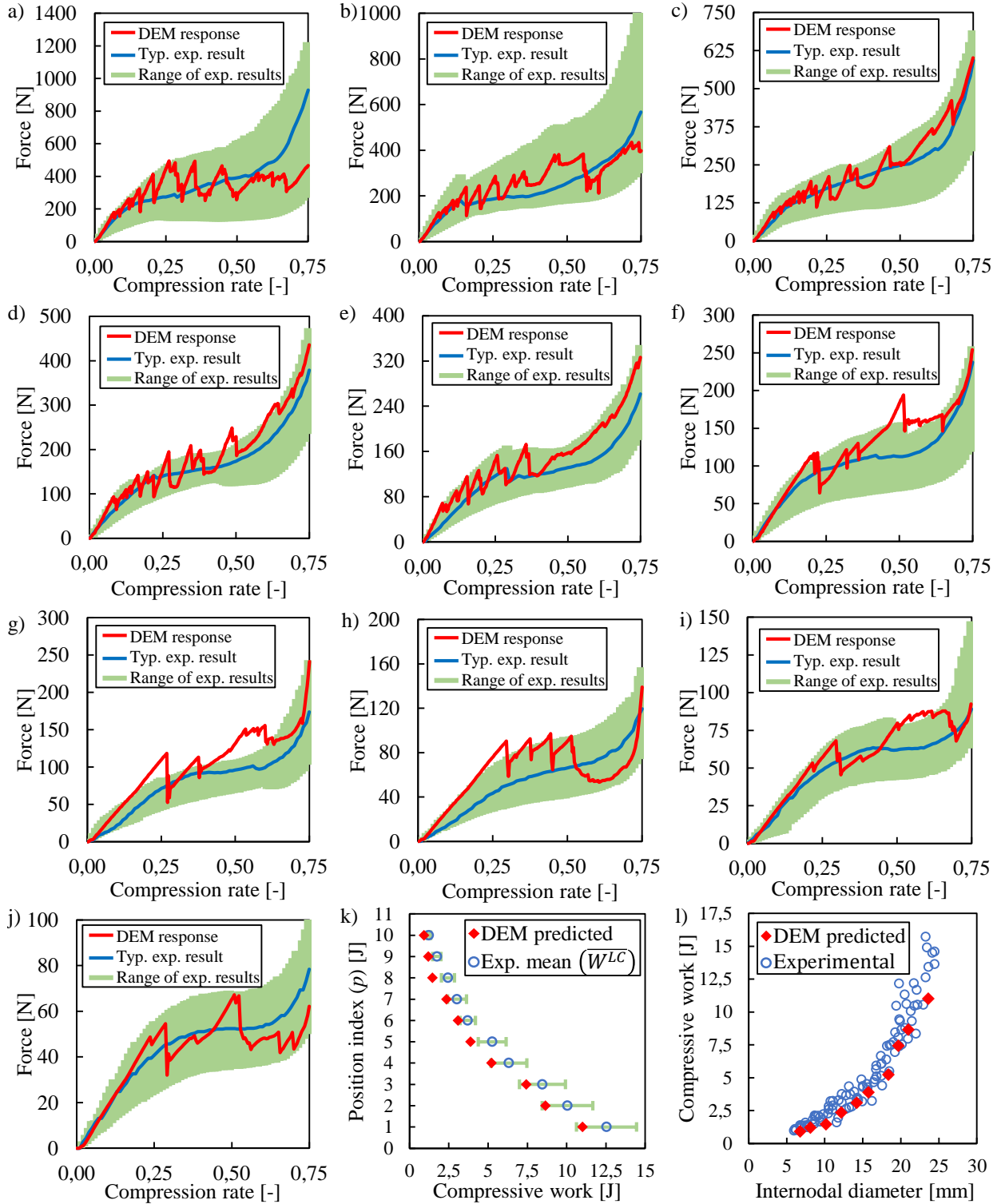


FIGURE 7.8: Comparison on the DEM predicted and experimental results by local transversal compression: force response of the 1<sup>st</sup> (a), 2<sup>nd</sup> (b), 3<sup>rd</sup> (c), 4<sup>th</sup> (d), 5<sup>th</sup> (e), 6<sup>th</sup> (f), 7<sup>th</sup> (g), 8<sup>th</sup> (h), 9<sup>th</sup> (i), 10<sup>th</sup> (j) internodal section; k) compression work distribution on the stalk and l) compressive work vs internodal diameter.

during the bilinear increasing and constant sections, however, the numerical response is constituted of short linear increasing segments and large drops. The final exponential increasing section showed the same characteristic in case of the 3<sup>rd</sup>, 4<sup>th</sup> and 5<sup>th</sup> (Figure 7.8(c-e)), while, the

grade of increasing is smaller in case of the the 1<sup>st</sup> and 2<sup>nd</sup> internodes (Figure 7.8(a)(b)). For the rest of the stalk, the difference between the DEM predicted and experimental force response is higher (Figure 7.8(f-j)), however, it is reasonable by taking into consideration the simplified structure. In these cases, the model usually simulates a stiffer response until occurring of the first break. After this the DEM response is also constituted of short linear increasing segments and large drops, while, the mean of this section shows an increasing trend. At the end of the compression, the skin particles get into contact, thus, the force response starts to increase significantly. Beyond the force response, the compressive work is also a crucial factor, thus, the compressive work distribution on the virtual maize stalk (Figure 7.8(k)) and relationship between the compressive work and the internodal diameter (Figure 7.8(l)) were also compared. The distribution of the compressive work on the virtual maize stalk showed the same characteristic as it was experimentally determined, however, the numerical results were below the measured mean values. The relationship between the compressive work and the internodal diameter perfectly fell within the experimentally determined results.

Breakage of the real and the virtual specimen are presented in Figure 7.9. The final deformation of the real and the virtual internodal sections are quite similar (Figure 7.9(a) and (b)), however, the zone of the longitudinal breaks in the skin is more extensive in case of the virtual specimen (Figure 7.9(c)). Under the plunger tool the deformed zone in longitudinal direction formed a V-shape, however, in case of the virtual specimen the shape of the deformed zone was U-shaped (Figure 7.9(d)). In case of the internodal sections above the maize ear the plunger tool usually cut the top fibres of the skin, thus, the shape of the compressed zone was more similar to the experimentally observed one, as shown in Figure 7.9(e).

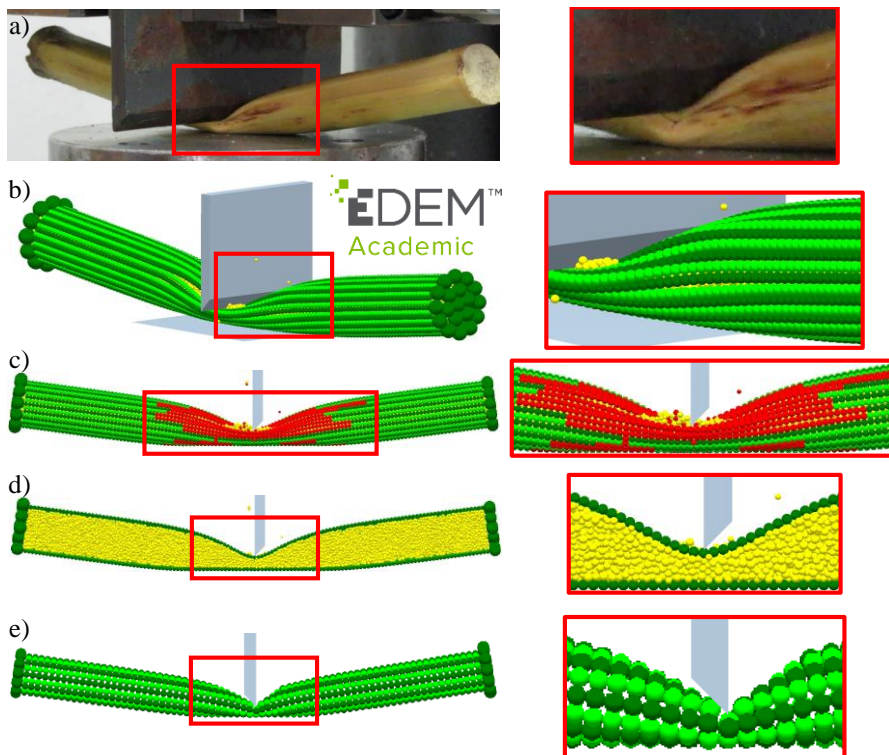


FIGURE 7.9: Comparison of the DEM predicted and experimental breakage by local transversal compression: a) experimental result on the breakage in the compressed area; b) DEM result on the deformation in the compressed area; c) DEM result on the breakage in the compressed area (particles coloured by damage parameter of 0.1); d) DEM simulated buckling under the plunger; e) initial skin cut for internodal sections (6-7-8-9-10<sup>th</sup>) above the maize ear.

Figure 7.10 presents the comparison of the DEM predicted and experimental results by **cantilever bending**. The DEM force response oscillated around a linearly increasing mean value, as shown in Figure 7.10(a). The grade of increasing perfectly fell within the experimentally determined range. Contrary to this, the structural collapse did not take place during the simulation, thus, the force response exceeded the determined range above the displacement of 150 mm, however, a smooth decreasing is observable on the characteristic here.

The reason behind the absence of the structural collapse can be detected through the visual comparison of the breakage in the zone of the 3<sup>rd</sup> node (right above the last support), as shown in Figure 7.10(b). Contrary to the real sample, breakage of the longitudinal or transversal bonds was not detected on the virtual maize stalk, thus, the structural collapse (buckling) did not take place and the stiffness of the stalk remained the same.

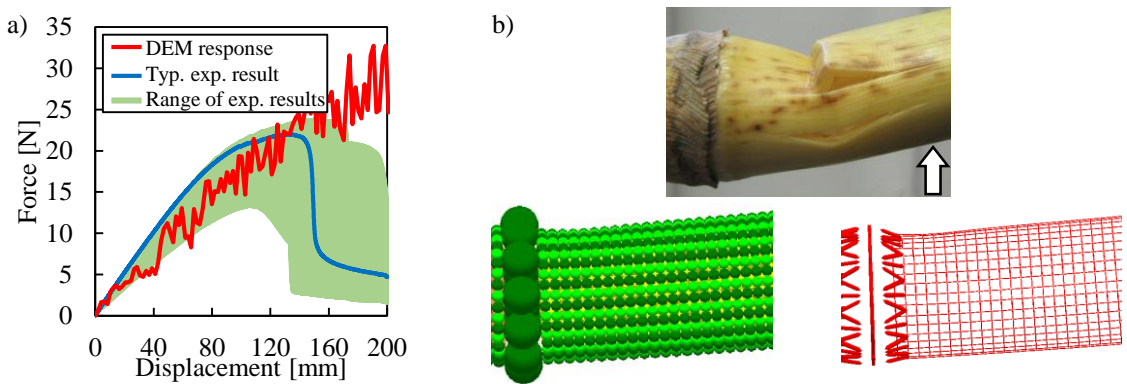


FIGURE 7.10: Comparison of the DEM predicted and experimental results by cantilever bending: a) force response; b) buckling in the zone of the 3<sup>rd</sup> node (top: real specimen, bottom-left: virtual specimen visualized by the particles, bottom-right: virtual specimen visualized by the bonds).

## 7.2 Virtual Ear and Shank

Figure 7.11(a) presents the comparison of the experimentally determined ideal and the virtual shape (that consists of spherical surfaces) of the maize ear. As it was expected, the shape of the virtual maize ear is in a good agreement with the real shape. By using the determined relationships (Equation 6.2 and 6.3), the coefficient of restitution ( $e_{P-G}^{ME}$ ) was chosen to 0.77 and 0.88 for steel and plastic materials, respectively. The selected values resulted in 117 and 173 mm bouncing heights after the collision on steel and plastic sheets that are in a good agreement with the calculated values (115 and 176 mm) based on the results of Chapter 4.2.6.

In the shank, the bond Young's modulus ( $E_B^{SH}$ ) was determined as 200 MPa, while, the mean tensile strength ( $S_T^{SH}$ ) was set to 40 MPa between the shank and the maize ear. In this manner, the specific force-displacement characteristic of the detachment process fell within the measured range and it shows good agreement with experimentally determined typical curve, as shown in Figure 7.11(b). The resulted detachment force was 447.0 N at the displacement of 125.2 mm that perfectly corresponds with the experimentally determined results of Chapter 4.2.6.

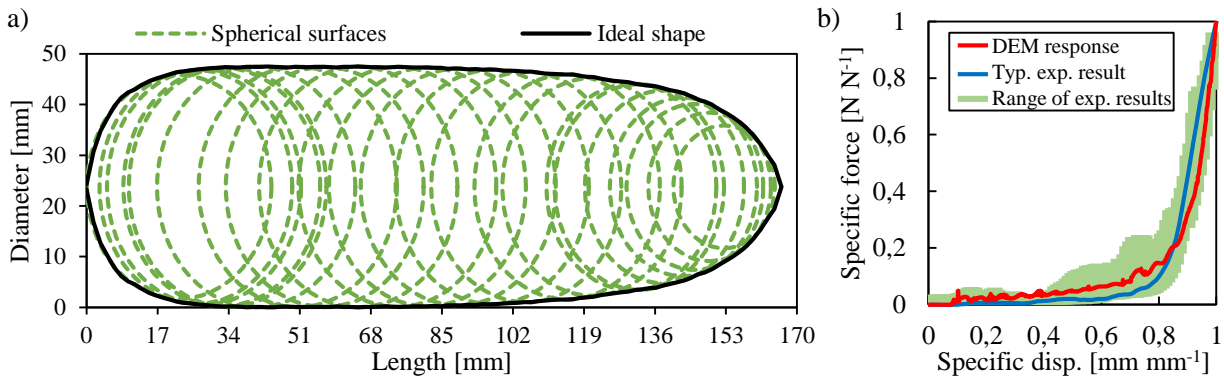


FIGURE 7.11: Comparison of the DEM predicted and experimental results by ear-detachment: a) shape of the virtual ear and b) specific force response.

### 7.3 Conclusions

The physical characteristics of the **virtual maize stalk** correspond with the nature of the real one in all aspects, however, larger difference can be observed between the length ratios of the upper parts. This comes from the calculation method of the geometrical properties in the well-structured skin because the particle diameter is calculated based on the equivalent diameter of the internodal section, thus, it is optimized for the highest accuracy in this aspect. Moreover, the particle diameter also defines the length of one cross-section which is larger as the number of skin particles is lower, thus, the length of the upper internodal sections (that contains a certain number of cross-sections) is more inaccurate.

The results clearly show that the stalk model can mimic the response of the real samples with high accuracy, however, there are some aspects where minor differences can be observed between the numerical and experimental results. For the sectional transversal compression experiment the DEM simulated response coincides with the measured curve very well, except in the zone of the first break, where it shows four smaller drops before the external load transfers to the core, while the experimental one presents one significant drop. During the experiments, the significant break occurs because of the plastic deformation (permanent micro-structural deformations) of the soft core without fracture during the increasing section of the curve (Niklas, 1992). After the cell walls in the core reach their limit of strength they start to rupture in a chain-reaction and the resistance of the structure drops immediately. The presented bonded structure of the core with the bonded model (TBBM) are not able to simulate this plastic behaviour of the core due to its fidelity and the elastic mechanical characteristic of the bonded model, therefore, this phenomenon is not reproducible. The response of the model is also accurate before the buckling phenomenon in case of the three-point bending, the local transversal compression and the cantilever bending simulations, however, the lack of plasticity of the model is also observable. After the buckling (without rupture of any fibres) of the most loaded cross-section, a plastic hinge that would result in the decreasing of the resistance of the material should be occurring, however, it is not formed in the model, thus, the resistance force curves exceed the range of experimental results. Even though resistance force curves were not recorded during the dynamic cutting experiment the DEM simulation result presents four stages of cut (compression, initial cut of the skin, skin and core cut, final cut of the skin) that were also reported by previous studies on the mechanical cutting of maize stalks (Igathinathane, Womac, and Sokhansanj, 2010).

By using the optimal set of bonded parameters, the DEM simulated required work of the processes fell within the experimentally determined range, however, larger differences could be observed for the the local transversal compression simulations, where the numerical results

were lower than the measured mean values. However, these errors are negligible by considering the high diversification of living materials and the continuously changing conditions during harvesting.

The breakage of the virtual internodal samples were also compared with observations during the experiments and the results clearly show that the model can simulate the major breaking events of the samples during harvesting despite of some minor differences. In case of the sectional transversal compression there are two differences between the breaking of the real and the virtual specimens: the vertical break of the core is not observable, and the vertical and horizontal breaks of the skin occur earlier, around 0.14 and 0.25 instead of 0.18 and 0.39 compression rate, during the simulation, however, the difference in the breakage of the skin is caused by the consciously miss-chosen bonded parameters in transversal direction of the skin to reproduce artificially the break of the core on the resistance force characteristic. The missing of the vertical break of the core can be explained by the lack of plasticity (as discussed earlier), the scaling and the structure of the virtual core. In the current model, the core was modelled by randomly distributed particles, however, the core of the real material is constituted of hundreds of longitudinal fibres (Huang et al., 2016) and its structure also provides a transversely isotropic mechanical behaviour as in the skin. In case of the three-point bending and local transversal compression the deformation and breakage of the virtual samples were very similar to the real phenomenon before buckling, however, the results also indicate the need for plasticity. Instead of the experimentally observed V-shaped zone under the bending and the plunger tool a U-shaped zone appears on the virtual samples due to the missing plastic hinge effect. Moreover, the DEM simulated propagation of the damage zone is more extensive than it was observed during the experiments to compensate the effect of the missing plastic hinge. The DEM simulated cutting surface was close to the experimentally observed one, however, the vertical breaks of the core were not observable, and the length of longitudinal breaks was longer than it was observed during the experiments because of the previously described effects.

The numerically determined parameters for the **virtual shank with the maize ear** provided excellent agreement between the DEM and experimental results. The difference between the modelled and real bounce height after the collision was less than 2%, while, the force-displacement characteristic and the resulted detachment force fell within the experimentally determined range.

Consequently, the applied DEM model of the maize plant with the optimized numerical parameters is capable of simulating the mechanical behaviour and breakage during each loading case, moreover, its accuracy is excellent by considering the high diversification of living materials and the continuously changing circumstances during the real process of harvesting. Therefore, the relevance of the optimization loop to determine the optimal set of parameters is justified.



## 8 Results of Harvesting Simulation

At the beginning of the harvesting simulation the maize header unit approaches the stalk without any contacts among its parts and the virtual plant. The first contact occurs between the stalk and the conical part of the stalk rollers, afterwards, its knives also get in contact with the stalk. As the stalk rollers rotate in opposite directions their knives compress the maize stalk locally and pull it down, while the chopping unit cuts it into small pieces. The maize ear is detached by the deck plates and transported into the gathering box by the gathering chains.

Between the knives of the **stalk rollers**, the stalk provides high resistance against compression that appears as a torque on the stalk rollers, as shown in Figure 8.1(a). At the beginning of the process, when the stalk is virgin, an extremely high peak torque (approx. 180 Nm) can be observed because of the supporting effect of the roots. In this case the stalk is compressed locally in its radial direction and in its longitudinal direction as well, that causes a special, initial loading case of the stalk rollers. After the first cut the stalk lost its connection to the ground and the torque peaks are more similar. In the steady state the peaks are between 40 and 70 Nm, while the mean torque on each stalk roller is 23.3 Nm. Except one peak torque on the left stalk roller around its third rotation the characteristics are nearly the same on both stalk rollers.

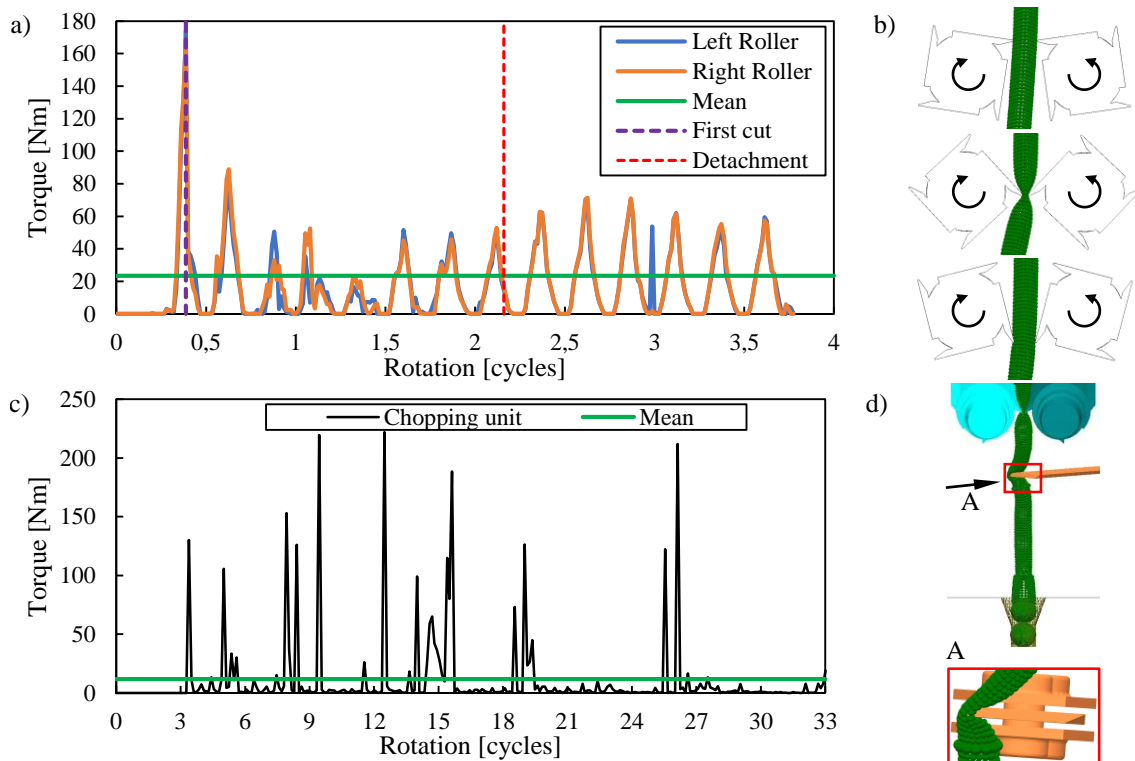


FIGURE 8.1: Process analysis on the stalk rollers and the chopping unit by harvesting simulation: a) external torque on the axle of each stalk roller vs. its rotation in cycles with highlights of the first cut and ear detachment; b) working process of the stalk rollers: approaching, maximal compression and distancing; c) external torque on the axis of the chopping blade vs its rotation in cycles; d) phenomena of the first cut.

The most important function of the **stalk rollers** is to control the movements of the stalk. On Figure 8.1(b), the main stages of the interaction among the stalk and stalk rollers can be observed: approaching, maximal compression and distancing. Analysis on the efficiency of this process can be significant for development of the number and shape of the knives.

During the chopping process the stalk provides resistance against the **chopping blade** and a resistance torque can be calculated on the axis of the chopping unit, as shown on Figure 8.1(c). The range of the appeared peaks fall between 8 and 230 Nm. The high peaks can be caused by a numerical error. By decreasing the time-step of the DEM simulation these extremely high peaks will probably disappear. The calculated mean torque on the chopping unit was 11.8 Nm during the analysed period.

The phenomenon of the **first cut** provides very important information about the speed of the maize header unit; the speed ratios and positions of stalk rollers and chopping unit, see on Figure 8.1(d). This is an optimal case because the stalk rollers fix the stalk before the first cut, thus, the chance of losing the maize ear is reduced.

To analyse the working quality of the **chopping unit** the size distribution and shape of the chopped material can be used. On Figure 8.2, two types of chopped material can be observed: fibrous and cylindrical. In both cases the DEM predicted shape and the real one are very similar. For the fibrous chopped material the stalk was torn up during cutting or the chopping blade hit it several times, while the cylindrical chopped material is the result of two perfect cut on the stalk.

The gathering process can be described by the external loads and velocity of the maize ear. Figure 8.3(a) clearly shows two of the crucial phenomena: the detachment by the **deck plates** and a collision between the maize ear and the **gathering chain**. As it was expected, the detachment took place through a collision with the deck plates, that resulted in a detachment force of 489.4 N. This corresponds with the calibrated value, as shown in Chapter 7.2. Afterwards, the maize ear was transported into the gathering box by another collision with the gathering chains. These collisions are also observed on the characteristics of the magnitude velocity of the maize ear, as shown in 8.3(b). Beyond these results, an image-based analysis on the gathering process can be also advantageously exploited for machine development.

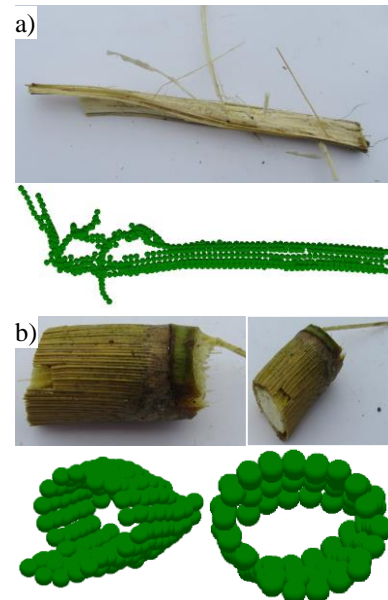


FIGURE 8.2: Fibrous a) and cylindrical b) chopped materials.

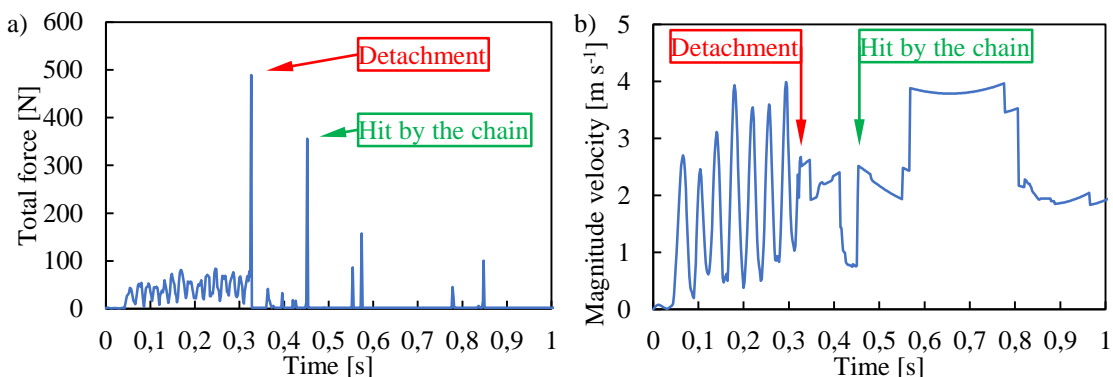


FIGURE 8.3: Process analysis on the detachment: a) total external force on the maize ear; b) magnitude velocity of the maize ear.

# 9 Conclusions and Recommendations

## 9.1 General Conclusions

The experiments in this thesis were carried out to explore the physical characteristics and mechanical behaviour of harvest-ready maize by using methods relating harvesting with a combine harvester. The conclusions drawn from the experimental work were used to form and calibrate a DEM model of the plant and advance the capability of DEM to reproduce the mechanical and breakage behaviour of fibrous agricultural materials. Finally, a simulation on maize harvesting was carried out to present a possible way for utilization of the model.

### 9.1.1 Experimental Work

A measurement method was established to determine the physical, morphological and mechanical properties of maize. The relationship among the physical and morphological properties and traits of maize were analysed based on in-situ and laboratorial measurements and observations. The typical mechanical behaviour, damage and breaking phenomena of maize parts were determined through sectional and local transversal compression, three-point bending, dynamic cutting, ear-detachment and ear-drop experiments.

The results of these experiments and observations prove that the natural structure of the plant is developed for growing an ear because the significance of the physical, morphological and mechanical properties and traits of maize parts below the maize ear is higher than the significance of its upper parts from the point of view of harvesting with a combine harvester. The presented results could be exploited advantageously to develop maize headers for combine harvesters.

### 9.1.2 DEM Simulations

Based on the measured and observed characteristics, the DEM model of the 4<sup>th</sup> internodal section was formed to simulate the transversely isotropic mechanical behaviour and breaking phenomena of the real material under scrutiny. An extensive parametric study was carried out to analyse the influence of the bonded input properties, moreover, based on a series of calibration experiments an optimization loop was established to obtain the most accurate mechanical behaviour of the model in each loading case simultaneously.

The DEM results correspond to the experimental results from the compression and the bending tests well, moreover, the required mechanical work for each experiment obtained from the DEM model was also close to the experimental results. The DEM simulated cutting process presents the typical stages of the real cutting process, while the breaking phenomenon of the virtual samples was similar to the observed phenomenon of the experiments in case of the compression and bending tests. Therefore, the results clearly show that the accuracy of the presented DEM model with the determined bonded parameter set is satisfactory to analyse the interactions among the maize stalk and the maize header during harvesting.

## 9.2 Recommendations for Future Work

Based on the results and the collected knowledge during the research, the following recommendations could be drawn for future work.

### 9.2.1 Experimental Work

The described measurement method was only tested on one maize variety from one experimental plot in the growing season of 2016. Thanks to the high diversity of maize varieties, it is not declared that the same physical or mechanical characteristics of maize can be obtained during the same experiments. Thus, the applied method should be extended to more samples, more maize species and different cultivating conditions to form a database on the physical, morphological and mechanical properties of maize during harvesting.

Several other physical (e.g. dynamic coefficient of friction), mechanical (e.g. soil-root relationship) and environmental (e.g. detailed fertilizing condition) properties can have an influence on maize harvesting, but our study only focuses on a few crucial properties. Thus, it is suggested to consider more properties that have a possible influence on the mechanical behaviour of the plant during harvesting.

The special apparatuses (plunger for local transversal compression, blade of dynamic cutting, apparatus for ear detachment force experiments, surfaces for drop test) were selected or designed based on the general parts of a combine harvester maize head. Thus, the applied apparatuses should be standardized.

The majority of the applied methods were quasi-static, however, the interaction among maize and machine parts takes place in milliseconds due to the operational parameters of a maize header. Thus, it is recommended to involve further experiments (e.g. field tests) to explore the mechanical behaviour of maize during rapid processes.

The mechanical behaviour of maize as related to the harvesting of shelled maize kernels were measured, observed and analysed. Accordingly, it is not justified that the measurement method is adaptable for other agricultural processes without consideration of major modifications.

### 9.2.2 DEM Simulations

The poly-disperse core of the first five internodes provides the majority of the computational costs. Thus, it is suggested to consider and analyse other geometrical structures to replace it.

The bonded structure between the poly-disperse core and the well-structured skin was proved to be the weakness of the bonded structure. Thus, it is recommended to consider a new bonded structure or method that ensures a better bond distribution here.

The results of the three-point bending, cantilever bending and local transversal compression simulations highlight the need for the development of the Timoshenko Beam Bonded Model (TBBM) to enable elastic-plastic (hardening) deformation of the virtual beam.

During the parametric study only a set of parameters were analysed in detail. Thus, it is suggested to involve more numerical parameters, especially regarding the dynamical behaviour of the DEM model, into the parametric study.

The results of the harvesting simulation could not be compared with experimental results. Again, it is highly recommended to involve further experiments (e.g. field tests) to improve the accuracy of the DEM model.

To keep the number of the variables under control, several assumptions and considerations were used during the model formation, parametric study and calibration through the optimization process. Thus, the presented results can be justified by using the same assumptions and considerations.

# 10 Theses

*The following theses can be drawn based on the experiments on the maize plant:*

**Thesis 1:** The mechanical resistance of the internodal stalk sections decreases as the equivalent internodal diameter decreases:

**Thesis 1.a:** An exponential relationship with a higher correlation coefficient than 0.95 between the mechanical work ( $W$ ) and the equivalent internodal diameter ( $d_e^{IN}$ ) was determined for sectional (Eq. 10.1) and local (Eq. 10.2) transversal compression, and for three-point bending (Eq. 10.3):

$$W^{SC} = 0.506 \cdot e^{0.1402 \cdot d_e^{IN}} \quad (d_e^{IN} = 5 - 25 \text{ mm}) \quad (10.1)$$

$$W^{LC} = 0.058 \cdot e^{0.2031 \cdot d_e^{IN}} \quad (d_e^{IN} = 5 - 25 \text{ mm}) \quad (10.2)$$

$$W^{TB} = 0.0459 \cdot e^{0.2376 \cdot d_e^{IN}} \quad (d_e^{IN} = 5 - 25 \text{ mm}) \quad (10.3)$$

**Thesis 1.b:** Taking into account the average diameter of the first node ( $\overline{d_{e1}^N} = 28.5 \pm 1.4 \text{ mm}$ ) and the bi-linear (Eq. 10.4 and 10.5) decreasing of the equivalent internodal diameter ( $d_e^{IN}$ ) from the bottom to the top of the stalk, more than 75% of the total mechanical work ( $p = 1 - 10$ ) is required to process the first five internodal sections ( $p = 1 - 5$ ), Equation 10.6:

$$d_e^{IN} = (-0.0594 \cdot p + 0.8673) \cdot \overline{d_{e1}^N} \quad (p = 1 - 5), \quad (10.4)$$

$$d_e^{IN} = (-0.0632 \cdot p + 0.8640) \cdot \overline{d_{e1}^N} \quad (p = 6 - 10), \quad (10.5)$$

$$W\% = \frac{\sum_{p=1}^{10} W - \sum_{p=6}^{10} W}{\sum_{p=1}^{10} W} \cdot 100\% \geq 75\%. \quad (10.6)$$

*Related publications:* [1]; [3]; [11]; [16].

**Thesis 2:** Based on the field observations on the harvest-ready maize plant, two different structural conditions of the shank can be determined:

- buckled, when a plastic joint was formed at one point of the shank;
- healthy, when there is no observable change on the shank.

A statistical two-sample t-test on the collected data justified that the detachment force required to separate the harvest-ready maize ear from the stalk is independent of the structural condition of the shank. Thus, an average detachment force of  $457.3 \pm 58.2 \text{ N}$  was determined by using all the collected data regardless the structural condition of the shank.

*Related publications:* [3]; [8]; [11]; [16].

**Thesis 3:** The coefficient of restitution among the harvest-ready maize ear, steel (S235, EN 10027) and plastic (Polyethylene, PE) plates is independent of the analysed directions of collision relative to the maize ear: axial and radial, as shown in Table 10.1:

TABLE 10.1: Coefficient of restitution among the maize ear and different plates.

	Radial	Axial
Steel (S235, EN 10027)	$0.34 \pm 0.05$	$0.34 \pm 0.04$
Polymer (Polyethylene, PE)	$0.42 \pm 0.03$	$0.41 \pm 0.09$

*Related publications:* [3]; [8]; [11]; [16].

*The following theses can be drawn based on the discrete element simulations on the maize plant:*

**Thesis 4:** Based on the biological structure of the maize plant, a special discrete element model was created that consists of spherical particles that are organized into complex (well-structured skin and poly-disperse core); hollow (well-structured skin) and chain of spheres geometrical substructures:

**Thesis 4.a:** A calibration method was established (Figure 10.1) to determine a possible combination of numerical parameters of the bonded (Timoshenko Beam Bond Model, TBBM) and non-bonded (Hertz-Mindlin Contact Model, HMCM) contact models describing the mechanical behaviour of the numerical maize plant. By using this combination of the numerical parameters it was justified that the mechanical behaviour of the model (stiffness, strength and breakage) is in a good agreement with the mechanical behaviour of the real maize plant in case of the applied experiments: sectional and local transversal compression; three-point bending; dynamic cutting; ear detachment and collision.

**Thesis 4.b:** It was justified that the experimentally validated complex discrete element model, that consists of spherical particles organized into a well-structured skin and a poly-disperse core, is capable of analysis the complex biological structure of the real stalk (*epidermis, cortex, medulla L.*) in case of quasi-static mechanical loadings resulting in residual deformation, when the internal structure plays an important role.

*Related publications:* [4]; [5]; [6]; [7]; [8]; [10]; [12]; [14]; [15].

**Thesis 5:** The influence of the location and direction of the external load, and the influence of the contact model parameters on the mechanical behaviour of the virtual maize plant were examined through a detailed sensitivity analysis:

**Thesis 5.a:** It was justified that the poly-disperse structure of the core compensates the loading direction dependency of the well-structured skin in the analysed loading cases, because the response of the model was identical in case of:

- compressing on the top, middle and bottom region of the internodal section during sectional transversal compression;
- cutting on a particle and between two particles of the skin during dynamic cutting;
- compressing and bending in different radial directions around the longitudinal axis ( $0^\circ - 45^\circ - 90^\circ - 135^\circ$ ) of the internodal section during sectional transversal compression and three-point bending.

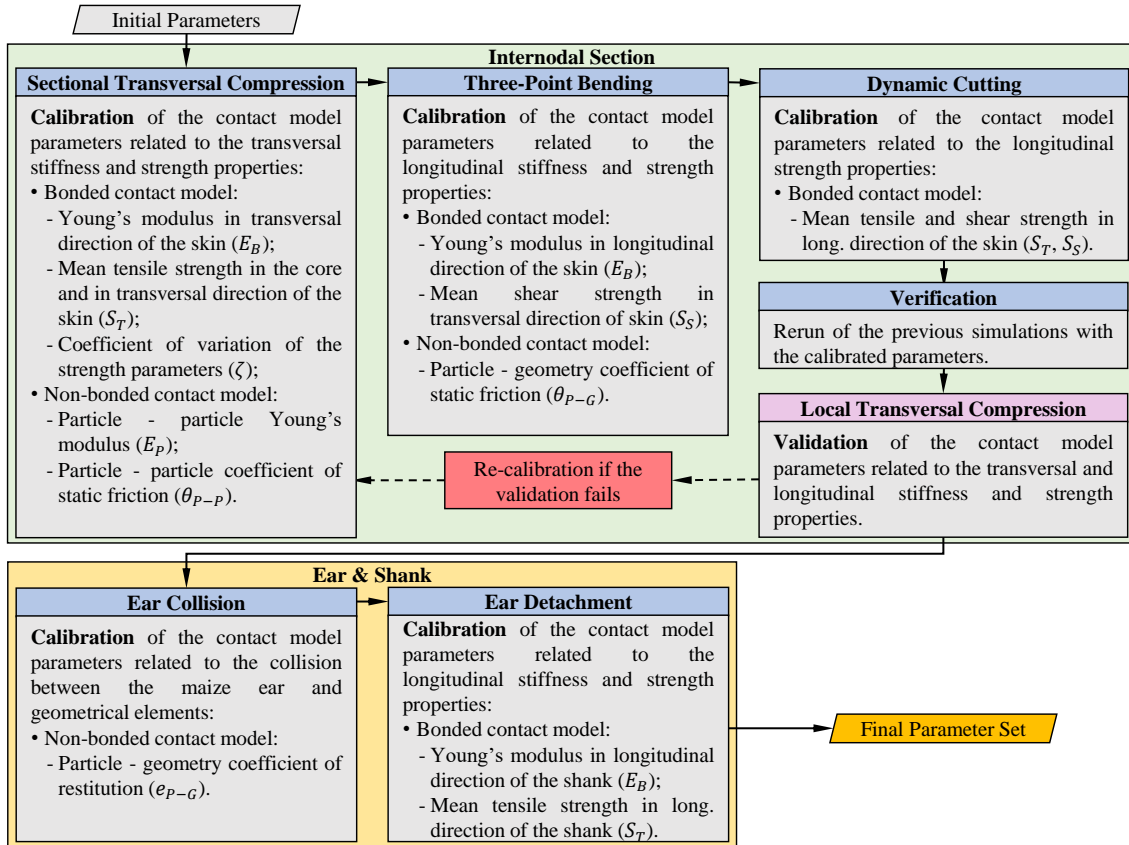


FIGURE 10.1: Calibration and validation method for the virtual maize plant.

TABLE 10.2: Range of the analysed contact model parameters.

Parameters of the bonded contact model (TBBM)					
Bonds	$E_B [MPa]$	$\nu_B [-]$	$S_T [MPa]$	$S_S [MPa]$	$\zeta [-]$
Skin, long.	2000-6000 ♠♦	0.1-0.4 ♠♦◊	100-1000 ◊	10-100 ◊	0.1-0.9 ♠♦◊
Skin, tr.	600-1800 ♣	0.1-0.4 ♣♦◊	10-100 ♣♦◊	5-15 ♣	0.1-0.9 ♣♦◊
Core	2-6 ♣	0.1-0.4 ♣♦◊	1-8 ♣♦	-	0.1-0.9 ♣♦◊
Ear & shank	200-600 ♡	-	20-60 ♡	-	-

Parameters of the non-bonded contact model (HMCM)				
Particles	$E_P [MPa]$	$\theta_{P-P} [-]$	$\theta_{P-G} [-]$	$e_{P-G} [-]$
Skin, core & shank	67.5-540 ♣	0.1-0.9 ♣	0.1-0.9 ♣◊	0.2-1.0 ◊
Ear	-	-	-	0.5-0.9 ⊙

Analysed by ♠ transversal compression; ♣ three-point bending; ◊ dynamic cutting;  
 ♡ ear-detachment and ⊙ ear-collision.

**Thesis 5.b:** The analysed range of the bonded contact model parameters (Timoshenko Beam Bond Model, TBBM) are shown in Table 10.2. The main influence of the bonded parameters on the mechanical behaviour of the virtual maize plant is determined in the following statements:

- In case of the **sectional transversal compression** experiment:
  - as the Young's modulus ( $E_B$ ) increases, the initial stiffness increases, the number of broken bonds increases and after the breakage of the skin the mechanical

resistance of the internodal section is higher;

- as the mean tensile strength in transversal direction of the skin ( $S_T^{S,tr.}$ ) increases, the number of broken bonds decreases in the skin;
- as the mean tensile strength in the core ( $S_T^C$ ) increases, the number of broken bonds decreases in the core, thus, the mechanical resistance of the internodal section is higher after the breakage of the skin;
- as the coefficient of variation of strength ( $\zeta$ ) increases, the number of broken bonds increases in the skin, thus, the transition between the initial and exponential sections of the force response is smoother.

– In case of the **three-point bending** experiment:

- as the Young's modulus in longitudinal direction of the skin ( $E_B^{S,long.}$ ) increases, the initial stiffness increases, the peak resistance force increases, the peak resistance force appears at lower displacement, the resistance of the bended cross-section is higher after the breakage and the number of longitudinal cracks in the skin increases;
- as the mean shear strength in transversal direction of the skin ( $S_S^{S,tr.}$ ) increases, the peak resistance force increases, the resistance of the bended cross-section is higher after the breakage and the number of longitudinal cracks in the skin decreases.

– In case of the **dynamic cutting** experiment:

- as the mean tensile strength in longitudinal direction of the skin ( $S_T^{S,long.}$ ) increases, the peak cutting force increases, the required cutting work increases, the bending resistance after cutting is higher and the resulted cutting surface is less even;
- as the mean shear strength in longitudinal direction of the skin ( $S_S^{S,long.}$ ) increases, the peak cutting force decreases, the required cutting work increases and the resulted cutting surface is less even.

– In case of the **ear detachment** experiment:

- as the Young's modulus in longitudinal direction of the shank ( $E_B^{SH}$ ) increases, the stiffness of the shank increases, while the detachment takes place at lower displacement;
- as the mean tensile strength between the shank and ear ( $S_T^{SH\&ME}$ ) increases, the ear detachment force increases, while the detachment takes place at higher displacement.

**Thesis 5.c:** The analysed range of the non-bonded contact model parameters (Hertz-Mindlin Contact Model, HMCM) are shown in Table 10.2. The main influence of the non-bonded parameters on the mechanical behaviour of the virtual maize plant is determined in the following statements:

- as the particle-particle Young's modulus ( $E_P$ ) and the particle-particle coefficient of static friction ( $\theta_{P-P}$ ) increases, the mechanical resistance of the internodal section is higher after the breakage of the skin in case of **sectional transversal compression**;
- as the particle-geometry coefficient of static friction ( $\theta_{P-G}$ ) increases, the mechanical resistance is higher after the breakage of the bended cross-section in case of **three-point bending**;
- in case of the **ear collision** test, the relationship between the bounce height of the ear ( $E^{ME}=27 \text{ GPa}$ ,  $\rho^{St}=930 \text{ kg} \cdot \text{m}^{-3}$ ) and the particle-geometry coefficient of restitution ( $e_{P-G}^{ME} = 0.5 - 1.0$ ) can be determined with a higher correlation coefficient than 0.95 as:

- a second order function (10.7) for steel ( $E^{St}=200 \text{ GPa}$ ,  $\rho^{St}=7850 \text{ kg} \cdot \text{m}^{-3}$ ) plate:

$$H^{St} = 1284.1 \cdot (e_{P-G}^{ME})^2 - 1336.5 \cdot (e_{P-G}^{ME}) + 385.14 \quad (10.7)$$

- a third order function (10.8) for polyethylene ( $E^{St}=0.7 \text{ GPa}$ ,  $\rho^{St}=950 \text{ kg} \cdot \text{m}^{-3}$ ) plate:

$$H^{Pl} = 3303.5 \cdot (e_{P-G}^{ME})^3 - 5489 \cdot (e_{P-G}^{ME})^2 + 3090 \cdot (e_{P-G}^{ME}) - 557.66 \quad (10.8)$$

*Related publications:* [2]; [5]; [8]; [10].



# 11 Tézisek

*A kukoricanövényen elvégzett vizsgálatok alapján a következő téziseket fogalmaztam meg:*

**1. Tézis:** A kukoricanövény szárát alkotó szárszakaszok mechanikai ellenállása a következők szerint csökken a szárszakaszok egyenértékű átmérőjének csökkenésével:

**1.a. Tézis:** Az összenyomáshoz, illetve hajlításhoz szükséges mechanikai munka ( $W$ ) legalább 0.95-ös korrelációs tényező értékkel a szártag egyenértékű átmérőjével ( $d_e^{IN}$ ) exponenciálisan arányos szakaszos (11.1) és helyi (11.2) oldalirányú összenyomás; valamint hárompontos hajlítás (11.3) esetén:

$$W^{SC} = 0.506 \cdot e^{0.1402 \cdot d_e^{IN}} \quad (d_e^{IN} = 5 - 25 \text{ mm}) \quad (11.1)$$

$$W^{LC} = 0.058 \cdot e^{0.2031 \cdot d_e^{IN}} \quad (d_e^{IN} = 5 - 25 \text{ mm}) \quad (11.2)$$

$$W^{TB} = 0.0459 \cdot e^{0.2376 \cdot d_e^{IN}} \quad (d_e^{IN} = 5 - 25 \text{ mm}) \quad (11.3)$$

**1.b. Tézis:** Ismerve az első szárcsomó átlagos átmérőjét ( $\overline{d_{e1}^N} = 28.5 \pm 1.4 \text{ mm}$ ), továbbá figyelembe véve a szártagok egyenértékű átmérőjének ( $d_e^{IN}$ ) bi-lineáris összefüggés (11.4, 11.5) szerinti csökkenését a talajfelszíntől számítva a teljes szár feldolgozásához szükséges mechanikai munka több mint 75%-a a kukoricacső alatti szárszakaszok ( $p = 1 - 5$ ) mechanikai ellenállásából származik a 11.6. összefüggés alapján:

$$d_e^{IN} = (-0.0594 \cdot p + 0.8673) \cdot \overline{d_{e1}^N} \quad (p = 1 - 5), \quad (11.4)$$

$$d_e^{IN} = (-0.0632 \cdot p + 0.8640) \cdot \overline{d_{e1}^N} \quad (p = 6 - 10), \quad (11.5)$$

$$W\% = \frac{\sum_{p=1}^{10} W - \sum_{p=6}^{10} W}{\sum_{p=1}^{10} W} \cdot 100\% \geq 75\%. \quad (11.6)$$

*Kapcsolódó publikációk: [1]; [3]; [11]; [16].*

**2. Tézis:** Szántóföldön végzett megfigyelések alapján, a betakarításhoz megfelelően érett kukoricacsövet tartó szárszakasz szerkezeti állapota kétféle lehet:

- hajlott, amikor a szárszakasz egy pontján képlékeny csukló alakult ki;
- ép, amikor a szárszakaszon nem látható szerkezeti változás.

Statisztikai kétmintás t-próbát alkalmazva megállapítottam azt, hogy a kukoricacső leválasztásához szükséges erő független a kukoricacsövet tartó szárszakasz szerkezeti állapotától. Az összes minta felhasználásával a kukoricacső leválasztásához szükséges átlagos erő  $457.3 \pm 58.2 \text{ N}$ -ra adódott.

*Kapcsolódó publikációk: [3]; [8]; [11]; [16].*

**3. Tézis:** A betakarításhoz megfelelően érett kukoricacső és acél (S235, EN 10027), valamint polimer (Polietilén, PE) lemezek ütközési tényezőjének értéke független attól, hogy az ütközés a kukoricacsőhöz viszonyított axiális vagy radiális irányban következett be, 11.1. táblázat:

TABLE 11.1: Kukoricacső ütközési tényezője különböző felületeken.

	Radiális	Axiális
Acél (S235, EN 10027)	$0.34 \pm 0.05$	$0.34 \pm 0.04$
Polimer (Polietilén, PE)	$0.42 \pm 0.03$	$0.41 \pm 0.09$

Kapcsolódó publikációk: [3]; [8]; [11]; [16].

*A diszkrét elemek módszerén alapuló szimulációk alapján a következő téziseket fogalmaztam meg:*

**4. Tézis:** A kukoricanövény szerkezeti felépítése alapján összeállítottam egy olyan diszkrét elemes modellt, amelyet gömb alakú elemekből létrehozott összetett (rendezett struktúrájú szárfal és polidiszperz struktúrájú szárbél), üreges (rendezett struktúrájú szárfal) és gömbsor geometriai struktúrájú részmodellek alkotnak:

**4.a. Tézis:** Kidolgoztam egy kalibrálási módszert (11.1. ábra), amely eredményül a kukoricanövény diszkrét elemes modelljének mechanikai viselkedését leíró gerenda (Timoshenko Beam Bond Model, TBBM) és szemcsés (Hertz-Mindlin Contact Model, HMC) kapcsolati modellek paramétereinek egy lehetséges kombinációját adja. A paraméterek ezen kombinációját felhasználva bizonyítottam, hogy a modell által visszaadott mechanikai jellemzők (merevség, szilárdság, tönkremenetel) kellő pontossággal közelítik a valós kukoricanövény mechanikai viselkedését az alkalmazott vizsgálatok esetén: szakaszos és helyi oldalirányú összenyomás; háromponos hajlítás; dinamikus vágás; cső leválasztó és ejtő vizsgálat.

**4.b. Tézis:** Igazoltam, hogy a kísérletekkel validált, gömb alakú diszkrét elemekből felépített rendezett struktúrájú szárfalfarból és polidiszperz struktúrájú szárbélből álló modell alkalmas a kukoricaszár összetett biológiai felépítésének (*epidermis, cortex, medulla L.*) elemzésére maradó alakváltozással járó kvázi statikus terhelések során, amikor a belső struktúrának is kiemelt szerepe van.

Kapcsolódó publikációk: [4]; [5]; [6]; [7]; [8]; [10]; [12]; [14]; [15].

**5. Tézis:** A kukoricanövény modellen elvégzett részletes numerikus érzékenységvizsgálat során elemeztem a külső terhelés helyének és irányának, valamint az elemek között definiált kapcsolati modellek paramétereinek hatását a modell mechanikai viselkedésére:

**5.a. Tézis:** Bizonyítottam, hogy a polidiszperz struktúrájú szárbél kiegyenlíti a szárfal rendezett struktúrájából adódó kitüntetett tönkremeneti irányok hatását a vizsgált terhelések esetén, ugyanis

- a modell érzéketlen a külső terhelés helyére a szárszakasz mentén, szárszakasz közepére vagy a szárcsomóhoz közelebbi része, szakaszos oldalirányú nyomó vizsgálat esetén;
- a modell érzékelten a vágókés behatolási pontjára, két diszkrét elem között vagy egy diszkrét elemen, dinamikus vágómunka vizsgálat esetén;
- a modell érzéketlen a külső terhelés irányára, a szárszakasz hosszanti tengelye körüli  $0^\circ - 45^\circ - 90^\circ - 135^\circ$  irányokban vizsgálva, szakaszos oldalirányú nyomó és háromponos hajlító vizsgálatok esetén.

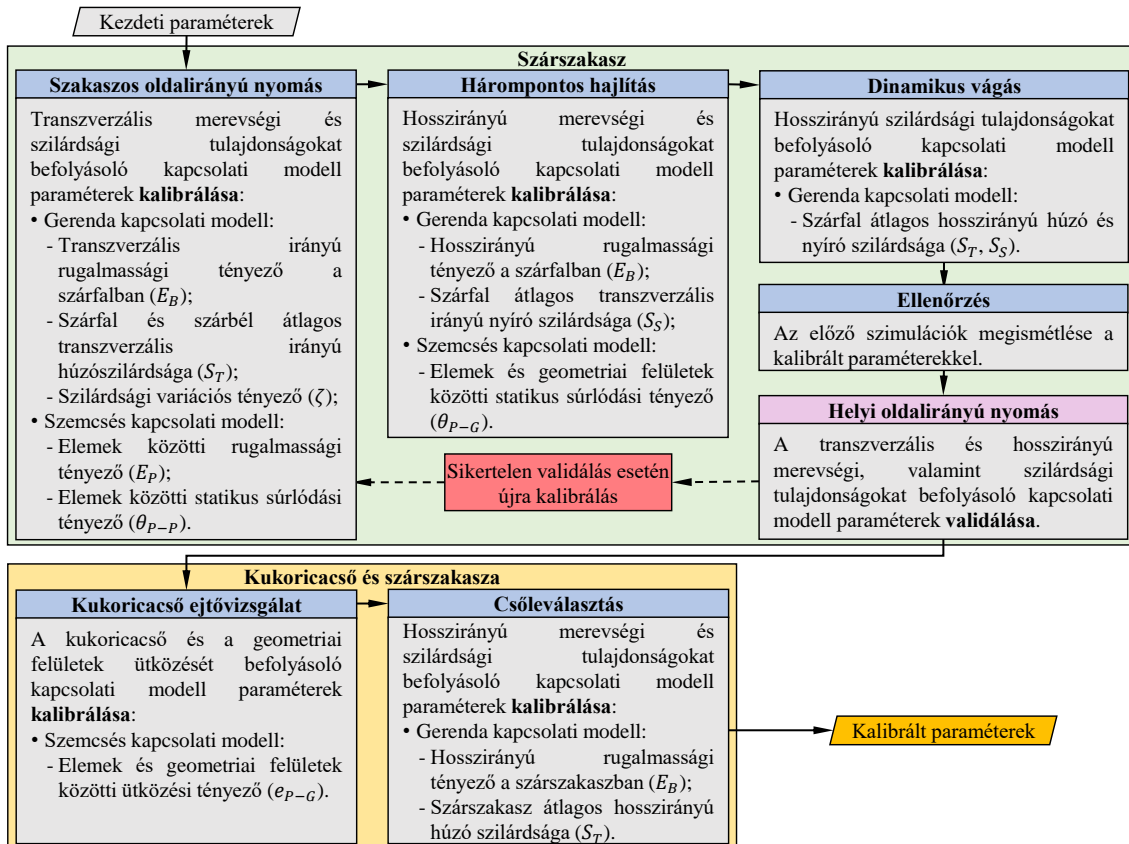


FIGURE 11.1: A kukoricanövény DEM modelljének kalibrálási és validálási módszere.

TABLE 11.2: A paraméterérzékenység vizsgálat során elemzett paraméterek érték tartományai.

Gerenda kapcsolati modell (TBBM) mechanikai paraméterei					
Kapcsolatok	$E_B [MPa]$	$\nu_B [-]$	$S_T [MPa]$	$S_S [MPa]$	$\zeta [-]$
Szárfal, h.	2000-6000 ♠♦	0.1-0.4 ♠♦◊	100-1000 ◊	10-100 ◊	0.1-0.9 ♠♦◊
Szárfal, tr.	600-1800 ♣	0.1-0.4 ♠♦◊	10-100 ♠♦◊	5-15 ♣	0.1-0.9 ♣♦◊
Szárbel	2-6 ♣	0.1-0.4 ♠♦◊	1-8 ♠♦	-	0.1-0.9 ♣♦◊
Cső és szár	200-600 ♩	-	20-60 ♩	-	-

Szemcsés kapcsolati modell (HMCM) mechanikai paraméterei				
Szemcsék	$E_P [MPa]$	$\theta_{P-P} [-]$	$\theta_{P-G} [-]$	$e_{P-G} [-]$
Szárfal, szárbel & szár	67.5-540 ♣	0.1-0.9 ♣	0.1-0.9 ♠♦◊	0.2-1.0 ◊
Kukorica cső	-	-	-	0.5-0.9 ⊙

Oldalirányú nyomó ♣; hárompontos hajlító ♠; dinamikus vágó ◊;  
csőleválasztó ♩ és cső ejtő ⊙ vizsgálatokkal elemezve.

**5.b. Tézis:** A kukoricanövényt leíró diszkrét elemes gerenda kapcsolati modell (Timoshenko Beam Bond Model, TBBM) paramétereit a 11.2. táblázatban látható tartományokban vizsgáltam. Megállapítottam, hogy:

- a szárszakaszon végzett **szakaszos oldalirányú nyomás** modellezése esetén:
  - az elemek között definiált rugalmassági tényező ( $E_B$ ) növekedésével a szárszakasz kezdeti merevsége növekedett, a szárfalban megijenő törések száma növe-

- kedett, illetve a szárszakasz ellenállása a szárfal tönkremenetelét követően növekedett;
- a szárfal transzverzális irányában definiált átlagos húzó szilárdság ( $S_T^{S,tr.}$ ) növekedésével szárfalban megjelenő törések száma csökkent;
  - a szárbélben definiált átlagos húzó szilárdság ( $S_T^C$ ) növekedésével a szárbélben megjelenő törések száma csökkent, így a szárszakasz ellenállása növekedett a szárfal tönkremenetelét követően;
  - a szárszakaszban definiált szilárdsági variációs tényező ( $\zeta$ ) növekedésével a szárfalban megjelenő törések száma növekedett, ezáltal lágyabbá vált a kezdeti és az exponenciális növekedési szakasz közötti átmenet.
- a szárszakaszon végzett **hárompontos hajlítás** modellezése esetén:
- a szárfal hosszirányában definiált rugalmassági tényező ( $E_B^{S,long.}$ ) növekedésével a szárszakasz kezdeti merevsége növekedett, a maximális ellenállása növekedett, a maximális ellenállás kisebb elmozdulásnál jelent meg, a hajlított keresztmetszet tönkremenetele utáni ellenállása növekedett, a szárfal hosszirányú töréseinek száma növekedett;
  - a szárfal transzverzális irányában definiált átlagos nyírószilárdságának ( $S_S^{S,tr.}$ ) növekedésével a szárszakasz maximális ellenállása növekedett, a hajlított keresztmetszet tönkremenetele utáni ellenállása növekedett, valamint a szárfalban megjelenő hosszirányú törések száma csökkent.
- a szárszakaszon végzett **dinamikus vágás** modellezése esetén:
- a szárfal hosszirányában definiált átlagos húzó szilárdság ( $S_T^{S,long.}$ ) növekedésével a maximális vágóerő értéke, a vágómunka, a szárszakasz átvágás utáni ellenállása növekedett, valamint a vágási felület egyenetlensége növekedett;
  - a szárfal hosszirányában definiált átlagos nyíró szilárdság ( $S_S^{S,long.}$ ) növekedésével a maximális vágóerő értéke csökkent, a teljes vágómunka értéke, valamint a vágási felület egyenetlensége növekedett.
- a kukoricacsövet tartó szárszakaszon végzett **csőleválasztó vizsgálat** modellezése esetén:
- a szárszakasz hosszirányában definiált rugalmassági tényező ( $E_B^{SH}$ ) növekedésével a szárszakasz merevsége növekedett, miközben a csőleválasztáshoz szükséges elmozdulás értéke csökkent;
  - a szárszakasz és a kukoricacső között definiált átlagos húzó szilárdság ( $S_T^{SH&ME}$ ) növekedésével a cső leválasztásához szükséges erő, valamint a csőleválasztáshoz szükséges elmozdulás értéke növekedett.

**5.c. Tézis:** A kukoricanövényt leíró diszkrét elemes szemcsés kapcsolati modell (Hertz-Mindlin Contact Model, HMCM) paramétereit a 11.2. táblázatban látható tartományokban vizsgáltam. Megállapítottam, hogy:

- a szárszakaszon végzett **szakaszos oldalirányú nyomás** modellezése esetén, az elemek között definiált rugalmassági tényező ( $E_P$ ), illetve az elemek között definiált statikus súrlódási tényező ( $\theta_{P-P}$ ) növekedésével a szárszakasz ellenállása a szárfal tönkremenetelét követően növekedett;
- a szárszakaszon végzett **hárompontos hajlítás** modellezése esetén, az elemek és a geometriai felületek között definiált statikus súrlódási tényező ( $\theta_{P-G}$ ) növekedésével a szárszakasz ellenállása növekedett a hajlított keresztmetszet tönkremenetele után;
- a kukoricacsövön végzett **ejtővizsgálat** modellezése esetén, a kukoricacső ( $E^{ME}=27$  GPa,  $\rho^{St}=930 \text{ kg} \cdot \text{m}^{-3}$ ) visszapattanási magassága, legalább 0.95-ös korrelációs tényező értékkel:

- másodrendű összefüggés (11.7) szerint változik az elemek és geometriai felületek között definiált ütközési tényezőtől ( $e_{P-G}^{ME} = 0.5 - 1.0$ ), acélra jellemző anyagtulajdonságú ( $E^{St}=200 \text{ GPa}$ ,  $\rho^{St}=7850 \text{ kg} \cdot \text{m}^{-3}$ ) lemezfelület,

$$H^{St} = 1284.1 \cdot (e_{P-G}^{ME})^2 - 1336.5 \cdot (e_{P-G}^{ME}) + 385.14 \quad (11.7)$$

- illetve harmadrendű összefüggés (11.8) szerint változik az elemek és geometriai felületek között definiált ütközési tényezőtől ( $e_{P-G}^{ME} = 0.5 - 1.0$ ), polietilénre jellemző anyagtulajdonságú ( $E^{St}=0.7 \text{ GPa}$ ,  $\rho^{St}=950 \text{ kg} \cdot \text{m}^{-3}$ ) lemezfelület esetén:

$$H^{Pl} = 3303.5 \cdot (e_{P-G}^{ME})^3 - 5489 \cdot (e_{P-G}^{ME})^2 + 3090 \cdot (e_{P-G}^{ME}) - 557.66 \quad (11.8)$$

*Kapcsolódó publikációk: [2]; [5]; [8]; [10].*



## 12 Összefoglalás

A numerikus modellezés hatékony mérnöki eszköz, így napjainkban az ipar számos területén sikeresen alkalmazzák. Ezzel szemben a mezőgazdasági anyagok és a velük kapcsolatba lépő mezőgazdasági berendezések közötti kölcsönhatások modellezése még gyerekcipőben jár. Ezért alapvetően a mezőgazdasági termények összetett szerkezete és mechanikai viselkedése, valamint a berendezésekben zajló összetett folyamatok felelősek. Ebből adódóan, PhD kutatásom során egy olyan Diszkrét Elemes Modell (DEM) megalkotására és validálására vállalkoztam, amely alkalmas a kukoricanövény betakarításának vizsgálatára.

Az irodalomkutatás során hamar világossá vált, hogy a kukoricanövény fizikai, morfológiai és mechanikai jellemzőit illetően kevés szakirodalom érhető el, így saját mérési eljárást alkottam. Az új módszer kialakítása során figyelembe vettet a kukoricanövény szemes betakarítása során fellépő jelenségeket és folyamatokat, valamint a numerikus modell paramétereinek meghatározásához szükséges adatokat. Az így meghatározott szántóföldi és laboratóriumi méréseket és megfigyeléseket sikeresen hajtottam végre a kísérleti állomány betakarítása során. A kukoricaszár fizikai paramétereit illetően a szártagok egyenértékű átmérőjének, hosszának, tömegének és nedvességtartalmának eloszlását vizsgáltam a kukoricaszár hossza mentén. A kukoricacsövek helyzete, alakja, átmérője, hossza és tömege, valamint a termést tartó szárszakasz átmérője és hossza szintén meghatározásra kerültek. A szárok mechanikai viselkedése szakaszos és lokális oldalirányú nyomóvizsgálat, hárompontos hajlítóvizsgálat, befogott hajlítóvizsgálat és dinamikus vágómunka-vizsgálat útján kerültek elemzésre. Ezzel párhuzamosan a termés és a termést tartó szárszakasz mechanikai viselkedését csőleválasztó és ejtővizsgálatokkal elemeztem. A mérési eredmények egyértelműen azt mutatják, hogy a kukoricanövény különböző részei nagyban eltérő fizikai és mechanikai tulajdonságokat mutatnak. Ebből adódóan a modellépítés során célszerű a különböző részeket különböző részletességgel szimulálni.

A DEM modellépítés során a növény legfontosabb részeire koncentráltam, így a szár, a kukoricacső és a csövet tartó szárszakasz modelljét dolgoztam ki. A szár esetében egy összetett szárfal-szárbél modell került kidolgozásra, amely a valós növény szerkezeti felépítésén alapul. A csövet tartó szárszakaszt egy egyszerűbb gömbsor modell alkotja. A kukoricacsövet, amely egyetlen diszkrét elem, több gömbhéj felület alkotja. Az adott geometriai struktúrába rendezett elemeket a gerenda kapcsolati modell (*Timoshenko Beam Bond Model, TBBM*) tartja össze, így létrehozva a növény szerkezetét. A kapcsolati és numerikus paraméterek hatását a növény különböző részeit reprezentáló modellek mechanikai viselkedésére és tönkrementelére egy átfogó paraméterérzékenység vizsgálat során határoztam meg, amelyhez a valós laboratóriumi mérések modelljeit használtam. Ahhoz, hogy a modell minél pontosabban képes legyen különböző terhelési esetekben megjósolni a valós növényi rész mechanikai és tönkremeneti viselkedését, kalibrálási folyamatot hoztam létre, amely során a legkedvezőbb paraméter-összehozzáírás határozható meg. A kalibrálási folyamat során a numerikus és a valós mérési eredmények kerültek összevetésre. Az eredmények egyértelműen azt mutatják, hogy a létrehozott kukoricanövény modell és a meghatározott paraméterek megfelelők a növény és gép közötti kölcsönhatások elemzésére.



# Bibliography

- Abedi, G. and E. Ahmadi (2013). "Design and evaluation a pendulum device to study postharvest mechanical damage in fruits: bruise modeling of red delicious apple". In: *Australian Journal of Crop Science* 7.7, pp. 962–968. ISSN: 1835-2707.
- Alexandratos, N. and J. Bruinsma (2012). "World agriculture towards 2030/2050: the 2012 revision". In: *ESA Working paper, FAO* 12.03, pp. 1–154.
- Azadbakht, M, A Rezaei Asl, and K Tamaskani Zahedi (2014). "Energy requirement for cutting corn stalks (Single Cross 704 var.)" In: *International Journal of Biological, Veterinary, Agricultural and Food Engineering* 8.5, pp. 1–4.
- Bagi, K. (2007). *A diszkret elemek modszere*. BME Tartoszerkezetek Mechanikaja Tanszek. ISBN: 978-963-420-929-4.
- Bakeer, B. et al. (2013). "On the characterisation of structure and properties of sorghum stalks". In: 4, pp. 265–271. ISSN: 2090-4479. DOI: [10.1016/j.asej.2012.08.001](https://doi.org/10.1016/j.asej.2012.08.001).
- Brown, N.J., J.F. Chen, and J.Y. Ooi (2014). "A bond model for DEM simulation of cementitious materials and deformable structures". In: *Granular Matter* 16.3, pp. 299–311. ISSN: 1434-5021, 1434-7636. DOI: [10.1007/s10035-014-0494-4](https://doi.org/10.1007/s10035-014-0494-4).
- Celik, H.K., A.E.W. Rennie, and I. Akinci (2011). "Deformation behaviour simulation of an apple under drop case by finite element method". In: *Journal of Food Engineering* 104.2, pp. 293–298. ISSN: 02608774. DOI: [10.1016/j.jfoodeng.2010.12.020](https://doi.org/10.1016/j.jfoodeng.2010.12.020).
- Chen, Y., J.L. Gratton, and J. Liu (2004). "Power Requirements of Hemp Cutting and Conditioning". In: *Biosystems Engineering* 87.4, pp. 417–424. ISSN: 1537-5110. DOI: [10.1016/j.biosystemseng.2003.12.012](https://doi.org/10.1016/j.biosystemseng.2003.12.012).
- Chen, Y. et al. (2007). "Effect of harvest date on shearing force of maize stems". In: *Livestock Science* 111.1–2, pp. 33–44. ISSN: 18711413. DOI: [10.1016/j.livsci.2006.11.013](https://doi.org/10.1016/j.livsci.2006.11.013).
- Coetzee, C.J. (2017). "Review: Calibration of the discrete element method". In: *Powder Technology* 310, pp. 104–142. ISSN: 0032-5910. DOI: [10.1016/j.powtec.2017.01.015](https://doi.org/10.1016/j.powtec.2017.01.015).
- Coetzee, C.J. and D.N.J. Els (2009). "Calibration of discrete element parameters and the modelling of silo discharge and bucket filling". In: *Computers and Electronics in Agriculture* 65.2, pp. 198–212. ISSN: 0168-1699. DOI: [10.1016/j.compag.2008.10.002](https://doi.org/10.1016/j.compag.2008.10.002).
- Coetzee, C.J. and S.G. Lombard (2013). "The destemming of grapes: Experiments and discrete element modelling". In: *Biosystems Engineering* 114.3, pp. 232–248. ISSN: 1537-5110. DOI: [10.1016/j.biosystemseng.2012.12.014](https://doi.org/10.1016/j.biosystemseng.2012.12.014).
- Cundall, P.A. and O.D.L. Strack (1979). "A discrete numerical model for granular assemblies". In: *Geotechnique* 29.1, pp. 47–65.
- Dange, A.R., S.K. Thakare, and I.B. Rao (2011). "Cutting energy and force as required for Pigeon pea stems". In: *Journal of Agricultural Technology* 7.6, pp. 1485–1493.
- DEM Solutions (2017). *EDEM User Manual and Documentation*. DEM Solutions Ltd, Edinburgh, UK.
- Di Paolo, E. and M. Rinaldi (2008). "Yield response of corn to irrigation and nitrogen fertilization in a Mediterranean environment". In: *Field Crops Research* 105.3, pp. 202–210. ISSN: 03784290. DOI: [10.1016/j.fcr.2007.10.004](https://doi.org/10.1016/j.fcr.2007.10.004).
- Forell, G.V. et al. (2015). "Preventing lodging in bioenergy crops: a biomechanical analysis of maize stalks suggests a new approach". In: *Journal of Experimental Botany* 66, pp. 4367–4371. ISSN: 0022-0957, 1460-2431. DOI: [10.1093/jxb/erv108](https://doi.org/10.1093/jxb/erv108).

- He, L. et al. (2017). "Effect of fruit location on apple detachment with mechanical shaking". In: *Biosystems Engineering* 157, pp. 63–71. ISSN: 1537-5110. DOI: [10.1016/j.biosystemseng.2017.02.009](https://doi.org/10.1016/j.biosystemseng.2017.02.009).
- Heckwolf, S. et al. (2015). "Image analysis of anatomical traits in stalk transections of maize and other grasses". In: *Plant Methods* 11.1, pp. 1–10. ISSN: 1746-4811. DOI: [10.1186/s13007-015-0070-x](https://doi.org/10.1186/s13007-015-0070-x).
- Homayoun, H. (2011). "Study of some morphological traits of corn hybrids". In: *American-Eurasian Journal of Agricultural and Environmental Sciences* 10.5, pp. 810–813.
- Horabik, J. et al. (2017). "Determination of the restitution coefficient of seeds and coefficients of visco-elastic Hertz contact models for DEM simulations". In: *Biosystems Engineering* 161, pp. 106–119. ISSN: 1537-5110. DOI: [10.1016/j.biosystemseng.2017.06.009](https://doi.org/10.1016/j.biosystemseng.2017.06.009).
- Huang, J. et al. (2016). "Mechanical properties of maize fibre bundles and their contribution to lodging resistance". In: *Biosystems Engineering* 151, pp. 298–307. ISSN: 1537-5110. DOI: [10.1016/j.biosystemseng.2016.09.016](https://doi.org/10.1016/j.biosystemseng.2016.09.016).
- Igathinathane, C., A.R. Womac, and S. Sokhansanj (2010). "Corn stalk orientation effect on mechanical cutting". In: *Biosystems Engineering* 107.2, pp. 97–106. ISSN: 1537-5110. DOI: [10.1016/j.biosystemseng.2010.07.005](https://doi.org/10.1016/j.biosystemseng.2010.07.005).
- Igathinathane, C. et al. (2006). "Mass and moisture distribution in aboveground components of standing corn plants". In: *Transactions of the ASABE* 49.1, pp. 97–106. ISSN: 2151-0040. DOI: [10.13031/2013.20217](https://doi.org/10.13031/2013.20217).
- Igathinathane, C. et al. (2009). "Size reduction of high- and low-moisture corn stalks by linear knife grid system". In: *Biomass and Bioenergy* 33.4, pp. 547–557. ISSN: 0961-9534. DOI: [10.1016/j.biombioe.2008.09.004](https://doi.org/10.1016/j.biombioe.2008.09.004).
- Igathinathane, C. et al. (2011). "Fast and simple measurement of cutting energy requirement of plant stalk and prediction model development". In: *Industrial Crops and Products* 33.2, pp. 518–523. ISSN: 0926-6690. DOI: [10.1016/j.indcrop.2010.10.015](https://doi.org/10.1016/j.indcrop.2010.10.015).
- Jia, H. et al. (2013). "Design of Bionic Saw Blade for Corn Stalk Cutting". In: *Journal of Bionic Engineering* 10, pp. 497–505. ISSN: 1672-6529. DOI: [10.1016/S1672-6529\(13\)60242-5](https://doi.org/10.1016/S1672-6529(13)60242-5).
- Jindal, V.K. and N.N. Mohsenin (1978). "Dynamic hardness determination of corn kernels from impact tests". In: *Journal of Agricultural Engineering Research* 23, pp. 77–84.
- Jünemann, D., S. Kemper, and L. Frerichs (2013). "Simulation of stalks in agricultural processes - Applications of the Discrete Element Method". In: *Landtechnik* 68.3, pp. 164–167.
- Johnson, K.L. (1987). *Contact mechanics*. Cambridge University Press. ISBN: 978-0521347969.
- Johnson, P.C. et al. (2012). "Cutting energy characteristics of Miscanthus x giganteus stems with varying oblique angle and cutting speed". In: *Biosystems Engineering* 112.1, pp. 42–48. ISSN: 1537-5110. DOI: [10.1016/j.biosystemseng.2012.02.003](https://doi.org/10.1016/j.biosystemseng.2012.02.003).
- Kattenstroth, R., H.H. Harms, and L. Frerichs (2012). "Influence of the straw alignment on the cutting quality of a combine's straw chopper". In: *Landtechnik* 67.4, pp. 244–246.
- Kemper, S., L. Thorsten, and L. Frerichs (2014). "The overlaid cut in a disc mower - results from field tests and simulation". In: *Landtechnik* 69.4, pp. 171–175.
- Keppler, I. et al. (2012). "Grain velocity distribution in a mixed flow dryer". In: *Advanced Powder Technology* 23.6, pp. 824–832. ISSN: 0921-8831. DOI: [10.1016/j.apt.2011.11.003](https://doi.org/10.1016/j.apt.2011.11.003).
- Labra, C. and E. Onate (2009). "High-density sphere packing for discrete element method simulations". In: *Communications in Numerical Methods in Engineering* 25, pp. 837–849. DOI: [10.1002/cnm.1193](https://doi.org/10.1002/cnm.1193).
- Leblanc, T. et al. (2015). "Mechanical analysis of the bending behaviour of plant stems". In: *Biosystems Engineering* 129, pp. 87–99. ISSN: 1537-5110. DOI: [10.1016/j.biosystemseng.2014.09.016](https://doi.org/10.1016/j.biosystemseng.2014.09.016).
- Leblanc, T. et al. (2016a). "A discrete element approach for modelling bendable crop stems". In: *Computers and Electronics in Agriculture* 124, pp. 141–149. ISSN: 0168-1699. DOI: [10.1016/j.compag.2016.03.022](https://doi.org/10.1016/j.compag.2016.03.022).

- Leblcq, T. et al. (2016b). "A discrete element approach for modelling the compression of crop stems". In: *Computers and Electronics in Agriculture* 123, pp. 80–88. ISSN: 01681699. DOI: [10.1016/j.compag.2016.02.018](https://doi.org/10.1016/j.compag.2016.02.018).
- Lenaerts, B. et al. (2014). "Simulation of grain-straw separation by Discrete Element Modeling with bendable straw particles". In: *Computers and Electronics in Agriculture* 101, pp. 24–33. ISSN: 0168-1699. DOI: [10.1016/j.compag.2013.12.002](https://doi.org/10.1016/j.compag.2013.12.002).
- Li, H. et al. (2012). "CFD-DEM simulation of material motion in air-and-screen cleaning device". In: *Computers and Electronics in Agriculture* 88, pp. 111–119. ISSN: 0168-1699. DOI: [10.1016/j.compag.2012.07.006](https://doi.org/10.1016/j.compag.2012.07.006).
- Li, Y. et al. (2016). "Development and application of mechanized maize harvesters". In: *International journal of agricultural and biological engineering* 9.3, pp. 15–28.
- Liang, L. and Y. Guo (2011). "Relationship between stalk shear strength and morphological traits of stalk crops". In: *International Conference on Agricultural and Biosystems Engineering*, pp. 288–290.
- Liang, Z. et al. (2016). "Sensor for monitoring rice grain sieve losses in combine harvesters". In: *Biosystems Engineering* 147, pp. 51–66. ISSN: 1537-5110. DOI: [10.1016/j.biosystemseng.2016.03.008](https://doi.org/10.1016/j.biosystemseng.2016.03.008).
- Ma, J. and J.F. Maystadt (2017). "The impact of weather variations on maize yields and household income: Income diversification as adaptation in rural China". In: *Global Environmental Change* 42, 93–106. ISSN: 09593780. DOI: [10.1016/j.gloenvcha.2016.12.006](https://doi.org/10.1016/j.gloenvcha.2016.12.006).
- Mathanker, S.K., T.E. Grift, and A.C. Hansen (2015). "Effect of blade oblique angle and cutting speed on cutting energy for energycane stems". In: *Biosystems Engineering* 133, pp. 64–70. ISSN: 1537-5110. DOI: [10.1016/j.biosystemseng.2015.03.003](https://doi.org/10.1016/j.biosystemseng.2015.03.003).
- Nagy, J. (2006). *Maize production*. Akademiai Kiado. ISBN: 978-963-05-8636-8.
- İnce, A. et al. (2005). "Bending and shearing characteristics of sunflower stalk residue". In: *Biosystems Engineering* 92.2, pp. 175–181. ISSN: 15375110. DOI: [10.1016/j.biosystemseng.2005.07.003](https://doi.org/10.1016/j.biosystemseng.2005.07.003).
- Niklas, K.J. (1992). *Plant Biomechanics - An Engineering Approach to Plant Form and Function*. The University of Chicago Press. ISBN: 0-226-58641-6.
- O'Dogherty, M.J. (1982). "A review of research on forage chopping". In: *Journal of Agricultural Engineering Research* 27.4, pp. 267–289. ISSN: 0021-8634. DOI: [10.1016/0021-8634\(82\)90068-3](https://doi.org/10.1016/0021-8634(82)90068-3).
- Olmedo, I. et al. (2016). "Discrete element model of the dynamic response of fresh wood stems to impact". In: 120, pp. 13–22. ISSN: 0141-0296. DOI: [10.1016/j.engstruct.2016.03.025](https://doi.org/10.1016/j.engstruct.2016.03.025).
- Pasha, M. et al. (2016). "Effect of particle shape on flow in discrete element method simulation of a rotary batch seed coater". In: *Powder Technology* 296, pp. 29–36. ISSN: 0032-5910. DOI: [10.1016/j.powtec.2015.10.055](https://doi.org/10.1016/j.powtec.2015.10.055).
- Prasad, J. and C.P. Gupta (1975). "Mechanical properties of maize stalk as related to harvesting". In: *Journal of Agricultural Engineering Research* 20.1, pp. 79–87. ISSN: 00218634. DOI: [10.1016/0021-8634\(75\)90098-0](https://doi.org/10.1016/0021-8634(75)90098-0).
- Rayleigh, J.W.S. (1885). "On waves propagated along the plane surface of an elastic solid". In: *Proceedings of the London Mathematical Society* IV, pp. 42–43. DOI: [10.1002/cbdv.200490137](https://doi.org/10.1002/cbdv.200490137).
- Robertson, D. et al. (2014). "An improved method for accurate phenotyping of corn stalk strength". In: *Crop Science* 54.5, pp. 2038–2044. ISSN: 0011-183X. DOI: [10.2135/cropsci2013.11.0794](https://doi.org/10.2135/cropsci2013.11.0794).
- Robertson, D.J., S.L. Smith, and D.D. Cook (2015). "On measuring the bending strength of septate grass stems". In: *American Journal of Botany* 102.1, pp. 5–11. ISSN: 0002-9122, 1537-2197. DOI: [10.3732/ajb.1400183](https://doi.org/10.3732/ajb.1400183).
- Robertson, D.J. et al. (2015). "Corn stalk lodging: a forensic engineering approach provides insights into failure patterns and mechanisms". In: *Crop Science* 55.6, pp. 2833–2841. ISSN: 0011-183X. DOI: [10.2135/cropsci2015.01.0010](https://doi.org/10.2135/cropsci2015.01.0010).

- Salarikia, A. et al. (2017). "Finite element analysis of the dynamic behavior of pear under impact loading". In: 4, pp. 64–77. ISSN: 2214-3173. DOI: [10.1016/j.inpa.2016.12.003](https://doi.org/10.1016/j.inpa.2016.12.003).
- Sheng, Y. et al. (2004). "Numerical studies of uniaxial powder compaction process by 3D DEM". In: *Engineering Computations* 21.2, pp. 304–317. DOI: [10.1108/02644400410519802](https://doi.org/10.1108/02644400410519802).
- Tongdi, Q., L. Yaoming, and C. Jin (2011). "Experimental study on flexural mechanical properties of corn stalks". In: *IEEE*, pp. 130–134. DOI: [10.1109/ICAE.2011.5943766](https://doi.org/10.1109/ICAE.2011.5943766).
- Torregrosa, A. et al. (2014). "Analysis of the detachment of citrus fruits by vibration using artificial vision". In: *Biosystems Engineering* 119, 1–12. ISSN: 1537-5110. DOI: [10.1016/j.biosystemseng.2013.12.010](https://doi.org/10.1016/j.biosystemseng.2013.12.010).
- Yiljep, Y.D. and U.S. Mohammed (2005). "Effect of Knife Velocity on Cutting Energy and Efficiency during Impact Cutting of Sorghum Stalk". In: *Agricultural Engineering International: the CIGR EJournal* 7, pp. 1–10.
- Yousefi, S., H. Farsi, and K. Kheiralipour (2016). "Drop test of pear fruit: Experimental measurement and finite element modelling". In: *Biosystems Engineering* 147, pp. 17–25. ISSN: 1537-5110. DOI: [10.1016/j.biosystemseng.2016.03.004](https://doi.org/10.1016/j.biosystemseng.2016.03.004).
- Yu, Y., H. Fu, and J. Yu (2015). "DEM-based simulation of the corn threshing process". In: *Advanced Powder Technology* 26.5, pp. 1400–1409. ISSN: 09218831. DOI: [10.1016/j.apt.2015.07.015](https://doi.org/10.1016/j.apt.2015.07.015).
- Yu, Y.J. et al. (2011). "Design of 3-D DEM boundary modelling software". In: *Trans. Chinese Soc. Agric. Mach.* 42.1, pp. 98–103.
- Zhan, Z. et al. (2013). "DEM simulation and physical testing of rice seed impact against a grain loss sensor". In: *Biosystems Engineering* 116.4, pp. 410–419. ISSN: 1537-5110. DOI: [10.1016/j.biosystemseng.2013.10.002](https://doi.org/10.1016/j.biosystemseng.2013.10.002).
- Zhang, K. et al. (2017). "Research on mechanical properties of corn stalk". In: *AIP Conference Proceedings*, pp. 1–7. DOI: [10.1063/1.4977311](https://doi.org/10.1063/1.4977311).
- Zhong-Zhen, S. et al. (2013). "The viscoelasticity model of corn straw under the different moisture contents". In: *Mathematical Problems in Engineering* 2013, pp. 1–5. ISSN: 1024-123X, 1563-5147. DOI: [10.1155/2013/320207](https://doi.org/10.1155/2013/320207).

## A Experimental Results



FIGURE A.1: Observed maize ears.

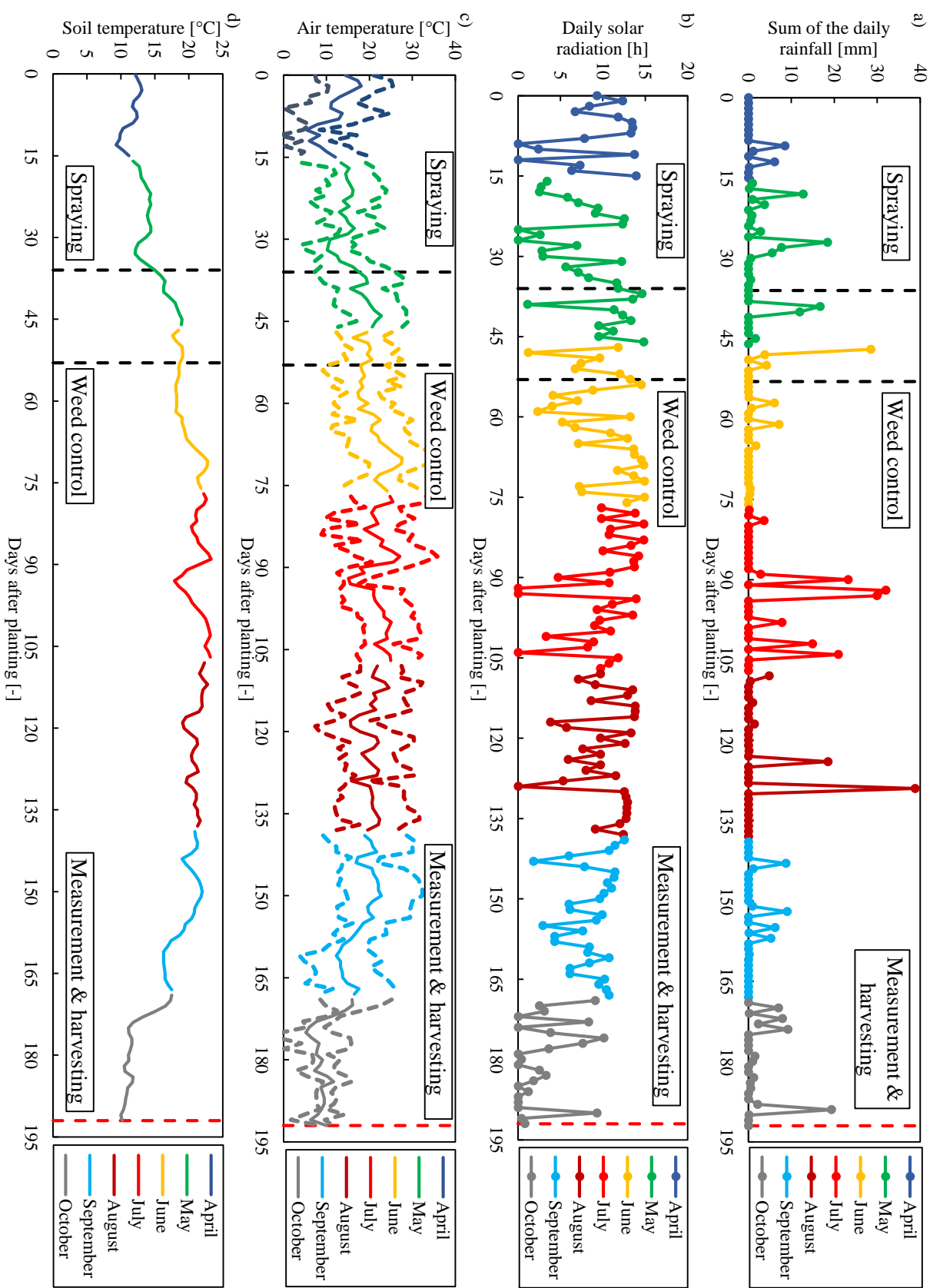


FIGURE A.2: Meteorological data from the experimental plot: a) sum of the daily rainfall; b) daily solar radiation; c) min., mean and max. air temperature; d) soil temperature at depth of 0.1 m.

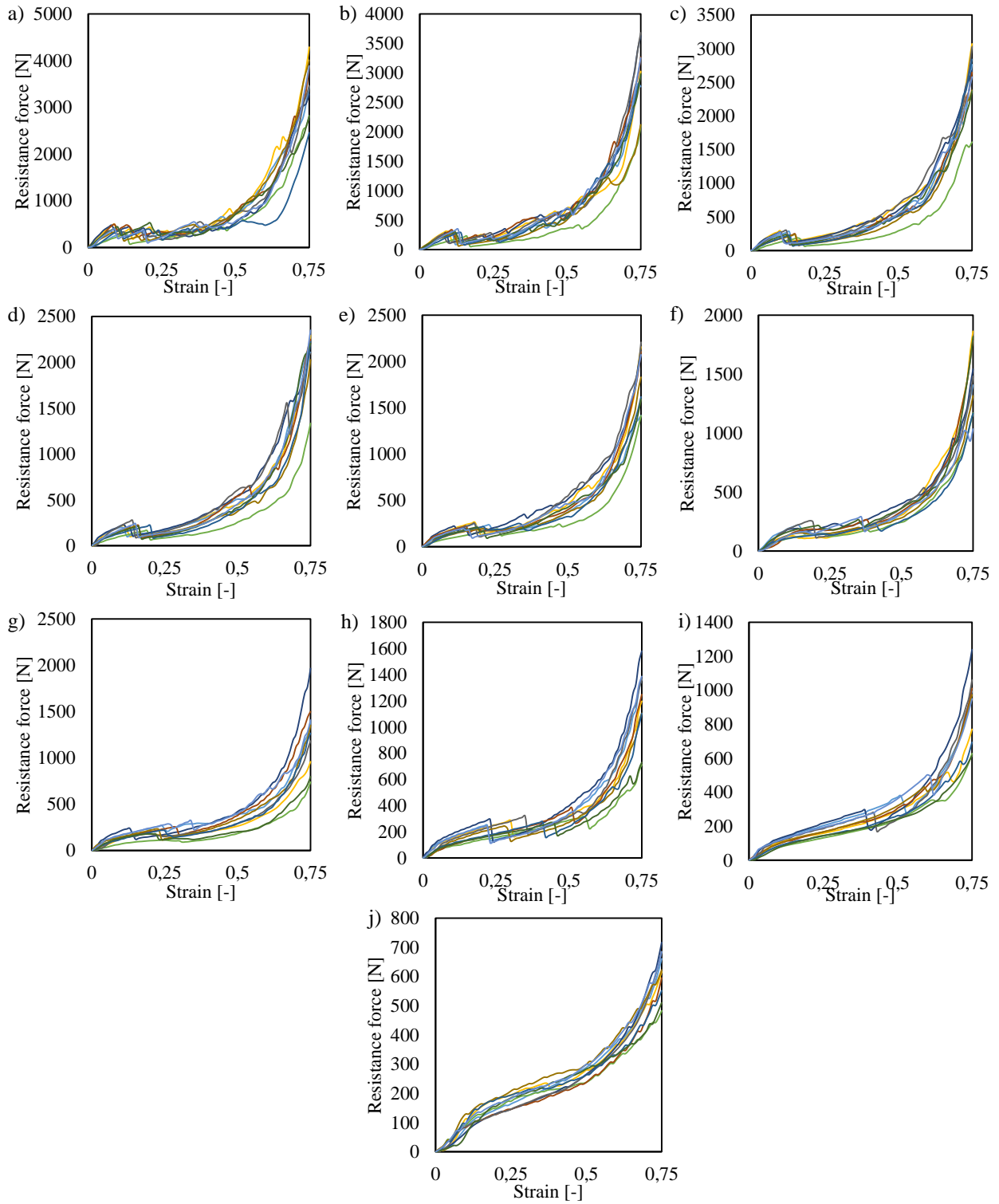


FIGURE A.3: Each measured force response on the 1<sup>st</sup> (a), 2<sup>nd</sup> (b), 3<sup>rd</sup> (c), 4<sup>th</sup> (d), 5<sup>th</sup> (e), 6<sup>th</sup> (f), 7<sup>th</sup> (g), 8<sup>th</sup> (h), 9<sup>th</sup> (i), 10<sup>th</sup> (j) internodal section by sectional transversal compression.

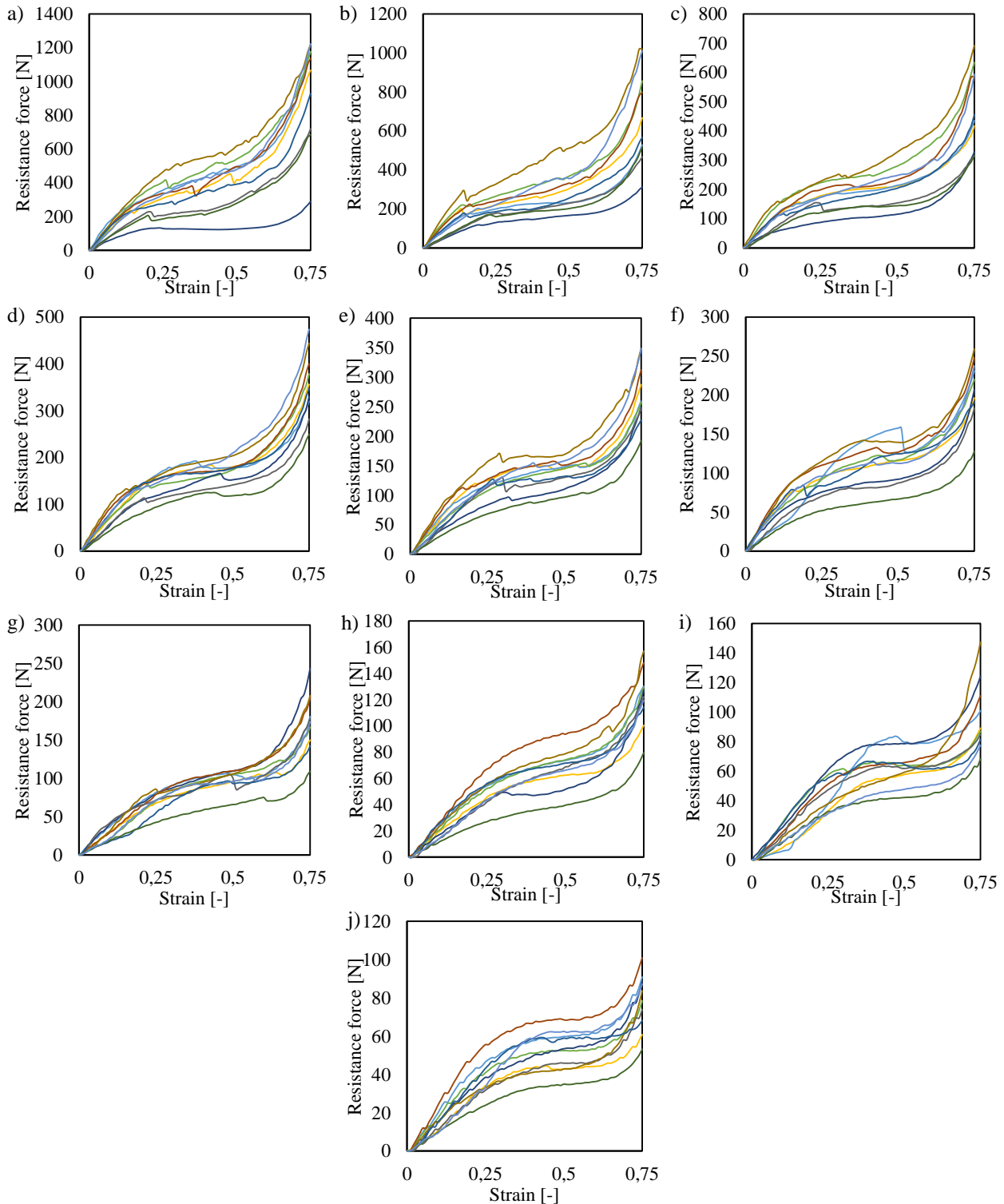


FIGURE A.4: Each measured force response on the 1<sup>st</sup> (a), 2<sup>nd</sup> (b), 3<sup>rd</sup> (c), 4<sup>th</sup> (d), 5<sup>th</sup> (e), 6<sup>th</sup> (f), 7<sup>th</sup> (g), 8<sup>th</sup> (h), 9<sup>th</sup> (i), 10<sup>th</sup> (j) internodal section by local transversal compression.

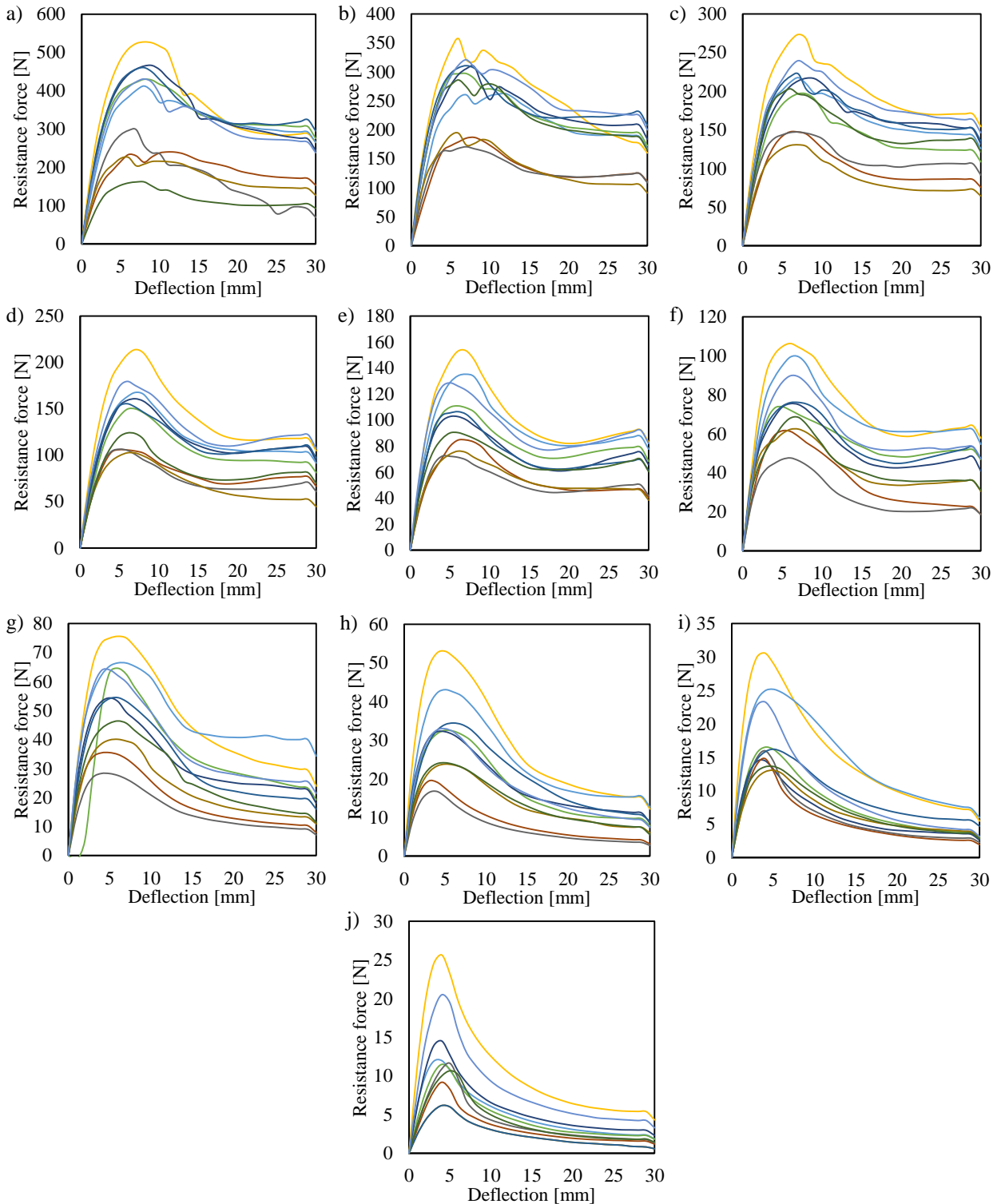


FIGURE A.5: Each measured force response on the 1<sup>st</sup> (a), 2<sup>nd</sup> (b), 3<sup>rd</sup> (c), 4<sup>th</sup> (d), 5<sup>th</sup> (e), 6<sup>th</sup> (f), 7<sup>th</sup> (g), 8<sup>th</sup> (h), 9<sup>th</sup> (i), 10<sup>th</sup> (j) internodal section by three-point bending.

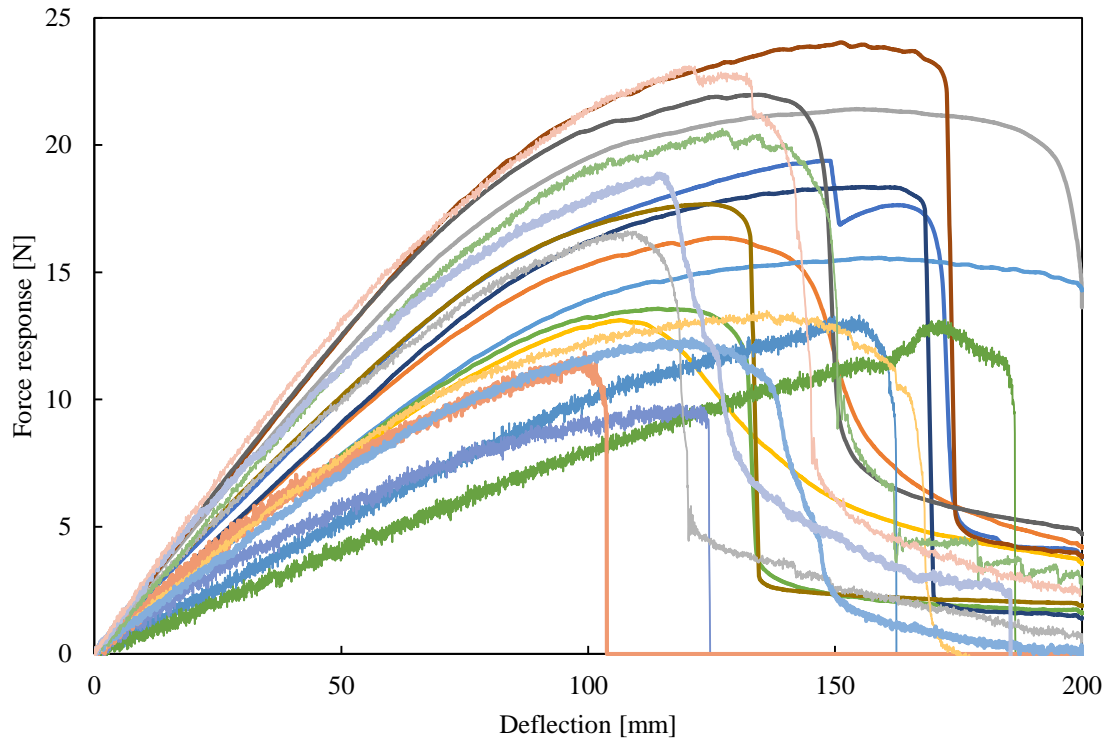


FIGURE A.6: Each measured force response by cantilever bending.

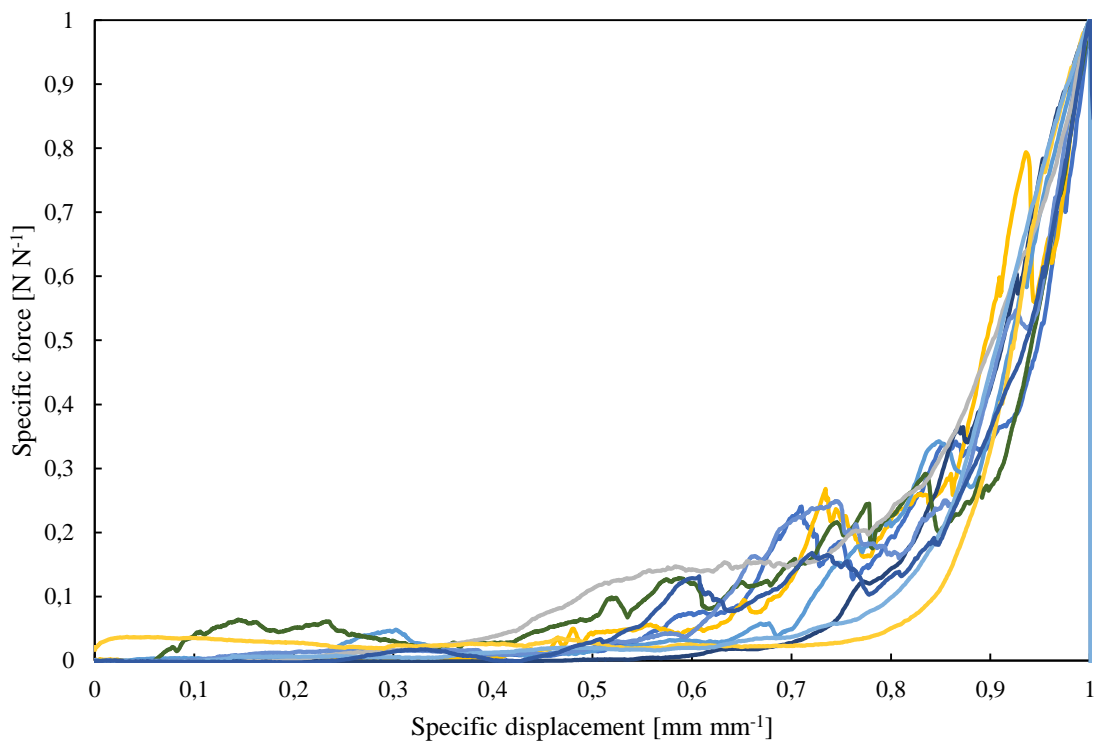


FIGURE A.7: Each measured force response by ear-detachment.

## B Reference Models

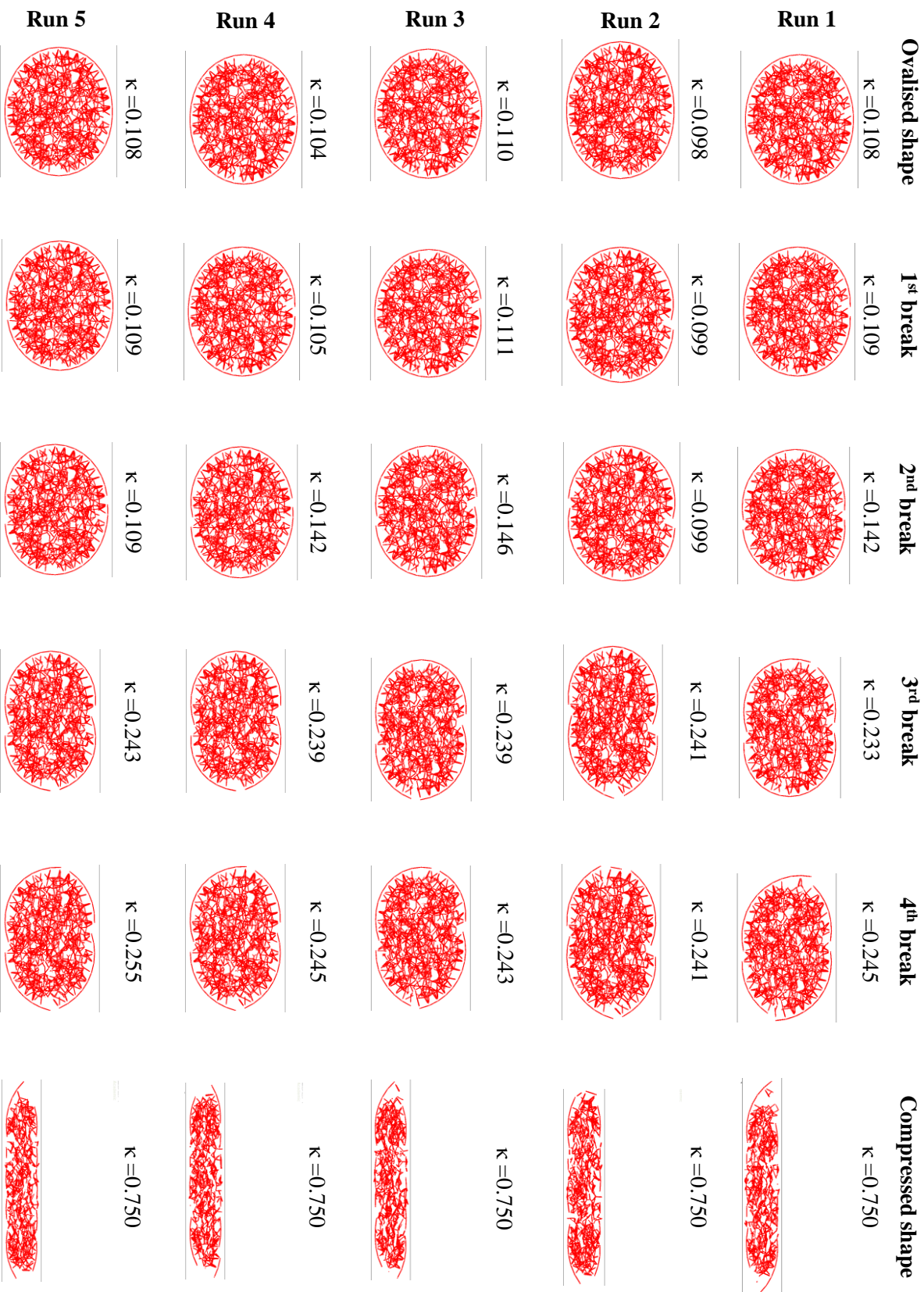


FIGURE B.1: Breakage during the reference simulation cases of sectional transversal compression: the existing bonds among the particles are visualized by red lines between the centre of the bonded particles.

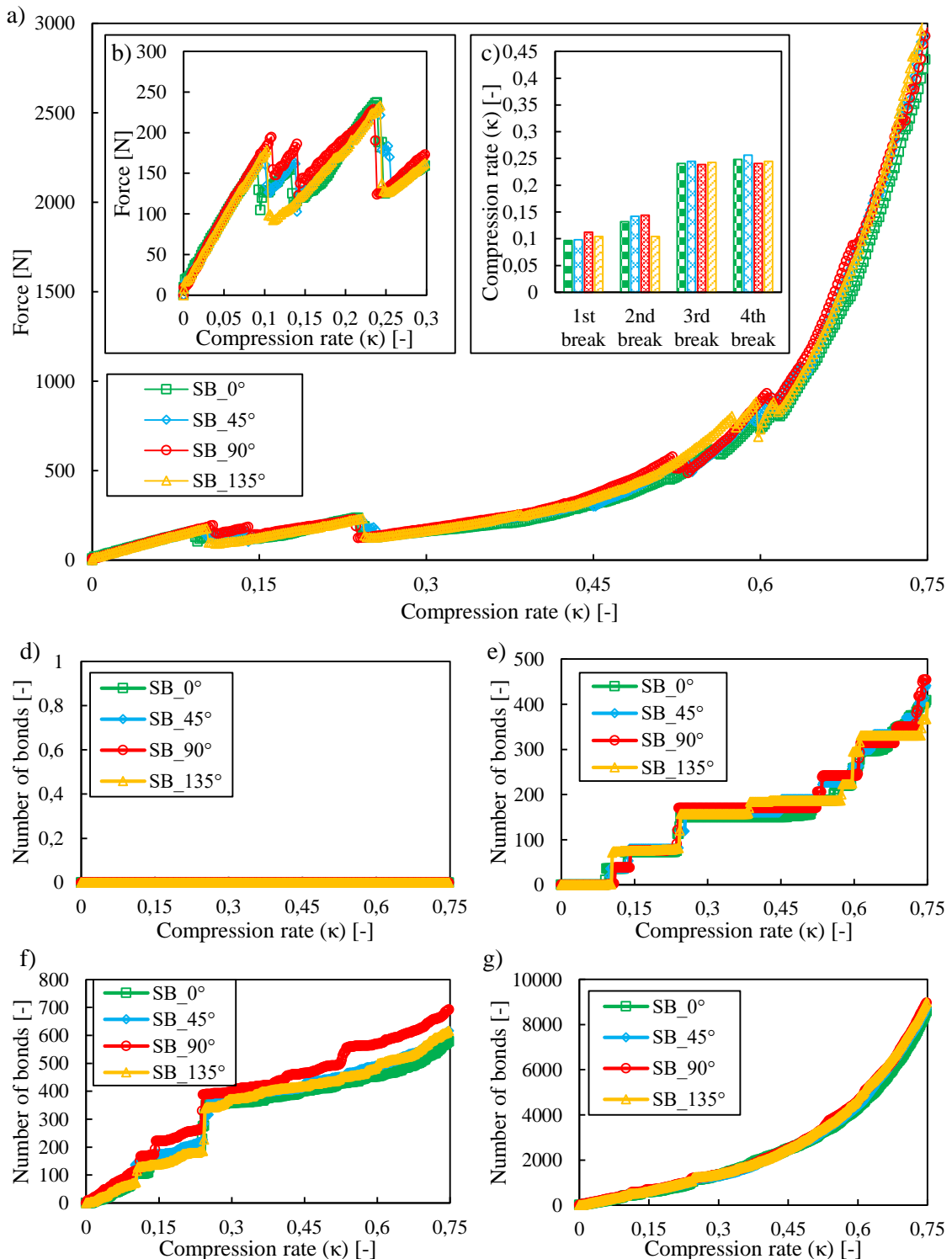


FIGURE B.2: Results of the analysis on the loading direction at the bottom position by sectional transversal compression: a) overall force-compression rate characteristics; b) force-compression rate characteristics in range of 0-0.3 compression rate; c) major break events in tangential direction of the skin; d) broken bonds of the skin in longitudinal direction; e) broken bonds of the skin in tangential direction; f) broken bonds between the skin and the core; g) broken bonds in the core.

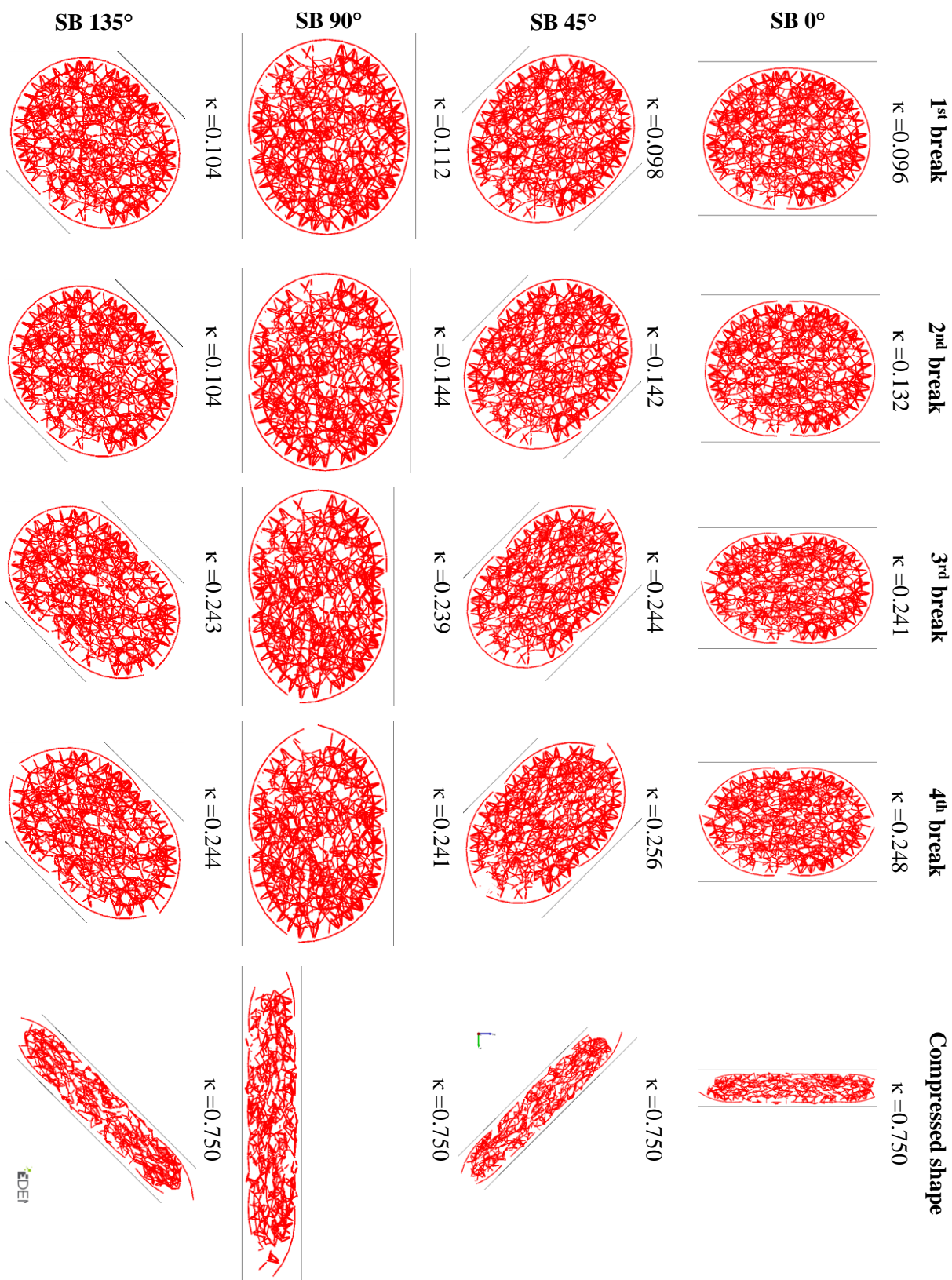


FIGURE B.3: Breakage during the analysis on the loading direction at the bottom position by sectional transversal compression (the existing bonds among the particles are visualized by red lines between the centre of the bonded particles).

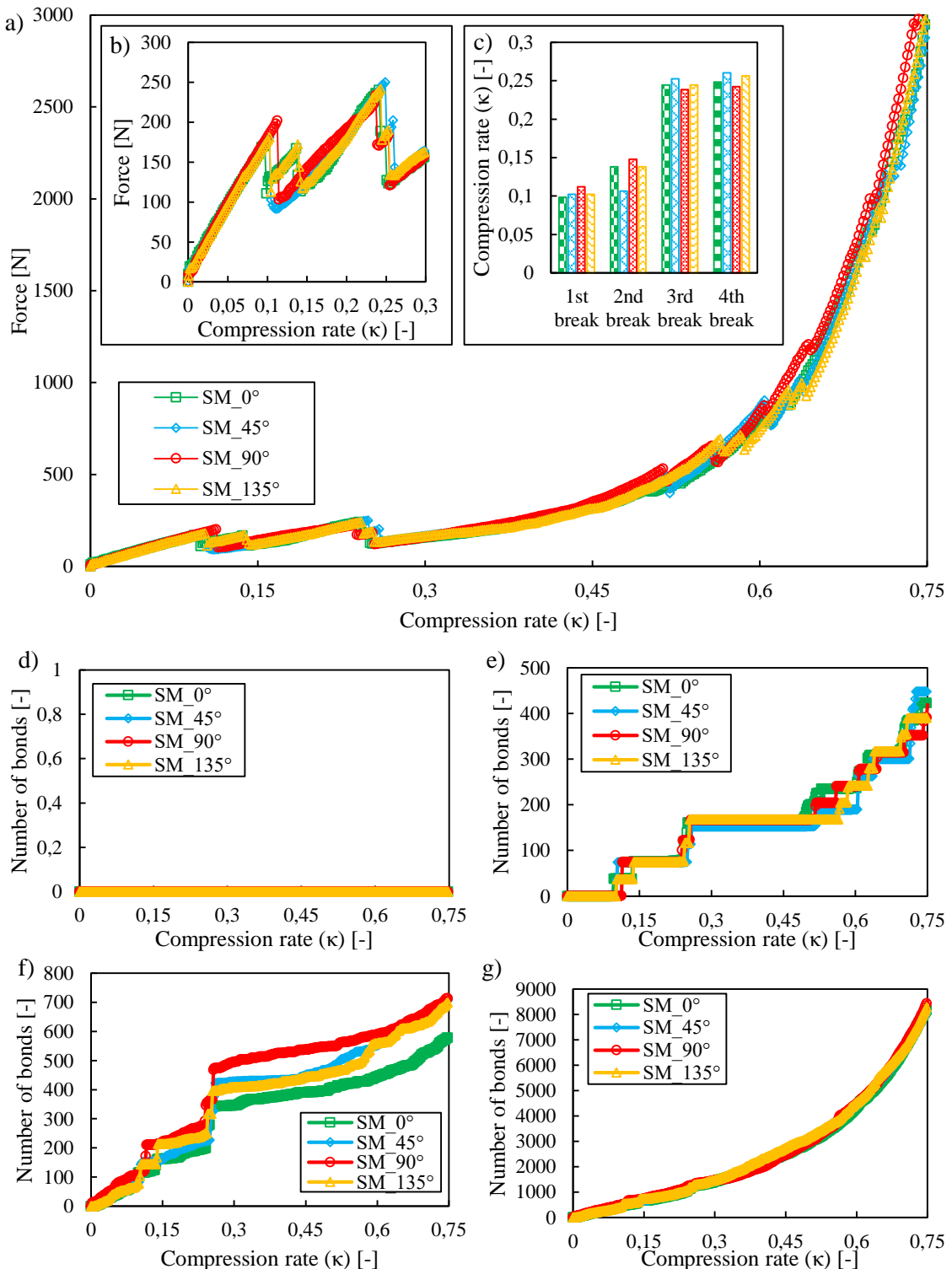


FIGURE B.4: Results of the analysis on the loading direction at the middle position by sectional transversal compression: a) overall force-compression rate characteristics; b) force-compression rate characteristics in range of 0-0.3 compression rate; c) major break events in tangential direction of the skin; d) broken bonds of the skin in longitudinal direction; e) broken bonds of the skin in tangential direction; f) broken bonds between the skin and the core; g) broken bonds in the core.

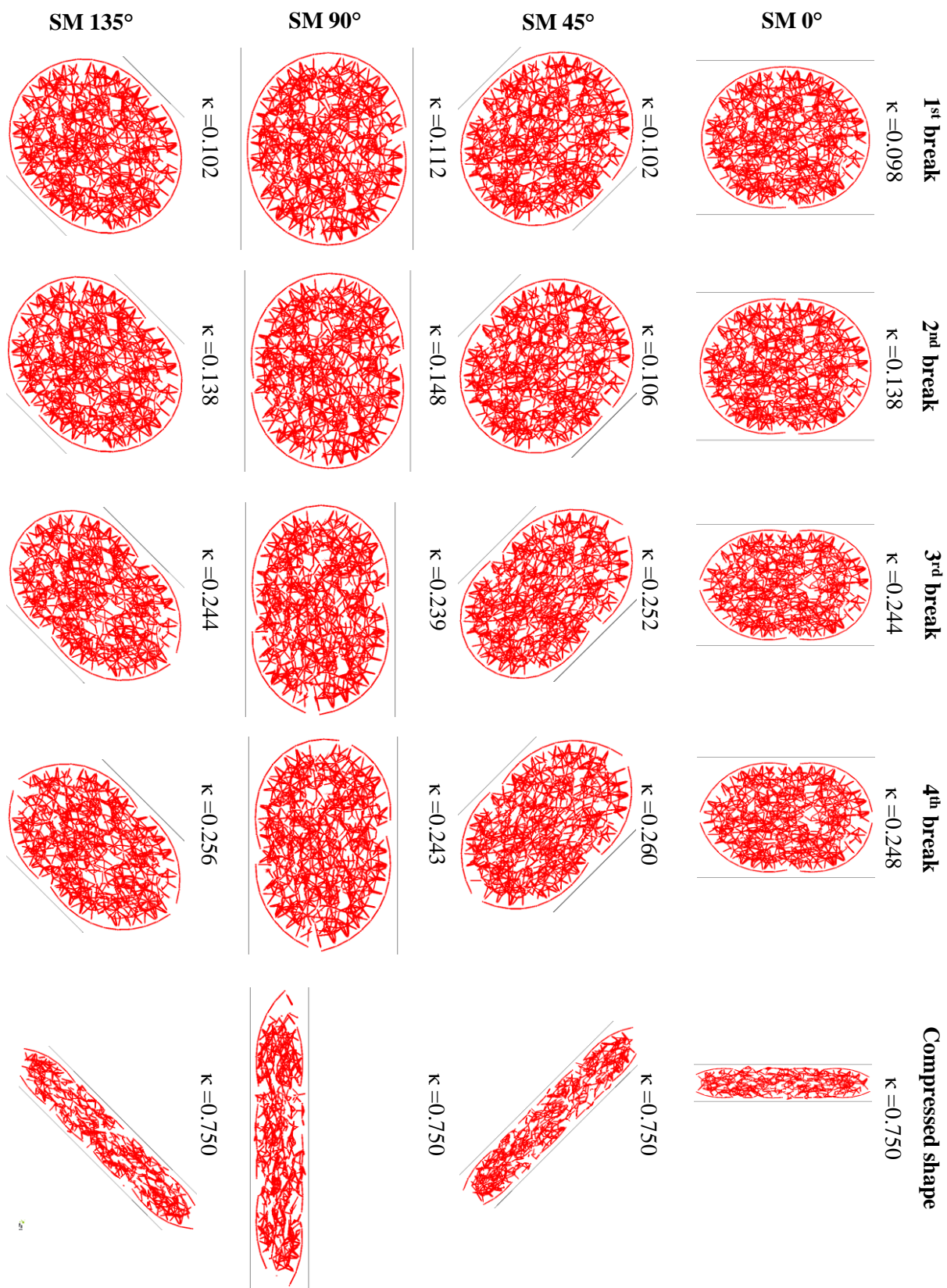


FIGURE B.5: Breakage during the analysis on the loading direction at the middle position by sectional transversal compression (the existing bonds among the particles are visualized by red lines between the centre of the bonded particles).

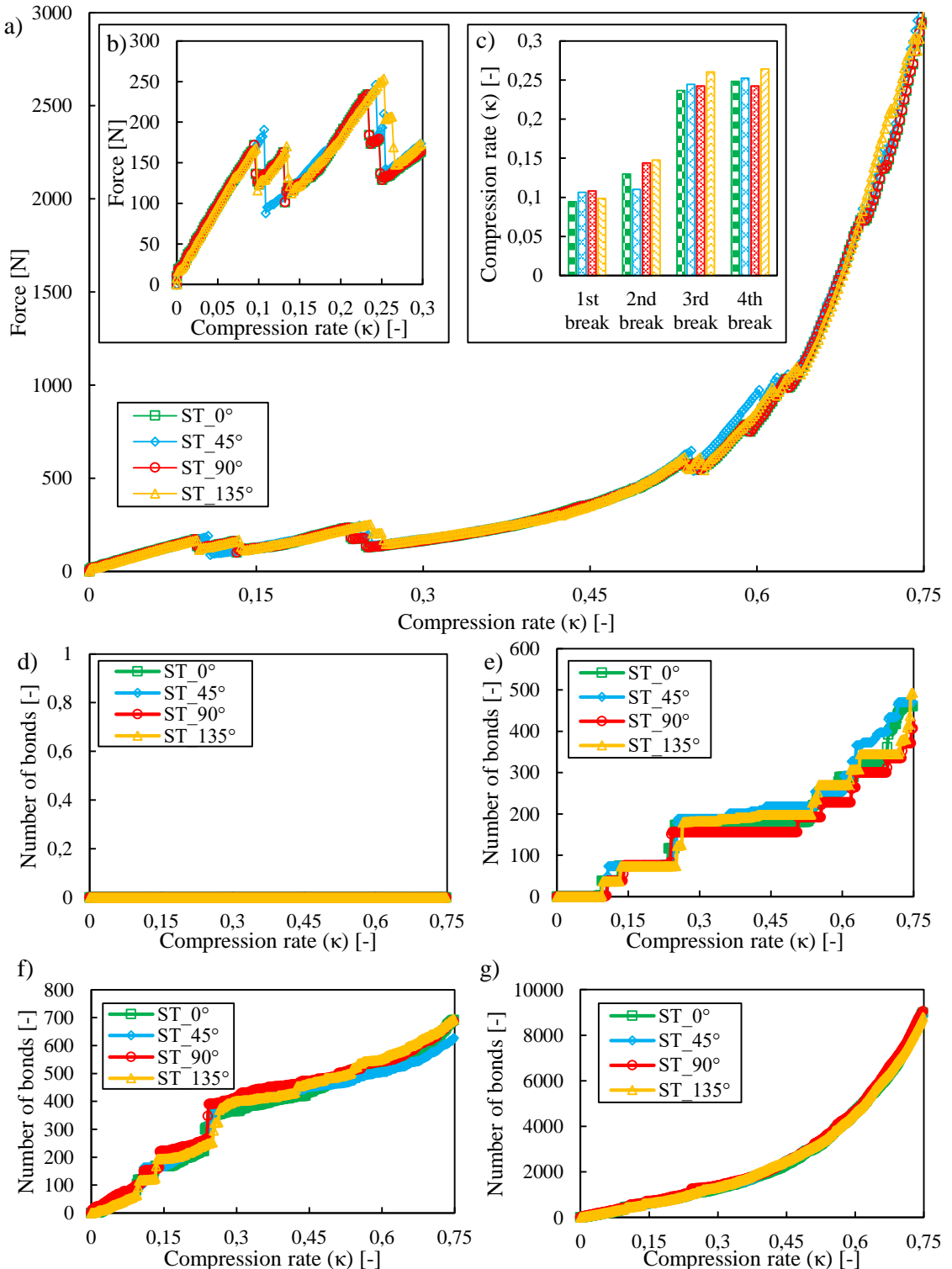


FIGURE B.6: Results of the analysis on the loading direction at the top position by sectional transversal compression: a) overall force-compression rate characteristics; b) force-compression rate characteristics in range of 0-0.3 compression rate; c) major break events in tangential direction of the skin; d) broken bonds of the skin in longitudinal direction; e) broken bonds of the skin in tangential direction; f) broken bonds between the skin and the core; g) broken bonds in the core.

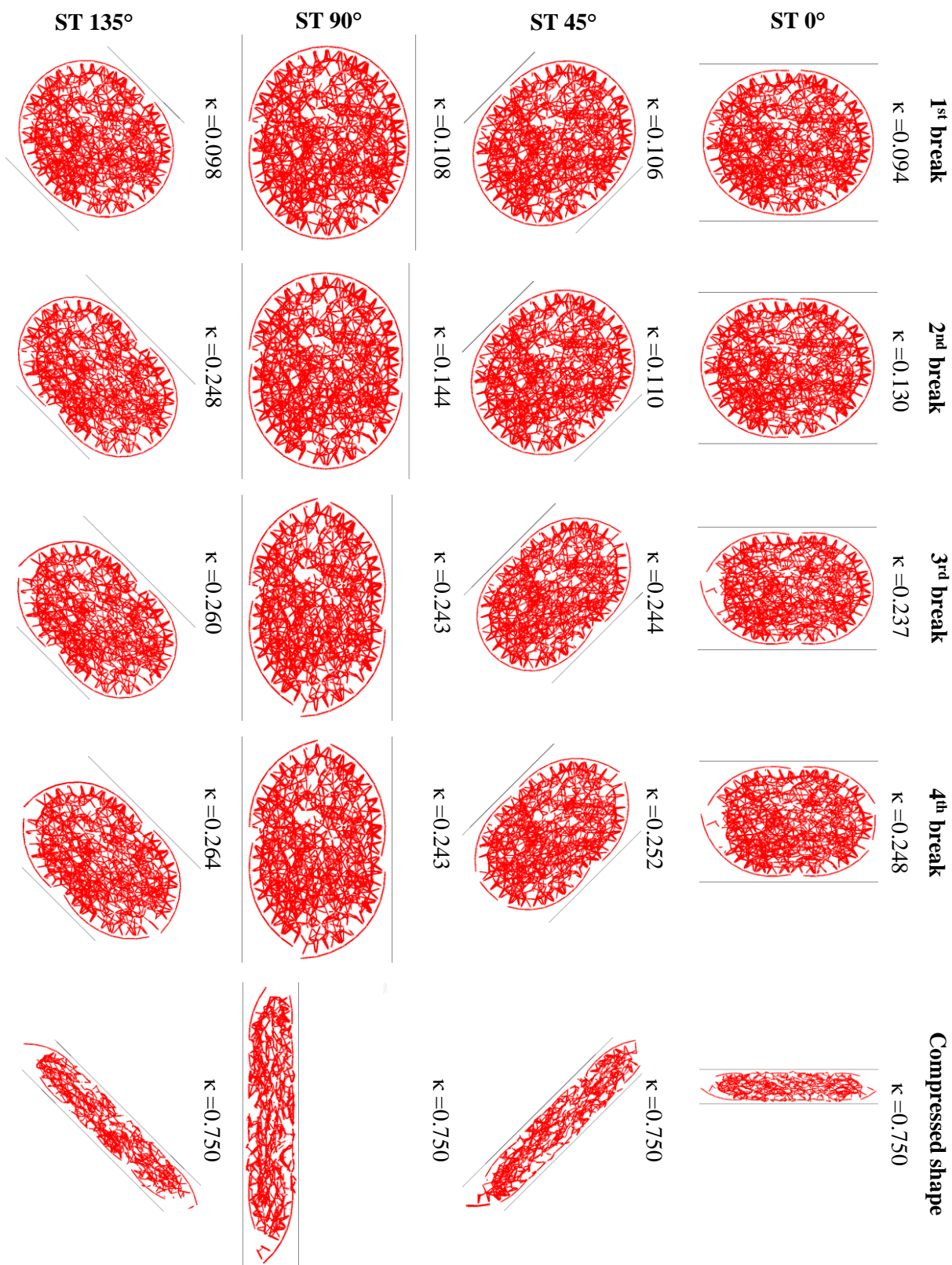


FIGURE B.7: Breakage during the analysis on the loading direction at the top position by sectional transversal compression (the existing bonds among the particles are visualized by red lines between the centre of the bonded particles).

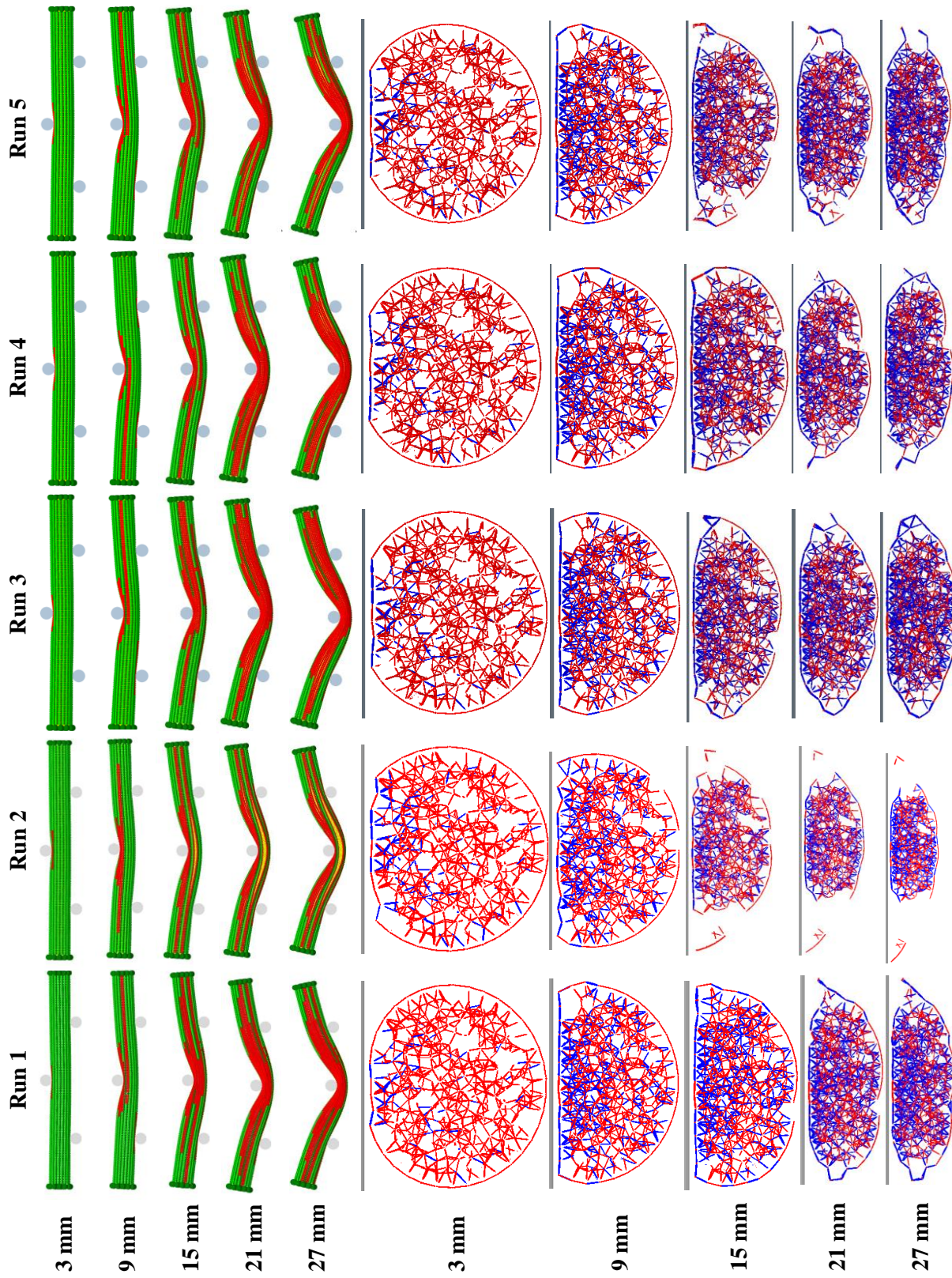


FIGURE B.8: Breakage during the reference simulation cases of three-point bending: comparison of the longitudinal crack propagation over the bending process (the particles of the skin are visualised by the damage parameter of 0.1) and the breakage of the cross-section under the bending tool (the existing bonds among the particles are visualized by red lines between the centre of the bonded particles).

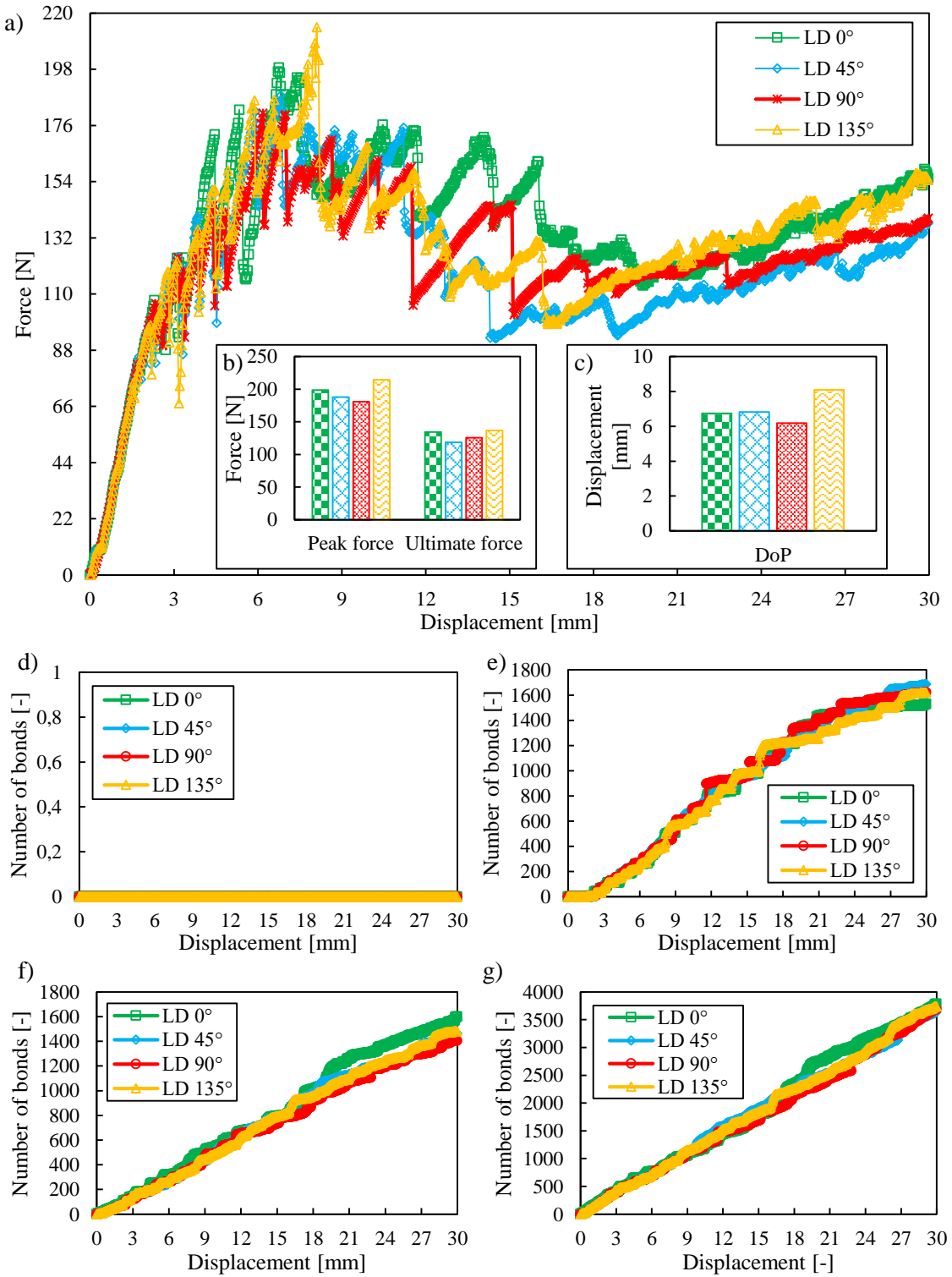


FIGURE B.9: Results of the analysis on the loading direction by three-point bending: a) overall force-compression rate characteristics; b) peak and ultimate forces; c) displacement of the peak forces; d) broken bonds of the skin in longitudinal direction; e) broken bonds of the skin in tangential direction; f) broken bonds between the skin and the core; g) broken bonds in the core.

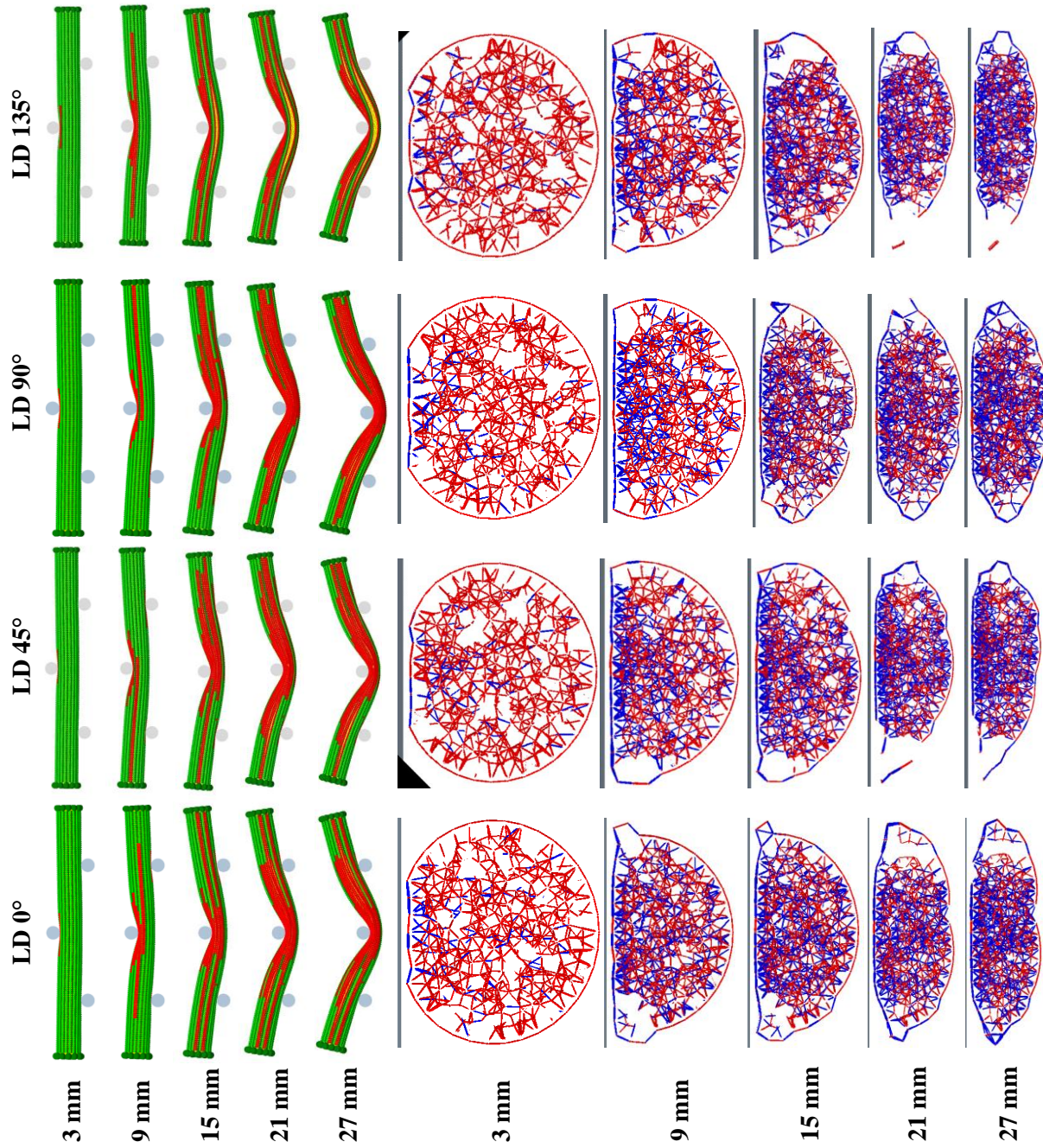


FIGURE B.10: Breakage during the analysis on the loading direction by three-point bending: comparison of the longitudinal crack propagation over the bending process (the particles of the skin are visualised by the damage parameter of 0.1) and the breakage of the cross-section under the bending tool (the existing bonds among the particles are visualized by red lines between the centre of the bonded particles).

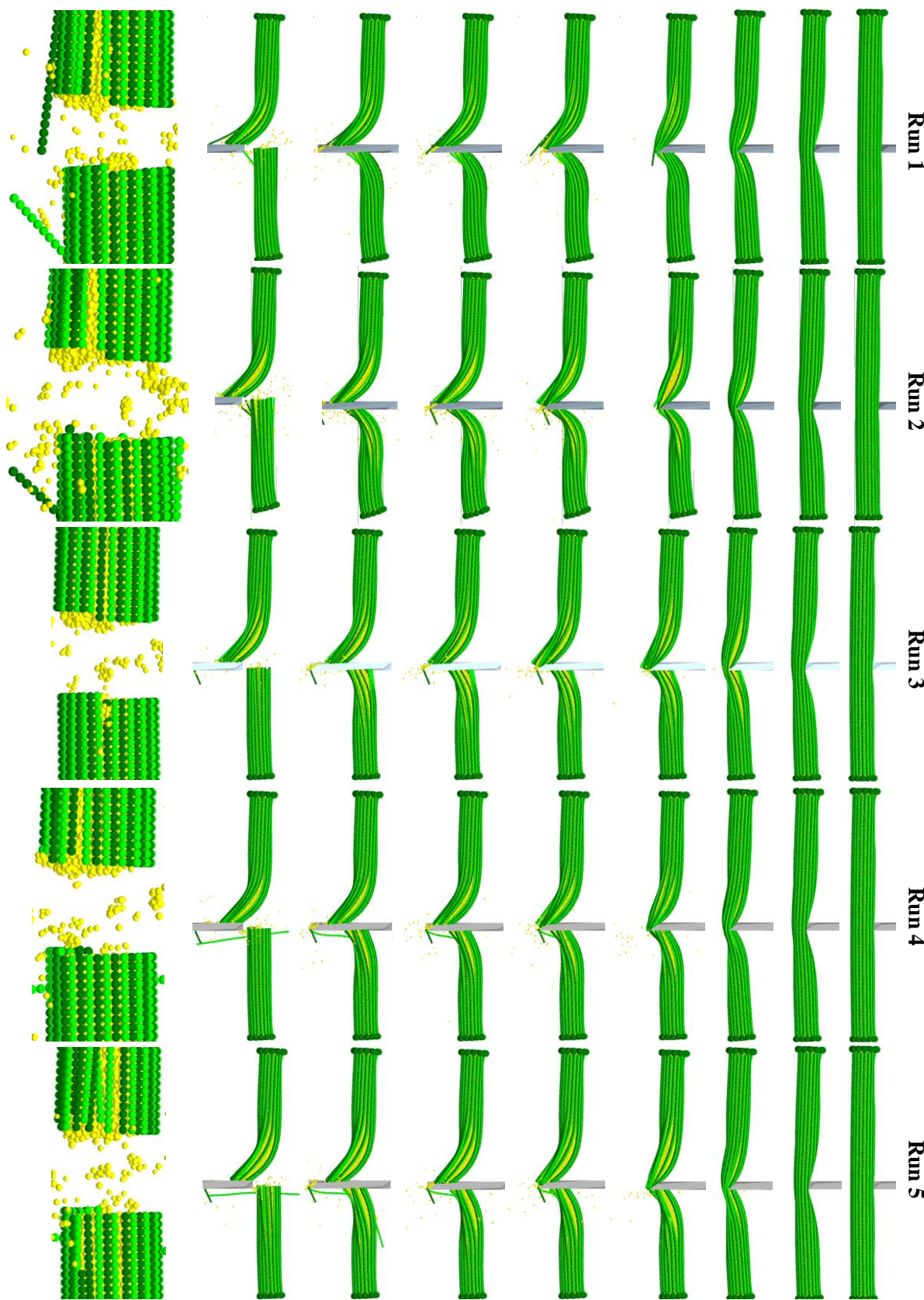


FIGURE B.11: Breakage during the reference simulation cases of dynamic cutting: comparison of the cutting processes and the resulted cutting surfaces.

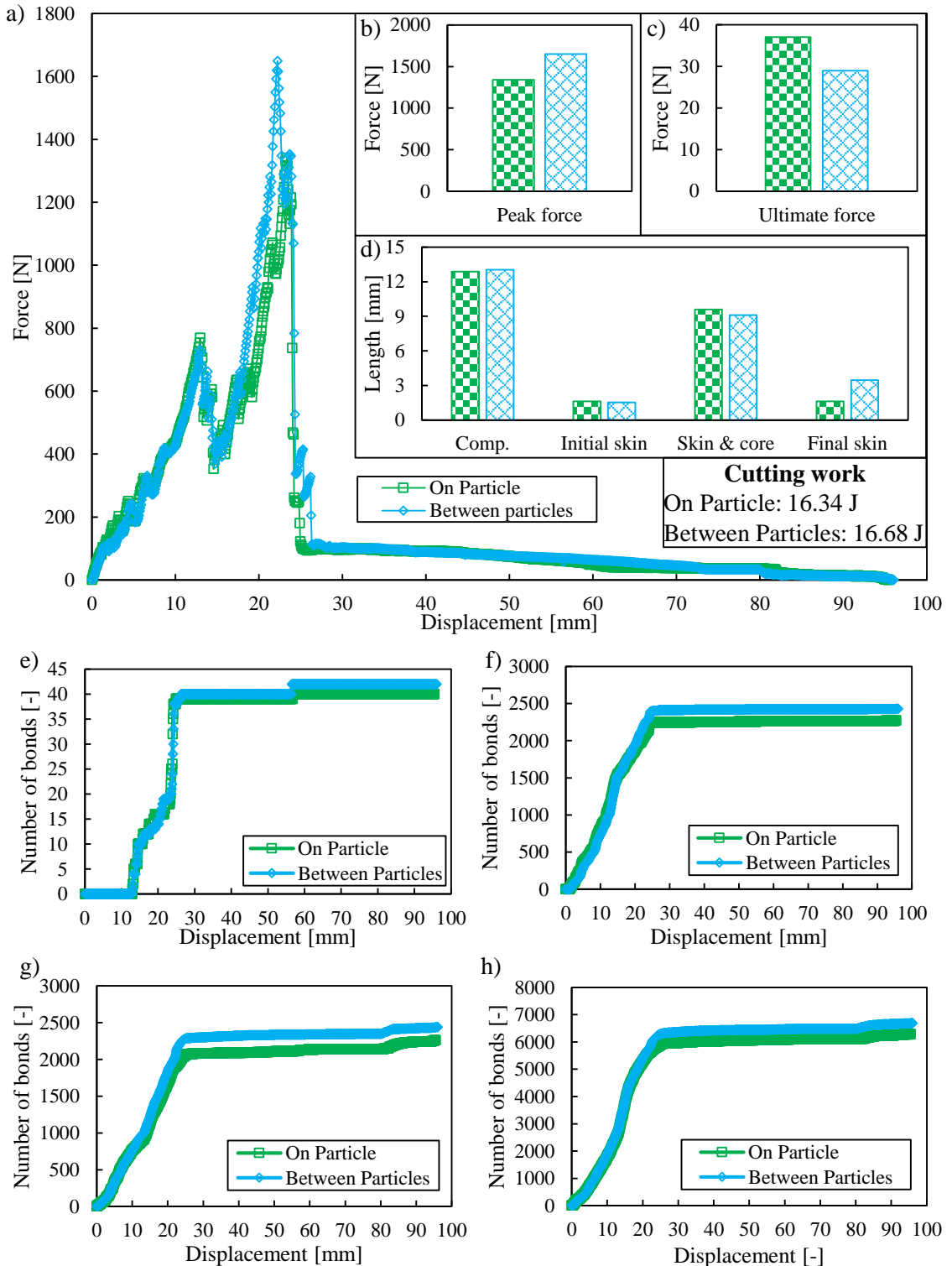


FIGURE B.12: Results of the analysis on the loading direction by dynamic cutting: a) overall force-displacement characteristics; b) range of the peak forces; c) range of the ultimate forces; d) length of the stages of cut; e) broken bonds of the skin in longitudinal direction; f) broken bonds of the skin in tangential direction; g) broken bonds between the skin and the core; h) broken bonds in the core.

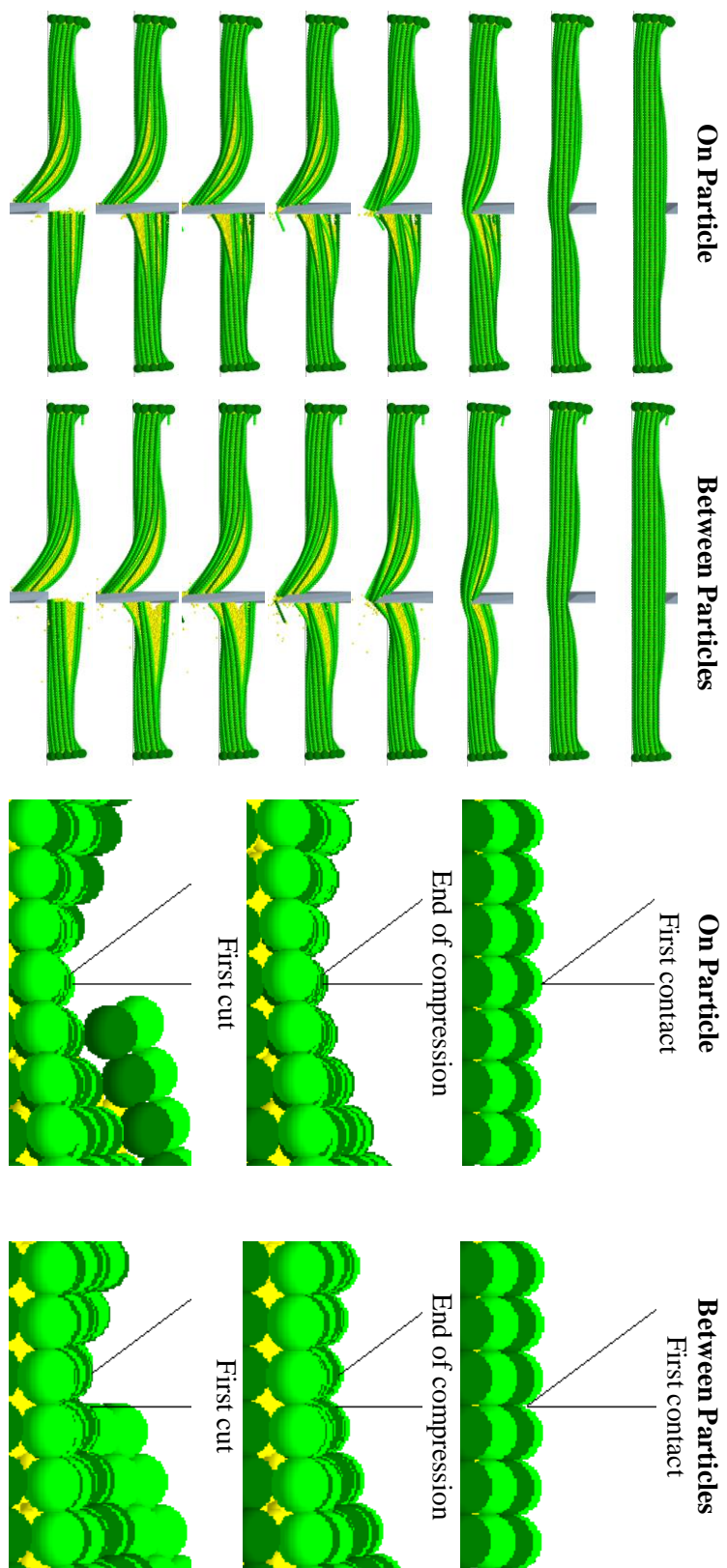


FIGURE B.13: Breakage during the loading direction simulation cases of dynamic cutting; comparison of the cutting processes.

## C Bonded Contact Parameters

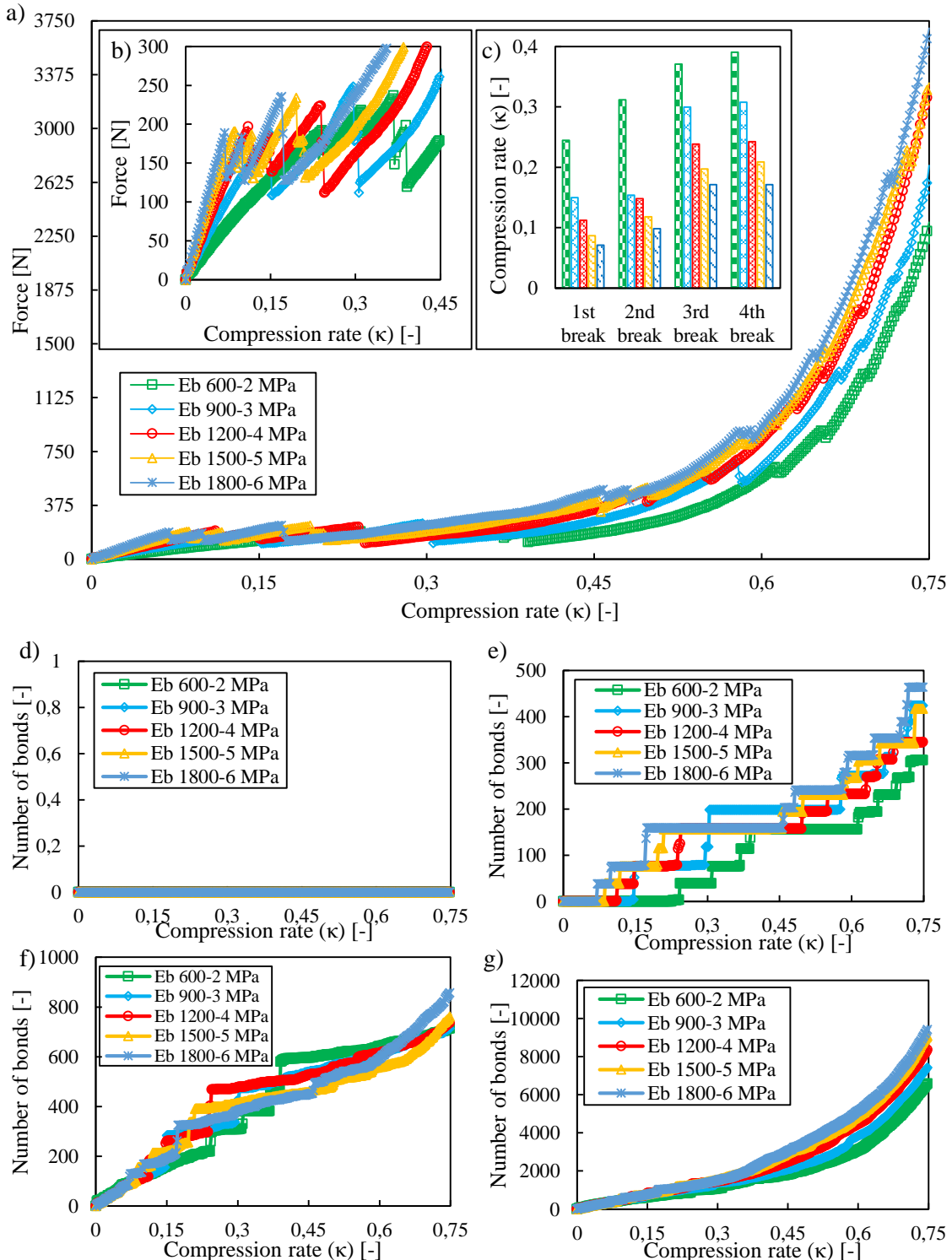


FIGURE C.1: Influence of the Young's modulus by sectional transversal compression: a) overall force-compression rate characteristics; b) force-compression rate characteristics in range of 0-0.3 compression rate; c) major break events in tangential direction of the skin; d) broken bonds of the skin in longitudinal direction; e) broken bonds of the skin in tangential direction; f) broken bonds between the skin and the core; g) broken bonds in the core.

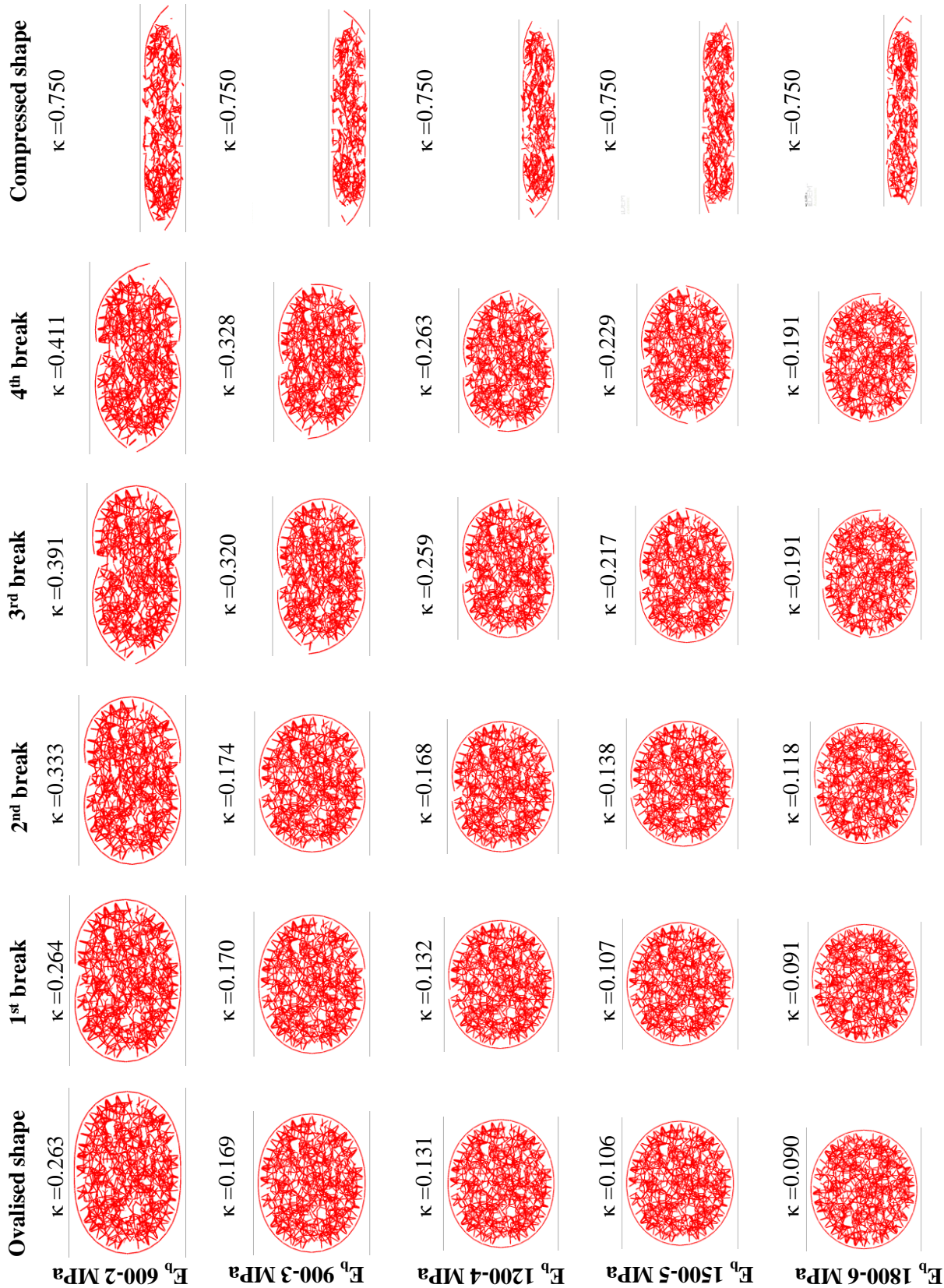


FIGURE C.2: Influence of the bond Young's modulus on the breakage by sectional transversal compression (the existing bonds among the particles are visualized by red lines between the centre of the bonded particles).

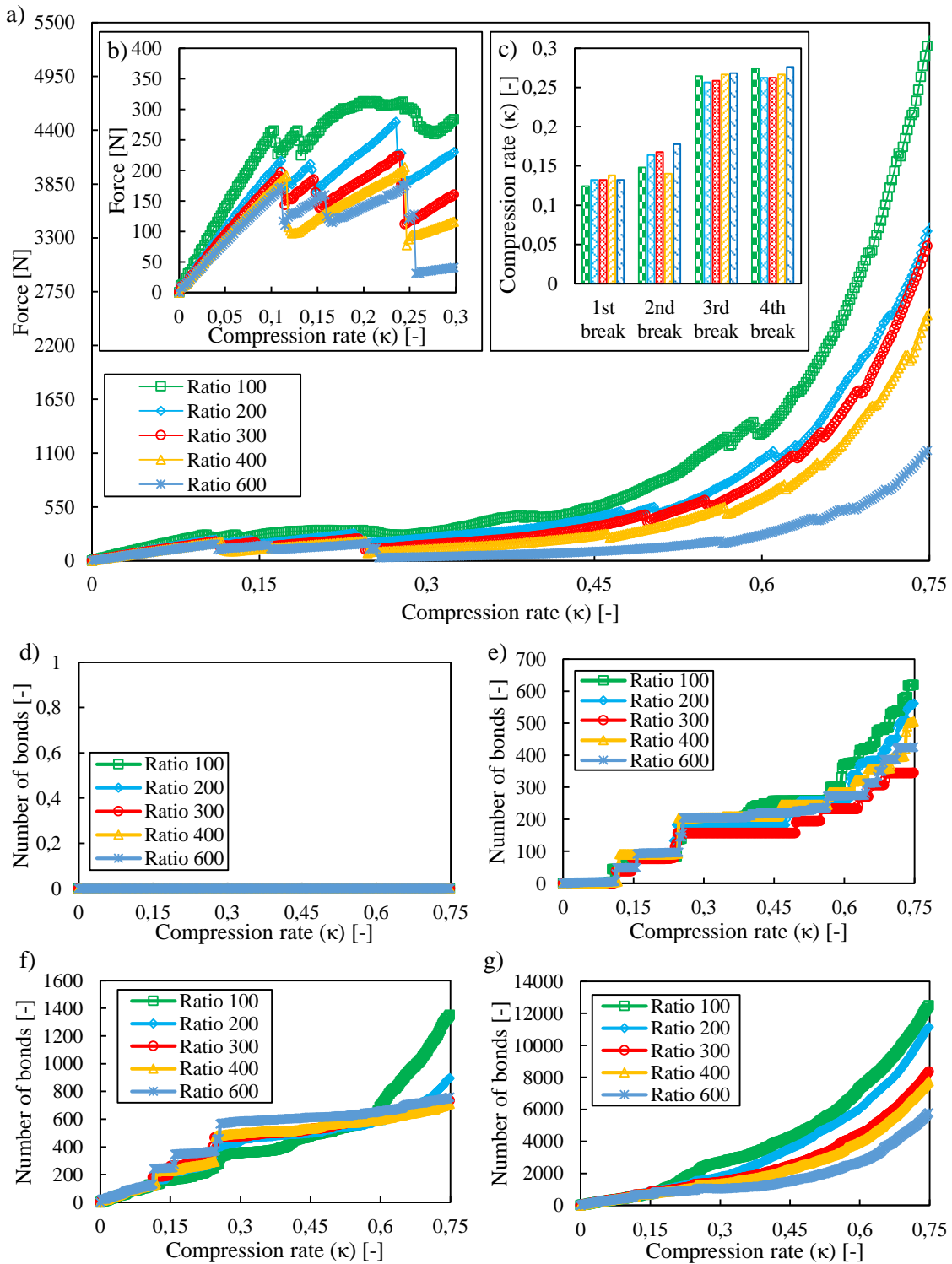


FIGURE C.3: Influence of the ratio between the bond Young's modulus in the core and in tangential direction of the skin by sectional transversal compression: a) overall force-compression rate characteristics; b) force-compression rate characteristics in range of 0-0.3 compression rate; c) major break events in tangential direction of the skin; d) broken bonds of the skin in longitudinal direction; e) broken bonds of the skin in tangential direction; f) broken bonds between the skin and the core; g) broken bonds in the core.

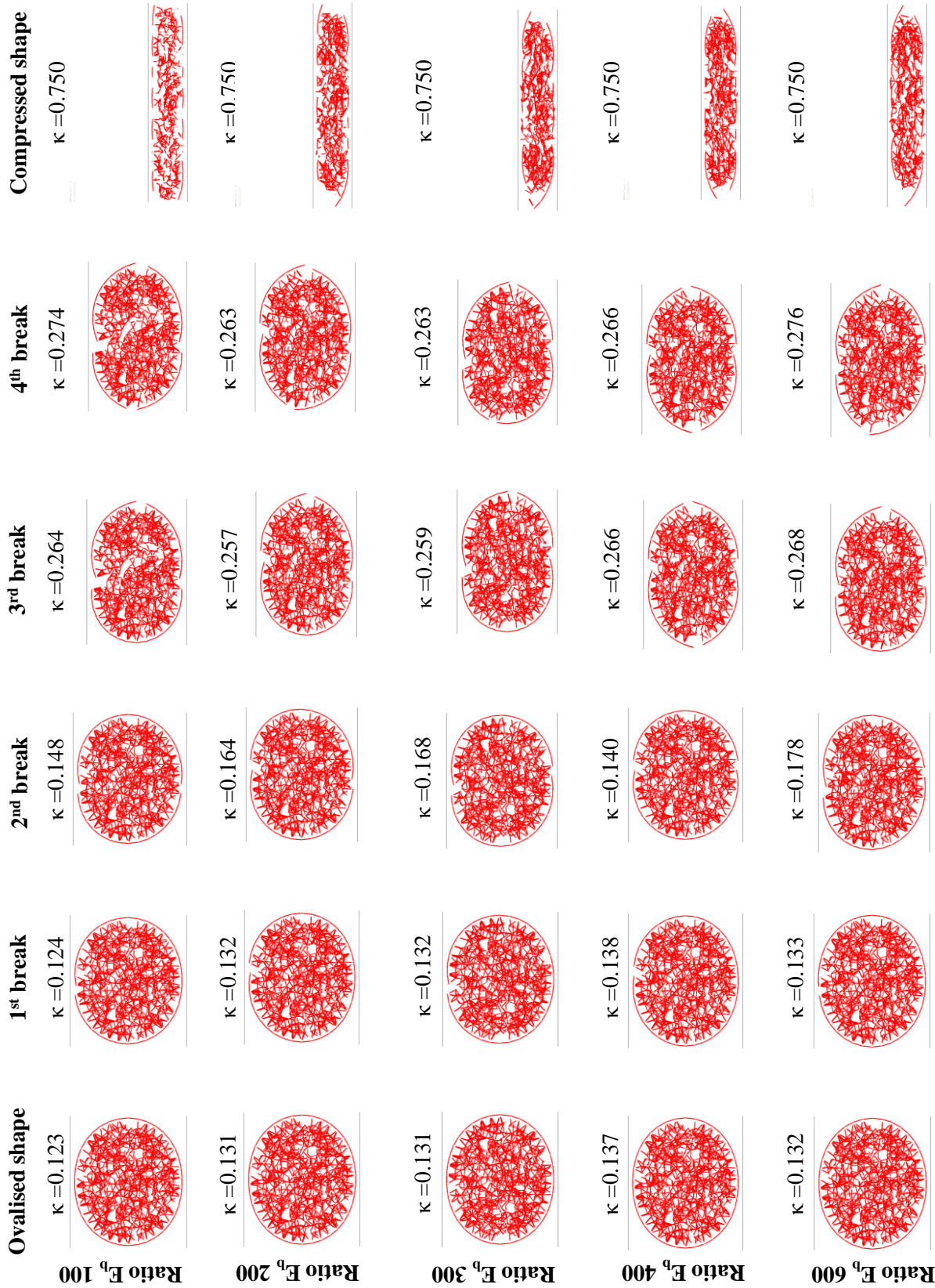


FIGURE C.4: Influence of the ratio between the bond Young's modulus in the core and in tangential direction of the skin on the breakage by sectional transversal compression (the existing bonds among the particles are visualized by red lines between the centre of the bonded particles).

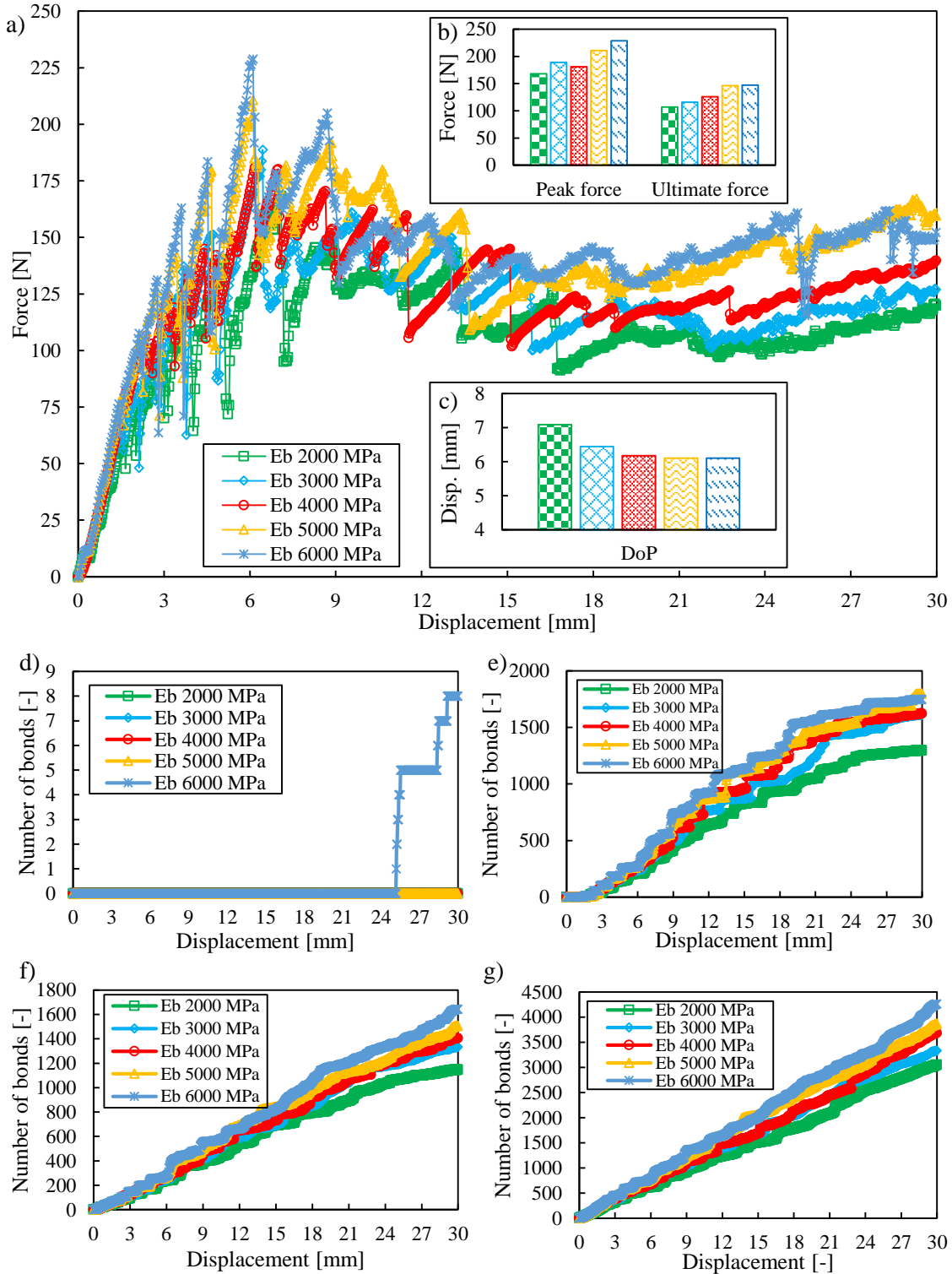


FIGURE C.5: Influence of the Young's modulus by three-point bending: a) overall force-compression rate characteristics; b) peak and ultimate forces; c) displacement of the peak forces; d) broken bonds of the skin in longitudinal direction; e) broken bonds of the skin in tangential direction; f) broken bonds between the skin and the core; g) broken bonds in the core.

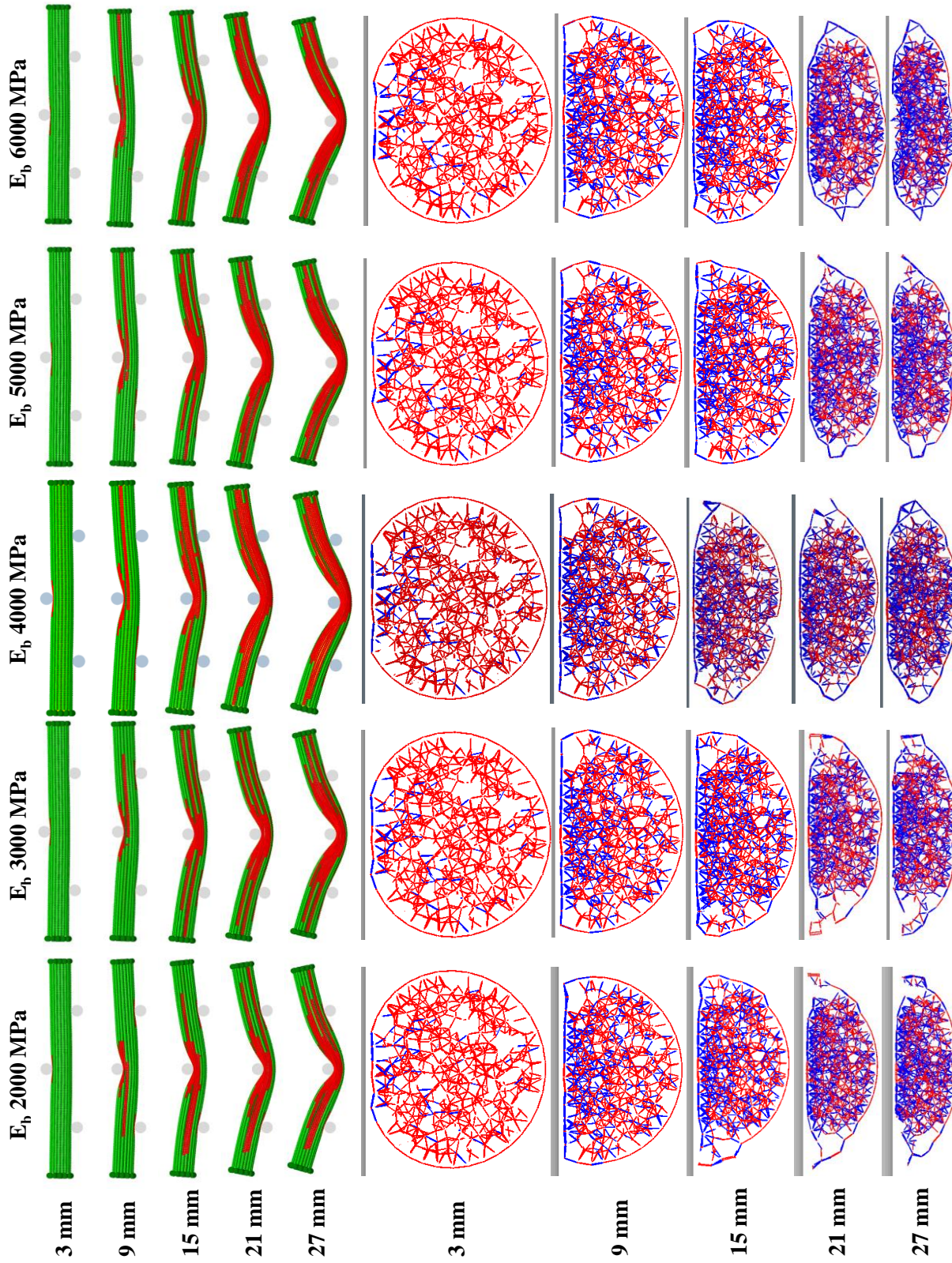


FIGURE C.6: Influence of the Young's modulus on the breakage process (the particles of the skin are visualised by the damage parameter of 0.1) and the breakage of the cross-section under the bending tool (the existing bonds among the particles are visualized by red lines between the centre of the bonded particles).

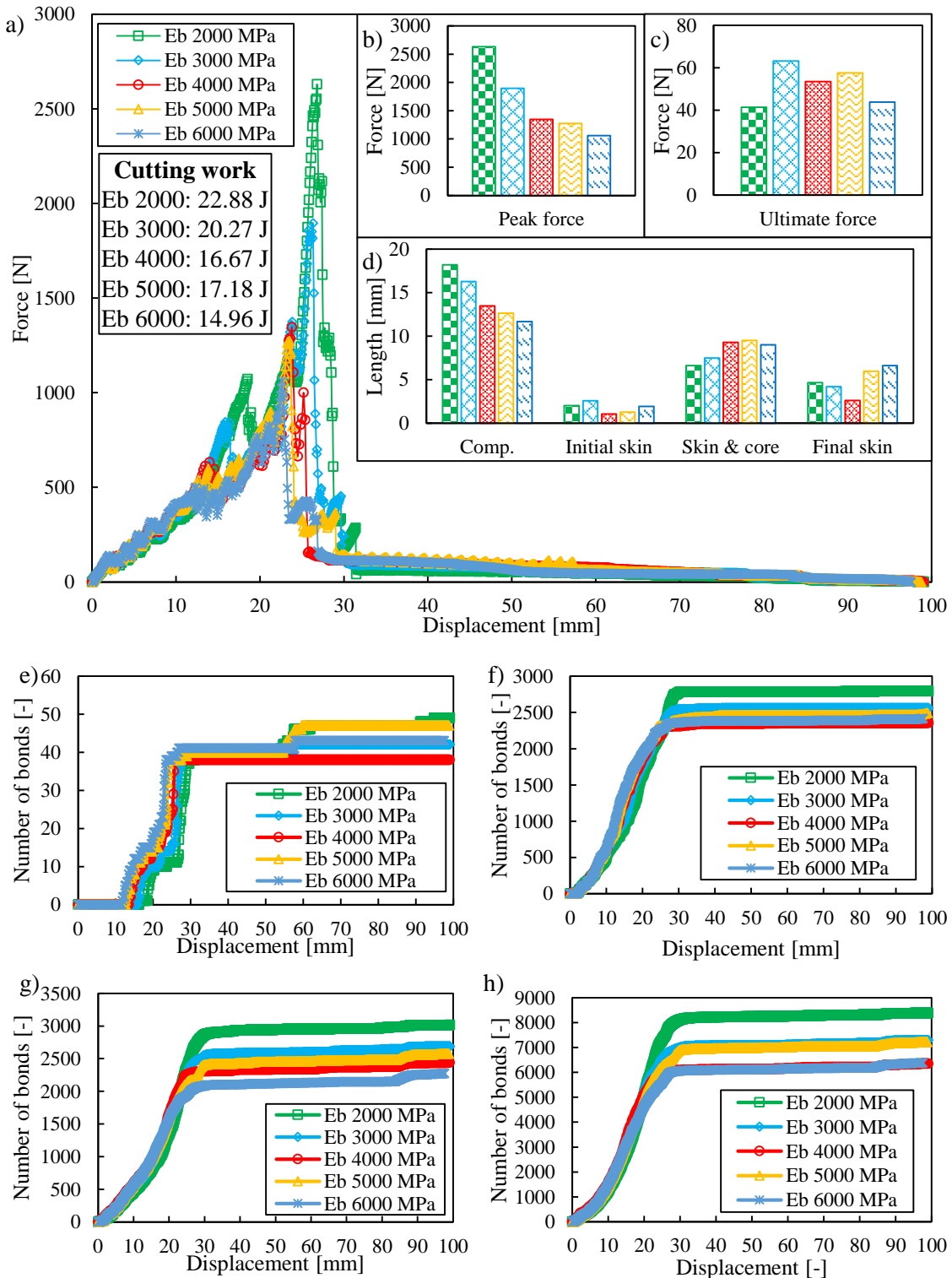


FIGURE C.7: Influence of the bond Young's modulus by dynamic cutting: a) overall force-displacement characteristics; b) range of the peak forces; c) range of the ultimate forces; d) length of the stages of cut; e) broken bonds of the skin in longitudinal direction; f) broken bonds of the skin in tangential direction; g) broken bonds between the skin and the core; h) broken bonds in the core.

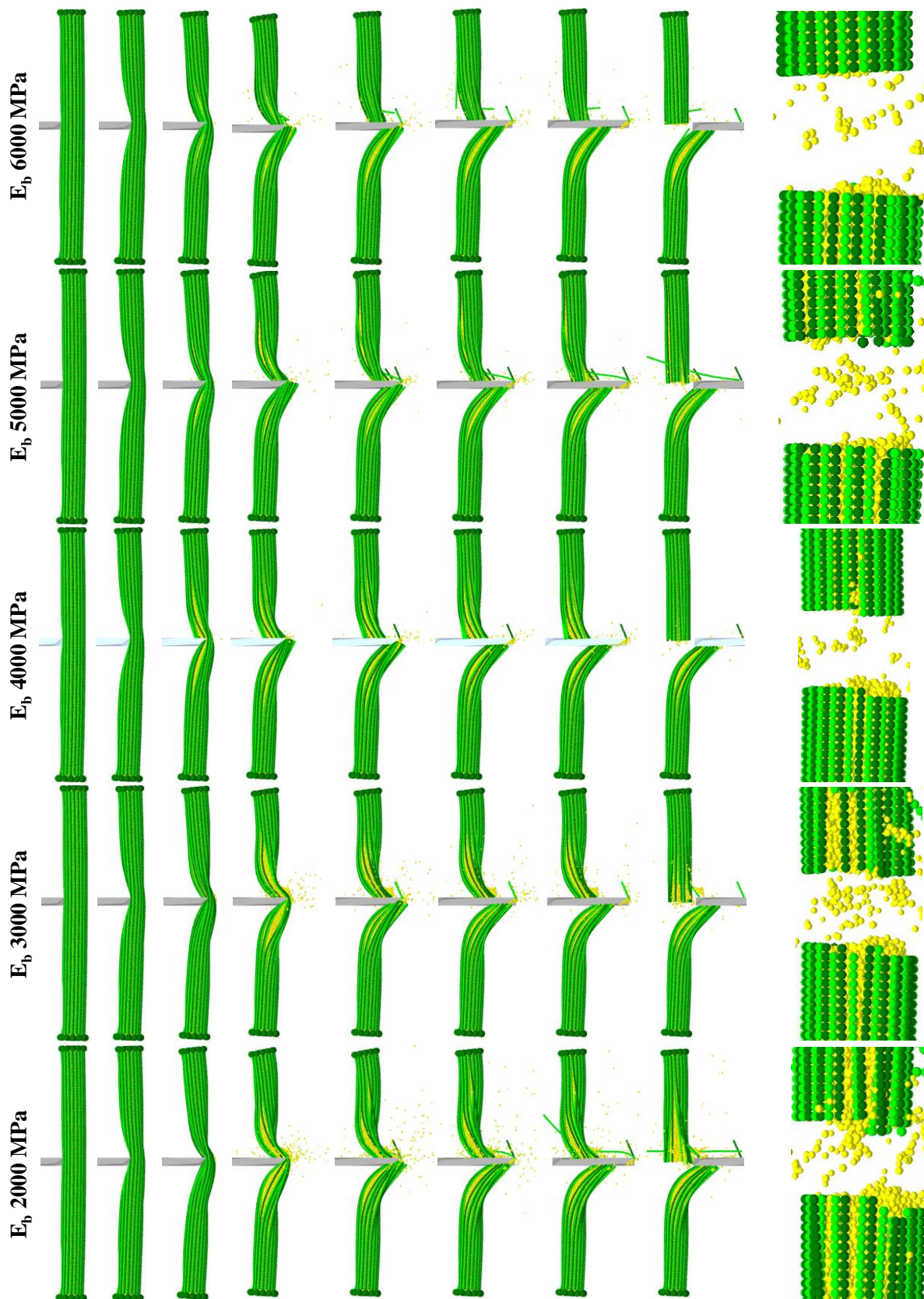


FIGURE C.8: Influence of the bond Young's modulus on the breakage by dynamic cutting dynamic cutting: comparison of the cutting processes and the resulted cutting surfaces.

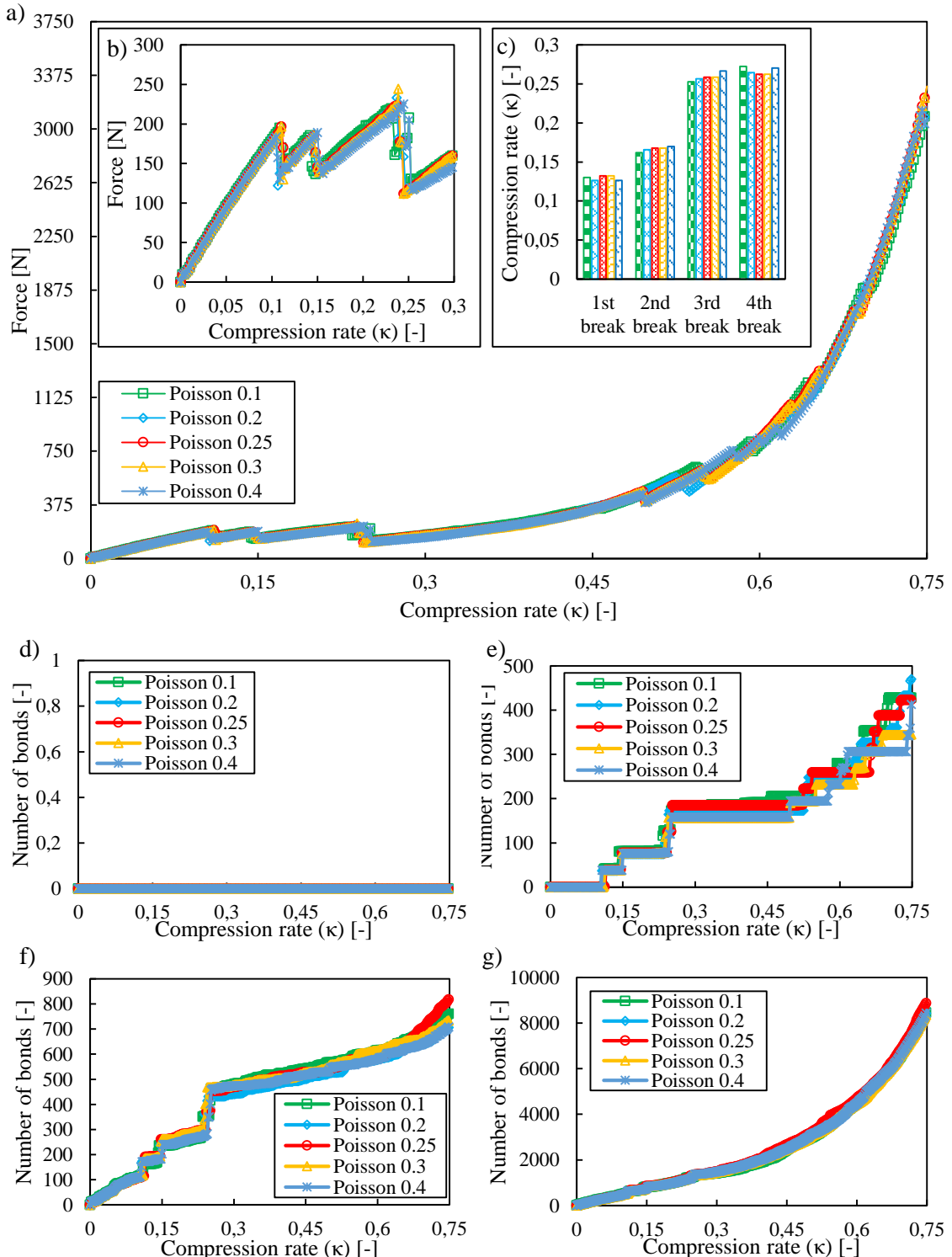


FIGURE C.9: Influence of the Poisson's ratio by sectional transversal compression: a) overall force-compression rate characteristics; b) force-compression rate characteristics in range of 0-0.3 compression rate; c) major break events in tangential direction of the skin; d) broken bonds of the skin in longitudinal direction; e) broken bonds of the skin in tangential direction; f) broken bonds between the skin and the core; g) broken bonds in the core.

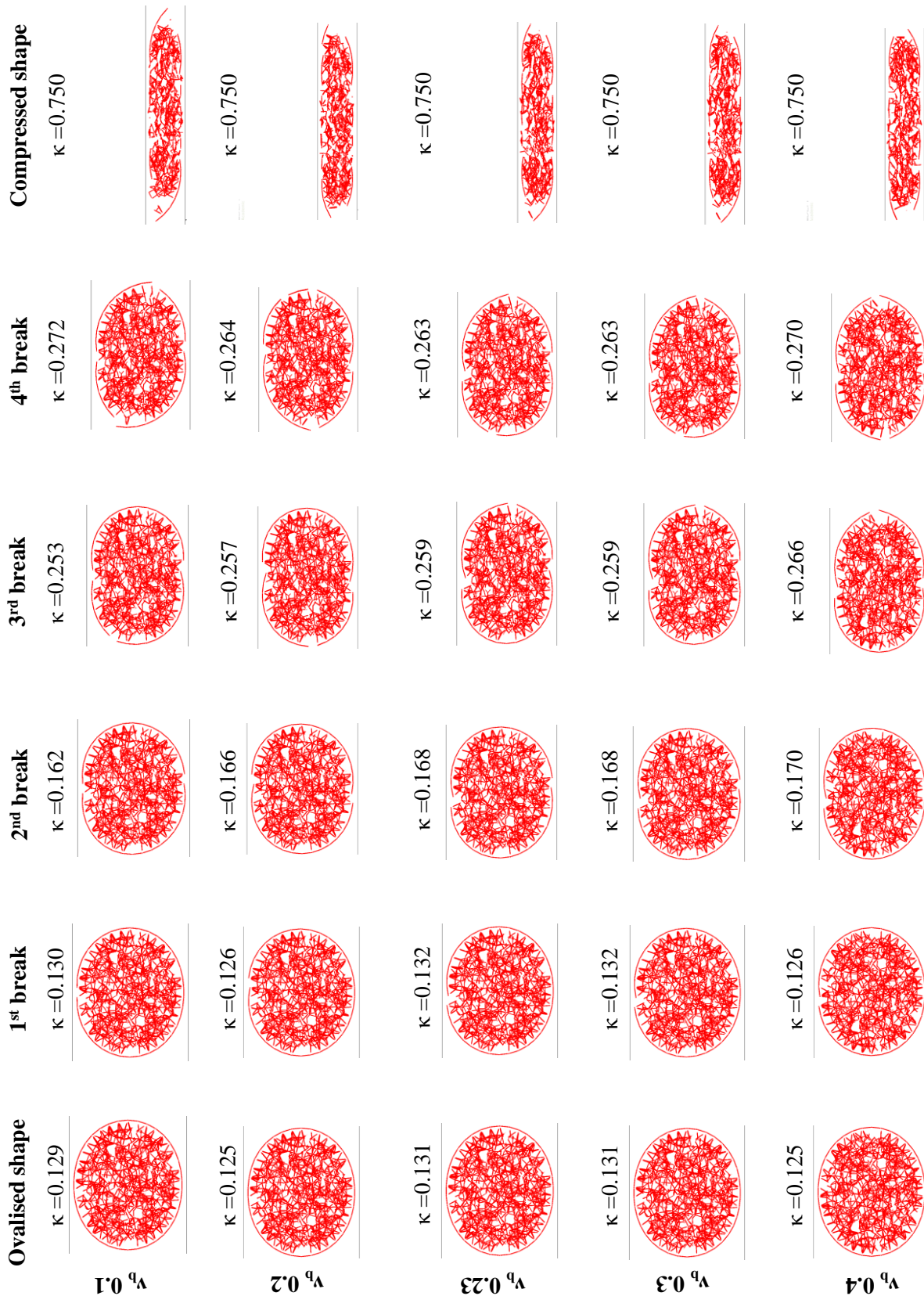


FIGURE C.10: Influence of the Poisson's ratio on the breakage by sectional transversal compression (the existing bonds among the particles are visualized by red lines between the centre of the bonded particles).

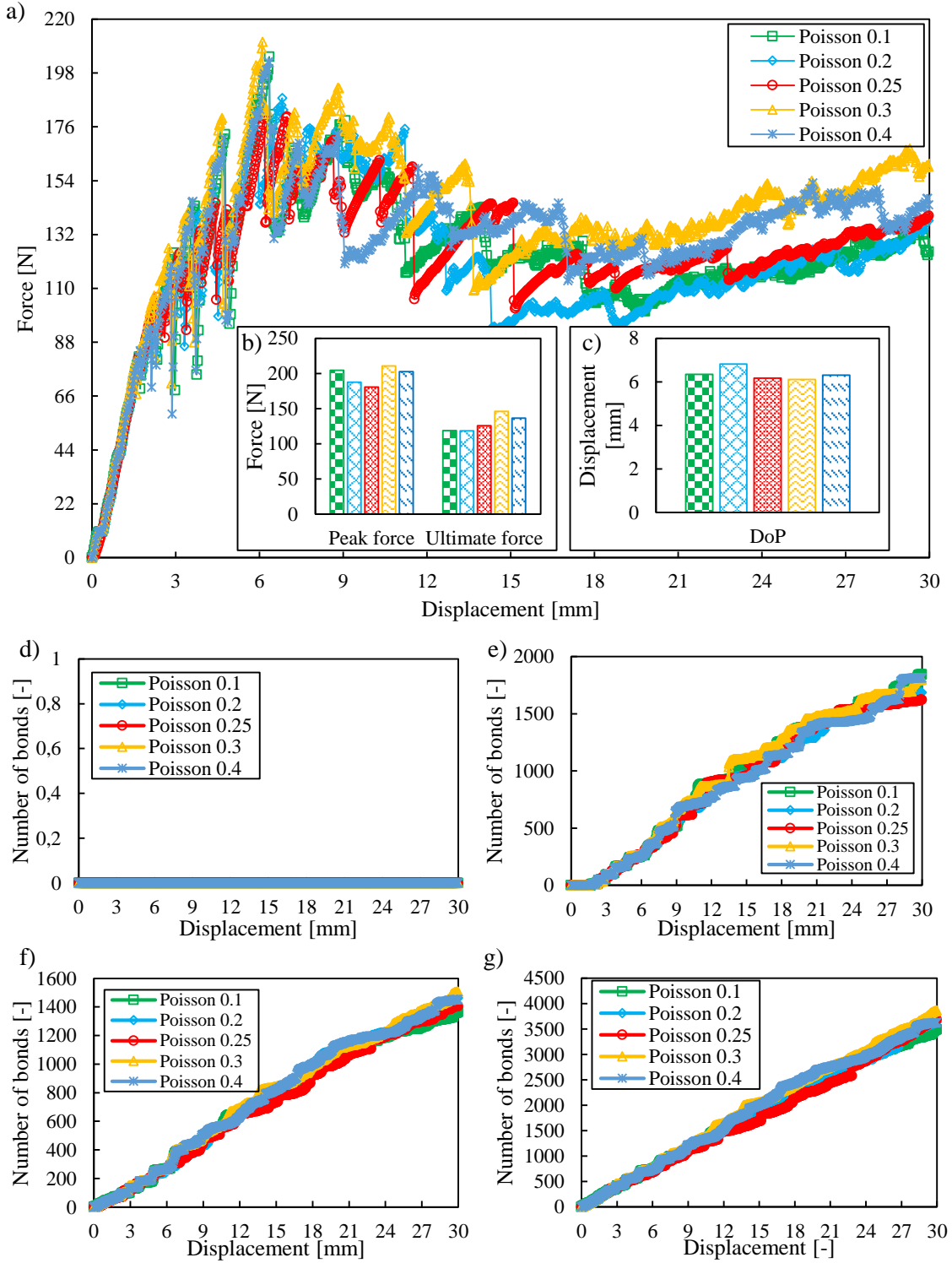


FIGURE C.11: Influence of the bond Poisson's ratio by three-point bending: a) overall force-compression rate characteristics; b) peak and ultimate forces; c) displacement of the peak forces; d) broken bonds of the skin in longitudinal direction; e) broken bonds of the skin in tangential direction; f) broken bonds between the skin and the core; g) broken bonds in the core.

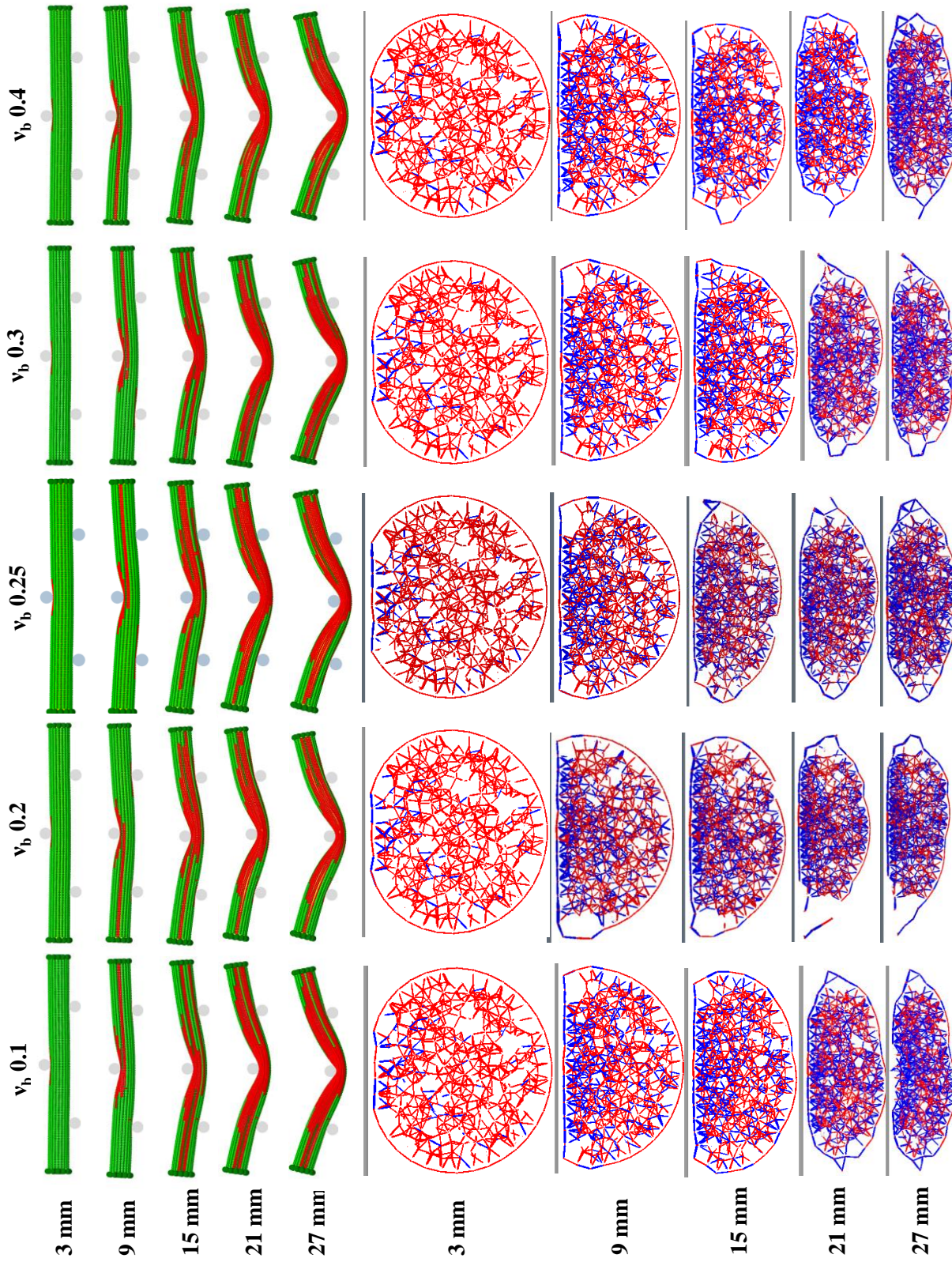


FIGURE C.12: Influence of the bond Poisson's ratio on the breakage by three-point bending: comparison of the longitudinal crack propagation over the bending process (the particles of the skin are visualised by the damage parameter of 0.1) and the breakage of the cross-section under the bending tool (the existing bonds among the particles are visualized by red lines between the centre of the bonded particles).

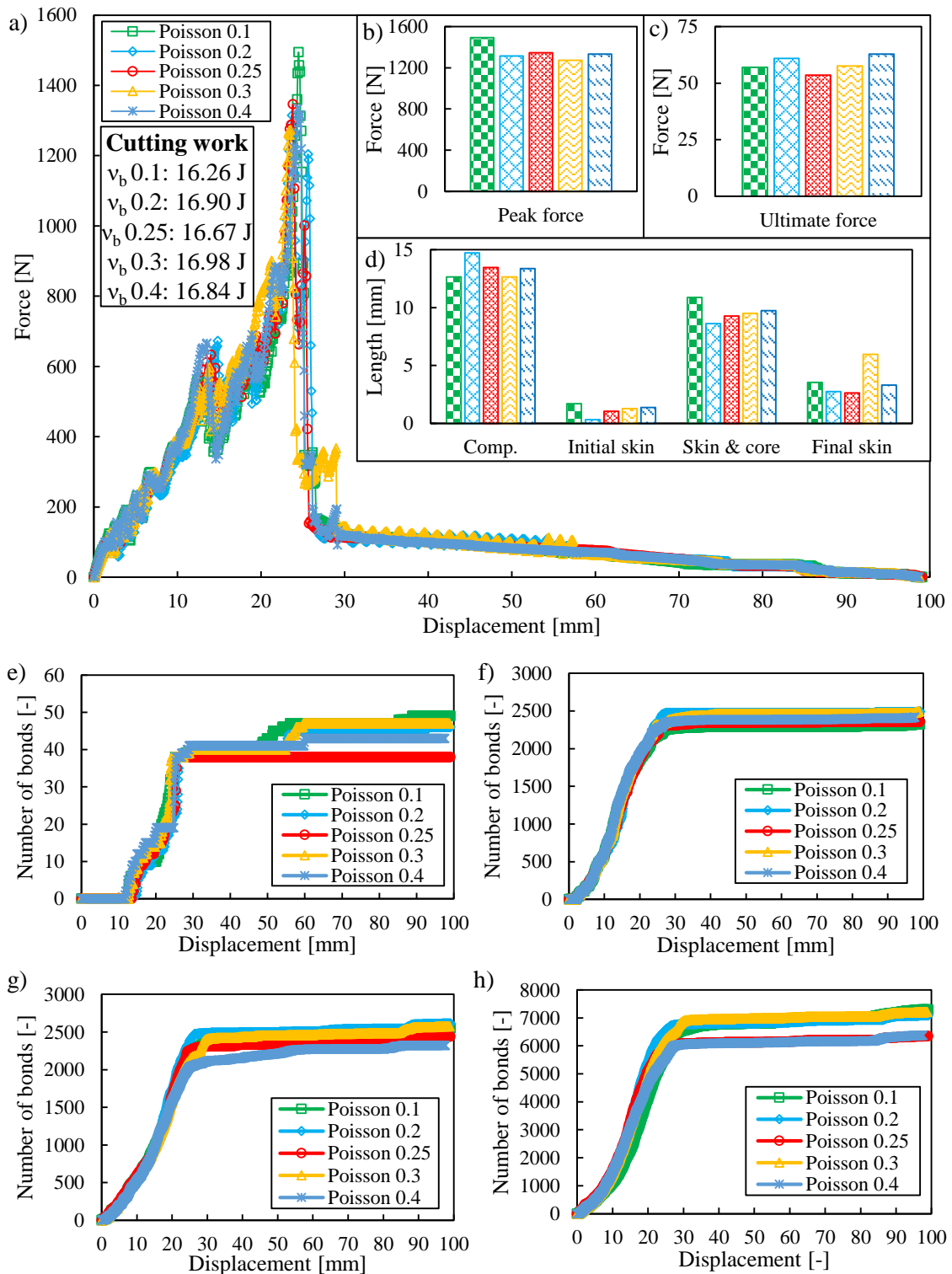


FIGURE C.13: Influence of the bond Poisson's ratio by dynamic cutting: a) overall force-displacement characteristics; b) range of the peak forces; c) range of the ultimate forces; d) length of the stages of cut; e) broken bonds of the skin in longitudinal direction; f) broken bonds of the skin in tangential direction; g) broken bonds between the skin and the core; h) broken bonds in the core.

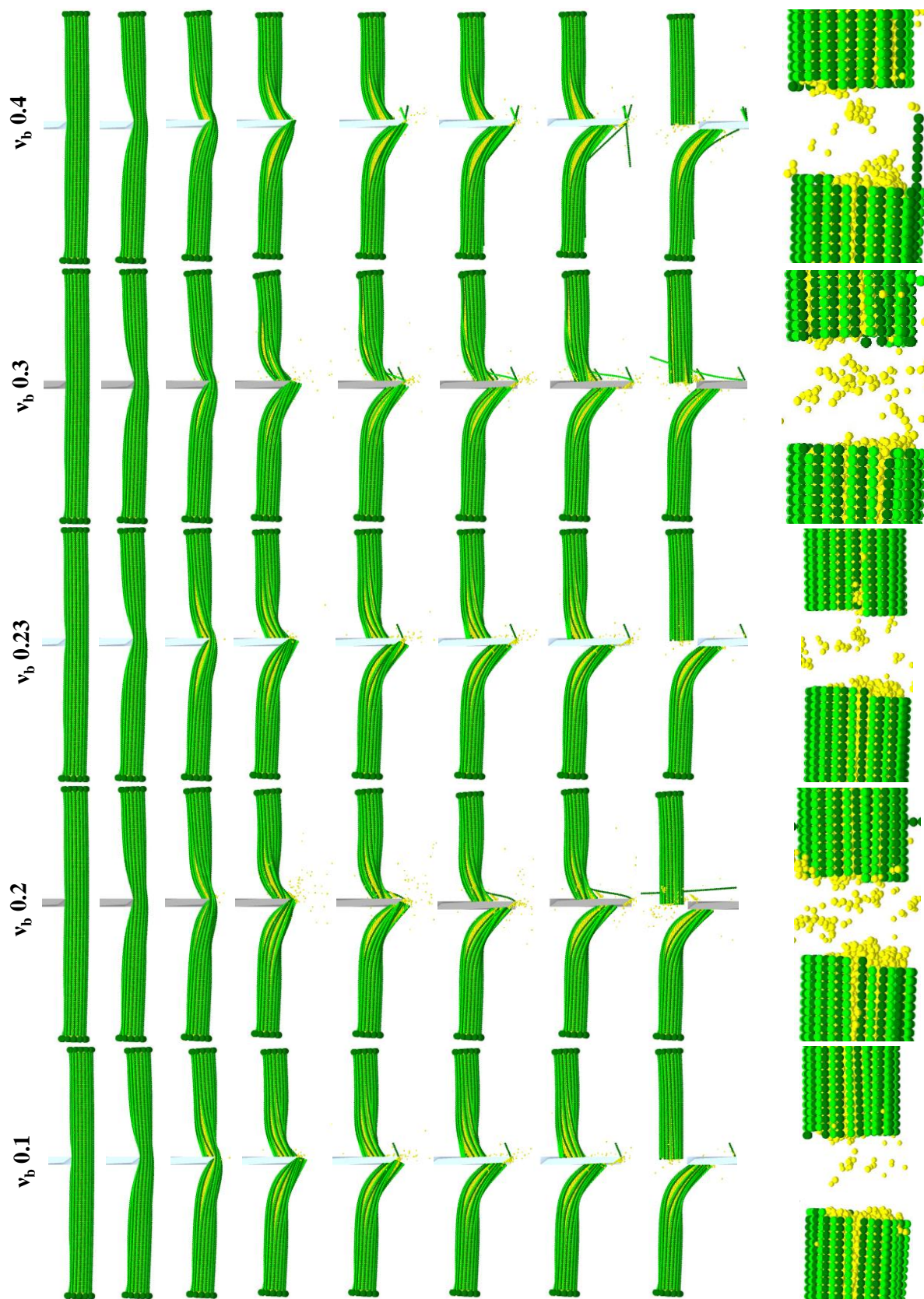


FIGURE C.14: Influence of the bond Poisson's ratio on the breakage by dynamic cutting dynamic cutting: comparison of the cutting processes and the resulted cutting surfaces.

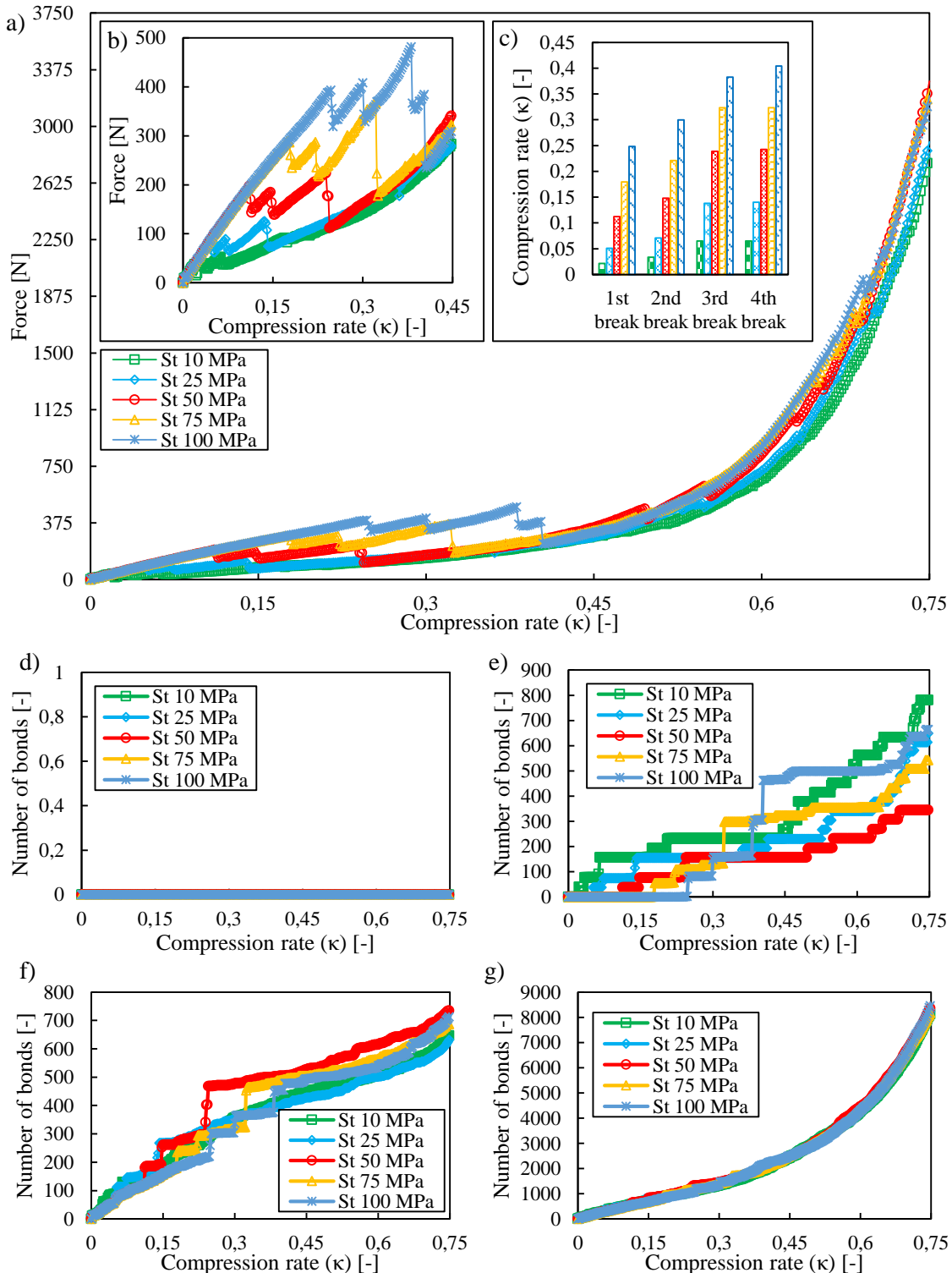


FIGURE C.15: Influence of the tensile strength of the bond in tangential direction of the skin by sectional transversal compression: a) overall force-compression rate characteristics; b) force-compression rate characteristics in range of 0-0.3 compression rate; c) major break events in tangential direction of the skin; d) broken bonds of the skin in longitudinal direction; e) broken bonds of the skin in tangential direction; f) broken bonds between the skin and the core; g) broken bonds in the core.

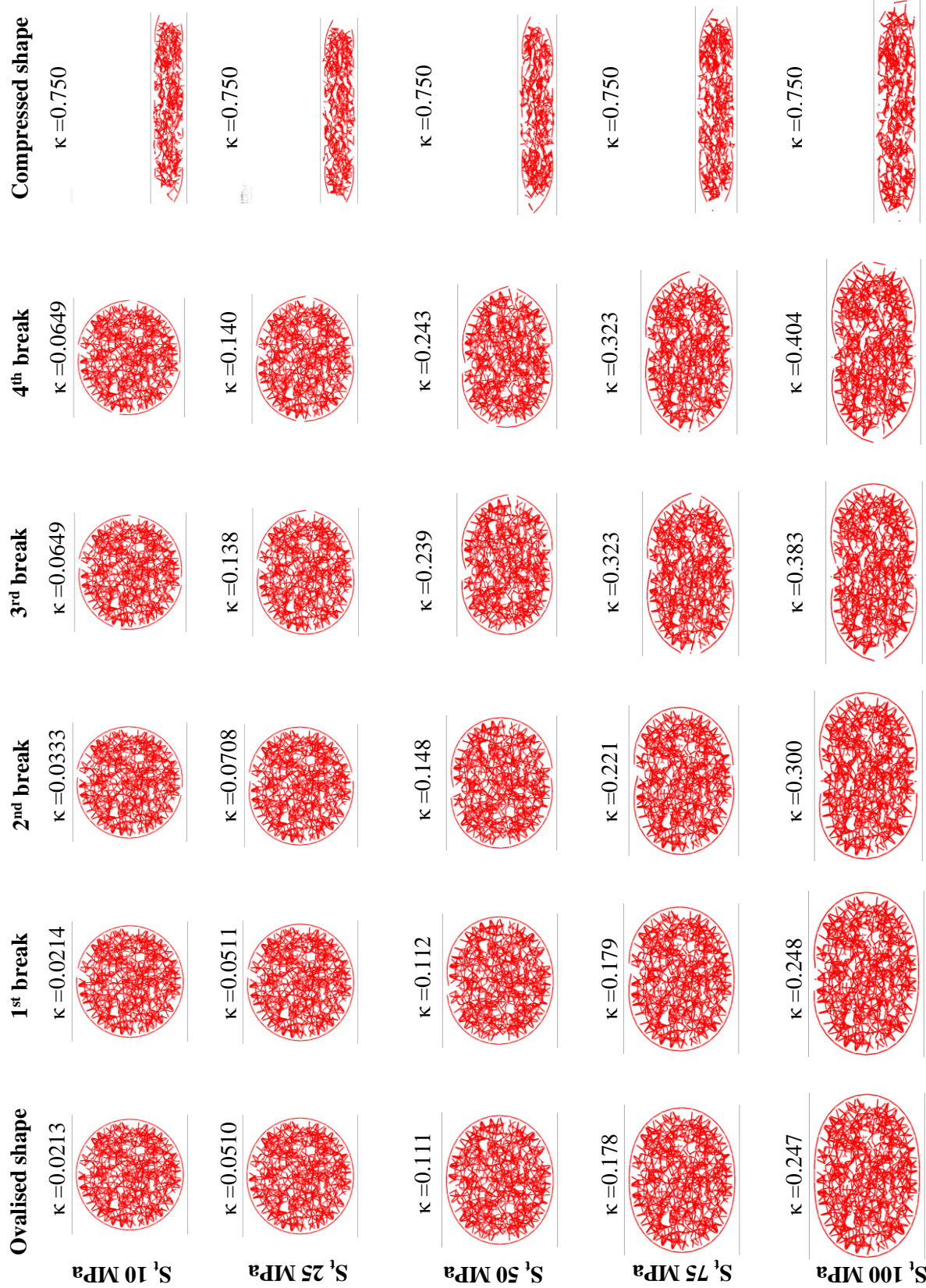


FIGURE C.16: Influence of the tensile strength of the bond in tangential direction of the skin on the breakage by sectional transversal compression (the existing bonds among the particles are visualized by red lines between the centre of the bonded particles).

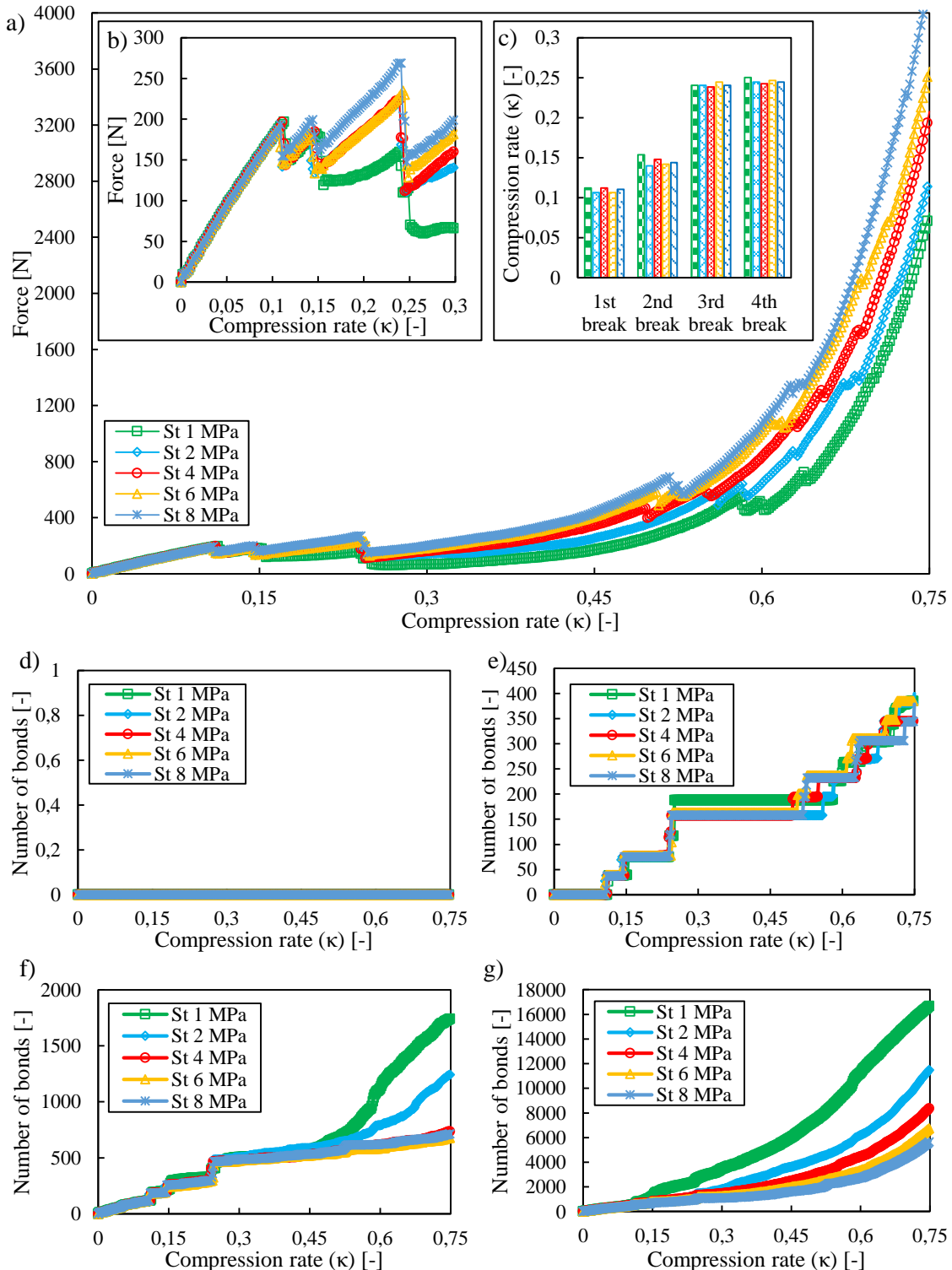


FIGURE C.17: Influence of the tensile strength of the bond in the core by sectional transversal compression: a) overall force-compression rate characteristics; b) force-compression rate characteristics in range of 0-0.3 compression rate; c) major break events in tangential direction of the skin; d) broken bonds of the skin in longitudinal direction; e) broken bonds of the skin in tangential direction; f) broken bonds between the skin and the core; g) broken bonds in the core.

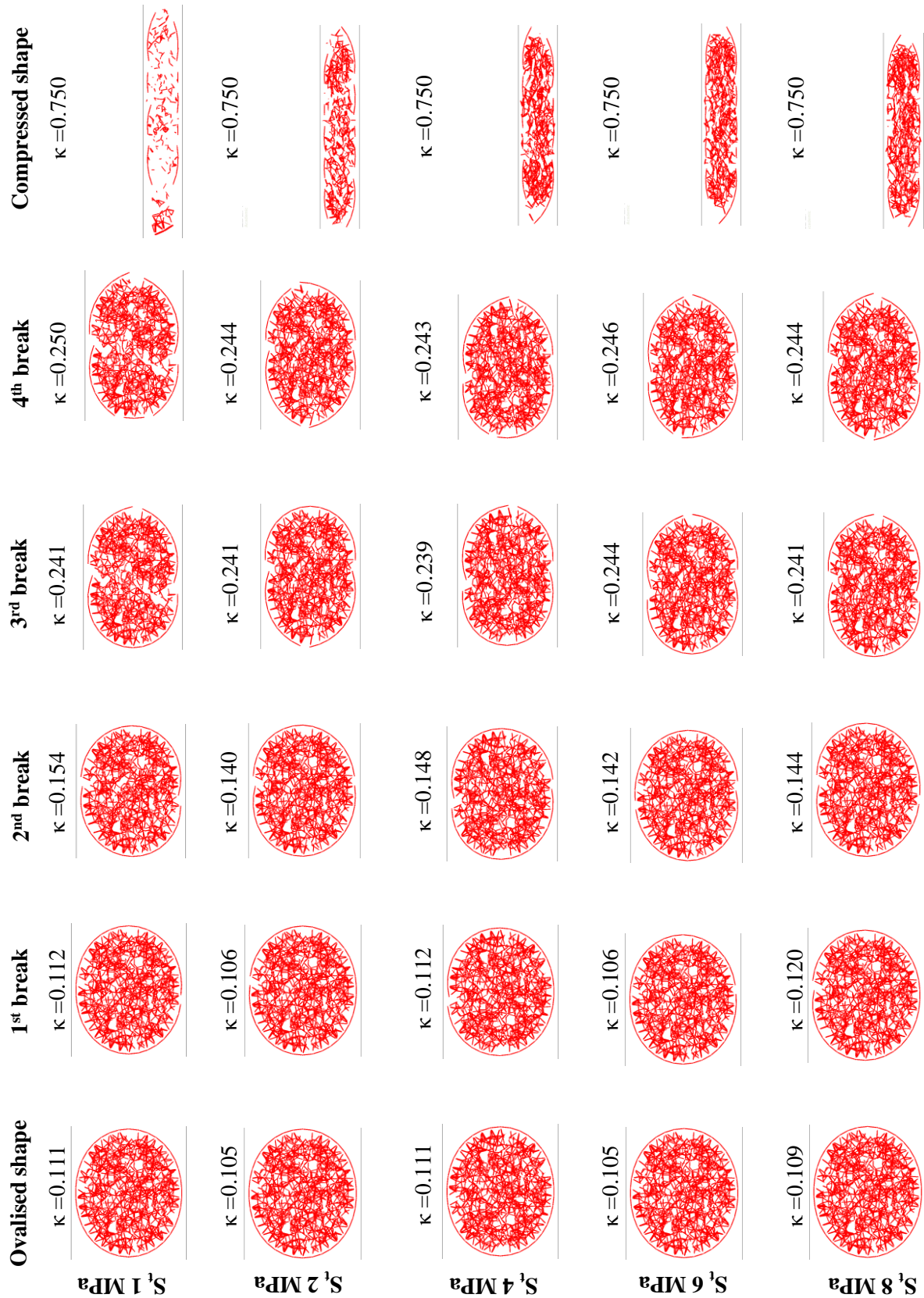


FIGURE C.18: Influence of the tensile strength of the bond in the core on the breakage by sectional transversal compression (the existing bonds among the particles are visualized by red lines between the centre of the bonded particles).

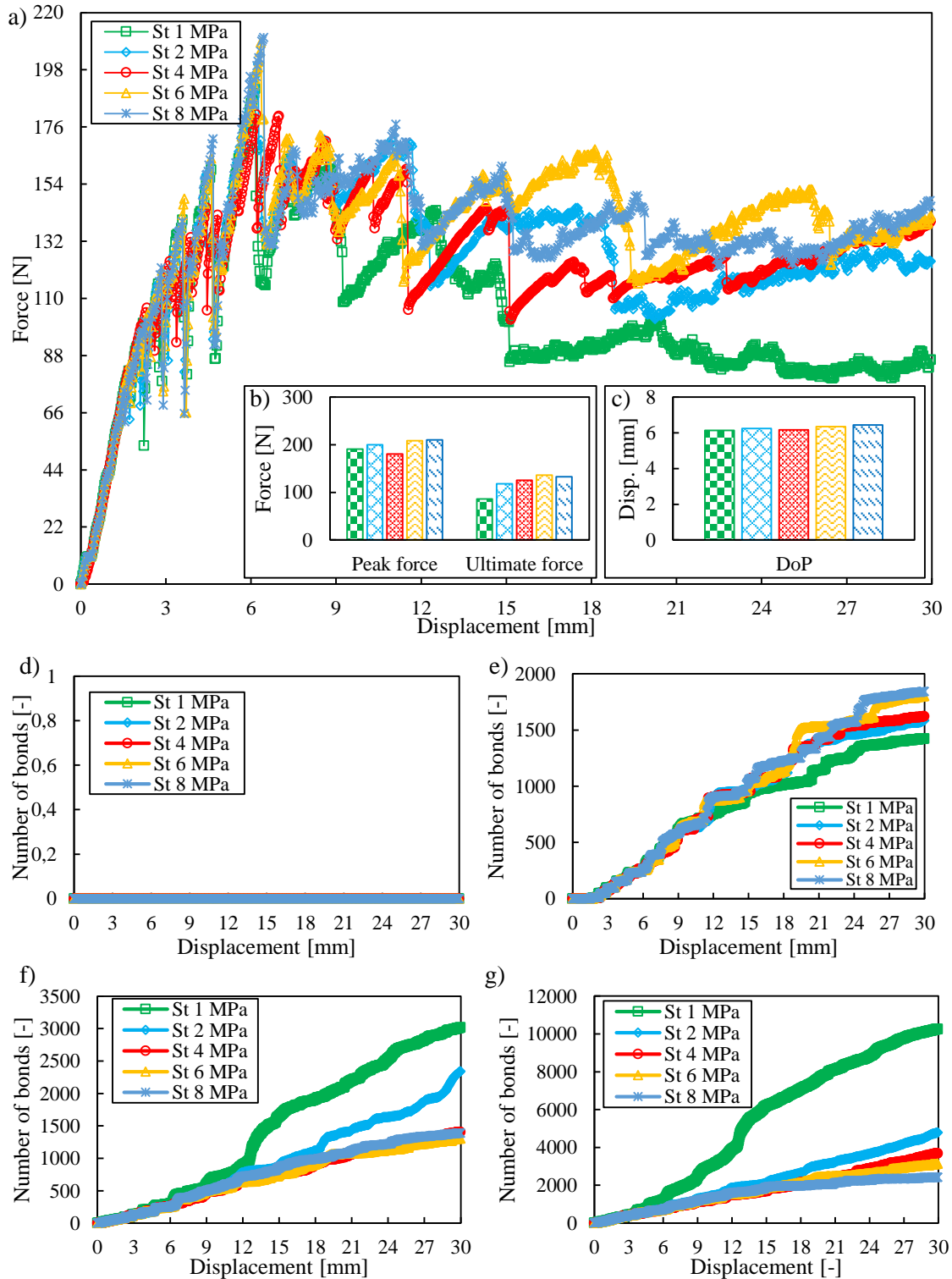


FIGURE C.19: Influence of the tensile strength of the bonds in the core by three-point bending: a) overall force-compression rate characteristics; b) peak and ultimate forces; c) displacement of the peak forces; d) broken bonds of the skin in longitudinal direction; e) broken bonds of the skin in tangential direction; f) broken bonds between the skin and the core; g) broken bonds in the core.

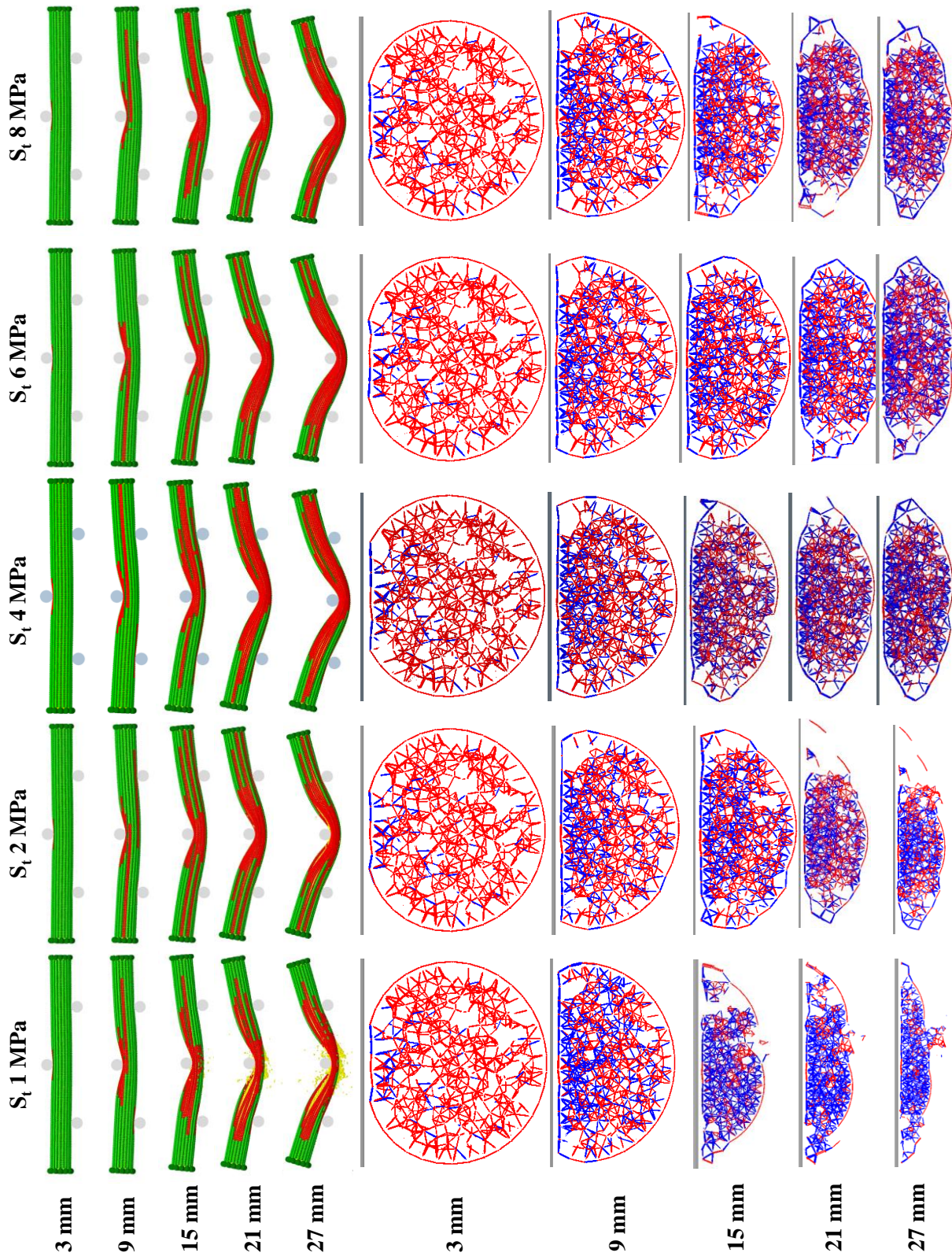


FIGURE C.20: Influence of the tensile strength of the bonds in the core on the breakage by three-point bending: comparison of the longitudinal crack propagation over the bending process (the particles of the skin are visualised by the damage parameter of 0.1) and the breakage of the cross-section under the bending tool (the existing bonds among the particles are visualized by red lines between the centre of the bonded particles).

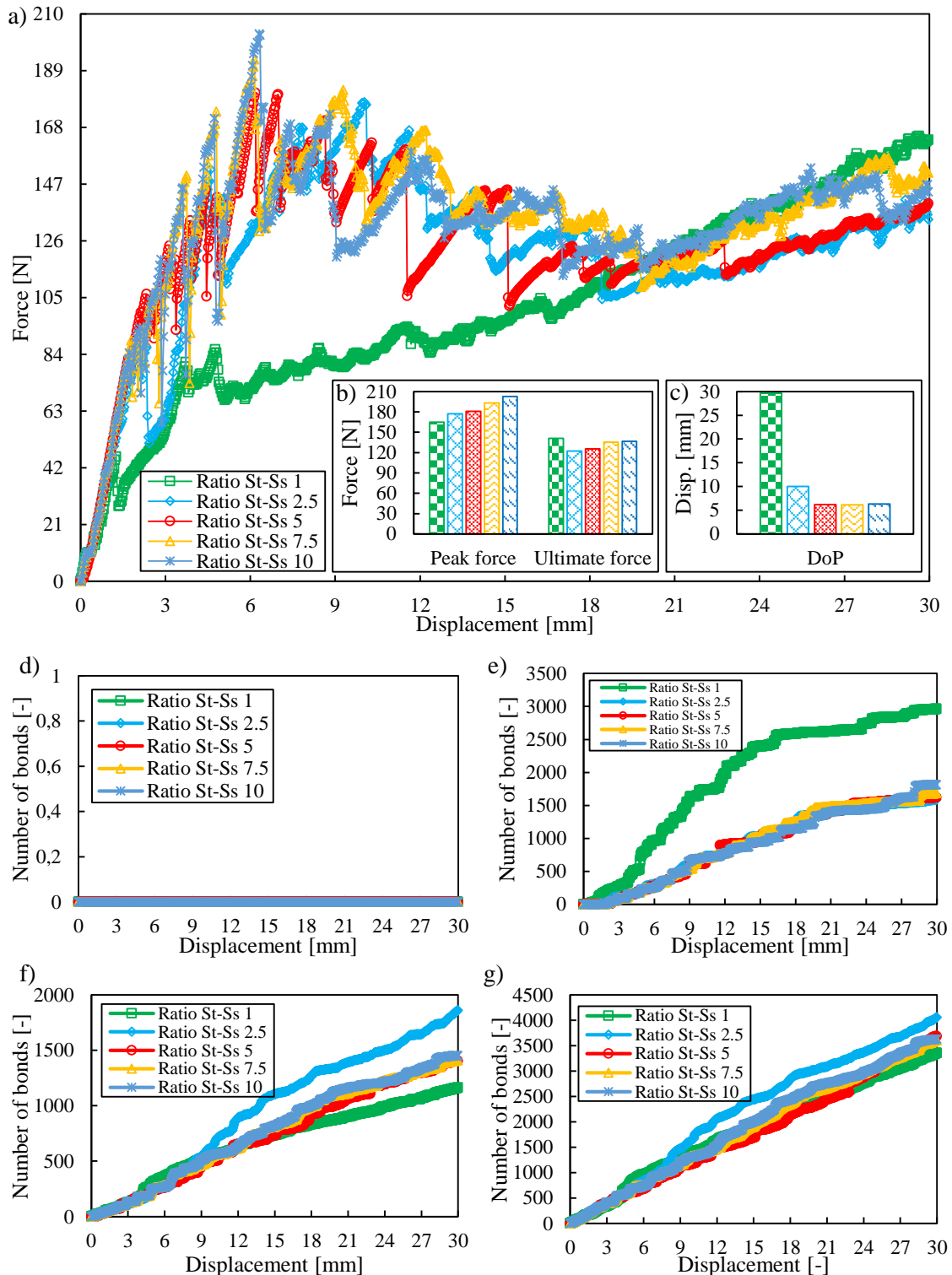


FIGURE C.21: Influence of the ratio between the tensile and shear strength of the bonds in tangential direction of the skin by three-point bending: a) overall force-compression rate characteristics; b) peak and ultimate forces; c) displacement of the peak forces; d) broken bonds of the skin in longitudinal direction; e) broken bonds of the skin in tangential direction; f) broken bonds between the skin and the core; g) broken bonds in the core.

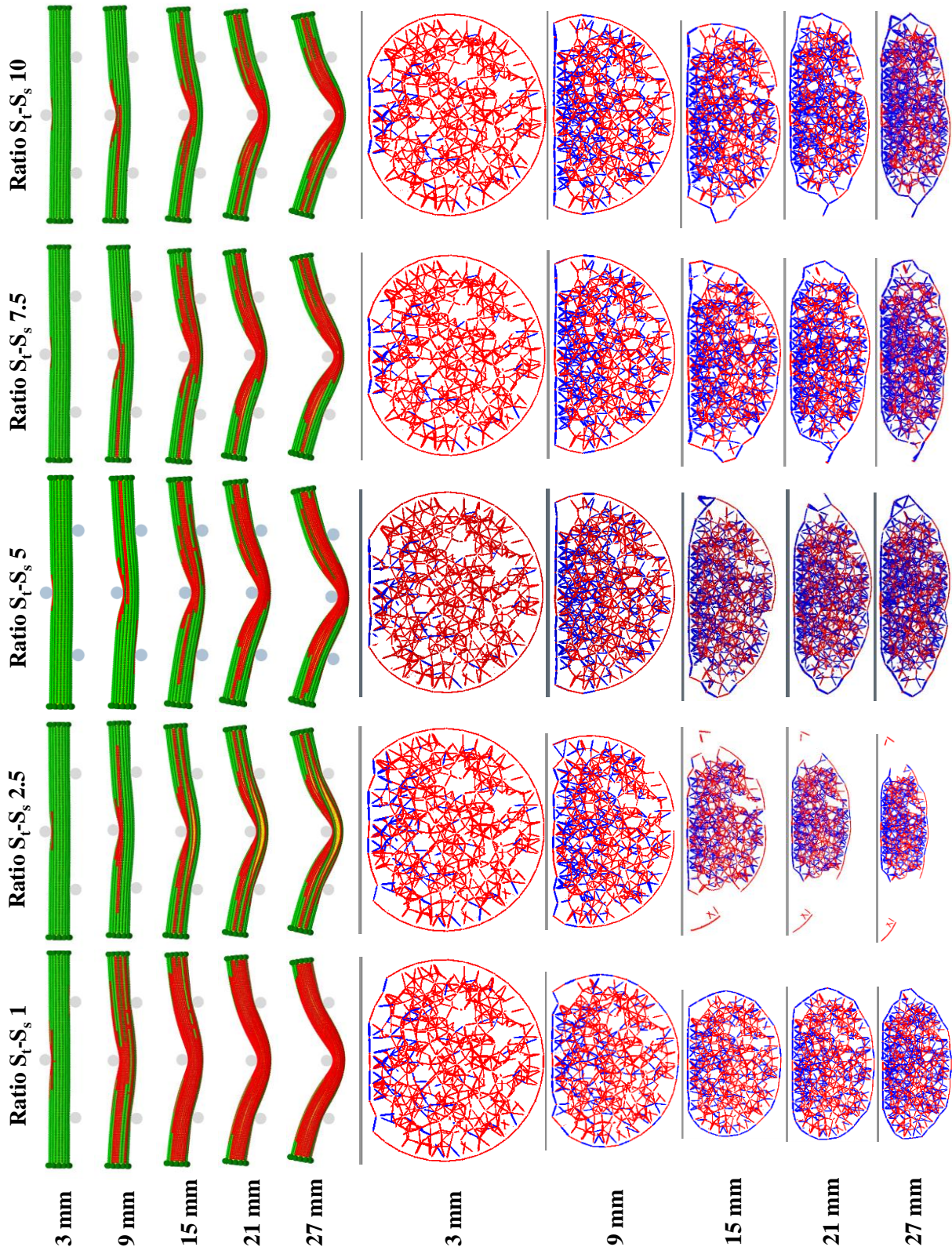


FIGURE C.22: Influence of the the ratio between the tensile and shear strength of the bonds in tangential direction of the skin on the breakage by three-point bending; comparison of the longitudinal crack propagation over the bending process (the particles of the skin are visualised by the damage parameter of 0.1) and the breakage of the cross-section under the bending tool (the existing bonds among the particles are visualized by red lines between the centre of the bonded particles).

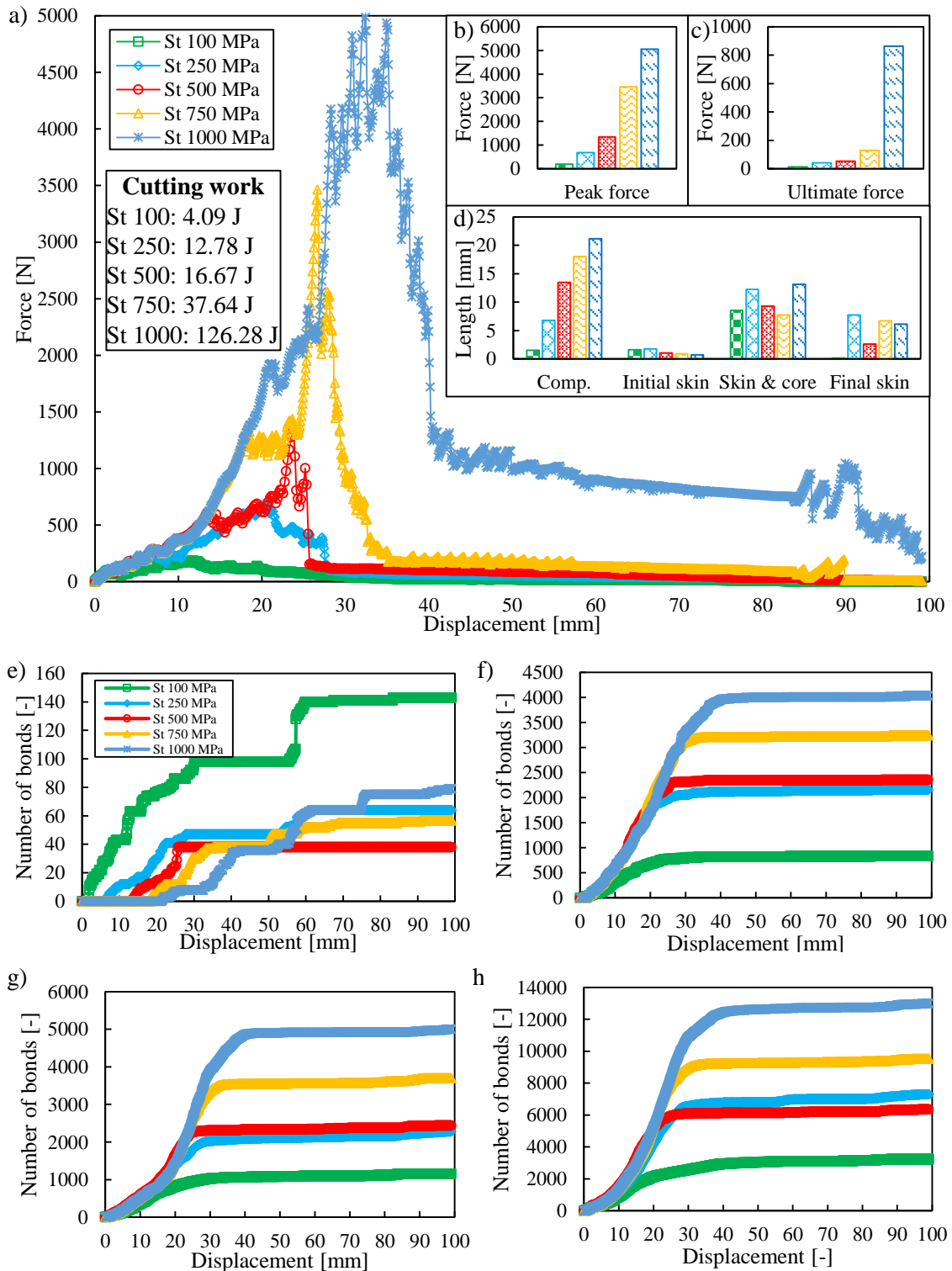


FIGURE C.23: Influence of the tensile strength of the bonds in longitudinal direction of the skin by dynamic cutting: a) overall force-displacement characteristics; b) range of the peak forces; c) range of the ultimate forces; d) length of the stages of cut; e) broken bonds of the skin in longitudinal direction; f) broken bonds of the skin in tangential direction; g) broken bonds between the skin and the core; h) broken bonds in the core.

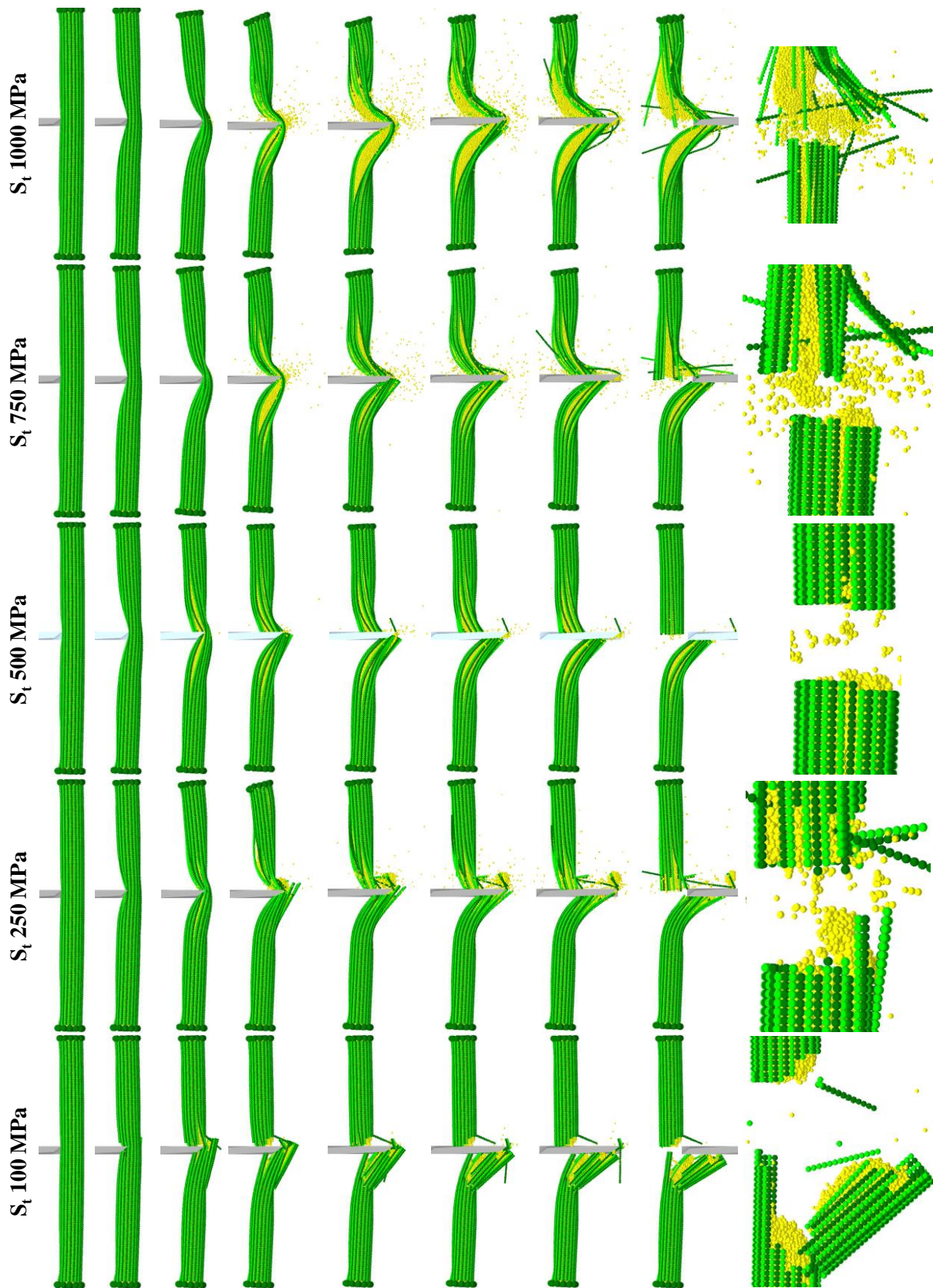


FIGURE C.24: Influence of the tensile strength of the bonds in longitudinal direction of the skin on the breakage by dynamic cutting dynamic cutting: comparison of the cutting processes and the resulted cutting surfaces.

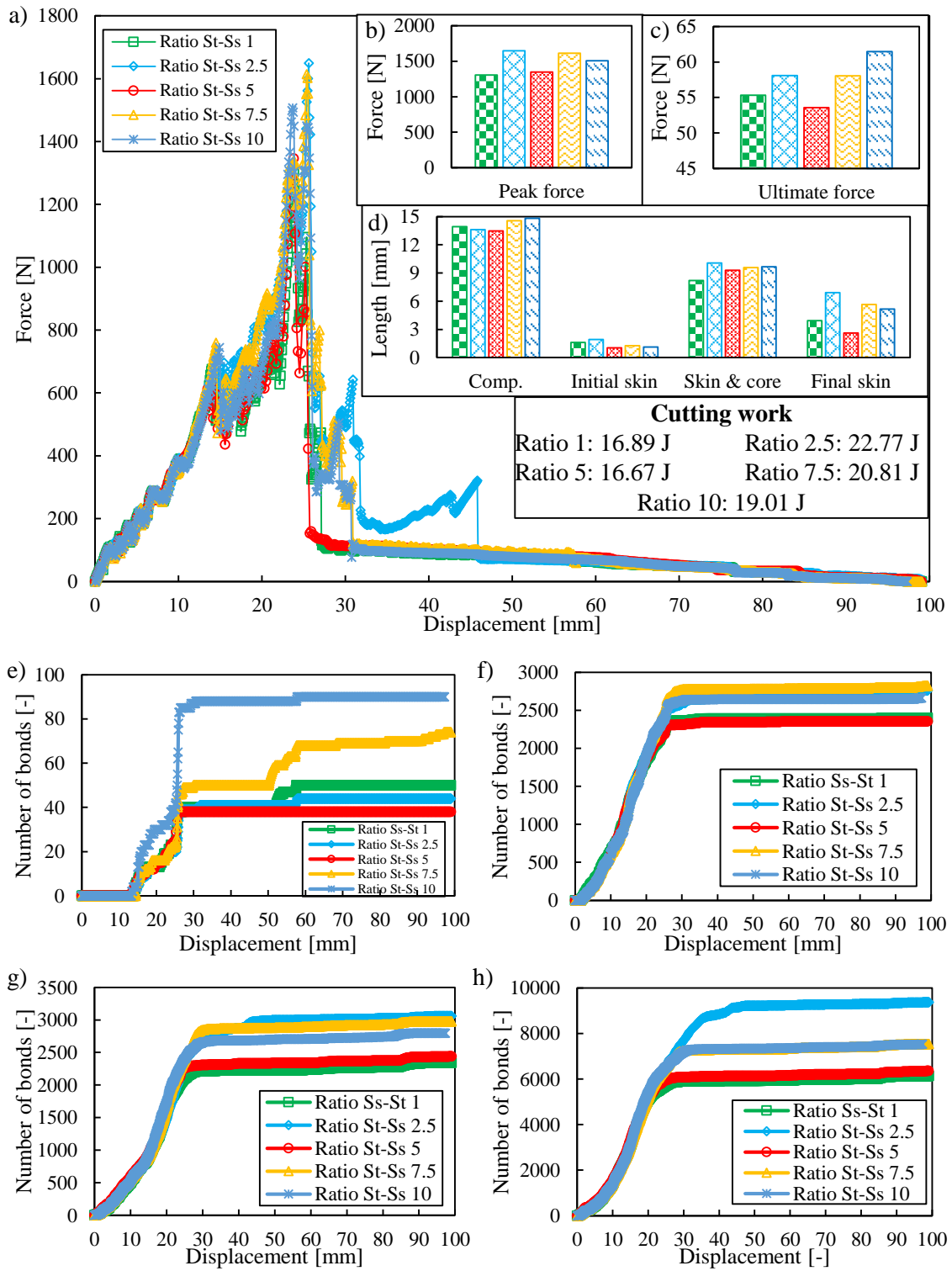


FIGURE C.25: Influence of the ratio between the tensile and shear strength of the bonds in longitudinal direction of the skin by dynamic cutting: a) overall force-displacement characteristics; b) range of the peak forces; c) range of the ultimate forces; d) length of the stages of cut; e) broken bonds of the skin in longitudinal direction; f) broken bonds of the skin in tangential direction; g) broken bonds between the skin and the core; h) broken bonds in the core.

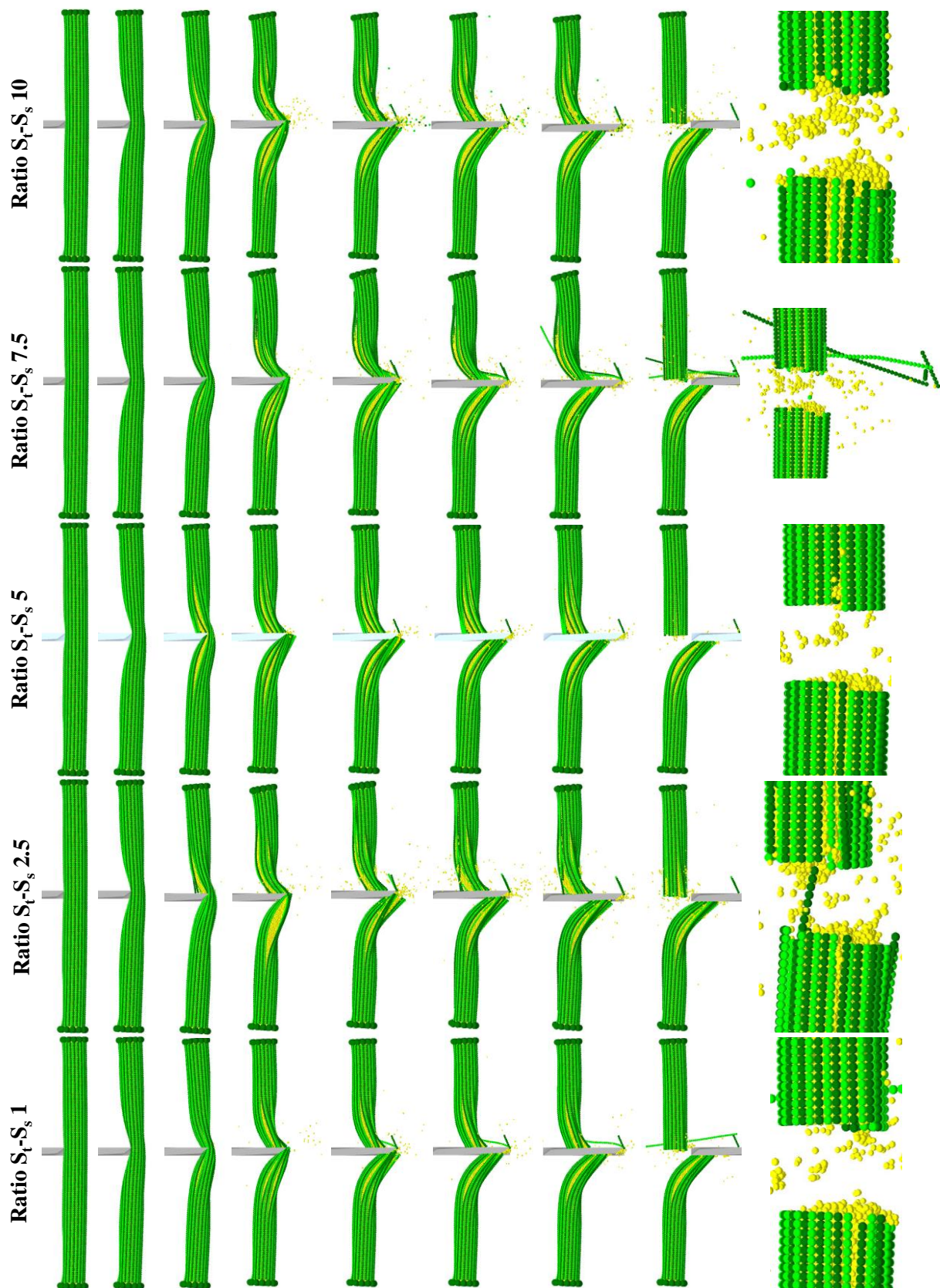


FIGURE C.26: Influence of the ratio between the tensile and shear strength of the bonds in longitudinal direction of the skin on the breakage by dynamic cutting dynamic cutting: comparison of the cutting processes and the resulted cutting surfaces.

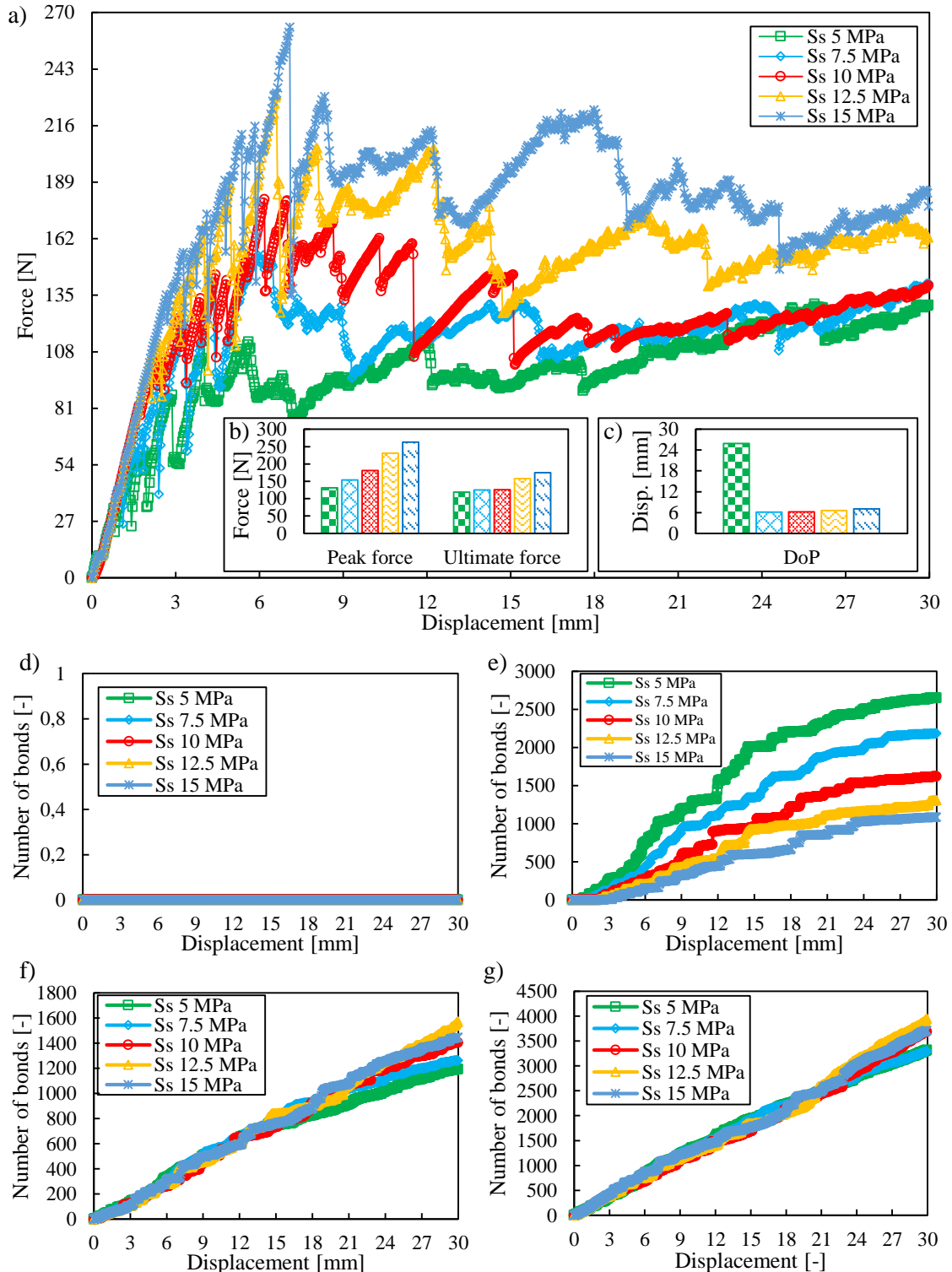


FIGURE C.27: Influence of the shear strength of the bonds in tangential direction of the skin by three-point bending: a) overall force-compression rate characteristics; b) peak and ultimate forces; c) displacement of the peak forces; d) broken bonds of the skin in longitudinal direction; e) broken bonds of the skin in tangential direction; f) broken bonds between the skin and the core; g) broken bonds in the core.

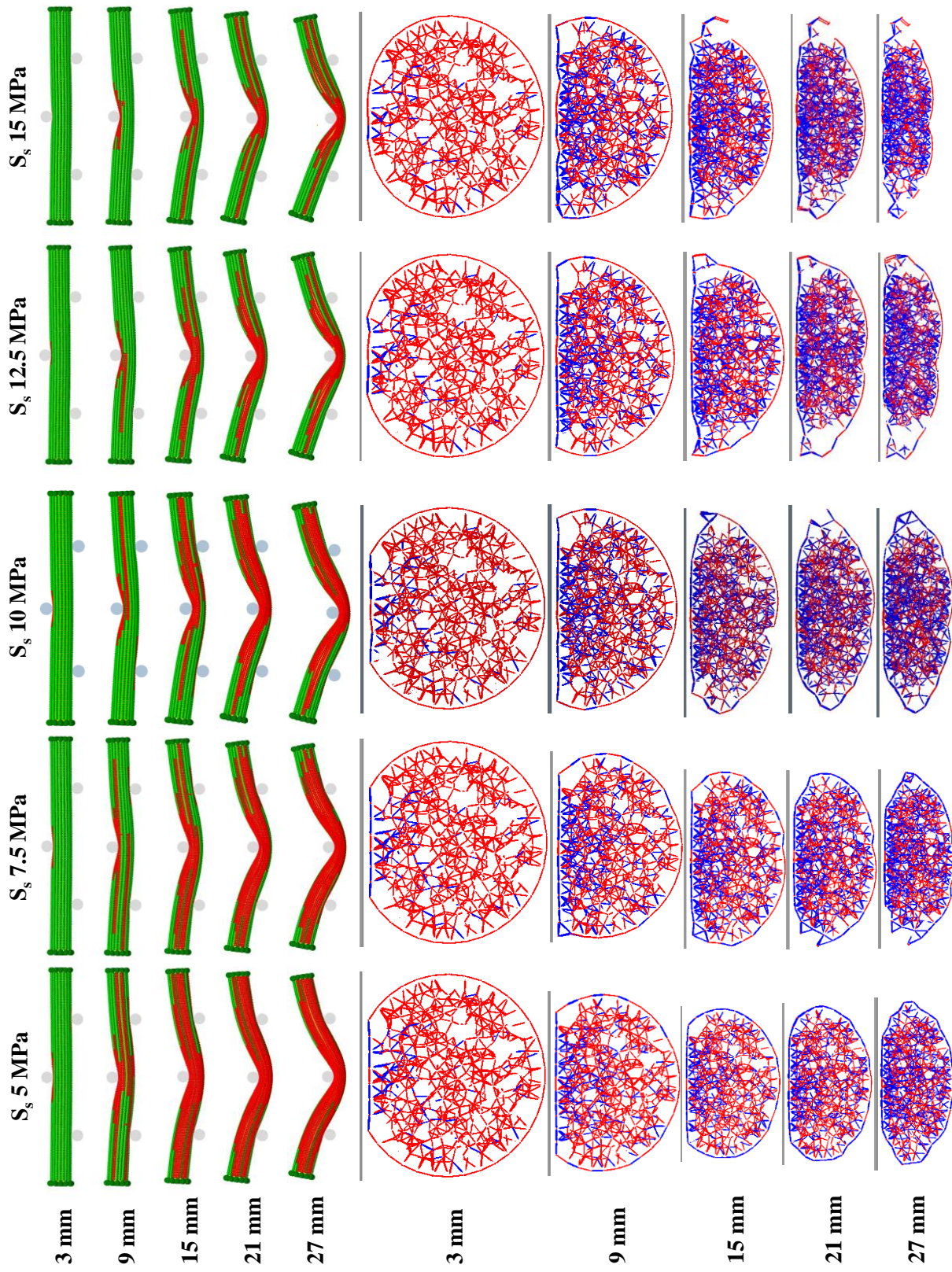


FIGURE C.28: Influence of the shear strength of the bonds in tangential direction of the skin on the breakage of the longitudinal crack propagation over the bending process (the particles of the skin are visualised by the damage parameter of 0.1) and the breakage of the cross-section under the bending tool (the existing bonds among the particles are visualized by red lines between the bonded particles).

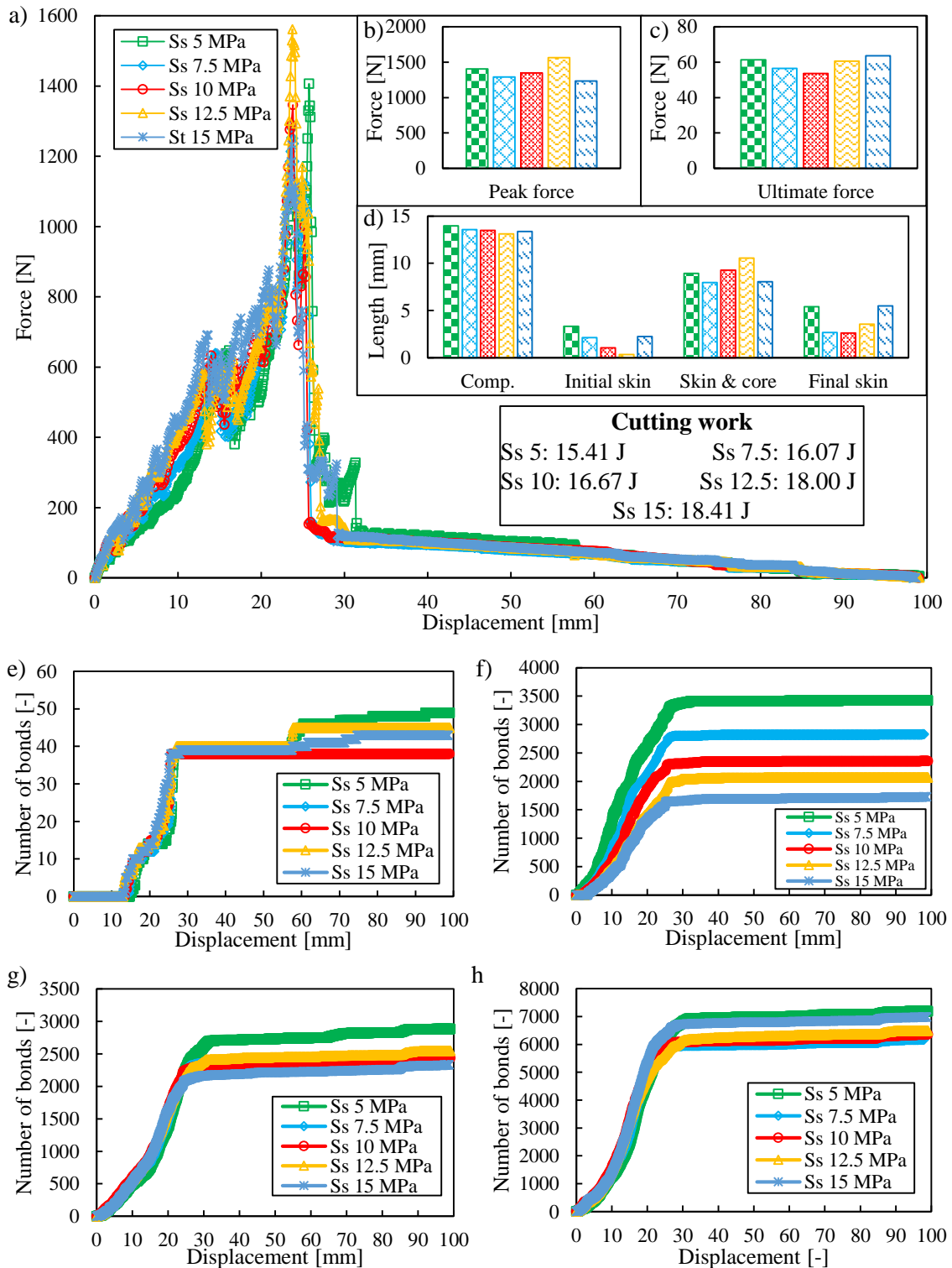


FIGURE C.29: Influence of the shear strength of the bonds in longitudinal direction of the skin by dynamic cutting: a) overall force-displacement characteristics; b) range of the peak forces; c) range of the ultimate forces; d) length of the stages of cut; e) broken bonds of the skin in longitudinal direction; f) broken bonds of the skin in tangential direction; g) broken bonds between the skin and the core; h) broken bonds in the core.

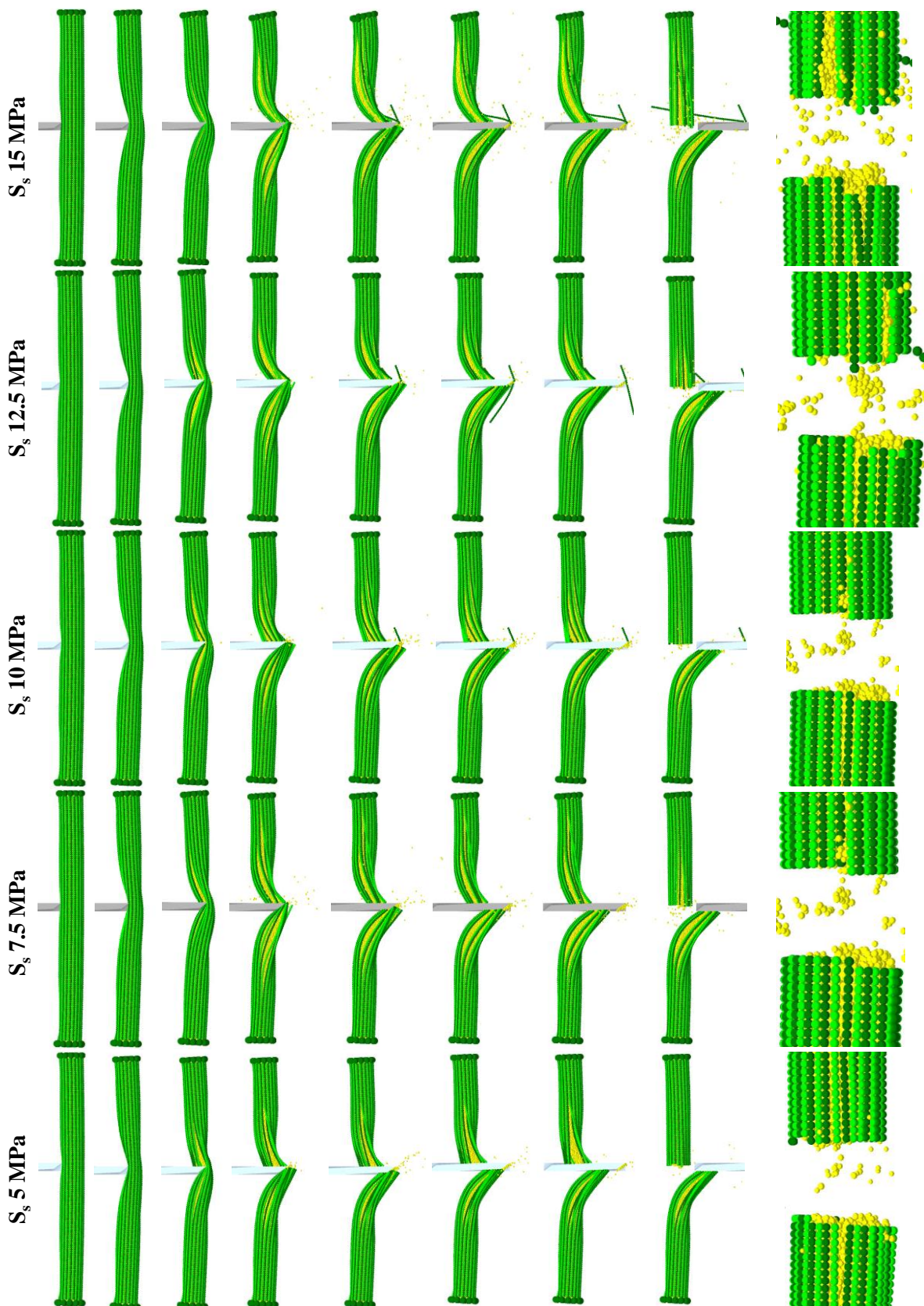


FIGURE C.30: Influence of the shear strength of the bonds in longitudinal direction of the skin on the breakage by dynamic cutting dynamic cutting: comparison of the cutting processes and the resulted cutting surfaces.

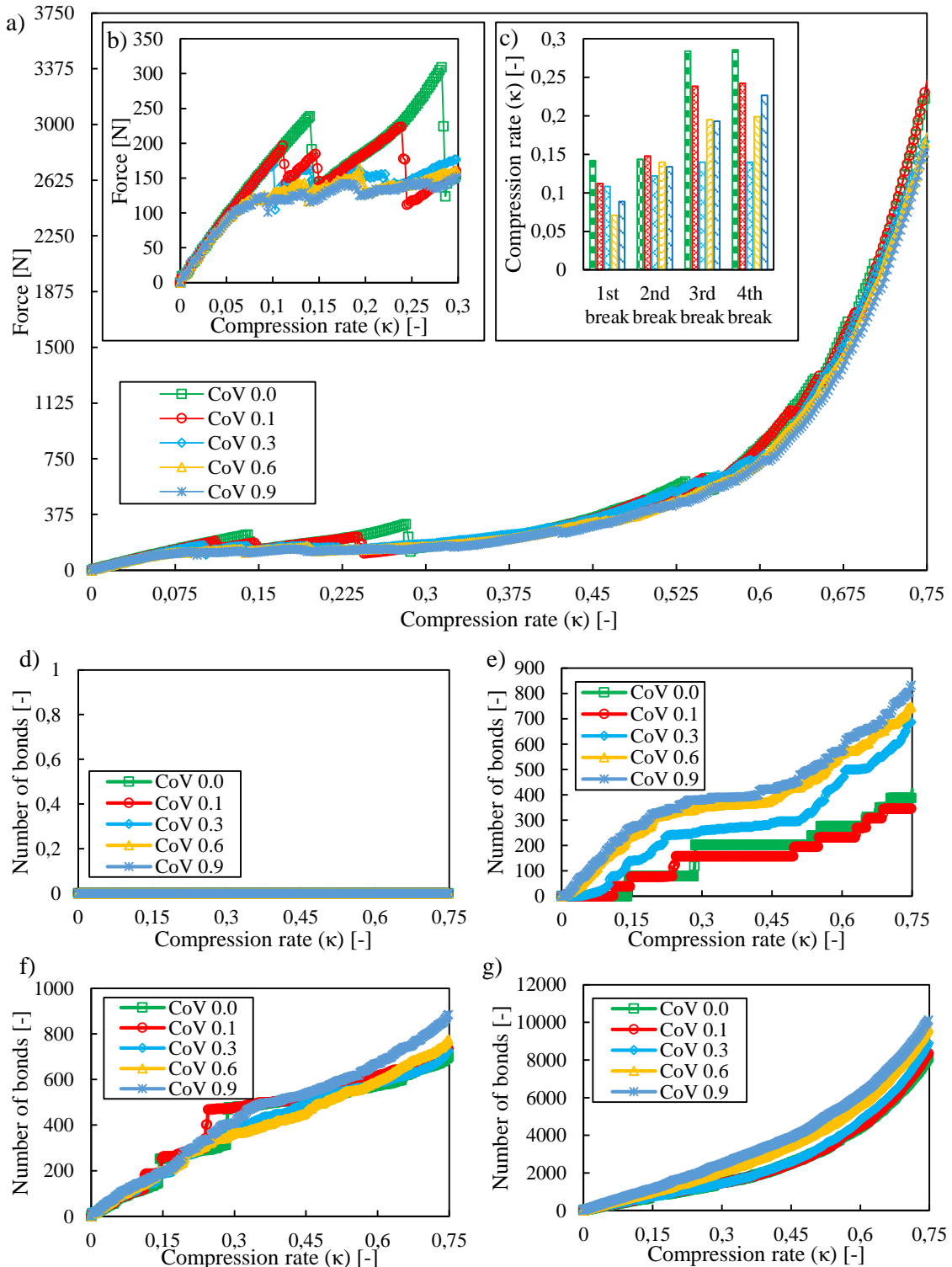


FIGURE C.31: Influence of the coefficient of variation of the bonded strength parameters by sectional transversal compression: a) overall force-compression rate characteristics; b) force-compression rate characteristics in range of 0-0.3 compression rate; c) major break events in tangential direction of the skin; d) broken bonds of the skin in longitudinal direction; e) broken bonds of the skin in tangential direction; f) broken bonds between the skin and the core; g) broken bonds in the core.

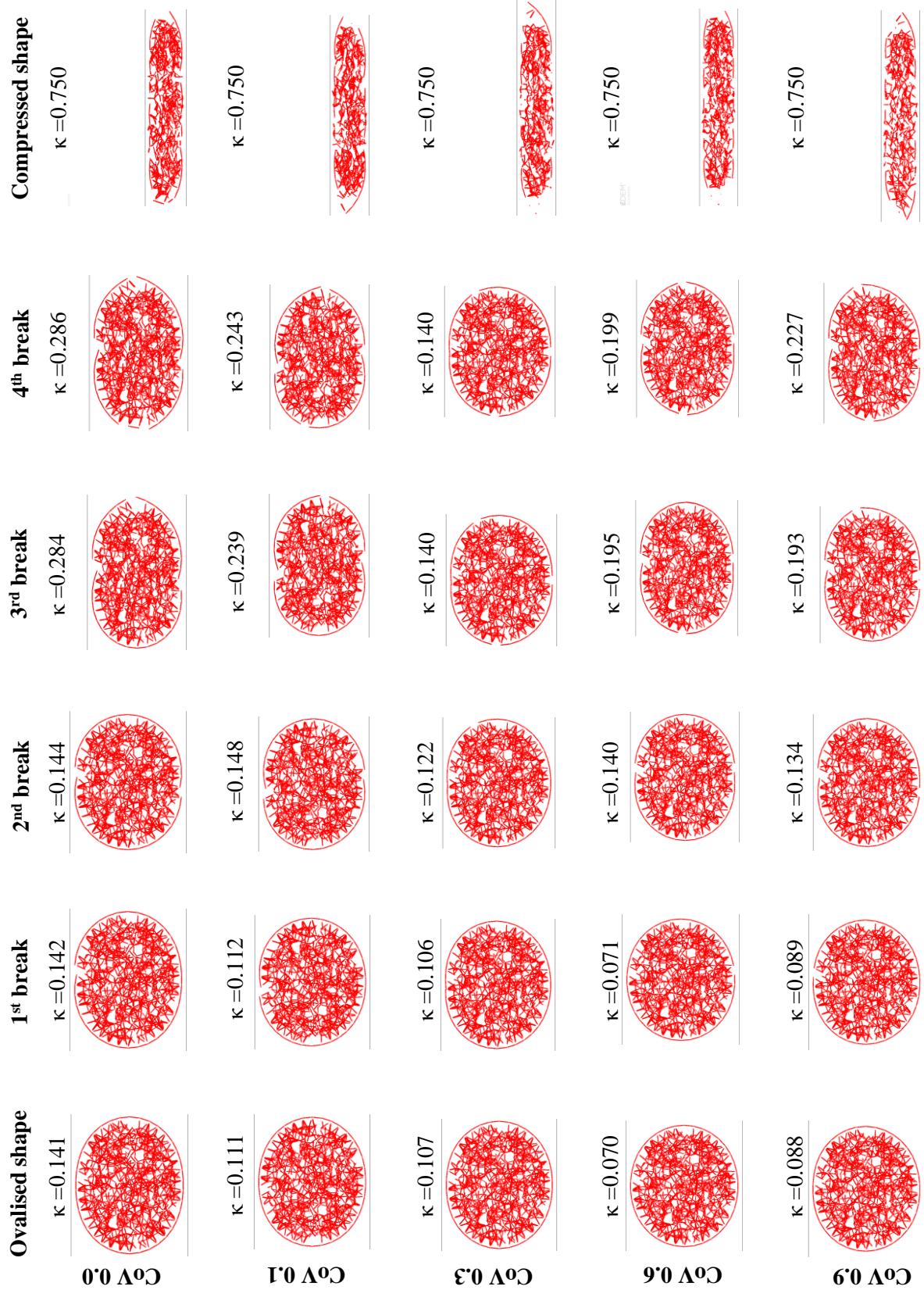


FIGURE C.32: Influence of the coefficient of variation of the bonded strength parameters in the core on the breakage by sectional transversal compression (the existing bonds among the particles are visualized by red lines between the centre of the bonded particles).

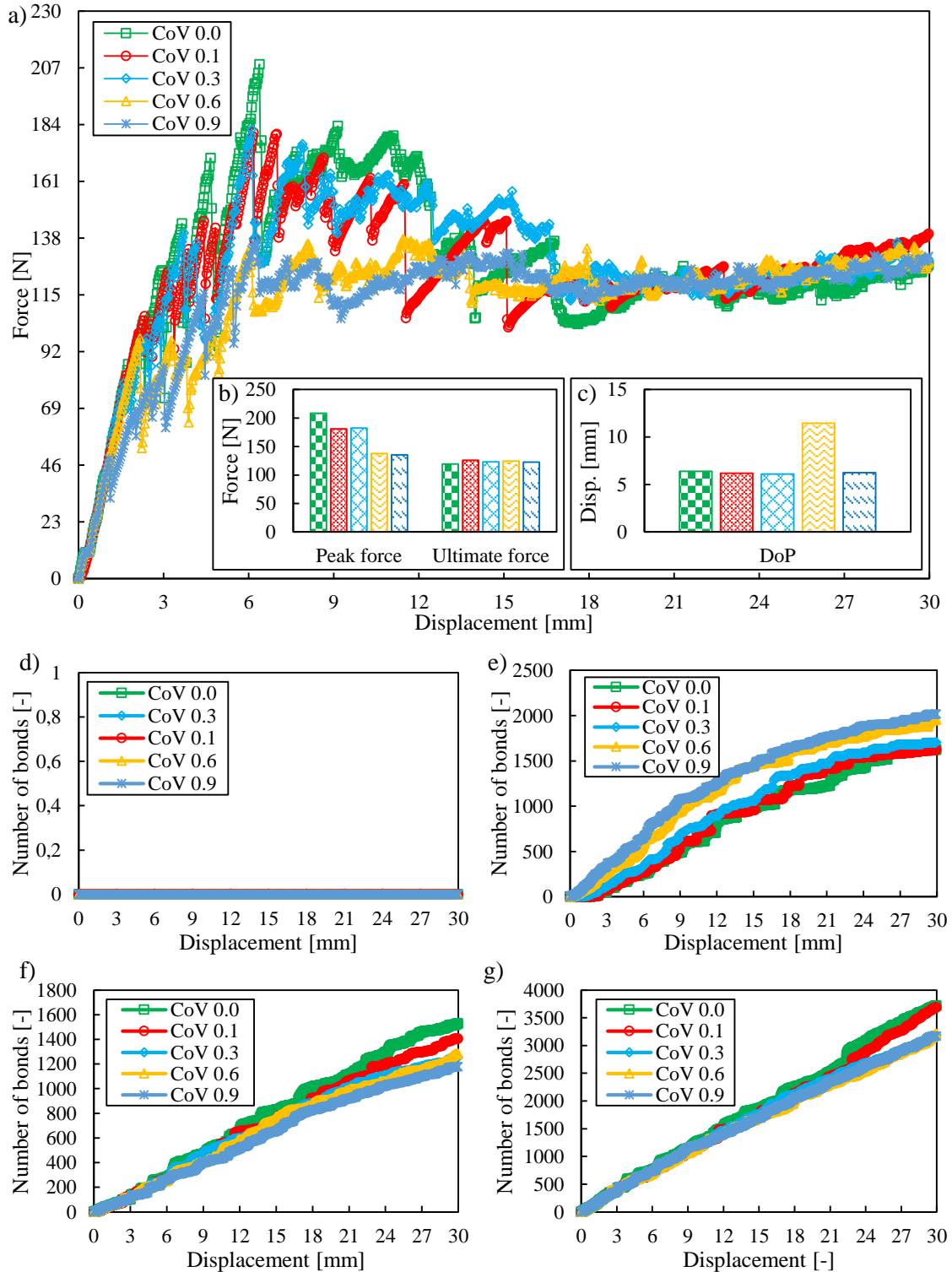


FIGURE C.33: Influence of the coefficient of variation of the bonded strength parameters by three-point bending: a) overall force-compression rate characteristics; b) peak and ultimate forces; c) displacement of the peak forces; d) broken bonds of the skin in longitudinal direction; e) broken bonds of the skin in tangential direction; f) broken bonds between the skin and the core; g) broken bonds in the core.

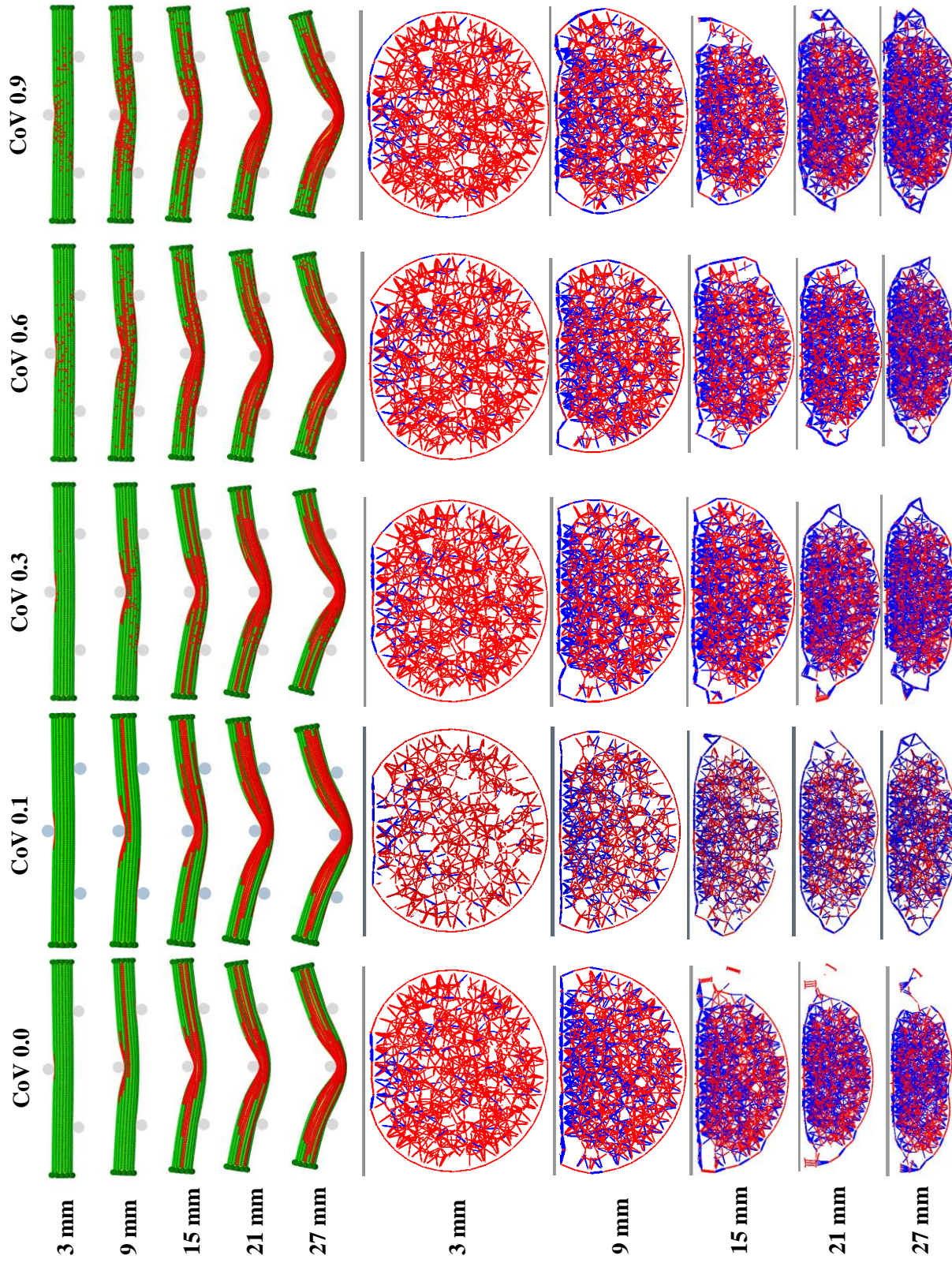


FIGURE C.34: Influence of the coefficient of variation of the bonded strength parameters on the breakage by three-point bending: comparison of the longitudinal crack propagation over the bending process (the particles of the skin are visualised by the damage parameter of 0.1) and the breakage of the cross-section under the bending tool (the existing bonds among the particles are visualized by red lines between the existing bonds).

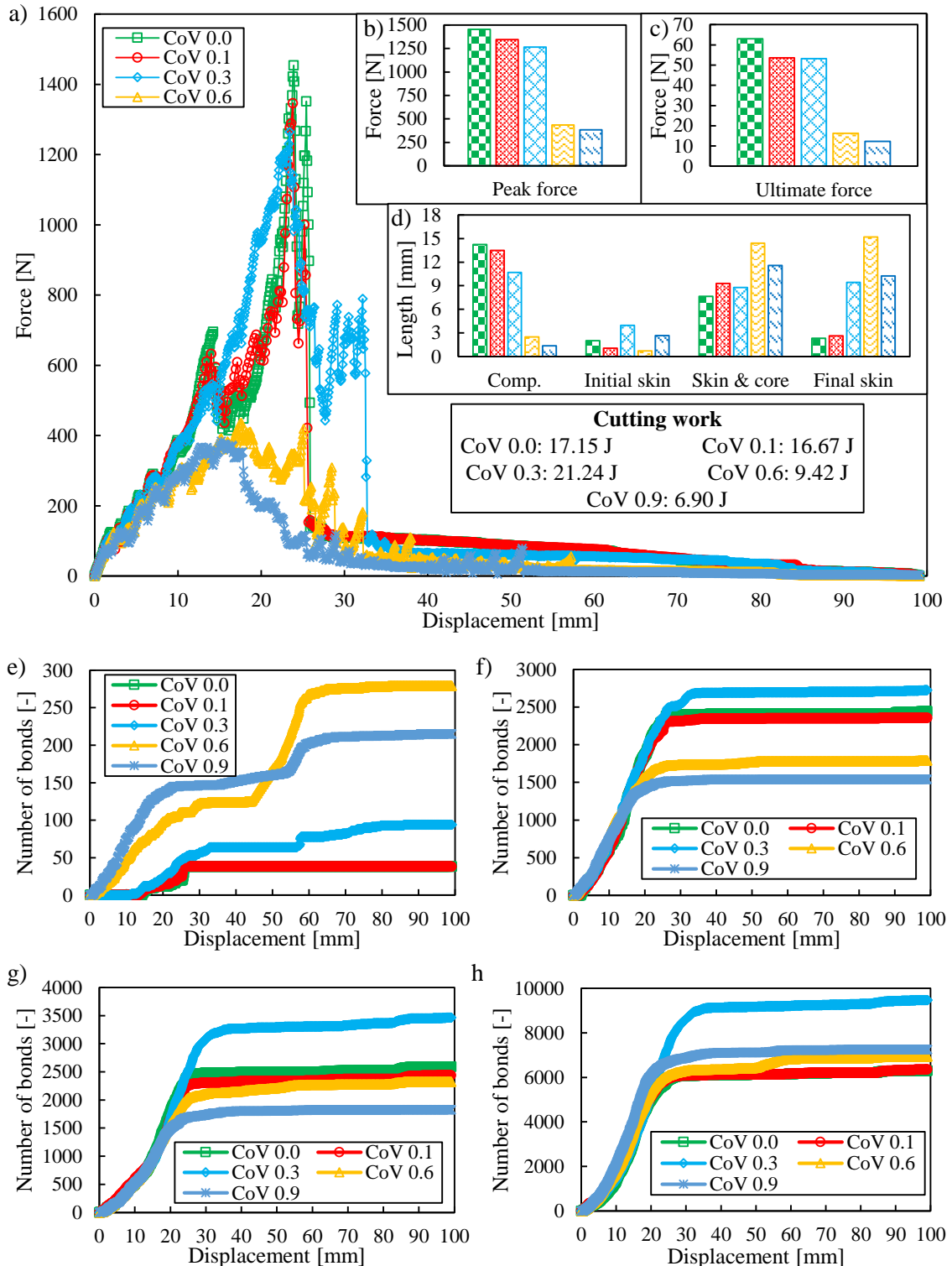


FIGURE C.35: Influence of the coefficient of variation of the bonded strength parameters by dynamic cutting: a) overall force-displacement characteristics; b) range of the peak forces; c) range of the ultimate forces; d) length of the stages of cut; e) broken bonds of the skin in longitudinal direction; f) broken bonds of the skin in tangential direction; g) broken bonds between the skin and the core; h) broken bonds in the core.

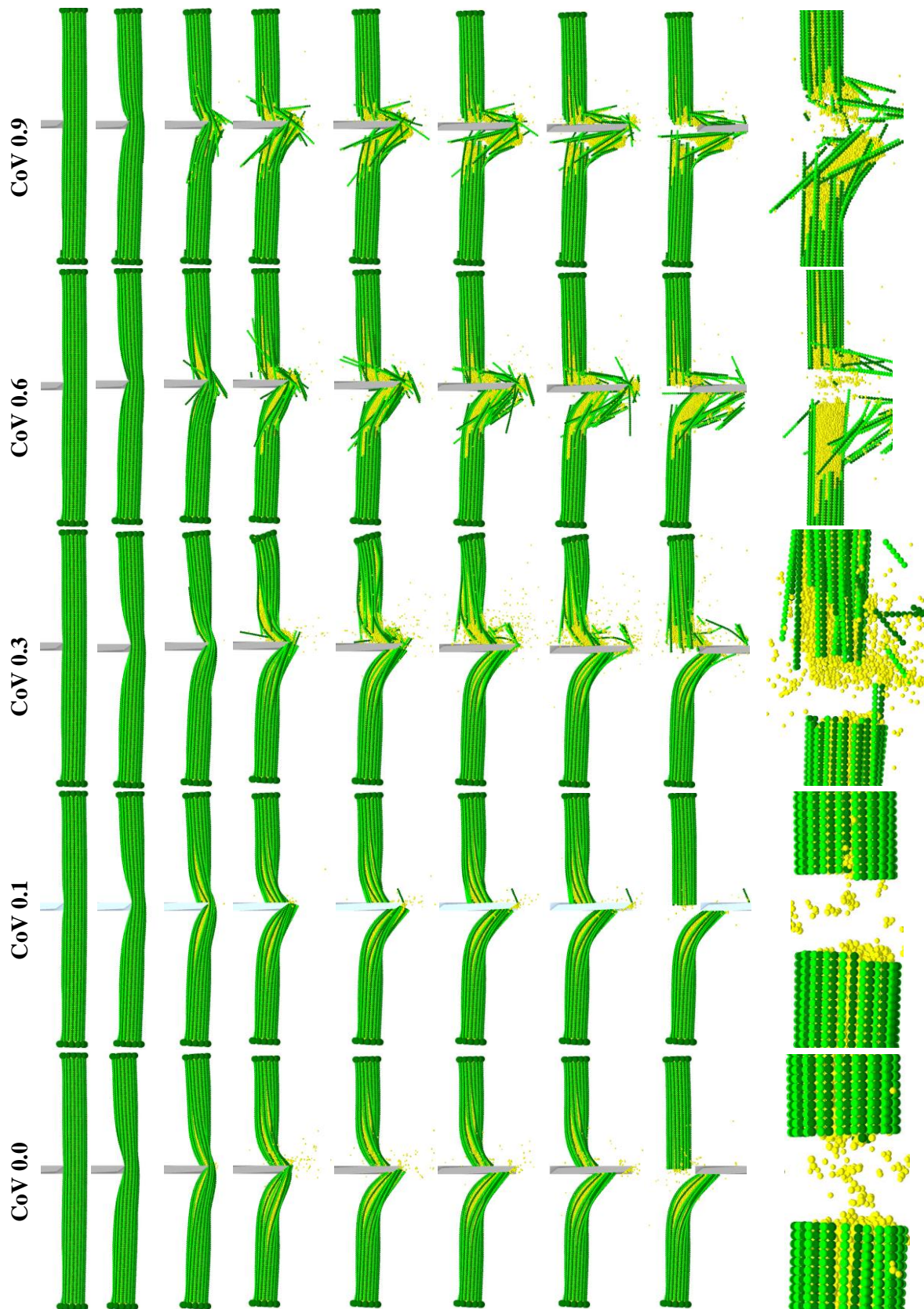


FIGURE C.36: Influence of the coefficient of variation of the bonded strength parameters on the breakage by dynamic cutting dynamic cutting: comparison of the cutting processes and the resulted cutting surfaces.



## D Non-Bonded Contact Parameters

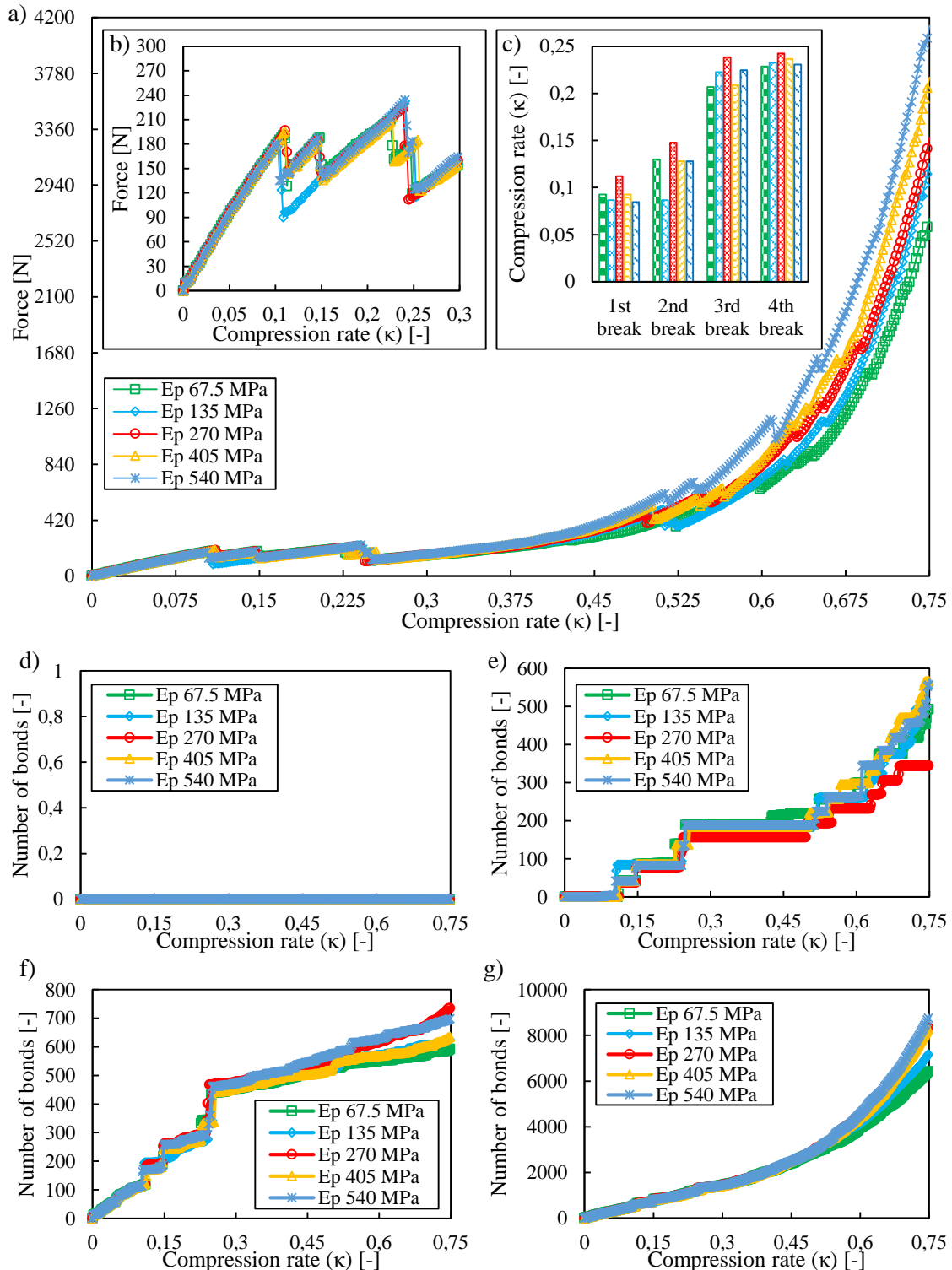
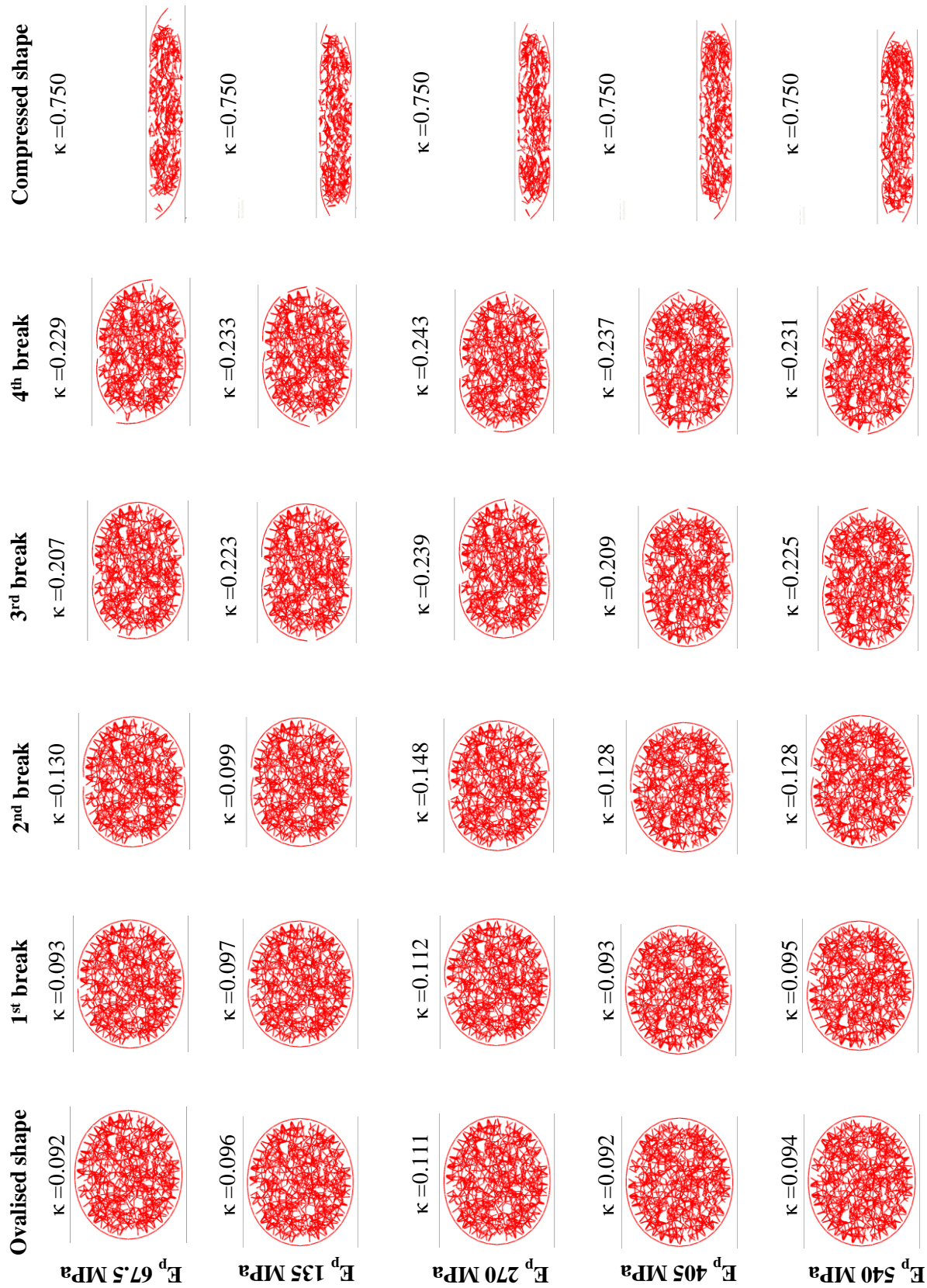


FIGURE D.1: Influence of the the particle Young's modulus by sectional transversal compression: a) overall force-compression rate characteristics; b) force-compression rate characteristics in range of 0-0.3 compression rate; c) major break events in tangential direction of the skin; d) broken bonds of the skin in longitudinal direction; e) broken bonds of the skin in tangential direction; f) broken bonds between the skin and the core; g) broken bonds in the core.



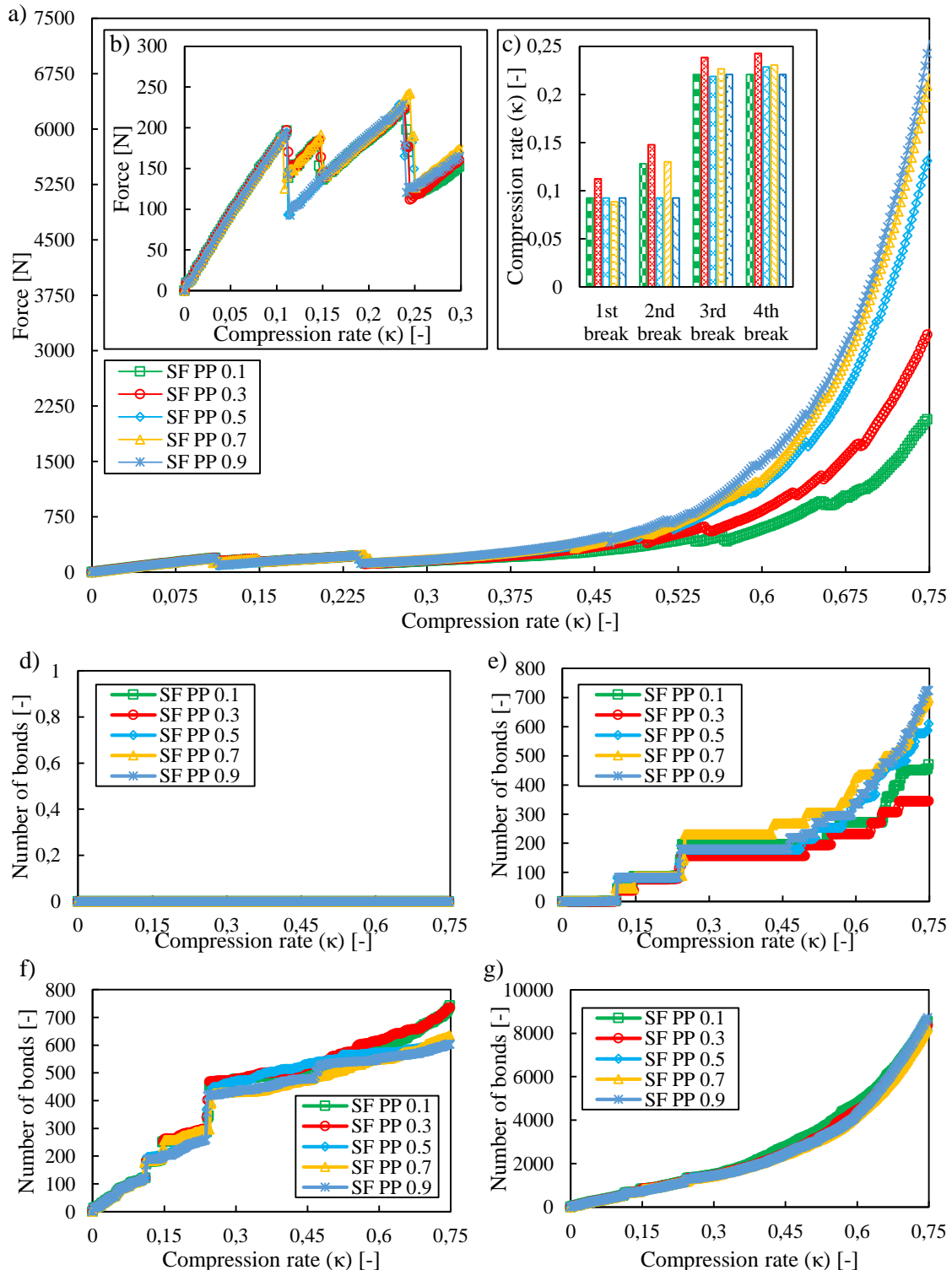


FIGURE D.3: Influence of the particle-particle coefficient of static friction by sectional transversal compression: a) overall force-compression rate characteristics; b) force-compression rate characteristics in range of 0-0.3 compression rate; c) major break events in tangential direction of the skin; d) broken bonds of the skin in longitudinal direction; e) broken bonds of the skin in tangential direction; f) broken bonds between the skin and the core; g) broken bonds in the core.

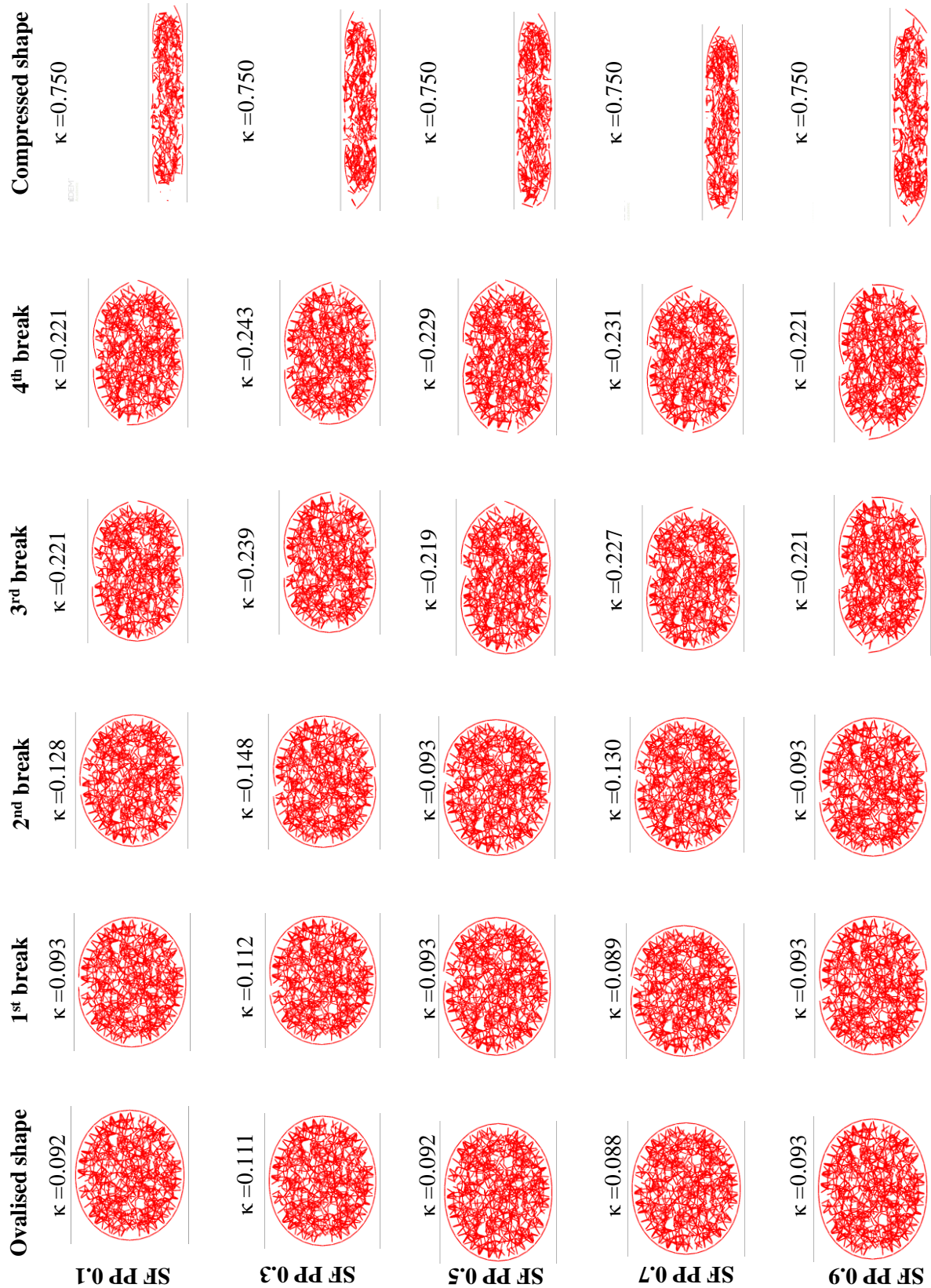


FIGURE D.4: Influence of the particle-particle coefficient of static friction on the breakage by sectional transversal compression (the existing bonds among the particles are visualized by red lines between the centre of the bonded particles).

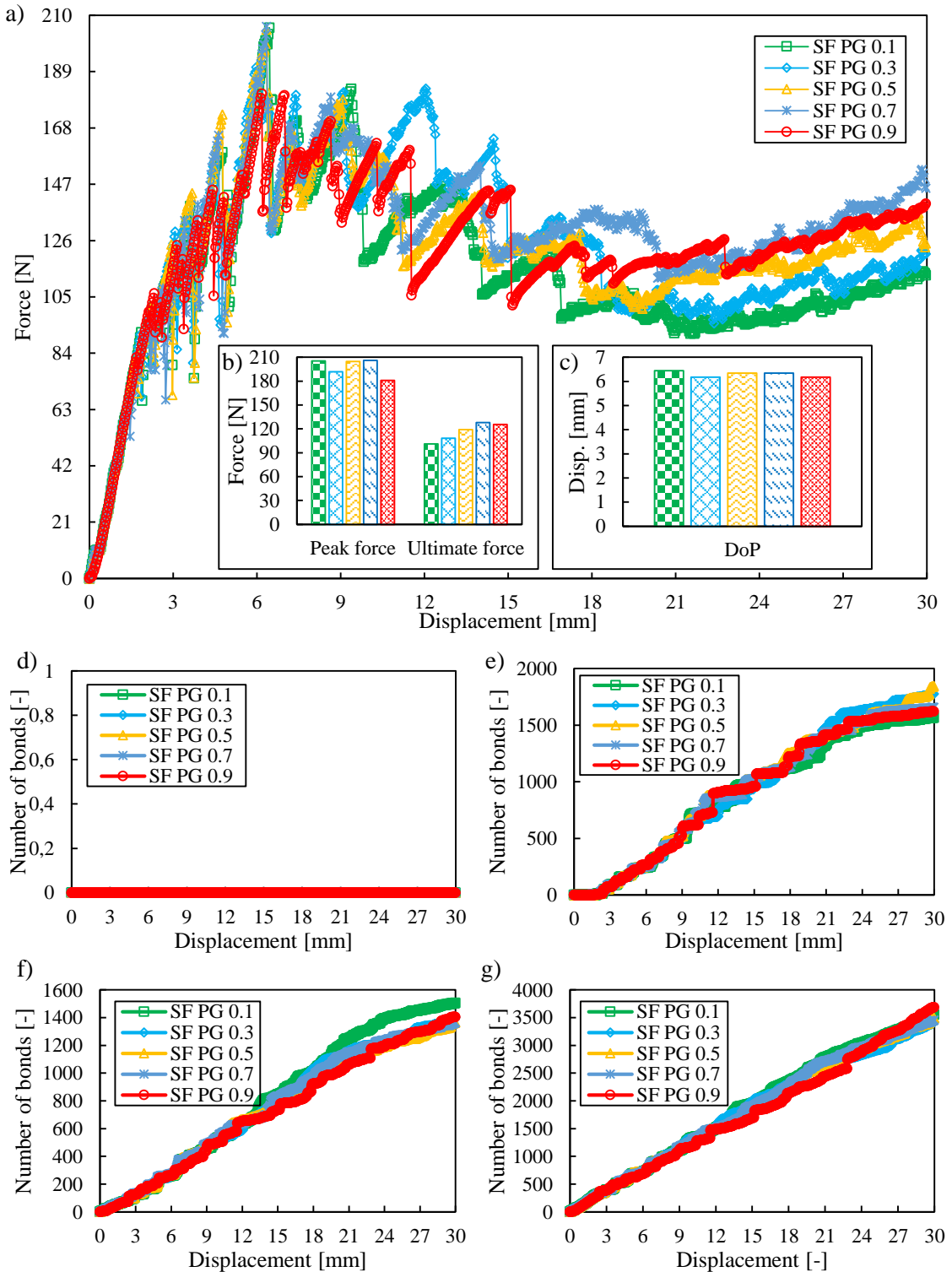


FIGURE D.5: Influence of the particle-geometry coefficient of static friction by three-point bending: a) overall force-compression rate characteristics; b) peak and ultimate forces; c) displacement of the peak forces; d) broken bonds of the skin in longitudinal direction; e) broken bonds of the skin in tangential direction; f) broken bonds between the skin and the core; g) broken bonds in the core.

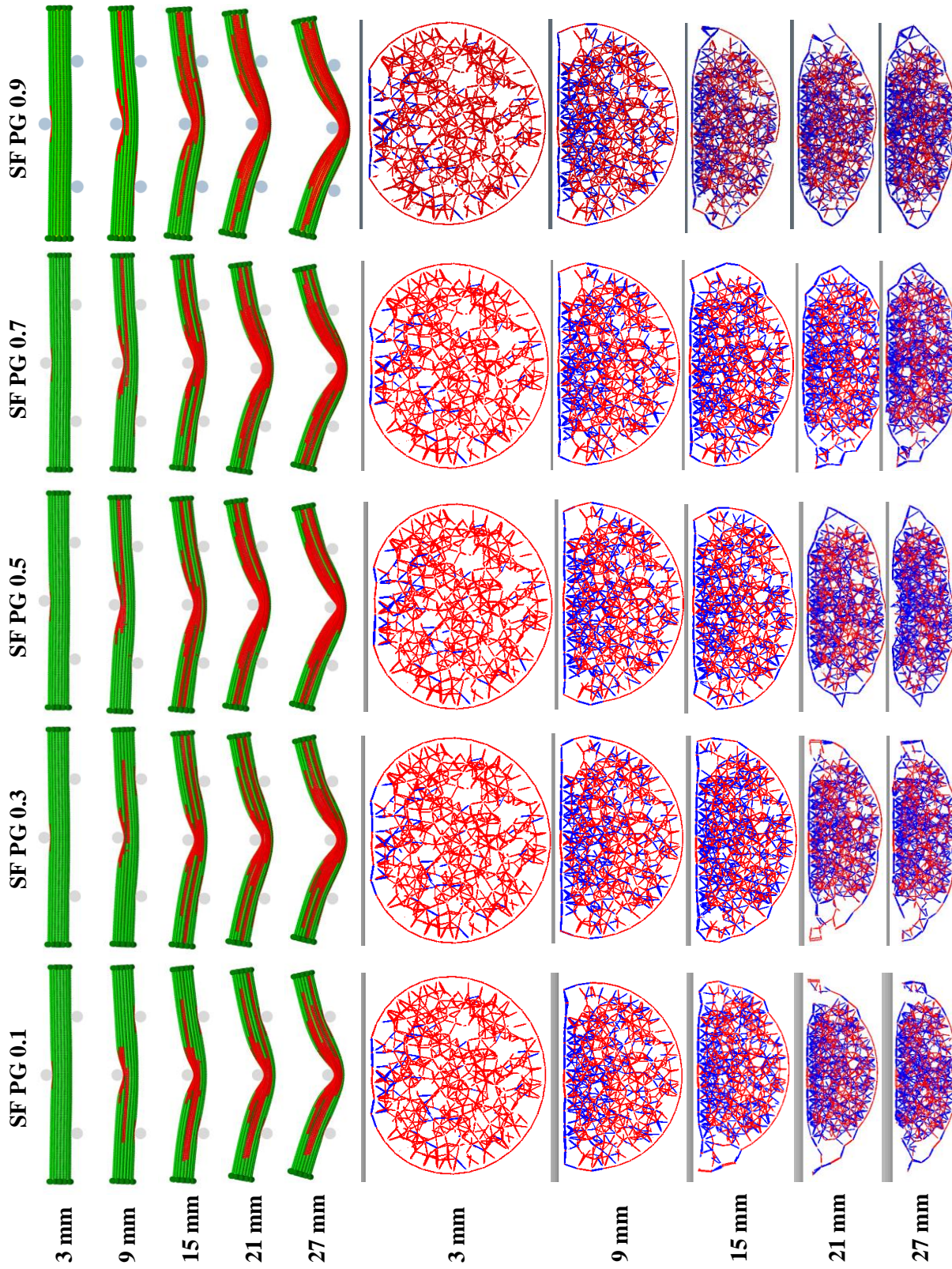


FIGURE D.6: Influence of the particle-geometry coefficient of static friction on the breakage over the bending process (the particles of the skin are visualised by the damage parameter of 0.1) and the breakage of the cross-section under the bending tool (the existing bonds among the particles are visualized by red lines between the centre of the bonded particles).

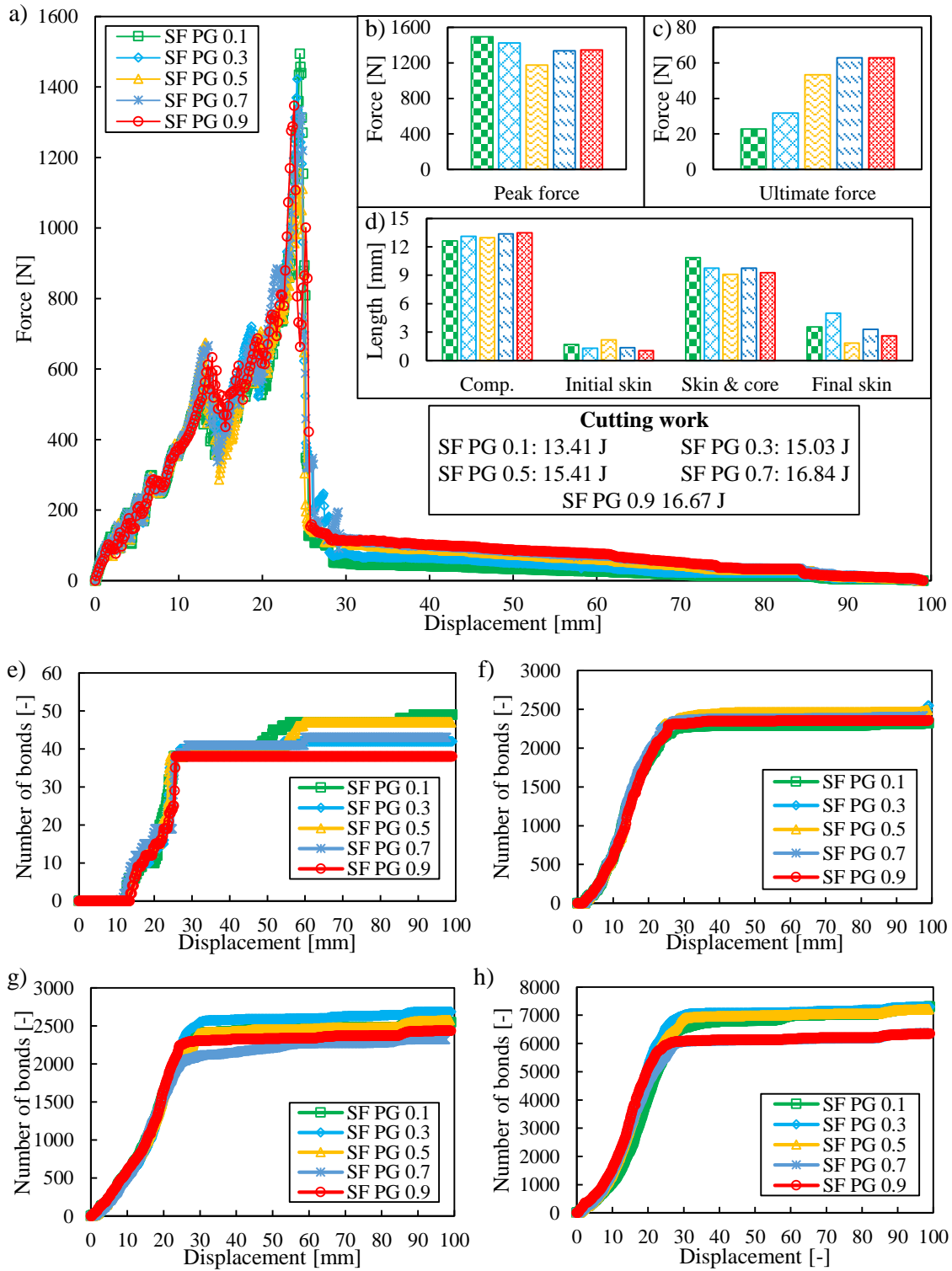


FIGURE D.7: Influence of the coefficient of variation of the particle-geometry coefficient of static friction by dynamic cutting: a) overall force-displacement characteristics; b) range of the peak forces; c) range of the ultimate forces; d) length of the stages of cut; e) broken bonds of the skin in longitudinal direction; f) broken bonds of the skin in tangential direction; g) broken bonds between the skin and the core; h) broken bonds in the core.

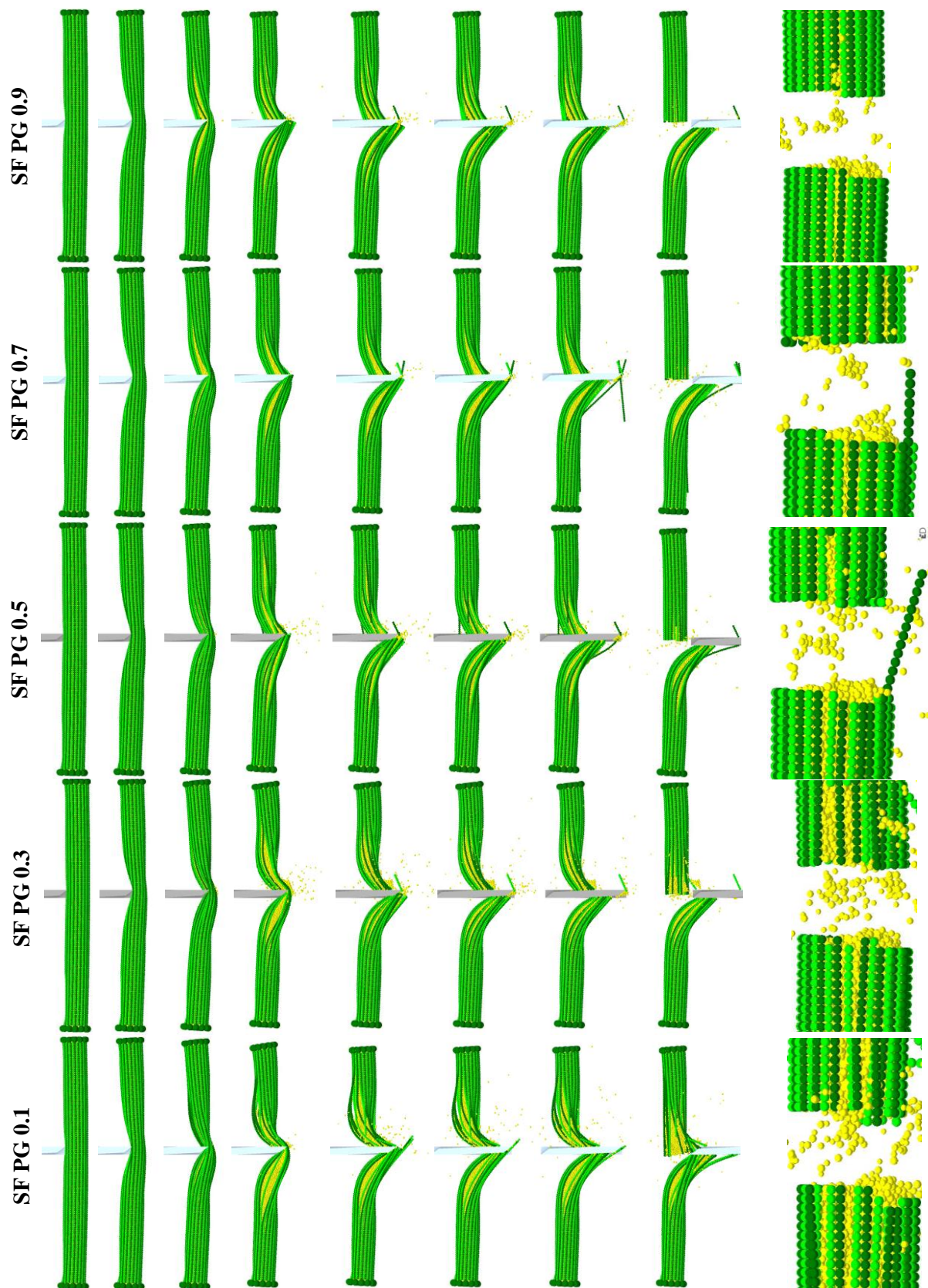


FIGURE D.8: Influence of the particle-geometry coefficient of static friction on the breakage by dynamic cutting dynamic cutting: comparison of the cutting processes and the resulted cutting surfaces.

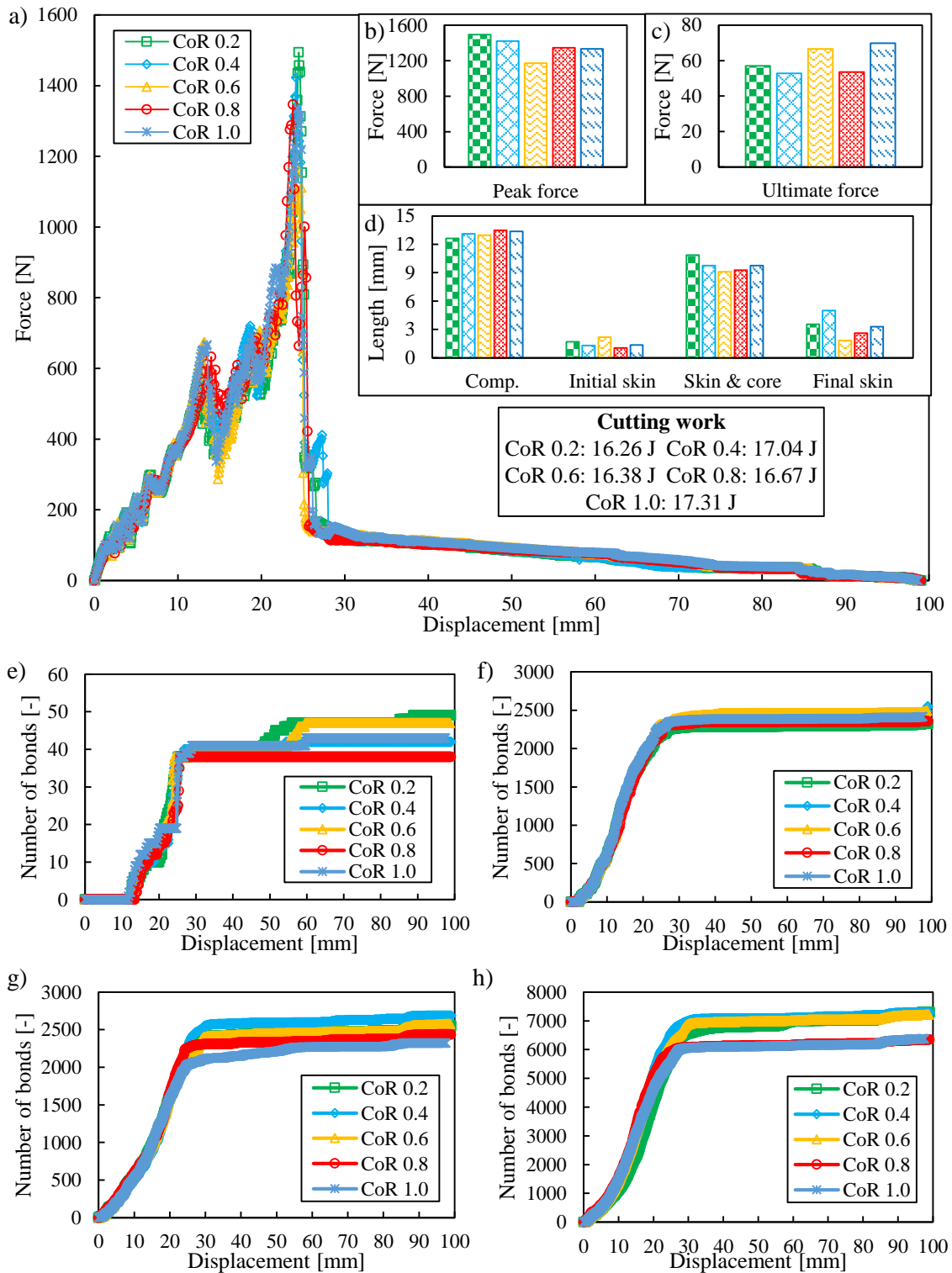


FIGURE D.9: Influence of the coefficient of restitution by dynamic cutting: a) overall force-displacement characteristics; b) range of the peak forces; c) range of the ultimate forces; d) length of the stages of cut; e) broken bonds of the skin in longitudinal direction; f) broken bonds of the skin in tangential direction; g) broken bonds between the skin and the core; h) broken bonds in the core.

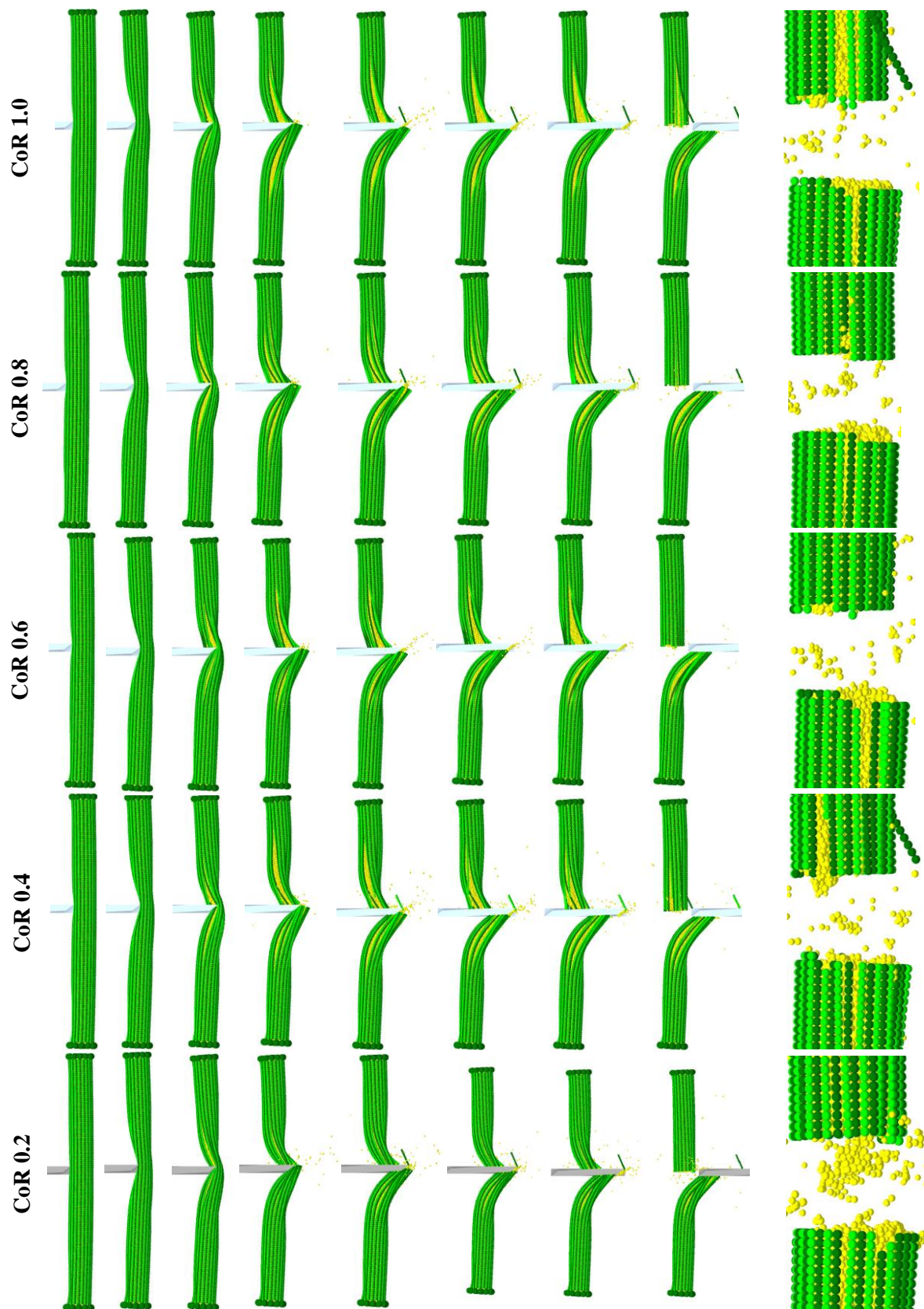


FIGURE D.10: Influence of the coefficient of restitution on the breakage by dynamic cutting dynamic cutting: comparison of the cutting processes and the resulted cutting surfaces.

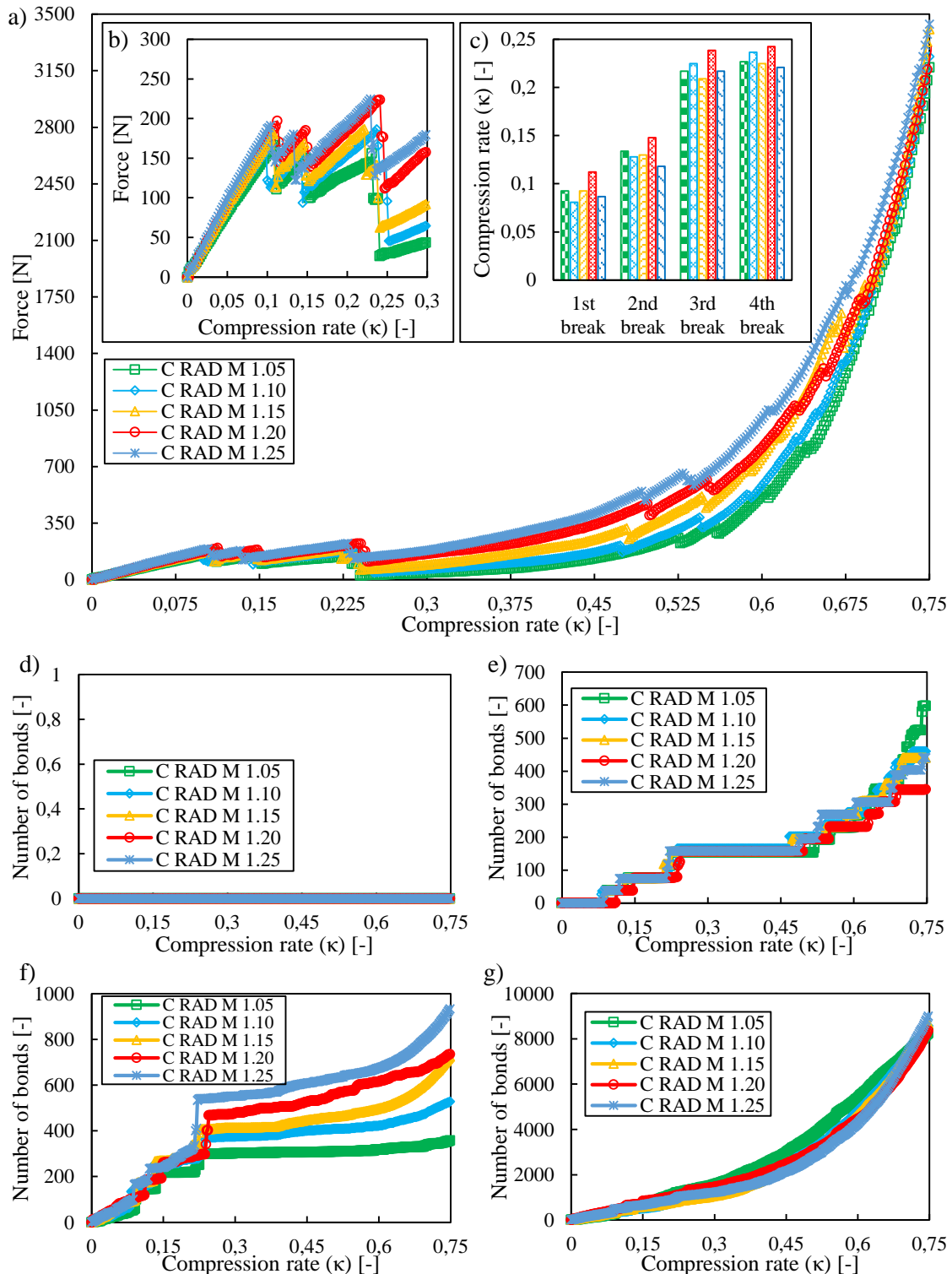


FIGURE D.11: Influence of the contact radius multiplier by sectional transversal compression: a) overall force-compression rate characteristics; b) force-compression rate characteristics in range of 0-0.3 compression rate; c) major break events in tangential direction of the skin; d) broken bonds of the skin in longitudinal direction; e) broken bonds of the skin in tangential direction; f) broken bonds between the skin and the core; g) broken bonds in the core.

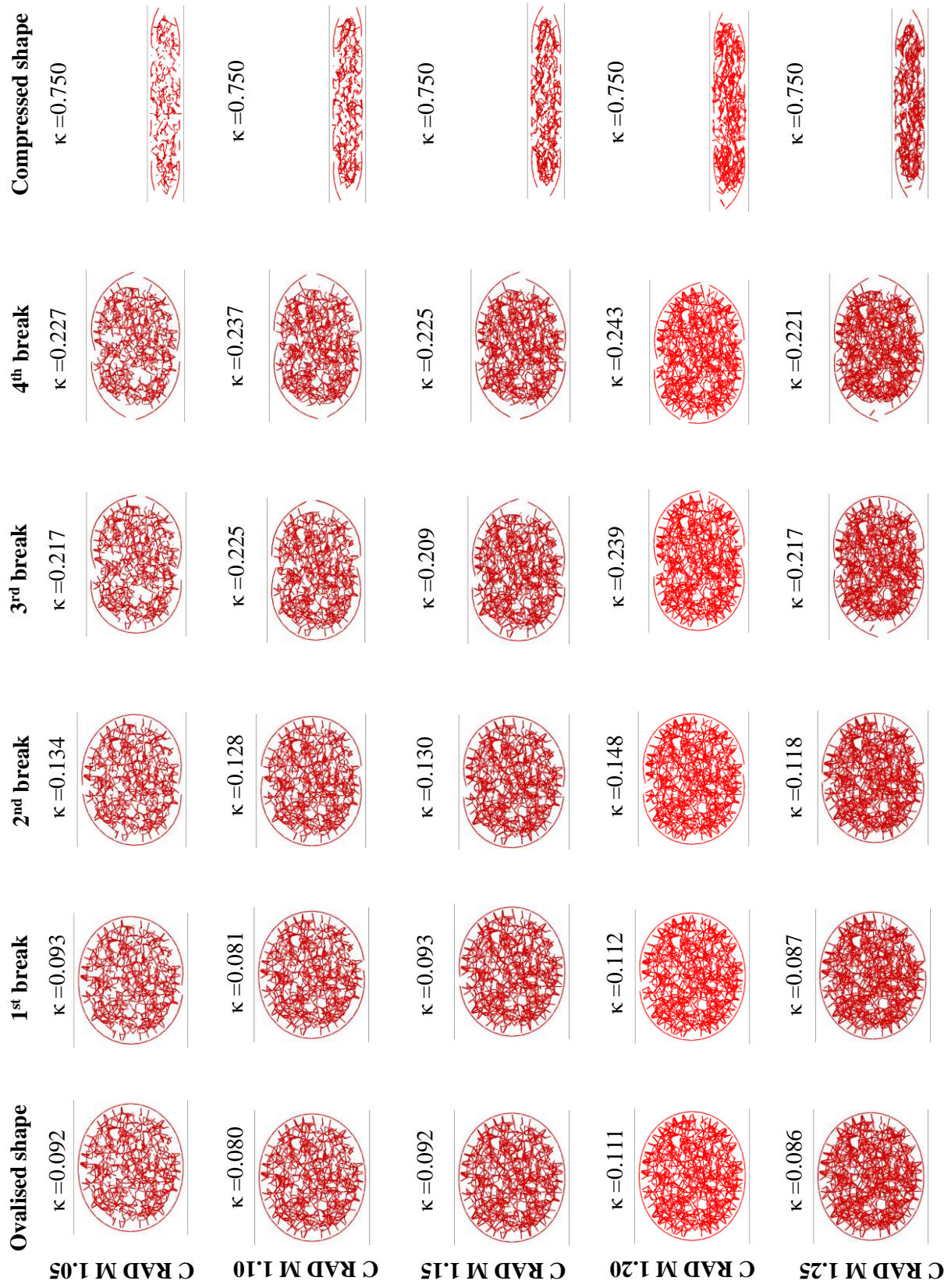


FIGURE D.12: Influence of the contact radius multiplier on the breakage by sectional transversal compression (the existing bonds among the particles are visualized by red lines between the centre of the bonded particles).

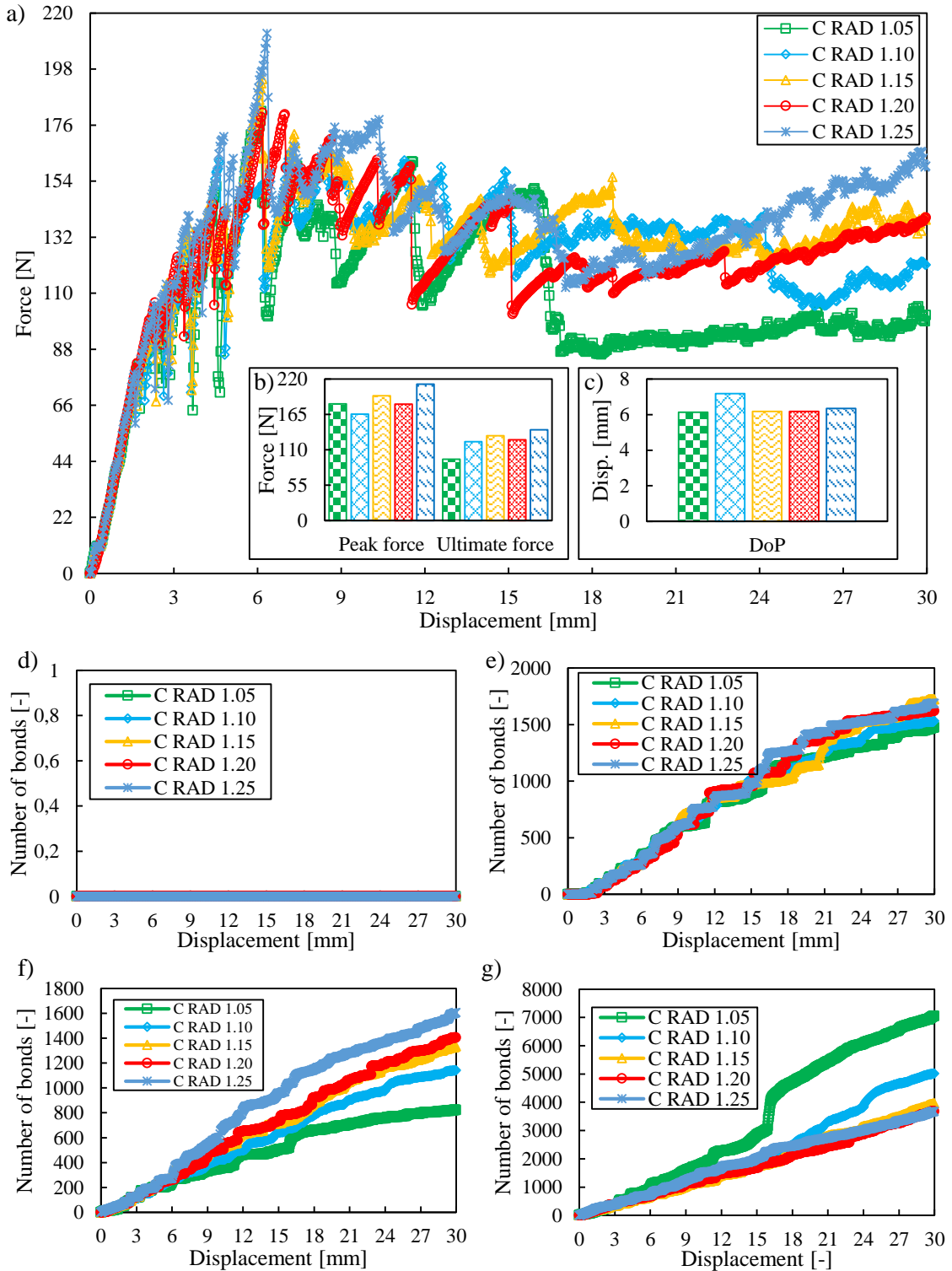


FIGURE D.13: Influence of the contact radius multiplier by three-point bending: a) overall force-compression rate characteristics; b) peak and ultimate forces; c) displacement of the peak forces; d) broken bonds of the skin in longitudinal direction; e) broken bonds of the skin in tangential direction; f) broken bonds between the skin and the core; g) broken bonds in the core.

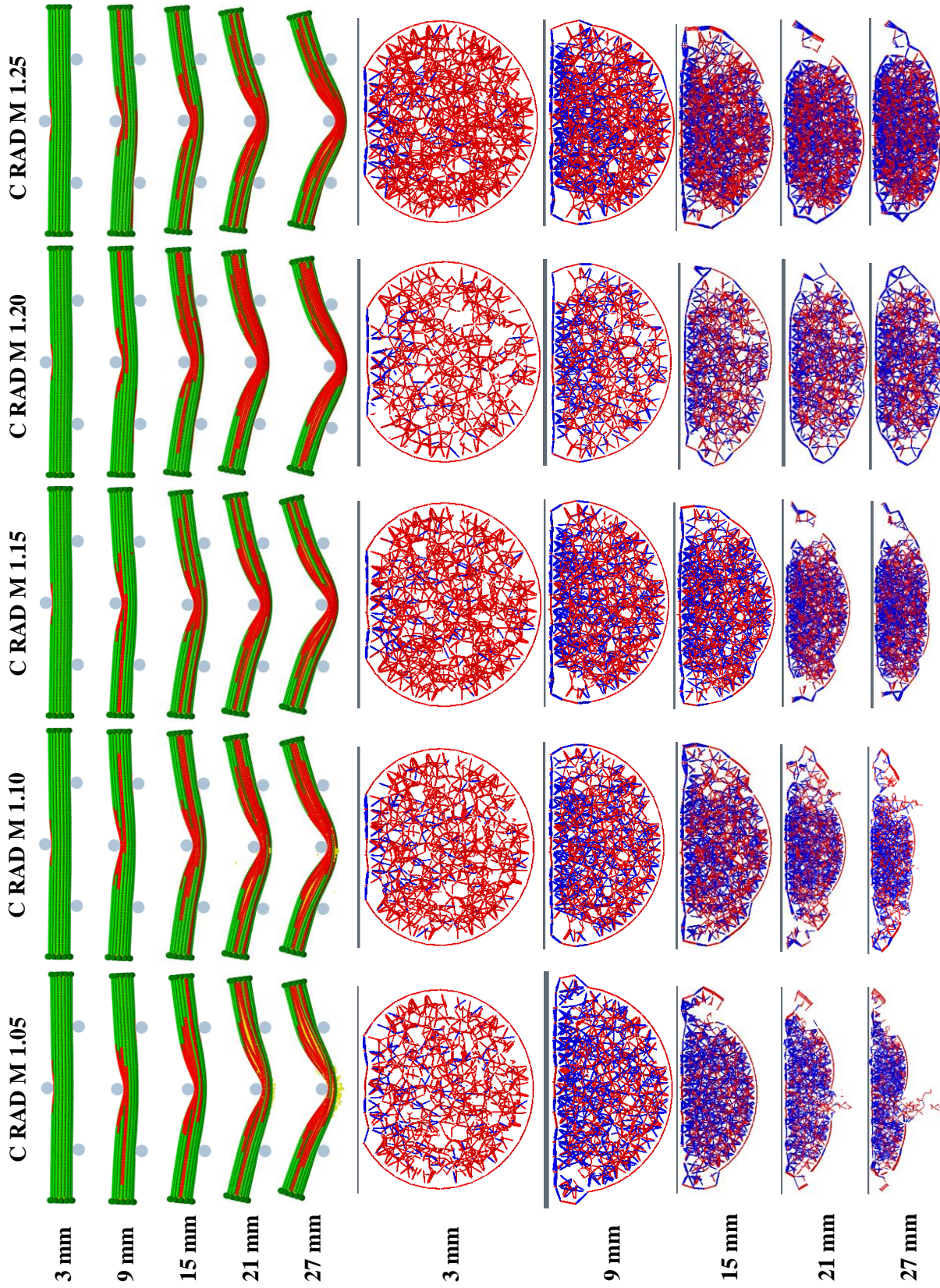


FIGURE D.14: Influence of the contact radius multiplier on the breakage by three-point bending: comparison of the longitudinal crack propagation over the bending process (the particles of the skin are visualised by the damage parameter of 0.1) and the breakage of the cross-section under the bending tool (the existing bonds among the particles are visualized by red lines between the centre of the bonded particles).

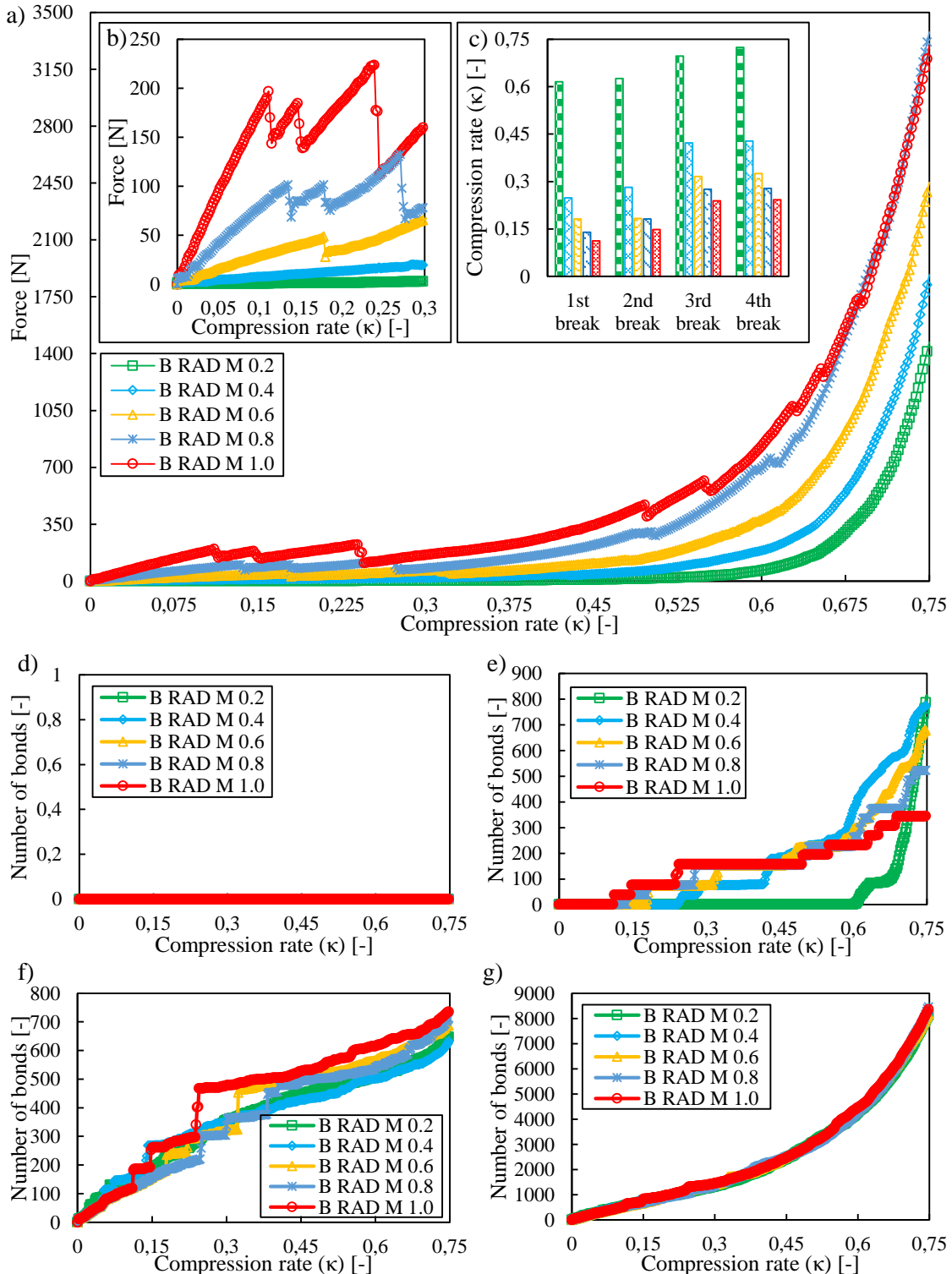


FIGURE D.15: Influence of the contact radius multiplier by sectional transversal compression: a) overall force-compression rate characteristics; b) force-compression rate characteristics in range of 0-0.3 compression rate; c) major break events in tangential direction of the skin; d) broken bonds of the skin in longitudinal direction; e) broken bonds of the skin in tangential direction; f) broken bonds between the skin and the core; g) broken bonds in the core.

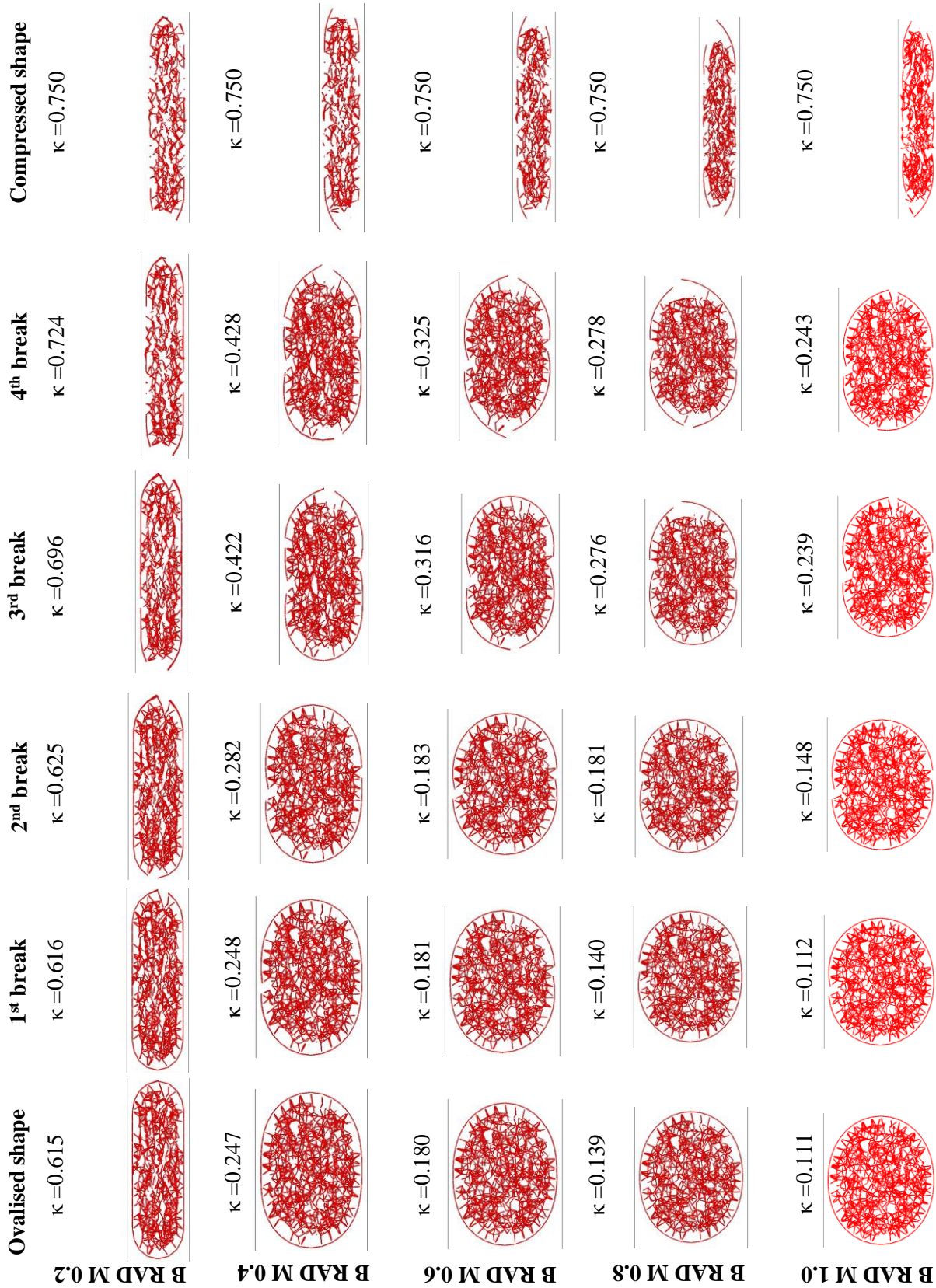


FIGURE D.16: Influence of the contact radius multiplier on the breakage by sectional transversal compression (the existing bonds among the particles are visualized by red lines between the centre of the bonded particles).

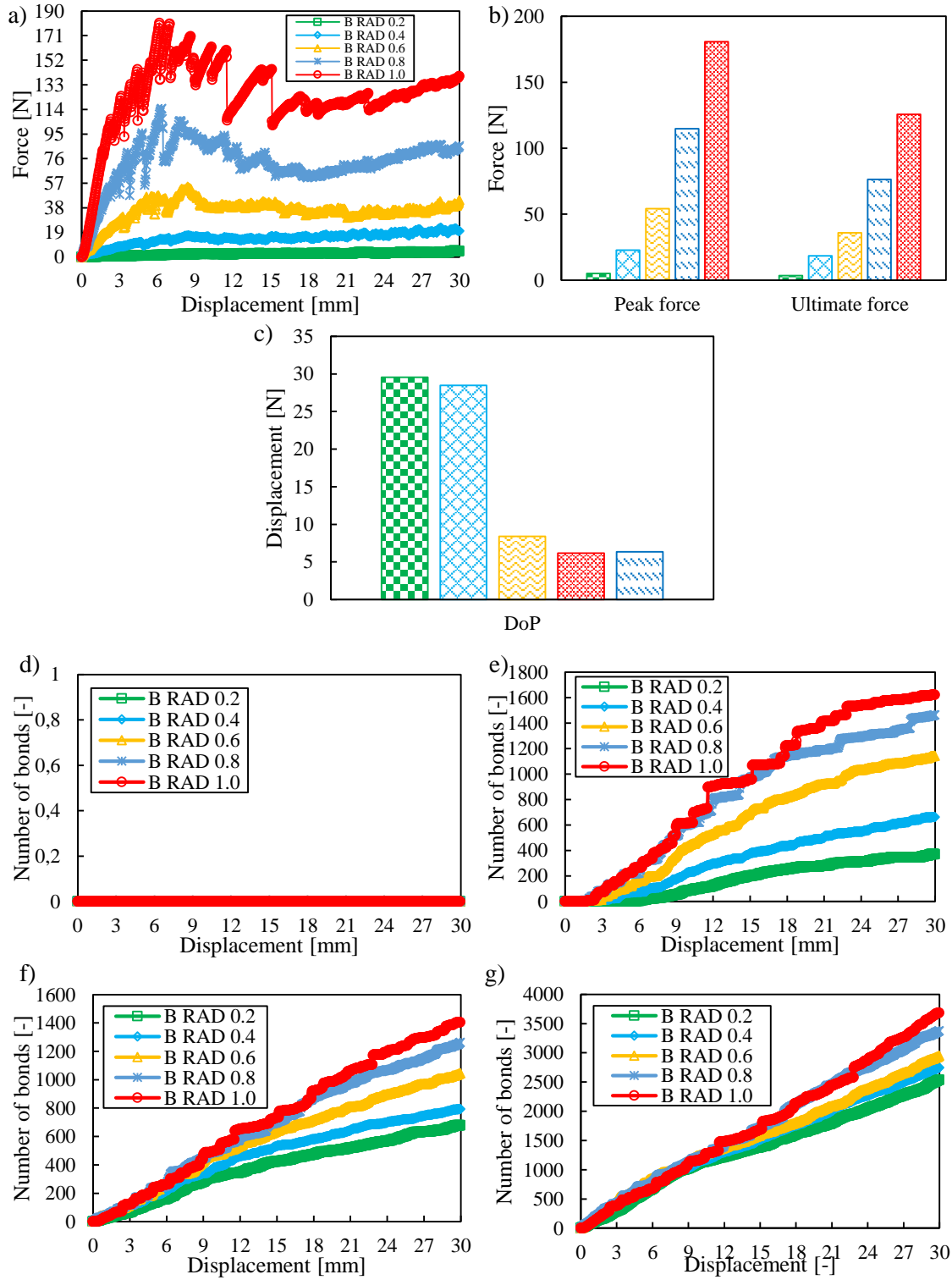


FIGURE D.17: Influence of the bond radius multiplier by three-point bending: a) overall force-compression rate characteristics; b) peak and ultimate forces; c) displacement of the peak forces; d) broken bonds of the skin in longitudinal direction; e) broken bonds of the skin in tangential direction; f) broken bonds between the skin and the core; g) broken bonds in the core.

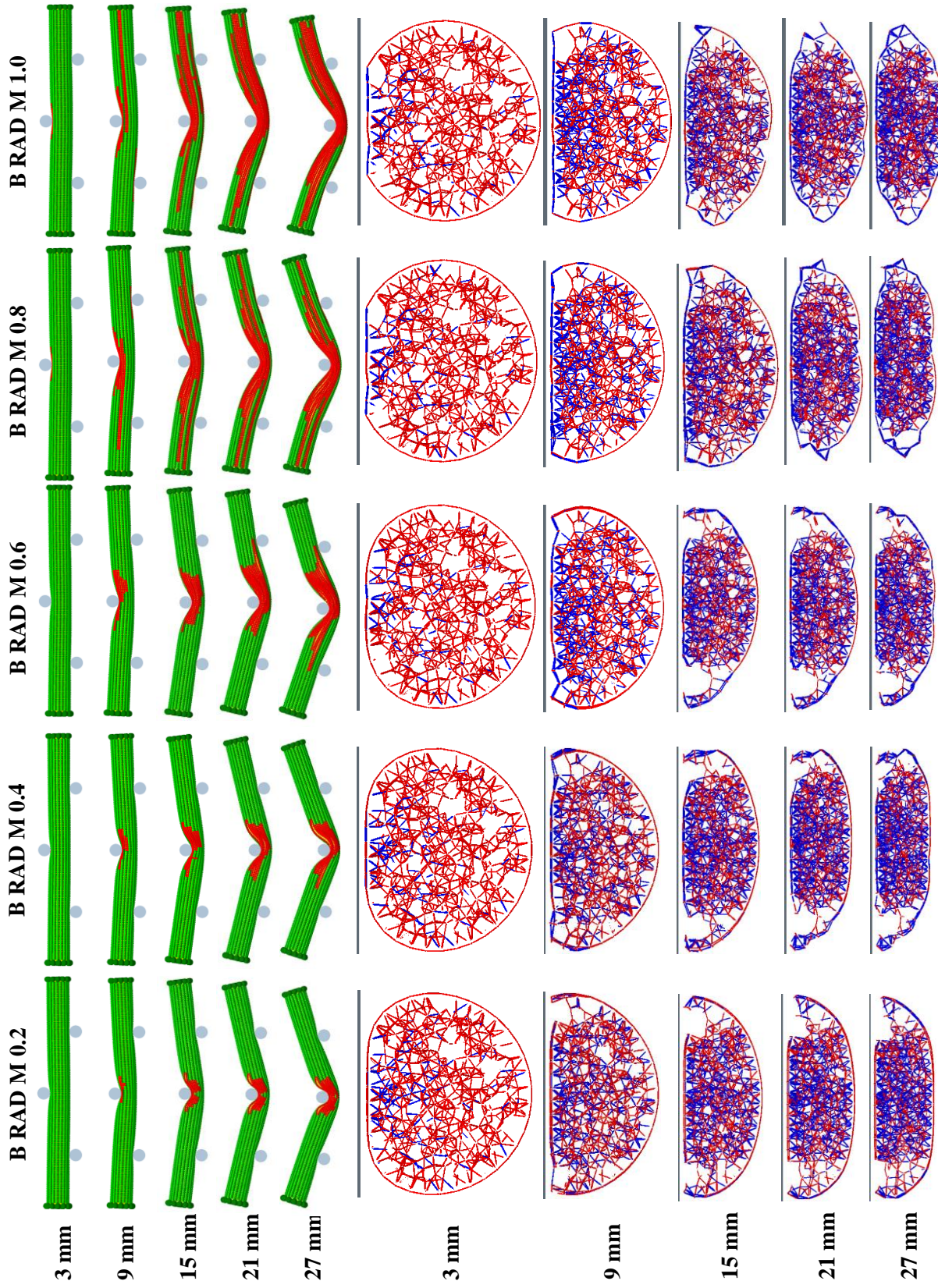


FIGURE D.18: Influence of the bond radius multiplier on the breakage by the bending process (the particles of the skin are visualised by the damage parameter of 0.1) and the breakage of the cross-section under the bending tool (the existing bonds among the particles are visualized by red lines between the centre of the bonded particles).

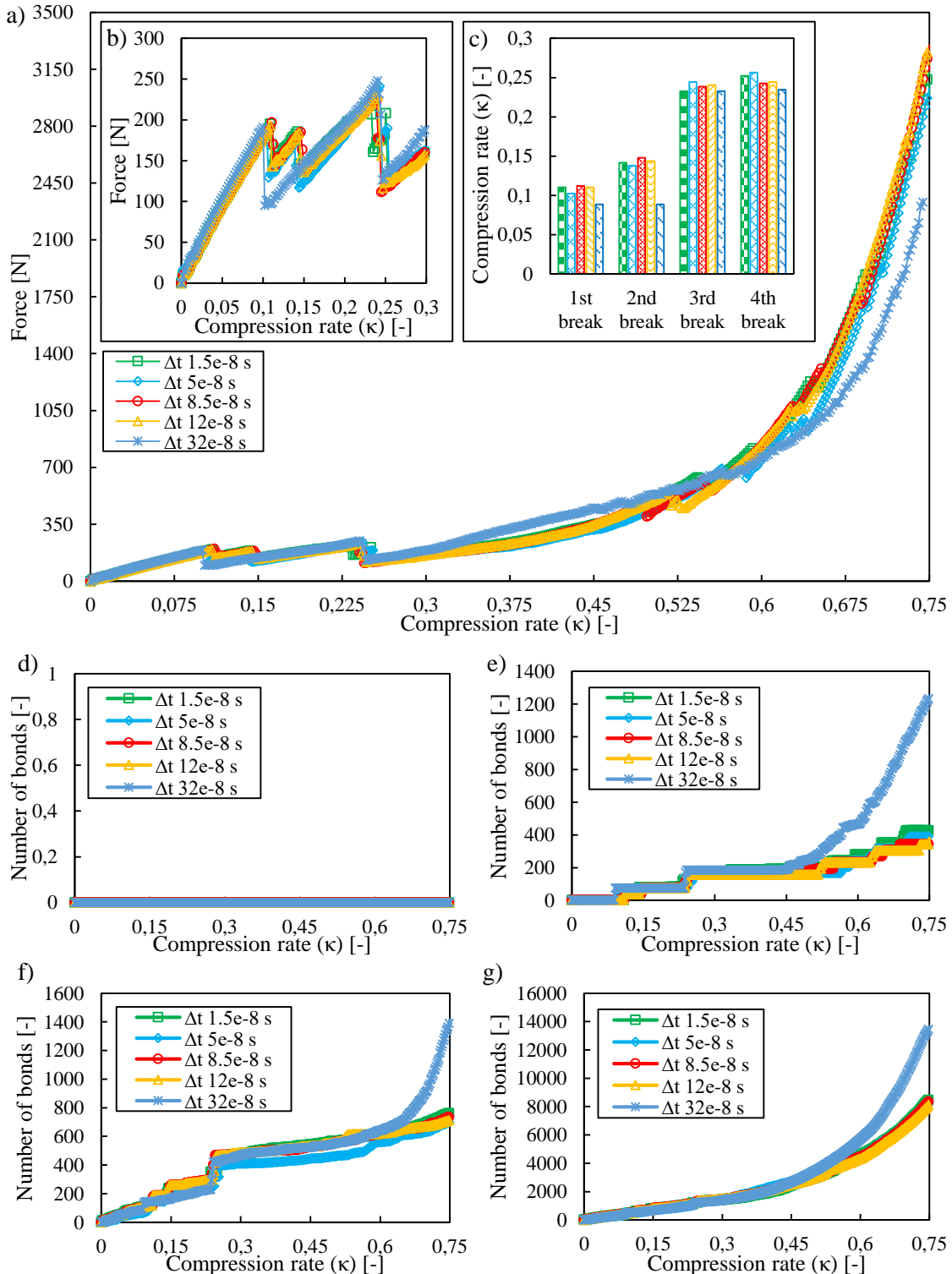


FIGURE D.19: Influence of the time step by sectional transversal compression: a) overall force-compression rate characteristics; b) force-compression rate characteristics in range of 0-0.3 compression rate; c) major break events in tangential direction of the skin; d) broken bonds of the skin in longitudinal direction; e) broken bonds of the skin in tangential direction; f) broken bonds between the skin and the core; g) broken bonds in the core.

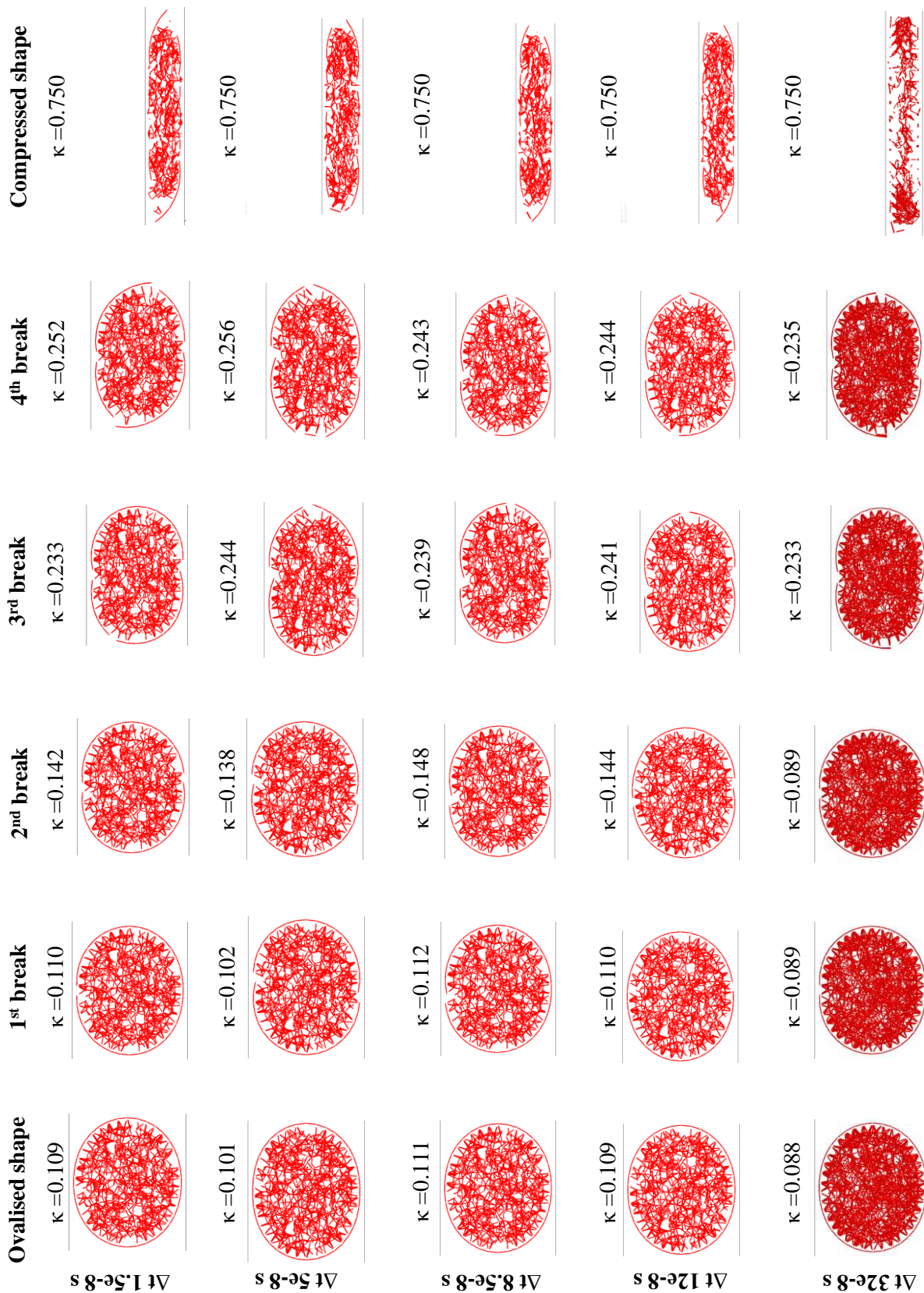


FIGURE D.20: Influence of the time step on the breakage by sectional transversal compression (the existing bonds among the particles are visualized by red lines between the centre of the bonded particles).

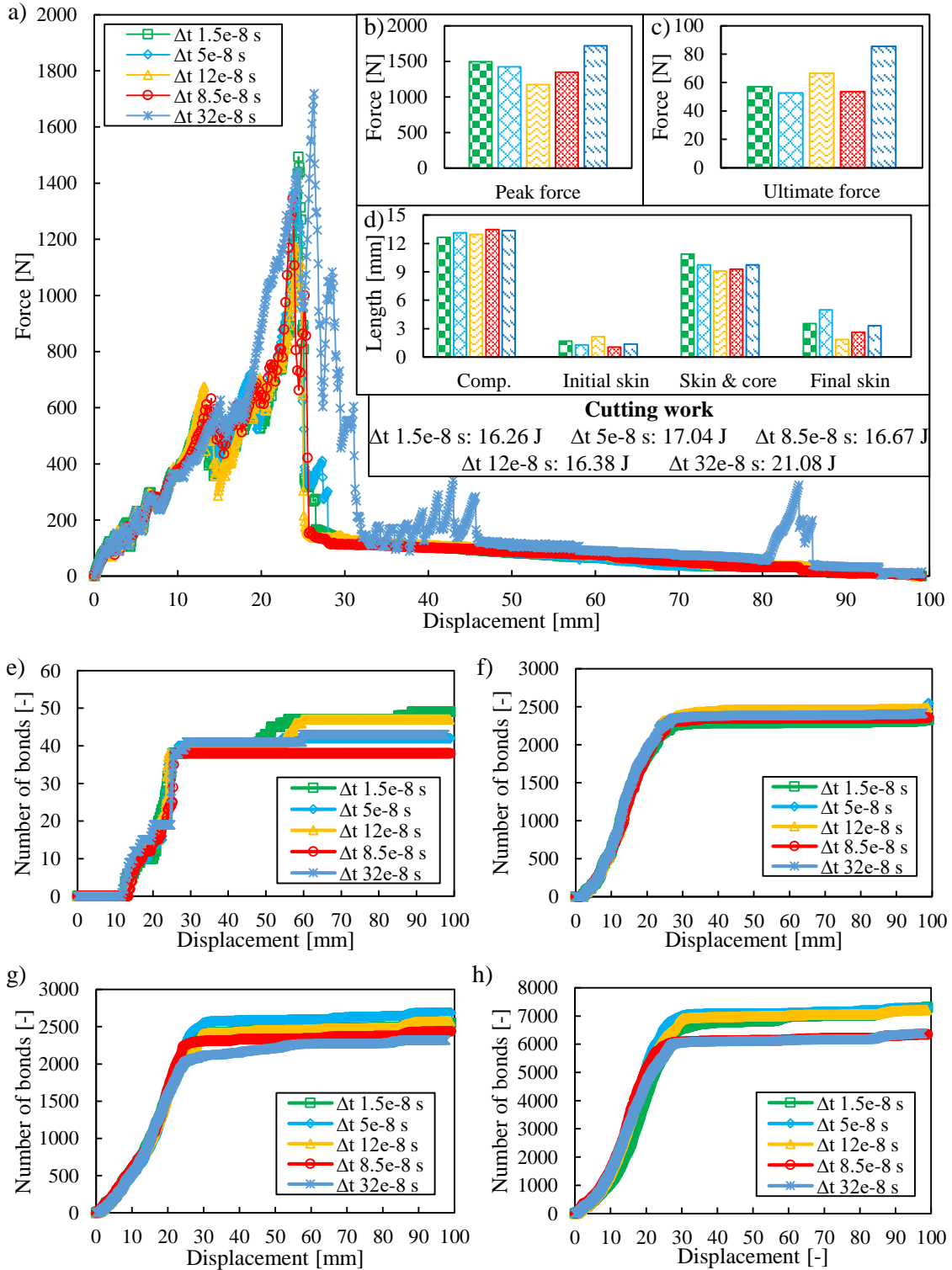


FIGURE D.21: Influence of the time step by dynamic cutting: a) overall force-displacement characteristics; b) range of the peak forces; c) range of the ultimate forces; d) length of the stages of cut; e) broken bonds of the skin in longitudinal direction; f) broken bonds of the skin in tangential direction; g) broken bonds between the skin and the core; h) broken bonds in the core.

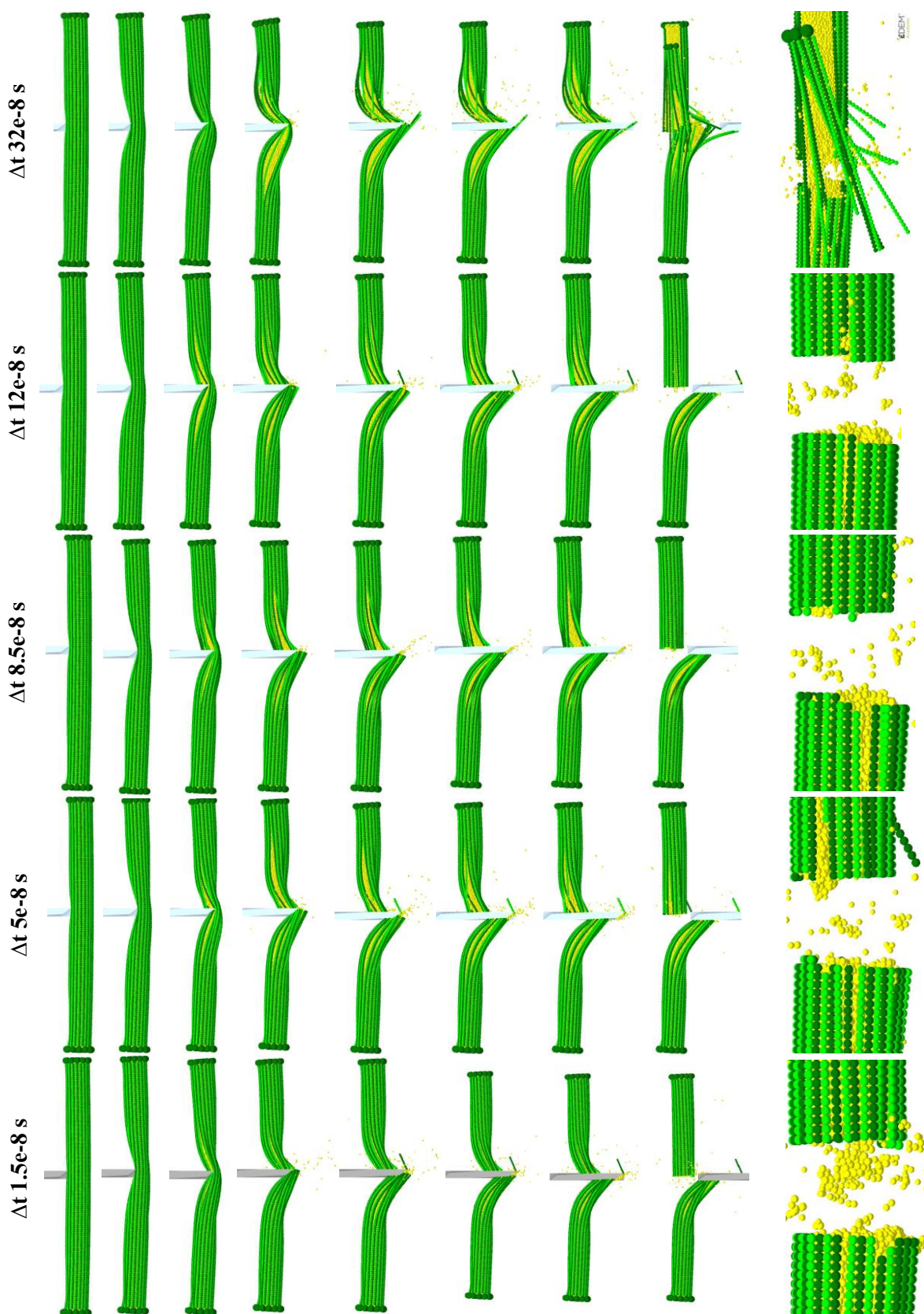


FIGURE D.22: Influence of the time step on the breakage by dynamic cutting: comparison of the cutting processes and the resulted cutting surfaces.

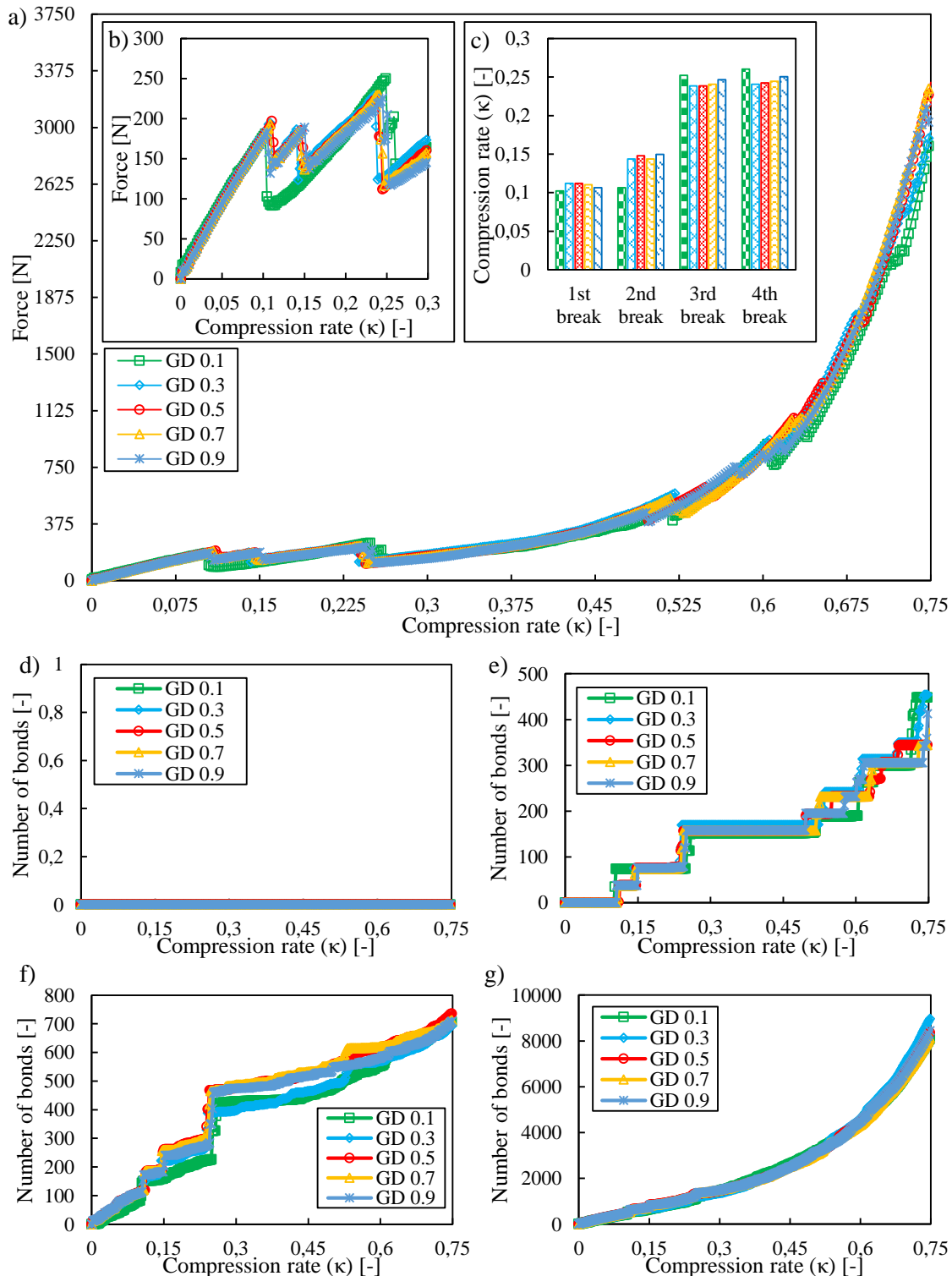


FIGURE D.23: Influence of the global damping by sectional transversal compression: a) overall force-compression rate characteristics; b) force-compression rate characteristics in range of 0-0.3 compression rate; c) major break events in tangential direction of the skin; d) broken bonds of the skin in longitudinal direction; e) broken bonds of the skin in tangential direction; f) broken bonds between the skin and the core; g) broken bonds in the core.

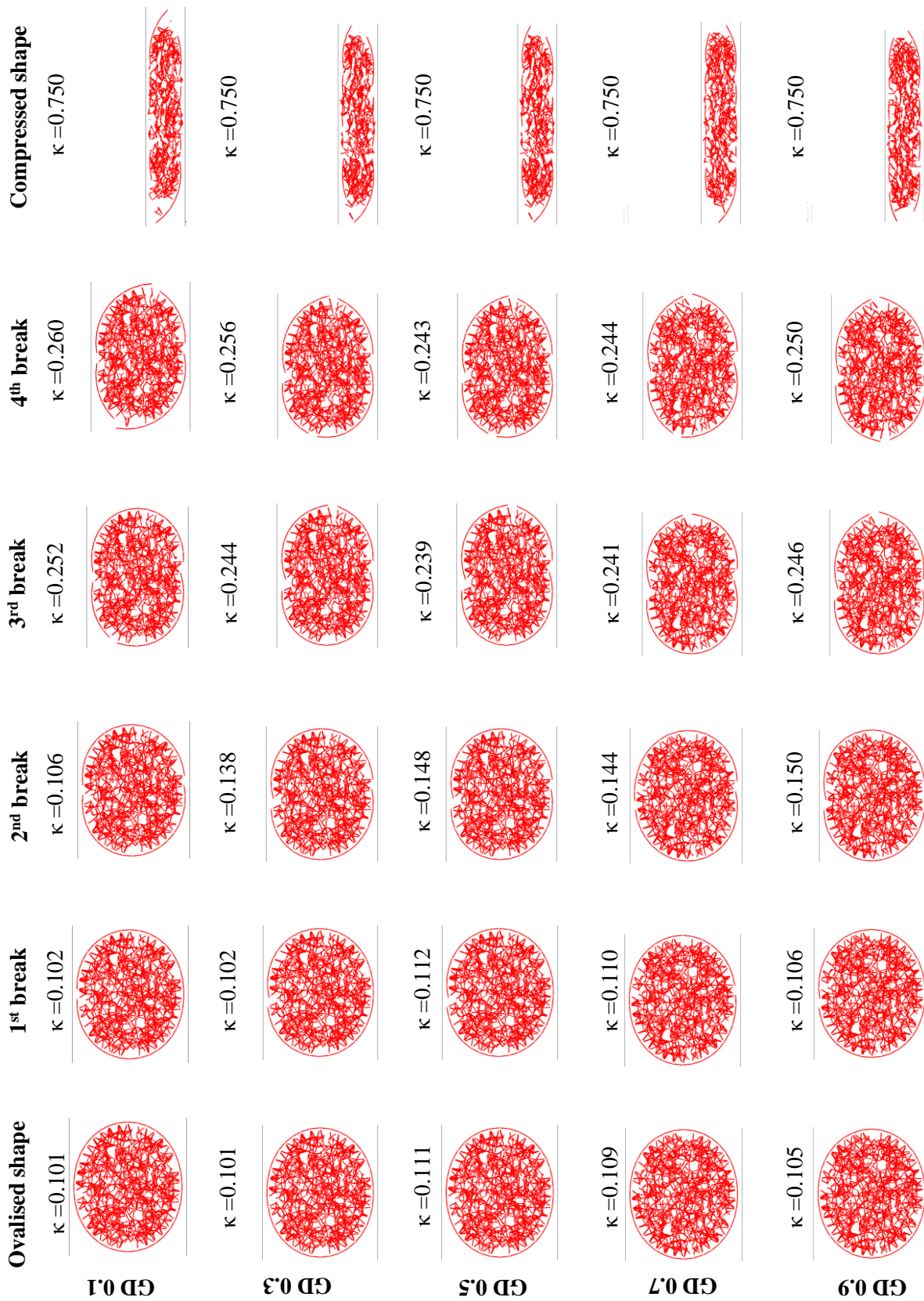


FIGURE D.24: Influence of the global damping on the breakage by sectional transversal compression (the existing bonds among the particles are visualized by red lines between the centre of the bonded particles).

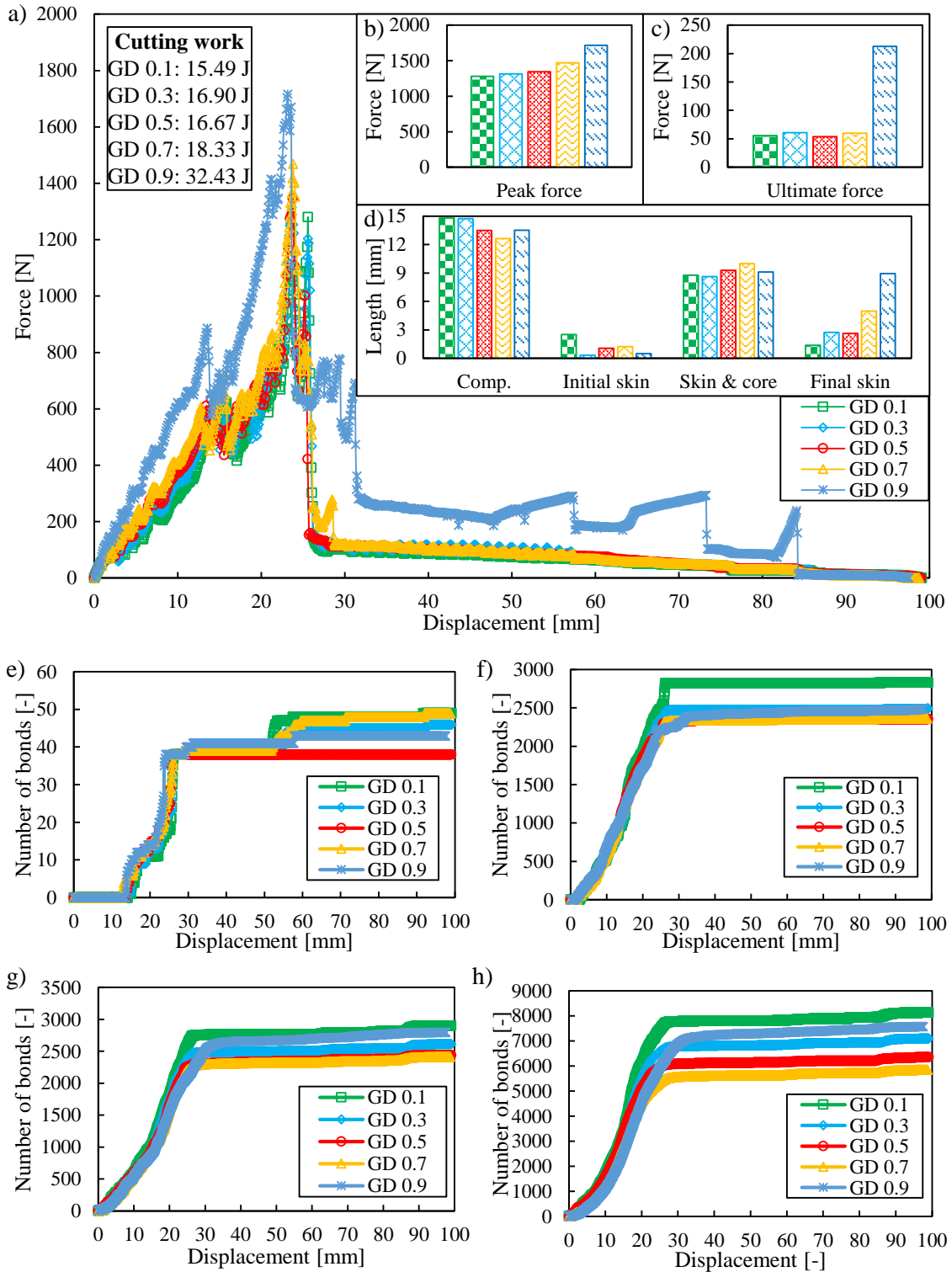


FIGURE D.25: Influence of the global damping by dynamic cutting: a) overall force-displacement characteristics; b) range of the peak forces; c) range of the ultimate forces; d) length of the stages of cut; e) broken bonds of the skin in longitudinal direction; f) broken bonds of the skin in tangential direction; g) broken bonds between the skin and the core; h) broken bonds in the core.

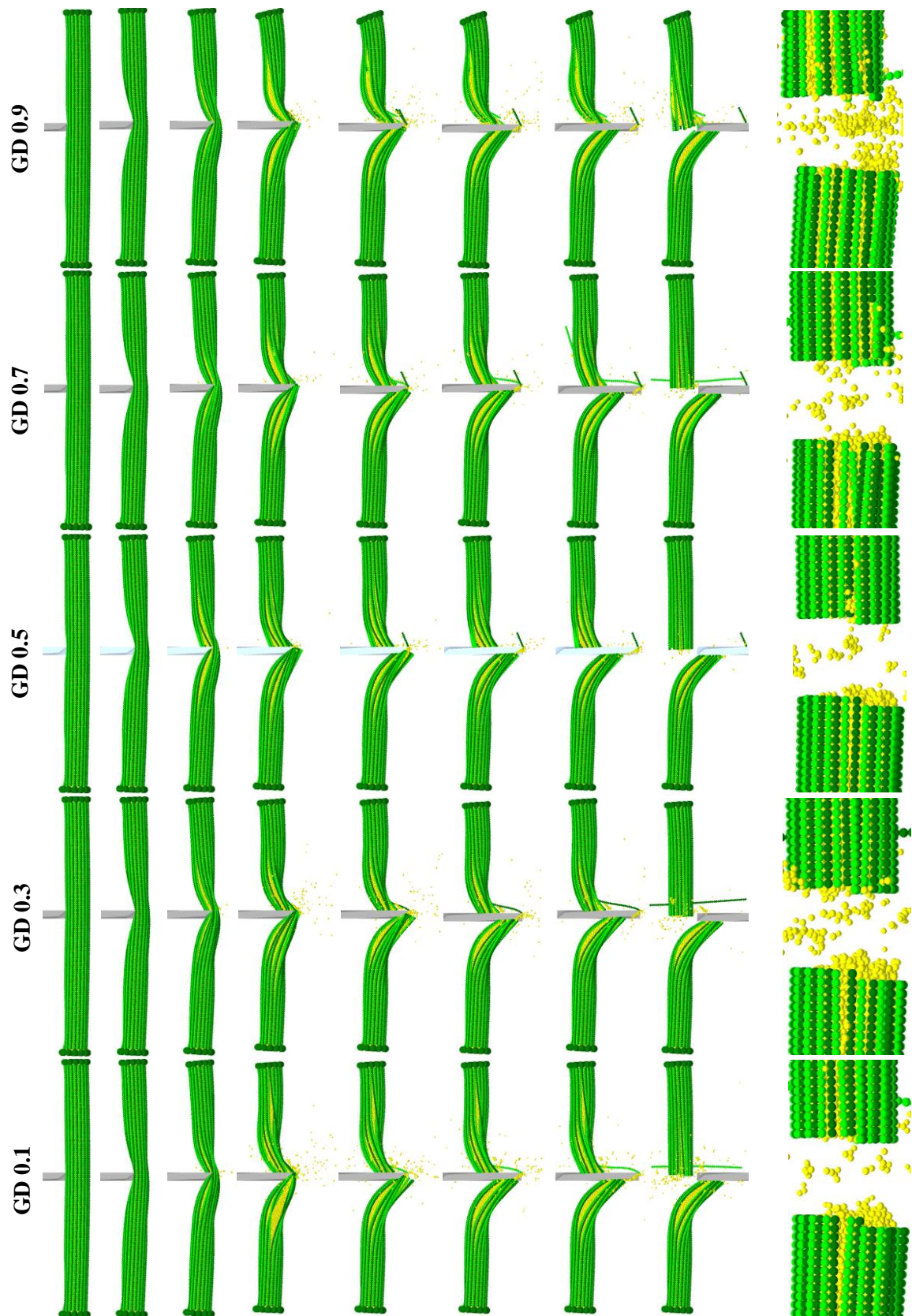


FIGURE D.26: Influence of the global damping on the breakage by dynamic cutting: comparison of the cutting processes and the resulted cutting surfaces.



# E Applied Contact Models

In this chapter, all the equations and figures come from the original publication regarding the applied contact model (Brown, Chen, and Ooi, 2014). The symbols differ from the symbols in the body text, thus, they will be introduced before each equation.

## E.1 Hertz-Mindlin Contact Model

In this case, there is no bonded (cemented or glued) contact between the particles, thus, they have free translational and rotational movements. The contact among the particles is described by the Hertz-Mindlin Contact Model (HMCM), as shown in Figure E.1.

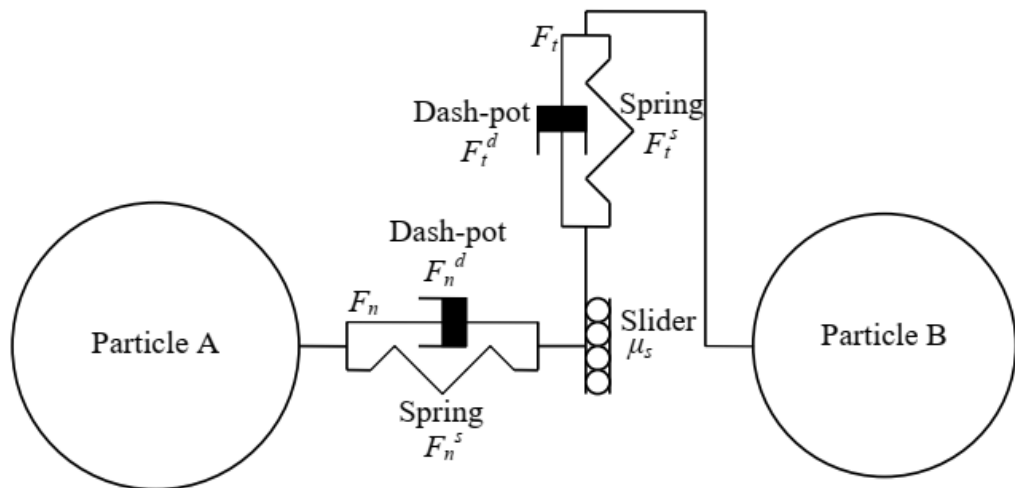


FIGURE E.1: A two particle spring dashpot configuration.

A contact of two particles, 'A' and 'B', consists of one spring and one dashpot in normal and tangential direction, and one slider in tangential direction. The contact parameters of the HMCM model are the followings:

- $E$ : particle Young's modulus;
- $\nu$ : particle Poisson's ratio;
- $\rho$ : particle density;
- $r$ : particle physical radius;
- $\mu$ : coefficient of static friction between the particles.

The normal contact force ( $F_n$ ) can be divided into spring ( $F_{ns}$ ) and damping forces ( $F_{nd}$ ), Equation E.1:

$$F_n = F_{ns} + F_{nd} \quad (\text{E.1})$$

The normal spring force ( $F_{ns}$ ) is calculated by using the equivalent Young's modulus ( $E^*$ ), the equivalent physical radius ( $r^*$ ) and the normal overlap between the particles ( $\delta_n$ ), Equation E.2:

$$F_{ns} = \frac{4}{3} \cdot E^* \cdot \sqrt{r^*} \cdot \delta_n^{1.5} \quad (\text{E.2})$$

The equivalent Young's modulus ( $E^*$ ) is calculated by using the Young's modulus ( $E_{A-B}$ ) and the Poisson's ratio ( $\nu_{A-B}$ ) of the particles, Equation E.3:

$$\frac{1}{E^*} = \frac{1 - \nu_A^2}{E_A} + \frac{1 - \nu_B^2}{E_B} \quad (\text{E.3})$$

The equivalent physical radius ( $r^*$ ) is calculated by using the physical radius of the particles ( $r_{A-B}$ ), Equation E.4:

$$r^* = \frac{r_A \cdot r_B}{r_A + r_B} \quad (\text{E.4})$$

The normal damping force ( $F_{nd}$ ) is calculated by using the damping coefficient ( $b_d$ ), the normal stiffness ( $S_n$ ), the equivalent mass ( $m^*$ ) and the relative normal velocity between the particles ( $V_{n,\text{relativ}}$ ), Equation E.5:

$$F_{nd} = -2 \cdot \sqrt{\frac{5}{6}} \cdot b_d \cdot \sqrt{S_n \cdot m^*} \cdot V_{n,\text{relativ}} \quad (\text{E.5})$$

The damping coefficient ( $b_d$ ) is calculated by using the viscous damping coefficient ( $e$ ), Equation E.6:

$$b_d = \frac{\ln e}{\sqrt{(\ln e)^2 + \pi^2}} \quad (\text{E.6})$$

The normal stiffness ( $S_n$ ) is calculated by using the equivalent Young's modulus ( $E^*$ ), the equivalent physical radius ( $r^*$ ) and the normal overlap between the particles ( $\delta_n$ ), Equation E.7:

$$S_n = 2 \cdot E^* \cdot \sqrt{r^* \cdot \delta_n} \quad (\text{E.7})$$

The equivalent mass ( $m^*$ ) is calculated by using the mass of the particles ( $m_{A-B}$ ), Equation E.8:

$$m^* = \frac{m_A \cdot m_B}{m_A + m_B} \quad (\text{E.8})$$

The tangential contact force ( $F_t$ ) can also be divided into spring ( $F_{ts}$ ) and damping forces ( $F_{td}$ ), Equation E.9:

$$F_t = F_{ts} + F_{td} \quad (\text{E.9})$$

The tangential spring force ( $F_{ts}$ ) is calculated by using the tangential stiffness ( $S_t$ ) and the tangential overlap ( $\delta_t$ ), Equation E.10:

$$F_{ts} = -S_t \cdot \delta_t \quad (\text{E.10})$$

The tangential stiffness ( $S_t$ ) is calculated by using the equivalent shear modulus ( $G^*$ ), the equivalent physical radius ( $r^*$ ) and the tangential overlap between the particles ( $\delta_t$ ), Equation E.11:

$$S_t = 8 \cdot G^* \cdot \sqrt{r^* \cdot \delta_t} \quad (\text{E.11})$$

The equivalent physical radius ( $r^*$ ) is calculated by the Equation E.4, while, the equivalent shear modulus ( $G^*$ ) is calculated by using the shear modulus ( $G_{A-B}$ ) and the Poisson's ratio

( $\nu_{A-B}$ ) of the particles, Equation E.12:

$$\frac{1}{G^*} = \frac{1 - \nu_A^2}{G_A} + \frac{1 - \nu_B^2}{G_B} \quad (\text{E.12})$$

The tangential damping force ( $F_{td}$ ) is calculated in similar way to the normal damping force, Equation E.13:

$$F_{td} = -2 \cdot \sqrt{\frac{5}{6}} \cdot b_d \cdot \sqrt{S_t \cdot m^*} \cdot V_{t,\text{relativ}} \quad (\text{E.13})$$

It is important to note the tangential force is limited by the Coulomb coefficient of static friction ( $\mu$ ), based on Equation E.14:

$$F_t \leq \mu \cdot F_n \quad (\text{E.14})$$

## E.2 Timoshenko Beam Bonded Model

In this case, there is a geometrically and mechanically well-defined bonded (glued or cemented) contact between the two particles that is described by the Timoshenko Beam Bonded Model (TBBM). The bond formation is controlled by two parameters, namely:

- bond formation time ( $t$ );
- contact radii ( $R_c$ ) of the particles.

The bond formation time ( $t$ ) is defined by the user, however, the bond formation usually takes place right at the beginning of the simulation. During the bond formation, the software creates bonded contacts among the particles where the contact radii ( $R_c$ ) have an overlap. It is important to note the contact ( $R_c$ ) and physical ( $R_p$ ) radii are not the same, as shown in Figure E.2. It is recommended by the developers to choose a ratio between 1.1 … 1.2 for the contact ( $R_c$ ) and physical ( $R_p$ ) radii, see Equation E.15:

$$\eta = \frac{R_c}{R_p} = 1.1 \dots 1.2 \quad (\text{E.15})$$

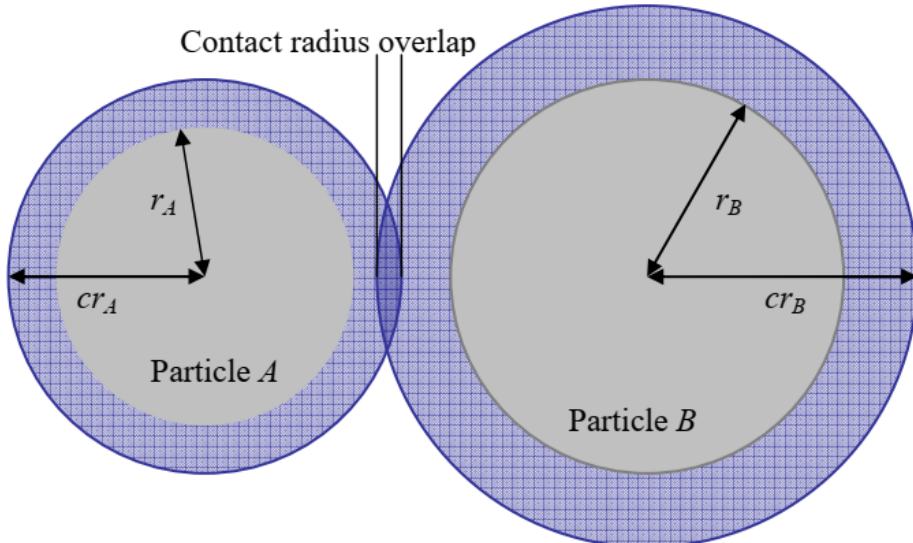


FIGURE E.2: Explanation for the contact and physical radii of the particles.

During the bond formation time, the bond between the right particles is formed, as shown in Figure E.3. A bond is a cylindrical beam element between the centre of the particles ( $\alpha, \beta$ ) that is assigned with the following properties:

- the bond has no real volume, thus, real mass neither;
- both end of the bond has the same degree of freedom as the connected particles.

The geometrical properties of the bond, as its length ( $L_b$ ) and radius ( $r_b$ ), are calculated by using the physical radii of the connected particles ( $r_{A-B}$ ), the position of their centre of mass ( $P_{A-B}$ ) and the radius multiplier ( $\lambda$ ), Equation E.16 and E.17

$$L_b = P_A - P_B \quad (\text{E.16})$$

$$r_b = \lambda \cdot \min(r_A, r_B) \quad (\text{E.17})$$

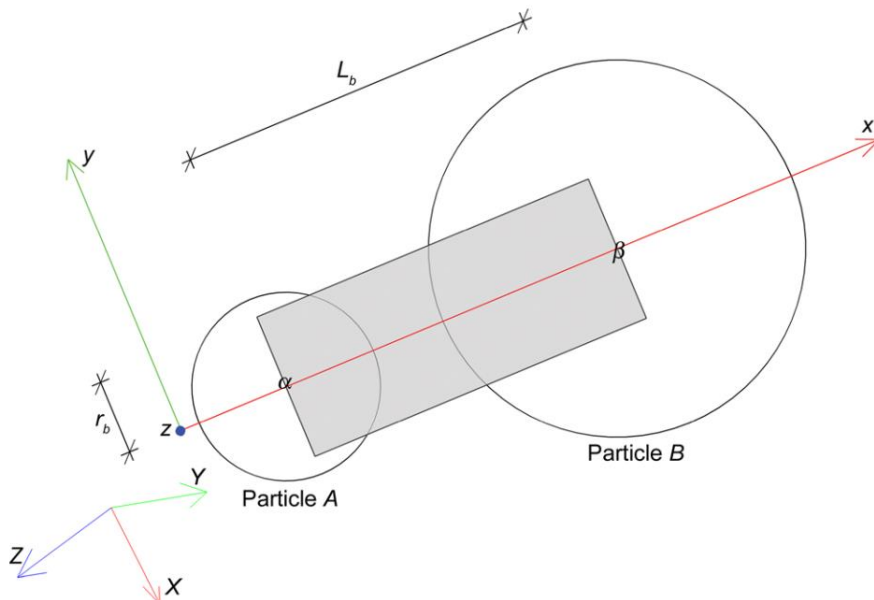


FIGURE E.3: Projected view through the central axis of a bond connecting particles A and B.

The mechanical behaviour of the bond is governed by the following parameters:

- $E_b$ : bond Young's modulus;
- $\nu_b$ : bond Poisson's ratio;
- $S_c$ : mean compressive strength;
- $\zeta_c$ : coefficient of variation for the compressive strength;
- $S_t$ : mean tensile strength;
- $\zeta_t$ : coefficient of variation for the tensile strength;
- $S_s$ : mean shear strength;
- $\zeta_s$ : coefficient of variation for the shear strength;
- $\iota_d$ : global damping.

During the bond formation, all the forces and moments of the bond are set to zero and stored in a vector, Equation E.18, where:

- $F_{\alpha x}, F_{\alpha y}, F_{\alpha z}$  are the force components at point  $\alpha$ ;

- $M_{\alpha x}, M_{\alpha y}, M_{\alpha z}$  are the moment components at point  $\alpha$ ;
- $F_{\beta x}, F_{\beta y}, F_{\beta z}$  are the force components at point  $\beta$ ;
- $M_{\beta x}, M_{\beta y}, M_{\beta z}$  are the moment components at point  $\beta$ .

$$\{F\} = \begin{Bmatrix} F_{\alpha x} \\ F_{\alpha y} \\ F_{\alpha z} \\ M_{\alpha x} \\ M_{\alpha y} \\ M_{\alpha z} \\ F_{\beta x} \\ F_{\beta y} \\ F_{\beta z} \\ M_{\beta x} \\ M_{\beta y} \\ M_{\beta z} \end{Bmatrix} = \begin{Bmatrix} 0 \\ 0 \\ 0 \\ 0 \\ 0 \\ 0 \\ 0 \\ 0 \\ 0 \\ 0 \\ 0 \\ 0 \end{Bmatrix} \quad (\text{E.18})$$

During the simulation, the force and moment components are incrementally summarized in each time step, Equation E.19:

$$\{F\} = \sum \Delta F \quad (\text{E.19})$$

The force and moment components are calculated by using the stiffness matrix ( $K$ ) and the increment of the deformation ( $\Delta\mu$ ) calculated in the local coordinate system of the bond, Equation E.20:

$$\Delta F = K \cdot \Delta\mu \quad (\text{E.20})$$

The stiffness matrix is composed in the following structure, Equation E.21:

$$[K] = \begin{bmatrix} k_1 & \cdot & \cdot & \cdot & \cdot & \cdot & -k_1 & \cdot & \cdot & \cdot & \cdot & \cdot \\ \cdot & k_2 & \cdot & \cdot & \cdot & k_3 & \cdot & -k_2 & \cdot & \cdot & \cdot & k_3 \\ \cdot & \cdot & k_2 & \cdot & -k_3 & \cdot & \cdot & \cdot & -k_2 & \cdot & -k_3 & \cdot \\ \cdot & \cdot & \cdot & k_4 & \cdot & \cdot & \cdot & \cdot & \cdot & -k_4 & \cdot & \cdot \\ \cdot & \cdot & -k_3 & \cdot & k_5 & \cdot & \cdot & \cdot & k_3 & \cdot & k_6 & \cdot \\ \cdot & k_3 & \cdot & \cdot & \cdot & k_5 & \cdot & -k_3 & \cdot & \cdot & \cdot & k_6 \\ -k_1 & \cdot & \cdot & \cdot & \cdot & \cdot & k_1 & \cdot & \cdot & \cdot & \cdot & \cdot \\ \cdot & -k_2 & \cdot & \cdot & \cdot & k_3 & \cdot & k_2 & \cdot & \cdot & \cdot & -k_3 \\ \cdot & \cdot & -k_2 & \cdot & k_3 & \cdot & \cdot & \cdot & k_2 & \cdot & k_3 & \cdot \\ \cdot & \cdot & \cdot & -k_4 & \cdot & \cdot & \cdot & \cdot & \cdot & k_4 & \cdot & \cdot \\ \cdot & \cdot & -k_3 & \cdot & k_6 & \cdot & \cdot & \cdot & k_3 & \cdot & k_5 & \cdot \\ \cdot & k_3 & \cdot & \cdot & \cdot & k_6 & \cdot & -k_3 & \cdot & \cdot & \cdot & k_5 \end{bmatrix} \quad (\text{E.21})$$

The stiffness components are calculated by using the bonded Young's modulus ( $E_b$ ), the cross sectional area of the bond ( $A_b$ ), the length of the bond ( $L_b$ ), the second moment of area of the bond ( $I_b$ ) and the Timoshenko shear coefficient ( $\Phi$ ), Equation E.22 - E.27:

$$k_1 = \frac{E_b \cdot A_b}{L_b} \quad (\text{E.22})$$

$$k_2 = \frac{12 \cdot E_b \cdot I_b}{L_b^3 \cdot (1 + \Phi)} \quad (\text{E.23})$$

$$k_3 = \frac{6 \cdot E_b \cdot I_b}{L_b^2 \cdot (1 + \Phi)} \quad (\text{E.24})$$

$$k_4 = \frac{E_b \cdot I_b}{L_b \cdot (1 + v_b)} \quad (\text{E.25})$$

$$k_5 = \frac{E_b \cdot I_b \cdot (4 + \Phi)}{L_b \cdot (1 + \Phi)} \quad (\text{E.26})$$

$$k_6 = \frac{E_b \cdot I_b \cdot (2 - \Phi)}{L_b \cdot (1 + \Phi)} \quad (\text{E.27})$$

The cross sectional area ( $A_b$ ) and the second moment of the area ( $I_b$ ) of the bond are calculated by using the radius of the bond ( $r_b$ ), Equation E.28 and E.29:

$$A_b = r_b^2 \cdot \pi \quad (\text{E.28})$$

$$I_b = \frac{r_b^4 \cdot \pi}{4} \quad (\text{E.29})$$

The Timoshenko shear coefficient is calculated by using the bond radius ( $r_b$ ), the bond Poisson's ratio ( $v_b$ ) and the bond length ( $L_b$ ), Equation E.30:

$$\Phi = \frac{20 \cdot r_b^2 \cdot (1 + v_b)}{3 \cdot L_b^2} \quad (\text{E.30})$$

The local deformation of the bond ( $\mu$ ) is stored in a vector, Equation E.31, where:

- $d_{\alpha x}, d_{\alpha y}, d_{\alpha z}$  are the local translational deformations at point  $\alpha$ ;
- $\Theta_{\alpha x}, \Theta_{\alpha y}, \Theta_{\alpha z}$  are the local rotational deformations at point  $\alpha$ ;
- $d_{\beta x}, d_{\beta y}, d_{\beta z}$  are the local translational deformations at point  $\beta$ ;
- $\Theta_{\beta x}, \Theta_{\beta y}, \Theta_{\beta z}$  are the local rotational deformations at point  $\beta$ .

$$\{\mu\} = \begin{Bmatrix} d_{\alpha x} \\ d_{\alpha y} \\ d_{\alpha z} \\ \Theta_{\alpha x} \\ \Theta_{\alpha y} \\ \Theta_{\alpha z} \\ d_{\beta x} \\ d_{\beta y} \\ d_{\beta z} \\ \Theta_{\beta x} \\ \Theta_{\beta y} \\ \Theta_{\beta z} \end{Bmatrix} \quad (\text{E.31})$$

The local displacement ( $\mu$ ) is calculated by using a geometrical transformation matrix ( $\gamma$ ) from the global displacement ( $\mu_g$ ), Equation E.32:

$$\{\mu\} = \begin{bmatrix} \gamma & . & . & . \\ . & \gamma & . & . \\ . & . & \gamma & . \\ . & . & . & \gamma \end{bmatrix} \cdot \{\mu_g\} \quad (\text{E.32})$$

The global deformation of the bond ( $\mu_g$ ) is stored in a vector, Equation E.33, where:

- $d_{gAx}, d_{gAy}, d_{gAz}$  are the global translational displacements at point A;
- $\Theta_{gAx}, \Theta_{gAy}, \Theta_{gAz}$  are the local rotational displacements at point A;
- $d_{gBx}, d_{gBy}, d_{gBz}$  are the local translational displacements at point B;
- $\Theta_{gBx}, \Theta_{gBy}, \Theta_{gBz}$  are the local rotational displacements at point B.

$$\{\mu_g\} = \begin{pmatrix} d_{gAx} \\ d_{gAy} \\ d_{gAz} \\ \Theta_{gAx} \\ \Theta_{gAy} \\ \Theta_{gAz} \\ d_{gBx} \\ d_{gBy} \\ d_{gBz} \\ \Theta_{gBx} \\ \Theta_{gBy} \\ \Theta_{gBz} \end{pmatrix} \quad (\text{E.33})$$

The global translational ( $d_{gij}$ ) and rotational ( $\Theta_{gij}$ ) displacements are calculated by using the translational ( $V_{A-B(x,y,z)}$ ) and angular ( $\omega_{A-B(x,y,z)}$ ) velocity components of the particles (A and B) and the time step ( $\Delta t$ ), Equation E.34 and E.35:

$$d_{gij} = V_{ij} \cdot \Delta t, \quad \text{where } i = A, B \quad \text{and} \quad j = x, y, z \quad (\text{E.34})$$

$$\Theta_{gij} = \omega_{ij} \cdot \Delta t, \quad \text{where } i = A, B \quad \text{and} \quad j = x, y, z \quad (\text{E.35})$$

The bond can break any time during the simulation, if one of the actual bond stresses (compressive, tensile, or shear) reaches its predefined maximal value. In case of the compressive stress, the break condition is defined by using the actual compressive stress in the bond ( $\sigma_C$ ) and the predefined maximal compressive stress ( $\sigma_{Cmax}$ ), Equation E.36

$$\sigma_C < \sigma_{Cmax} \quad (\text{E.36})$$

The actual compressive stress of the bond ( $\sigma_C$ ) is calculated by using the compressive force at the contact points ( $F_{\alpha x-\beta x}$ ), the cross sectional area of the bond ( $A_b$ ), the second moment of area of the bond ( $I_b$ ), the radius of the bond ( $r_b$ ) and the bending moment components ( $M_{\alpha y} - \beta z$ ), Equation E.37:

$$\sigma_C = -\min(\sigma_{Ci}) = -\min\left(\frac{F_{ix}}{A_b} - \frac{r_b \cdot \sqrt{M_{iy}^2 + M_{iz}^2}}{I_b}\right), \quad \text{where } i = \alpha, \beta \quad (\text{E.37})$$

The predefined maximal compressive stress ( $\sigma_{Cmax}$ ) is calculated by using the mean compressive strength ( $S_C$ ), the coefficient of variation for the compressive strength ( $\zeta_C$ ) and a random multiplier ( $N$ ), Equation E.38:

$$\sigma_{Cmax} = S_C \cdot ((\zeta_C \cdot N) + 1) \quad (\text{E.38})$$

The value of the random multiplier ( $N$ ) is constant during the calculations, while, the value of the coefficient of variation usually varies in the range of 0.0 ... 1.0. If we take into consideration the limits, the following statements can be drawn:

- when  $\zeta_C=0$ , all the bonds have the same predefined maximal stress ( $\sigma_{Cmax}$ ) that is equal with the mean compressive strength ( $S_C$ );
- when  $\zeta_C=1$ , the predefined maximal stress ( $\sigma_{Cmax}$ ) of the bonds show a Gaussian distribution in such a way, the mean of the predefined maximal stress ( $\sigma_{Cmax}$ ) is equal with the mean compressive strength ( $S_C$ ).

An comparison on three different values (0.2-0.4-0.8) for the coefficient of variation of strength ( $\zeta_C$ ) is presented on Figure E.4, where the mean compressive strength ( $S_C$ ) was 500 MPa in each case. The same methodology is also applied for the maximal tensile ( $\sigma_{Tmax}$ ) and shear ( $\tau_{max}$ ) stresses.

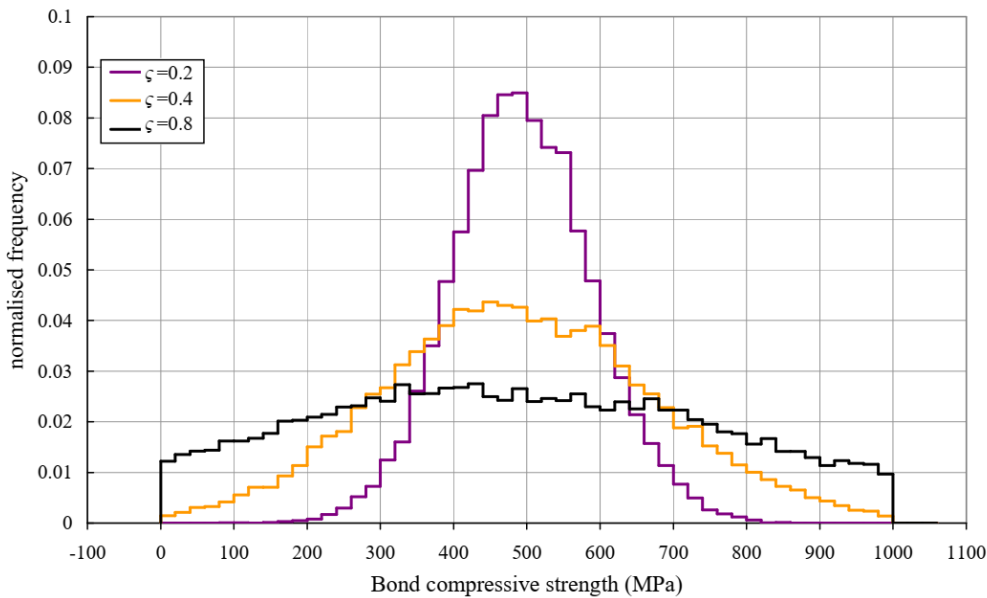


FIGURE E.4: Comparing three values for coefficient of variation of strength.

In case of the tensile stress, the break condition is defined by using the actual tensile stress in the bond ( $\sigma_T$ ) and the predefined maximal tensile stress ( $\sigma_{Tmax}$ ), Equation E.39

$$\sigma_T < \sigma_{Tmax} \quad (\text{E.39})$$

The actual tensile stress of the bond ( $\sigma_T$ ) is calculated by using the tensile force at the contact points ( $F_{\alpha x-\beta x}$ ), the cross sectional area of the bond ( $A_b$ ), the second moment of area of the bond ( $I_b$ ), the radius of the bond ( $r_b$ ) and the bending moment components ( $M_{\alpha y} - \beta z$ ), Equation E.40:

$$\sigma_T = \max(\sigma_{Ti}) = \max \left( \frac{F_{ix}}{A_b} + \frac{r_b \cdot \sqrt{M_{iy}^2 + M_{iz}^2}}{I_b} \right), \text{ where } i = \alpha, \beta \quad (\text{E.40})$$

The predefined maximal tensile stress ( $\sigma_{Tmax}$ ) is calculated by using the mean tensile strength ( $S_T$ ), the coefficient of variation for the tensile strength ( $\zeta_T$ ) and a random multiplier ( $N$ ), Equation E.41:

$$\sigma_{Tmax} = S_T \cdot ((\zeta_T \cdot N) + 1) \quad (\text{E.41})$$

In case of the shear stress, the break condition is defined by using the actual shear stress in the bond ( $\tau$ ) and the predefined maximal shear stress ( $\tau_{max}$ ), Equation E.42

$$\tau < \tau_{max} \quad (\text{E.42})$$

The actual shear stress of the bond ( $\tau$ ) is calculated by using the shear force at the contact point  $\alpha$  ( $F_{\alpha y-z}$ ), the cross sectional area of the bond ( $A_b$ ), the second moment of area of the bond ( $I_b$ ), the radius of the bond ( $r_b$ ) and the bending moment components ( $M_{\alpha x}$ ), Equation E.43:

$$\tau = \left( \frac{|M_{\alpha x}| \cdot r_b}{2 \cdot I_b} + \frac{4 \cdot \sqrt{F_{\alpha y}^2 + F_{\alpha z}^2}}{3 \cdot A_b} \right) \quad (\text{E.43})$$

The predefined maximal shear stress ( $\tau_{max}$ ) is calculated by using the mean shear strength ( $S_S$ ), the coefficient of variation for the shear strength ( $\zeta_S$ ) and a random multiplier ( $N$ ), Equation E.44:

$$\tau_{max} = S_S \cdot ((\zeta_S \cdot N) + 1) \quad (\text{E.44})$$

A built-in viscous damping is responsible for the numerical stability of the bonded system. By using the value of the global damping coefficient ( $\iota_d$ ), the damping forces and moments are calculated by Equation E.45 and E.46:

$$F_{di} = -\iota_d \cdot |F_i| \cdot \frac{V_i}{|V_i|}, \text{ where } i = x, y, z \quad (\text{E.45})$$

$$M_{di} = -\iota_d \cdot |M_i| \cdot \frac{\omega_i}{|\omega_i|}, \text{ where } i = x, y, z \quad (\text{E.46})$$

If the bond between two particles breaks, then the Hertz-Mindlin contact model will be activated between them.